

UNIVERSITY OF NOTTINGHAM  
SCHOOL OF CIVIL ENGINEERING

**CFD and Field Testing of a Naturally  
Ventilated Full-scale Building**

by

Tong Yang, BEng MSc

Thesis submitted to The University of Nottingham for  
the degree of Doctor of Philosophy

May 2004

*This thesis is dedicated to my beloved parents, who have been giving me  
never-ending love and absolute support through life.*

## ABSTRACT

Natural ventilation has the potential to provide good indoor air quality, thermal comfort for occupants, and can also save energy and reduce CO<sub>2</sub> emissions. Computational fluid dynamics (CFD) offers detailed information about indoor flow patterns, air movement, temperature and local draught distribution in buildings, so it has unique advantages as an efficient and cost-effective tool for optimum design in a complex built environment.

This thesis shows the use of CFD to simulate the coupled external and internal flow field around a 6m cubic building with two small openings. To study both wind driven and combined wind and buoyancy driven cross ventilation through a full-scale cubic structure, un-structured grid CFD and a steady envelope flow model were applied to calculate mean ventilation rates. To validate the CFD results, full-scale experiments were undertaken under various weather conditions in England.

For wind driven ventilation RANS model predictions were proved reliable when wind directions were near normal to the ventilation openings, i.e. 0°~30°. However, when the fluctuating ventilation played a more dominant role than the mean flow (90°) RANS models were incapable of predicting the total ventilation rate. Improved results may be expected by applying more sophisticated turbulence models, such as LES, weighted quasi-steady approximations, or unsteady envelope flow models. In the thesis experience on the modelling of combined wind and thermal effects is outlined and feedback is provided to CFD code developers to enable further improvements for building ventilation studies. The full-scale field testing data from this study is valuable for comparison with wind tunnel results and validation of CFD applications.

## **ACKNOWLEDGEMENTS**

This research could never have come about without the financial support of the School of Civil Engineering, the University of Nottingham and Silsoe Research Institute.

First and foremost, my thanks go to my principal supervisor Dr Nigel G. Wright for his great support and guidance throughout the project. His encouragement and broad influences have given me so much confidence to pursue professional knowledge and develop my career.

I am also grateful to Dr David W. Etheridge for his invaluable comments and error-spotting skills in data analysis. His experience in academia and industry has provided me a vivid insight into theory and design practice.

My sincere thanks also go to Dr Andrew D. Quinn who has helped me with his inspirational contributions, constructive comments during CFD simulation, experimental program and proof reading. His bright smile has enlightened my time spent in Silsoe Research Institute.

Additional thanks go to Dr Roger Hoxey for his valuable advice in wind engineering applications, Dr David Hargeraves for his expertise and practical help for applying CFD effectively, and Dr Guohui Gan for his supportive comments to comprehend CFD technique and ventilation modelling.

I must also express my gratitude to Buro Happold Consulting Engineers (industrial sponsor), who provided me a wonderful opportunity to apply research findings into commercial design project. I would also like to acknowledge the assistance of the staff of Silsoe Research Institute.

Last, but no means least, special thanks to my great friends who have stood by me during difficult times.

## TABLE OF CONTENTS

	Pages
Abstract	i
Acknowledgements	ii
Table of Contents	iii-vii
List of Figures	viii-xiii
List of Tables	xiv
Nomenclature	xv-xvii
Published Papers	xviii
<b>CHAPTER 1 INTRODUCTION.....</b>	<b>1</b>
1.1 RESEARCH OBJECTIVES .....	4
1.2 STRUCTURE OF THE THESIS.....	5
<b>CHAPTER 2 LITERATURE REVIEW.....</b>	<b>8</b>
2.1 INTRODUCTION.....	9
2.2 BUILDING VENTILATION DESIGN.....	9
2.2.1 <i>Critical parameters in ventilation system design</i> .....	10
2.2.2 <i>Natural ventilation versus mechanical ventilation</i> .....	11
2.2.3 <i>Key barriers for implementing a natural ventilation strategy</i> .....	15
2.3 DESIGN PROCEDURE .....	16
2.4 ANALYSIS AND DESIGN TOOLS.....	18
2.4.1 <i>Natural ventilation system</i> .....	20
2.4.2 <i>Envelope flow theories</i> .....	22
2.5 CFD APPLICATION IN VENTILATION STUDIES.....	24
2.6 EXPERIMENTAL TECHNOLOGY.....	27
2.6.1 <i>Tracer gas techniques</i> .....	28
2.6.2 <i>Scale (physical) modelling</i> .....	28
2.6.2.1 Wind tunnel technique .....	28
2.6.2.2 Salt-bath technique.....	30

2.6.2.3 Fine-bubble technique.....	30
2.6.2.4 Pros and cons of scale-modelling techniques .....	30
2.7 SUMMARY .....	32
2.8 UNRESOLVED ISSUES .....	33
<b>CHAPTER 3    METHODOLOGY.....</b>	<b>34</b>
3.1 INTRODUCTION.....	35
3.2 WIND ENGINEERING.....	35
3.2.1 <i>The atmospheric boundary layer (ABL)</i> .....	35
3.2.2 <i>Wind effects on buildings</i> .....	37
3.2.2.1 Turbulent flow.....	38
3.3 COMPUTATIONAL FLUID DYNAMICS (CFD).....	39
3.3.1 <i>Overview of CFD applications</i> .....	40
3.3.2 <i>Governing Equations</i> .....	41
3.3.3 <i>Numerical grid</i> .....	44
3.3.4 <i>Turbulence modelling</i> .....	45
3.3.4.1 Overview of turbulence models .....	46
3.3.4.2 Reynolds Averaged Navier-Stokes (RANS) models .....	48
3.3.4.3 Non-linear $k$ - $\varepsilon$ model.....	53
3.3.4.4 Large Eddy Simulation (LES).....	54
3.3.5 <i>Wall functions</i> .....	54
3.3.6 <i>Discretisation scheme</i> .....	55
3.3.7 <i>Credibility of CFD simulation</i> .....	58
3.3.8 <i>Unstructured grid CFD code – CFX5</i> .....	59
3.3.8.1 Turbulence models.....	60
3.3.8.2 Numerical scheme.....	60
3.3.8.3 Coupled solver .....	60
3.3.8.4 Near wall treatment methods .....	61
3.4 BUILDING ENVELOPE FLOWS .....	61
3.4.1 <i>Wind effect</i> .....	61
3.4.2 <i>Buoyancy effect</i> .....	62
3.4.3 <i>Combined wind and buoyancy effects</i> .....	63
3.5 MATHEMATICAL MODELS OF ENVELOPE FLOWS .....	63
3.5.1 <i>Air leakage</i> .....	63

3.5.2 <i>Envelope flow models</i> .....	64
3.5.2.1 Pseudo-steady model with Boussinesq approximation .....	66
3.5.2.2 Pseudo-steady model without Boussinesq approximation.....	68
3.6 EXPERIMENTAL TECHNOLOGY .....	69
3.6.1 <i>Ultrasonic technique</i> .....	70
3.6.1.1 Principle of operation.....	70
3.6.2 <i>Tracer Gas Techniques</i> .....	70
3.6.2.1 Concentration-decay technique.....	71
3.6.2.2 Constant injection technique.....	71
3.7 WIND TUNNEL MODELLING .....	73
3.7.1 <i>Similarity requirements</i> .....	73
3.7.2 <i>Similarity parameters in building ventilation studies</i> .....	74
3.7.2.1 Wind effect alone - Reynolds numbers.....	75
3.7.2.2 Combined wind and buoyancy effects - Archimedes number .....	76
3.8 SUMMARY .....	77
<b>CHAPTER 4 PRELIMINARY CFD STUDY OF VENTILATION IN A BUILDING MODEL .....</b>	<b>79</b>
4.1 INTRODUCTION.....	80
4.2 CFD PREDICTIONS.....	81
4.3 COMPARISON OF CFD AND WIND TUNNEL TEST RESULTS.....	83
4.4 DISCUSSION.....	91
<b>CHAPTER 5 VERIFICATION &amp; VALIDATION OF THE CFD MODEL. 93</b>	
5.1 INTRODUCTION.....	94
5.2 ATMOSPHERIC BOUNDARY LAYER (ABL) REPRODUCTION IN CFD .....	94
5.2.1 <i>ABL boundary condition specification</i> .....	94
5.2.2 <i>Grid sensitivity tests results</i> .....	96
5.2.3 <i>Comparison of CFX5 and CWE2000 competition results</i> .....	103
5.3 FLOW FIELD MODELLING AROUND A CUBE .....	107
5.3.1 <i>Computational domain and boundary conditions</i> .....	107
5.3.2 <i>Grid independence tests</i> .....	108
5.3.3 <i>Convergence criteria</i> .....	114
5.3.4 <i>Surface pressure distribution for the 0° case</i> .....	116
5.3.5 <i>Velocity field and turbulence intensity for the 0° case</i> .....	121

5.3.6	<i>Surface pressure distribution for the 45° case</i> .....	126
5.3.7	<i>Velocity field and turbulence intensity for the 45° case</i> .....	129
5.4	DISCUSSION.....	132
<b>CHAPTER 6   CFD SIMULATIONS OF CUBE ENVELOPE .....</b>		<b>136</b>
6.1	INTRODUCTION.....	137
6.2	CFD TEST CONFIGURATION.....	137
6.3	CFD SIMULATIONS OF WIND INDUCED VENTILATION .....	138
6.3.1	<i>Grid settings</i> .....	138
6.3.2	<i>Convergence tests and solution accuracy</i> .....	141
6.3.3	<i>Turbulence model effect</i> .....	146
6.3.4	<i>Surface pressure distribution on the ventilated cube</i> .....	153
6.3.5	<i>Mean airflow pattern inside the cube</i> .....	153
6.3.6	<i>CFD predictions of wind induced ventilation rates</i> .....	156
6.3.7	<i>CFD predictions of wind and thermal effects</i> .....	158
6.3.7.1	<i>Geometry set-up for coupled external and internal flows</i> .....	158
6.3.7.2	<i>Combined wind and forced (or natural) convection scenario</i> .....	161
6.3.7.3	<i>Possible improvement in the CFX5 software</i> .....	172
6.4	SUMMARY AND DISCUSSION .....	173
<b>CHAPTER 7   FIELD STUDY OF VENTILATION RATES IN THE 6M</b>		
<b>          CUBE .....</b>		<b>175</b>
7.1	INTRODUCTION.....	176
7.2	DESCRIPTION OF THE CUBE STRUCTURE .....	176
7.3	LEAKAGE TEST.....	177
7.3.1	<i>Leakage tester</i> .....	177
7.3.2	<i>Leakage rate measurements</i> .....	178
7.4	INFILTRATION TEST .....	179
7.4.1	<i>Experiment apparatus</i> .....	181
7.4.2	<i>Infiltration rates test</i> .....	182
7.4.2.1	<i>CO analyser calibration</i> .....	182
7.4.2.2	<i>Infiltration rates measurements</i> .....	182
7.4.3	<i>Building leakage/infiltration feature</i> .....	185
7.5	VENTILATION FLOW RATE MEASUREMENTS.....	187
7.5.1	<i>Sampling system</i> .....	187

7.5.2 <i>Experimental methods</i> .....	191
7.5.2.1 Tracer gas decay method.....	192
7.5.2.2 Point pressure difference method.....	193
7.5.2.3 Surface pressure difference method.....	194
7.5.2.4 Mean flow speed method.....	194
7.5.3 <i>Results and discussions</i> .....	194
7.5.3.1 Wind directions at 0°~30° cases.....	196
7.5.3.2 Wind directions at 34°~60° cases.....	201
7.5.3.3 Wind directions at 75°~110° cases.....	203
7.5.3.4 Wind directions at 155°~180° cases.....	205
7.6 SUMMARY OF FIELD STUDY.....	207
<b>CHAPTER 8 COMPARISON OF RESULTS FOR CFD AND FULL-SCALE TESTS.....</b>	<b>209</b>
8.1 INTRODUCTION.....	210
8.2 MEASURED VENTILATION RATES AND CFD PREDICTIONS.....	211
8.2.1 <i>Wind directions between 0°~30°</i> .....	211
8.2.2 <i>Wind directions at 90°</i> .....	215
8.2.3 <i>Wind directions at 180°</i> .....	217
8.3 DISCUSSION.....	217
<b>CHAPTER 9 CONCLUSIONS.....</b>	<b>220</b>
9.1 SUMMARY OF CONTRIBUTIONS.....	221
9.2 MAIN CONCLUSIONS.....	222
9.3 OTHER CONCLUSIONS.....	223
9.3.1 <i>CFD Simulations</i> .....	223
9.3.2 <i>Ventilation measurements in a full-scale cubic building</i> .....	224
9.4 RECOMMENDATIONS FOR FUTURE RESEARCH.....	226
 REFERENCES	
 APPENDIX A	
 APPENDIX B	

## LIST OF FIGURES

<i>Figure 1-1</i>	<i>The building – an integrated dynamic system</i> .....	2
<i>Figure 2-1</i>	<i>European climate zones</i> .....	11
<i>Figure 2-2</i>	<i>A traditional dwelling in Britain</i> .....	12
<i>Figure 2-3</i>	<i>Architecture responding to the tropical environment in Australia</i> .....	12
<i>Figure 2-4</i>	<i>Evaporative cooling in hot arid climate</i> .....	13
<i>Figure 2-5</i>	<i>Inland Revenue Building, Nottingham</i> .....	14
<i>Figure 2-6</i>	<i>Schematic of single-sided ventilation</i> .....	21
<i>Figure 2-7</i>	<i>Schematic of cross ventilation</i> .....	22
<i>Figure 3-1</i>	<i>Wind speed variation with height and terrain conditions</i> .....	36
<i>Figure 3-2</i>	<i>Hierarchy of turbulence models</i> .....	47
<i>Figure 3-3</i>	<i>Flow parameters in ventilation studies</i> .....	64
<i>Figure 3-4</i>	<i>Ultrasonic anemometer (Gill Instrument Research R3)</i> .....	69
<i>Figure 3-5</i>	<i>Schematic diagram of constant injection technique</i> .....	72
<i>Figure 4-1</i>	<i>The 1/30 scale building model with two identical circular openings (diameter = 10.9mm)</i> .....	80
<i>Figure 4-2</i>	<i>CFD computational domain for the 1/30 scale building model</i> .....	82
<i>Figure 4-3</i>	<i>The unstructured surface mesh around the 1/30 model</i> .....	82
<i>Figure 4-4</i>	<i>CFD prediction of the surface pressure distribution on 1/30 model for 0° case (<math>U_{ref}=4m/s</math>)</i> .....	85
<i>Figure 4-5</i>	<i>CFD prediction of the surface pressure distribution on 1/30 model for 180° case (<math>U_{ref}=5m/s</math>)</i> .....	85
<i>Figure 4-6</i>	<i>CFD prediction of the velocity vector plot around 1/30 model for 0° case – central section view (<math>U_{ref}=4m/s</math>)</i> .....	86
<i>Figure 4-7</i>	<i>CFD prediction of the velocity vector plot around 1/30 model for 180° case – central section view (<math>U_{ref}=5m/s</math>)</i> .....	86
<i>Figure 4-8</i>	<i>CFD and wind tunnel tests results comparison – lower opening discharge coefficient vs opening Reynolds number</i> .....	88
<i>Figure 4-9</i>	<i>CFD and wind tunnel tests results comparison – roof opening discharge coefficient vs opening Reynolds number</i> .....	88
<i>Figure 4-10</i>	<i>CFD and wind tunnel tests results comparison - square root of pressure coefficient difference vs building Reynolds number</i> .....	89

Figure 4-11	Ventilation rates comparison between CFD and wind tunnel tests (discharge coefficient = 0.65) .....	90
Figure 4-12	Ventilation rates comparison between CFD and wind tunnel tests (discharge coefficient = 0.77) .....	90
Figure 5-1	Grid sensitivity tests – inlet & outlet profiles on coarse & medium grids .....	99
Figure 5-2	Grid sensitivity tests – inlet & outlet profiles on two medium grids ..	100
Figure 5-3	Grid sensitivity tests – inlet & outlet profiles on fine & medium grids .....	101
Figure 5-4	ABL comparisons – inlet & outlet profiles.....	104
Figure 5-5	Mean streamwise velocity profile near the ground.....	106
Figure 5-6	CFD simulation domain for a 6m cube.....	107
Figure 5-7	Unstructured mesh around the cube .....	109
Figure 5-8	Grid independence tests - pressure coefficients along the streamwise vertical centreline of the cube .....	110
Figure 5-9	Grid independent tests - pressure coefficients along the transverse vertical centreline of the cube .....	110
Figure 5-10	Grid independent tests - pressure coefficients along the horizontal mid- height centreline of the cube .....	111
Figure 5-11	Turbulence models effects on the streamwise pressure distribution..	114
Figure 5-12	Pressure coefficients comparison for the cube - streamwise vertical centreline section [0° case] .....	117
Figure 5-13	Streamwise vertical centreline section pressure coefficients from the Silsoe full-scale test and 15 wind tunnel tests (0° case) .....	118
Figure 5-14	Pressure coefficients comparison for the cube - transverse vertical centreline section [0° case] .....	120
Figure 5-15	Pressure coefficients comparison for the cube - horizontal mid-height section [0° case] .....	120
Figure 5-16	Pressure coefficients comparison for the cube - roof corner tapping points [0° case] .....	121
Figure 5-17	Illustration of measurement points around the cube.....	122
Figure 5-18	Velocity coefficients comparison around the cube - streamwise component $u/U_{ref}$ [0° case] .....	123

Figure 5-19	Velocity coefficients comparison around the cube - transverse component $v/U_{ref}$ [ $0^\circ$ case] .....	123
Figure 5-20	Velocity coefficients comparison around the cube - vertical component $w/U_{ref}$ [ $0^\circ$ case] .....	124
Figure 5-21	Turbulence level comparison around the cube - turbulent kinetic energy $k/U_{ref}^2$ [ $0^\circ$ case] .....	124
Figure 5-22	Pressure coefficients comparison on the cube - vertical centreline section [ $45^\circ$ case] .....	127
Figure 5-23	Pressure coefficients comparison on the cube - horizontal mid-height section [ $45^\circ$ case] .....	127
Figure 5-24	Pressure coefficients comparison on the cube - roof corner tapping points [ $45^\circ$ case] .....	128
Figure 5-25	Velocity coefficients comparison around the cube - streamwise component $u/U_{ref}$ [ $45^\circ$ case] .....	130
Figure 5-26	Velocity coefficients comparison around the cube - transverse component $v/U_{ref}$ [ $45^\circ$ case] .....	130
Figure 5-27	Velocity coefficients comparison around the cube - vertical component $w/U_{ref}$ [ $45^\circ$ case] .....	131
Figure 5-28	Turbulence level comparison around the cube - turbulent kinetic energy $k/U_{ref}^2$ [ $45^\circ$ case] .....	131
Figure 6-1	Schematic diagram of the 6m cube with two rectangular openings...	137
Figure 6-2	Unstructured mesh around the cube with openings .....	139
Figure 6-3	Two pressure tapping points located 0.5m apart from each opening centre vertically.....	140
Figure 6-4	Grid sensitivity tests – pressure coefficients along vertical centreline on coarse, medium and fine grids .....	140
Figure 6-5	Solution accuracy tests – mean speed & mass flowrate through the lower & higher level openings .....	143
Figure 6-6	Mesh details at the ventilation opening.....	143
Figure 6-7	Convergence sensitivity tests – pressure coefficients on the fine grid	145
Figure 6-8	Turbulence model effects – mean speed & mass flowrate through the lower & higher level openings .....	147
Figure 6-9	Turbulence model effects - pressure coefficients along vertical centreline .....	148

<i>Figure 6-10 Velocity vector plot around the cube predicted by the standard <math>k-\varepsilon</math> model</i>	150
<i>Figure 6-11 Velocity vector plot around the cube predicted by the RNG <math>k-\varepsilon</math> model</i>	150
<i>Figure 6-12 Turbulent kinetic energy distribution around the ventilated cube predicted by the standard <math>k-\varepsilon</math> model</i>	151
<i>Figure 6-13 Turbulent kinetic energy distribution around the ventilated cube predicted by the RNG <math>k-\varepsilon</math> model</i>	151
<i>Figure 6-14 Velocity vector plot around the cube [0° case]</i>	154
<i>Figure 6-15 Velocity vector plot around the cube [180° case]</i>	154
<i>Figure 6-16 Velocity vector plot around the cube [90° case]</i>	155
<i>Figure 6-17 Velocity vector plot around the cube [45° case]</i>	155
<i>Figure 6-18 Geometry set-up1 (cube with a heating patch at floor level)</i>	159
<i>Figure 6-19 Temperature contour plot on centre plane (cube with a heating patch at floor level)</i>	160
<i>Figure 6-20 Geometry set-up2 (cube with a 0.6m cubic box above the floor)</i>	160
<i>Figure 6-21 Velocity vector plot in the cube with a centre heater</i>	162
<i>Figure 6-22 Temperature stratification in the cube with a centre heater</i>	162
<i>Figure 6-23 Velocity vector plot above the ground 5m in the cube with a centre heater</i>	163
<i>Figure 6-24 Velocity vector plot above the ground 1m in the cube with a centre heater</i>	163
<i>Figure 6-25 Velocity vector plot in the cube with a side heater</i>	165
<i>Figure 6-26 Temperature stratification in the cube with a side heater</i>	165
<i>Figure 6-27 Velocity vector plot above the ground 5m in the cube with a side heater</i>	166
<i>Figure 6-28 Velocity vector plot above the ground 1m in the cube with a side heater</i>	166
<i>Figure 6-29 Temperature contour plots in the cube with a centre heater (y=-2.5,-1.5,-0.5,0.5,1.5&amp;2.5m)</i>	167
<i>Figure 6-30 Temperature contour plots in the cube with a centre located hot surface (y=-2.5,-1.5,-0.5,0.5,1.5&amp;2.5m)</i>	168

Figure 6-31	Temperature contour plots in the cube with a side heater ( $y=-2.5,-1.5,-0.5,0.5,1.5&2.5m$ ).....	169
Figure 6-32	Temperature contour plots in the cube with a side located hot surface ( $y=-2.5,-1.5,-0.5,0.5,1.5&2.5m$ ).....	170
Figure 7-1	The full-scale 6m cube on the SRI wind engineering site.....	176
Figure 7-2	Schematic of leakage measurement .....	178
Figure 7-3	Reference mast located 18m upstream of the cube .....	180
Figure 7-4	Leakage rate against pressure difference across the cube.....	180
Figure 7-5	Schematic of experiment rig .....	181
Figure 7-6	Infiltration test using tracer gas decay method.....	184
Figure 7-7	Non-dimensional curves for determining ventilation of a building with openings on only two walls (Etheridge and Standberg, 1996).....	185
Figure 7-8	Two ventilation openings on the opposite walls of the 6m cube .....	188
Figure 7-9	Pressure tapping points on the cube surface.....	189
Figure 7-10	Wind incident angles (cube plan view).....	189
Figure 7-11	Reference weather data – 10-minute mean wind speed and direction.....	190
Figure 7-12	Reference weather data - 1-minute mean outdoor & indoor temperatures.....	191
Figure 7-13	Tracer gas decay record (logarithm linear fitting-curve).....	192
Figure 7-14	Nondimensional ventilation rates at wind directions $0^{\circ}\sim 30^{\circ}$ .....	197
Figure 7-15	Relative error band of the measured ventilation rates at $0^{\circ}\sim 30^{\circ}$ .....	199
Figure 7-16	Nondimensional ventilation rates at wind directions $34^{\circ}\sim 60^{\circ}$ .....	202
Figure 7-17	Nondimensional ventilation rates at wind directions $75^{\circ}\sim 110^{\circ}$ .....	204
Figure 7-18	Nondimensional ventilation rates at wind directions $155^{\circ}\sim 180^{\circ}$ .....	206
Figure 8-1	Measured and predicted nondimensional ventilation rates at $0^{\circ}\sim 30^{\circ}$ .....	212
Figure 8-2	Measured and predicted ventilation rates around $0^{\circ}$ .....	213
Figure 8-3	Measured and predicted ventilation rates around $10^{\circ}$ .....	214
Figure 8-4	Measured and predicted ventilation rates around $30^{\circ}$ .....	214
Figure 8-5	Measured and predicted nondimensional ventilation rates around $90^{\circ}$ .. .....	216
Figure 8-6	Measured and predicted ventilation rates around $90^{\circ}$ .....	216
Figure 8-7	Measured and predicted nondimensional ventilation rates around $180^{\circ}$ .....	218
Figure 8-8	Measured and predicted ventilation rates around $180^{\circ}$ .....	218

<i>Figure A-1</i>	<i>Surface pressure distribution1 [0° case]</i> .....	<i>A1</i>
<i>Figure A-2</i>	<i>Surface pressure distribution2 [0° case]</i> .....	<i>A1</i>
<i>Figure A-3</i>	<i>Surface pressure distribution1 [180° case]</i> .....	<i>A2</i>
<i>Figure A-4</i>	<i>Surface pressure distribution2 [180° case]</i> .....	<i>A2</i>
<i>Figure A-5</i>	<i>Surface pressure distribution1 [90° case]</i> .....	<i>A3</i>
<i>Figure A-6</i>	<i>Surface pressure distribution2 [90° case]</i> .....	<i>A3</i>
<i>Figure A-7</i>	<i>Surface pressure distribution1 [45° case]</i> .....	<i>A4</i>
<i>Figure A-8</i>	<i>Surface pressure distribution2 [45° case]</i> .....	<i>A4</i>
<i>Figure A-9</i>	<i>Velocity vector plot plan view above the ground 5m [0° case]</i> .....	<i>A5</i>
<i>Figure A-10</i>	<i>Velocity vector plot plan view above the ground 1m [0° case]</i> .....	<i>A5</i>
<i>Figure A-11</i>	<i>Velocity vector plot plan view above the ground 5m [180° case]</i> .....	<i>A6</i>
<i>Figure A-12</i>	<i>Velocity vector plot plan view above the ground 1m [180° case]</i> .....	<i>A6</i>
<i>Figure A-13</i>	<i>Velocity vector plot plan view above the ground 5m [90° case]</i> .....	<i>A7</i>
<i>Figure A-14</i>	<i>Velocity vector plot plan view above the ground 1m [90° case]</i> .....	<i>A7</i>
<i>Figure A-15</i>	<i>Velocity vector plot plan view above the ground 5m [45° case]</i> .....	<i>A8</i>
<i>Figure A-16</i>	<i>Velocity vector plot plan view above the ground 1m [45° case]</i> .....	<i>A8</i>
<i>Figure B-1</i>	<i>Site plan of the Silsoe 6m cube</i> .....	<i>B1</i>

## LIST OF TABLES

<i>Table 2-1</i>	<i>Approaches for natural ventilation design</i> .....	19
<i>Table 4-1</i>	<i>Assessment of ventilation rates from CFD simulation</i> .....	87
<i>Table 5-1</i>	<i>Boundary conditions in CFX5.5.1</i> .....	96
<i>Table 5-2</i>	<i>Mesh types for ABL simulation</i> .....	97
<i>Table 5-3</i>	<i>The ABL profile differences on four types of grids (%)</i> .....	98
<i>Table 5-4</i>	<i>ABL Modelling details</i> .....	103
<i>Table 5-5</i>	<i>Mesh settings for a 6m cube in the ABL</i> .....	108
<i>Table 5-6</i>	<i>Modelling details for the cube</i> .....	116
<i>Table 6-1</i>	<i>Mesh types for the cube with ventilation openings</i> .....	138
<i>Table 6-2</i>	<i>Convergence tests criteria for the cube with openings</i> .....	141
<i>Table 6-3</i>	<i>CFD solutions accuracy for the cube with openings</i> .....	142
<i>Table 6-4</i>	<i>CFD solutions by different turbulence models</i> .....	147
<i>Table 6-5</i>	<i>Wind induced nondimensional mean ventilation rates in CFX5</i> .....	157
<i>Table 6-6</i>	<i>Mean ventilation rates introduced by combined wind and forced (or natural) convection [0° case]</i> .....	171
<i>Table 7-1</i>	<i>Infiltration test results using tracer gas decay technique</i> .....	183
<i>Table 7-2</i>	<i>Ventilation flow rate data analysis</i> .....	195
<i>Table 7-3</i>	<i>Nondimensional ventilation rates for 0°~30° cases</i> .....	196
<i>Table 7-4</i>	<i>Nondimensional ventilation rates for 34°~60° cases</i> .....	201
<i>Table 7-5</i>	<i>Nondimensional ventilation rates for 75°~110° cases</i> .....	203
<i>Table 7-6</i>	<i>Nondimensional ventilation rates for 155°~180° cases</i> .....	205
<i>Table 8-1</i>	<i>Experimental values selected for CFD simulations</i> .....	211
	<i>Summary of Tables 7-3, 4, 5 &amp; 6</i> .....	B2

## NOMENCLATURE

$a, b$	width, height of ventilation opening	m
$A$	area of the ventilation opening $A = a \cdot b$	m <sup>2</sup>
$Ar$	Archimedes number	dimensionless
$c$	speed of sound in air	340.3 m/s
$C_d$	discharge coefficient	dimensionless
$C_i, C_e$	internal, external concentration of tracer gas	ppm
$C_p$	surface pressure coefficient on buildings	dimensionless
$d$	opening diameter	m
$g$	gravitational acceleration	m/s <sup>2</sup>
$h$	relative height of ventilation openings	m
$H$	building height	m
$k$	kinetic energy of turbulence	m <sup>2</sup> /s <sup>2</sup>
$p$	pressure due to wind	Pa
$q_m$	mass flow rate	kg/s
$q_o$	volume flow rate through opening	m <sup>3</sup> /s
$Q$	mean ventilation rate	m <sup>3</sup> /s
$Re_b$	building Reynolds number, $Re_b \equiv \frac{U_{ref} H}{\nu}$	dimensionless
$Re_o$	opening Reynolds number, $Re_o \equiv \frac{q_o d}{A \nu}$	dimensionless

$t$	time	s
$T$	absolute temperature of air	K
$u, v, w$	streamwise, transverse, vertical velocity components	m/s
$u', v', w'$	fluctuating velocity components in $x, y, z$ directions	m/s
$\overline{u_i' u_j'}$	Reynolds stresses, ( $i, j$ , the tensor indicator)	$\text{m}^2/\text{s}^2$
$U, V, W$	mean velocity components in $x, y, z$ direction	m/s
$U_{ref}$	wind speed at reference height	m/s
$U_b$	buoyancy speed	m/s
$z$	height above ground	m
$z_0$	aerodynamic roughness length	m
$z_{ref}$	wind velocity reference height	m
$\alpha$	wind direction	deg
$\delta_{ij}$	Kronecker delta $\{ \delta_{ij} = 1 \text{ if } i = j \text{ or}$ $\delta_{ij} = 0 \text{ if } i \neq j \}$	
$\varepsilon$	turbulence dissipation rate	$\text{m}^2/\text{s}^3$
$\kappa$	von Karman's constant, $\kappa = 0.40$	
$\mu_t$	turbulent or eddy viscosity	$\text{kg}/\text{m}\cdot\text{s}$
$\nu$	kinematic viscosity	$\text{m}^2/\text{s}$
$\tau_w$	wall shear stress	$\text{kg}/\text{m}\cdot\text{s}^2$
$\rho$	air density	$\text{kg}/\text{m}^3$
$\rho_a$	average air density, $\rho_a \equiv \frac{\rho_e + \rho_i}{2}$	$\text{kg}/\text{m}^3$

$dC_p$	pressure coefficient difference, $C_{p1}-C_{p2}$ ,	dimensionless
$dp$	mean pressure difference	Pa
$dT$	mean temperature difference between interior and exterior	K
$d\rho$	density difference, $d\rho \equiv \rho_e - \rho_i$	kg/m <sup>3</sup>

#### Subscripts

1,2	opening number
$e$	external
$i$	internal
0	at ground level, $z = 0$

## PUBLISHED PAPERS

The following papers have been published as a result of this research:

**Yang, T.**, Wright, N.G., Etheridge, D.W. and Quinn, A.D. (2002), *Unstructured-grid CFD modelling of Natural Ventilation in a Full-scale Cube*, Proceedings of the 5<sup>th</sup> UK Conference on Wind Engineering (WES2002), Nottingham, UK, pp.141-144.

**Yang, T.**, Wright, N.G., Etheridge, D.W. and Quinn, A.D. (2003), *Natural Ventilation in a 6m Cube – Fullscale & CFD Investigation*, Proceedings of the 11<sup>th</sup> International Conference on Wind Engineering (ICWE2003), Lubbock, Texas, USA, pp.1127-1134.

**Yang, T.**, Wright, N.G., Etheridge, D.W. and Quinn, A.D. (2004), *CFD Application in Natural Ventilation Design*, Proceedings of the 3<sup>rd</sup> International Conference on Sustainable Energy Technologies (SET2004), Nottingham, UK, POE041.

# **Chapter 1 Introduction**

People spend 90% of their time live and work in buildings. Building ventilation provides the required amount of fresh air into a building under specified weather and environmental conditions. The process includes supplying air to and removing it from enclosures, distributing and circulating the air therein, or preventing indoor contamination. Maintaining the indoor thermal comfort for occupants imposes an energy load on buildings as illustrated in Figure 1-1.

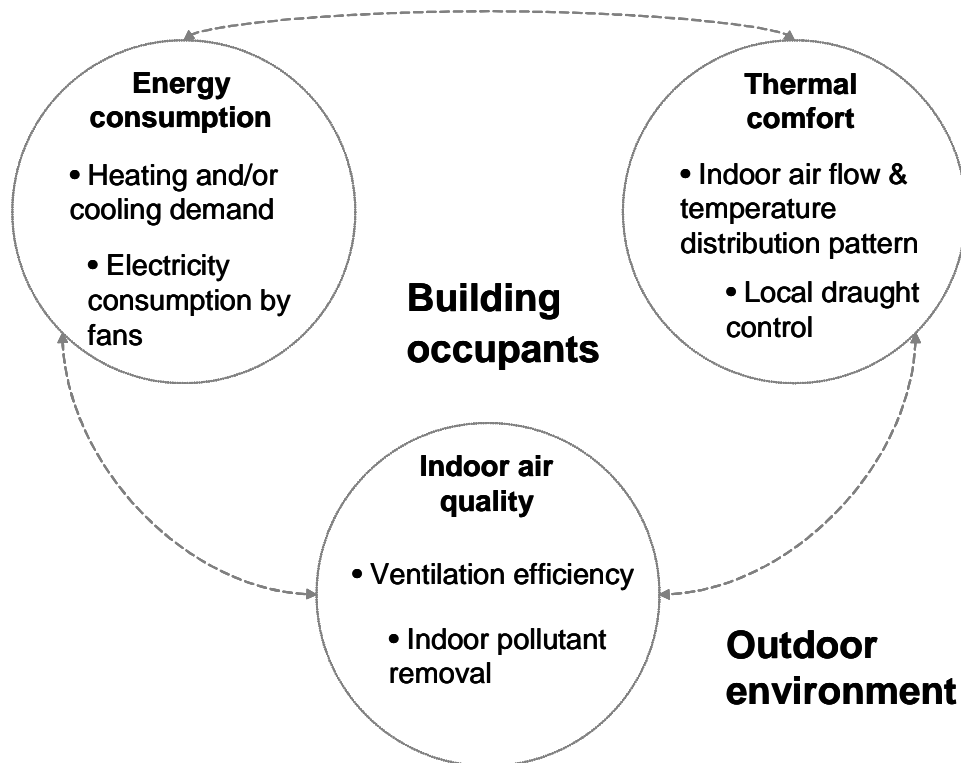


**Figure 1-1 The building – an integrated dynamic system**

Buildings use 40 to 50% of primary energy in the UK and other EU countries [Liddament and Orme 1998; CIBSE Briefing 6 2003]. Under the Kyoto protocol, the UK government set out the challenging goal in the Energy White Paper to reduce emissions of greenhouse gases – the main contributor to global warming - by 60% by around 2050 [DTI Energy White Paper 2003]. Energy efficiency in designing and operating buildings can make a big contribution to CO<sub>2</sub> emission reduction. New

low-energy buildings consume 50% less energy than existing buildings [CIBSE Briefing 8 2003].

Energy efficient design can only be achieved successfully through careful design of built form and services using renewable energy sources (wind, solar energy, etc.) and passive solutions [Liddament 1996]. Incorporating passive energy efficiency measures, such as daylighting and natural ventilation, offers the following potential environmental and commercial benefits:

- financial - from reduced construction, maintenance and energy costs
- employment – employees are usually more productive in quality work environments
- market share – from improved corporate reputation and profile
- greener image - symbolizes the designing and operating aspects.

The natural variation in wind and thermal buoyancy forces continuously changes the air flow into a naturally ventilated building. The development of useful tools dealing with the potential of natural ventilation and of design guidelines can have a significant effect on the utilisation of natural ventilation systems. Case studies in the European Energy Comfort 2000 project demonstrated the latest low energy techniques and the experiences gained during the design, construction and monitoring of non-domestic buildings [EC2000 Information Dossier 2 2000].

Recently developed hybrid ventilation technologies combine both natural ventilation and mechanical systems but use different features of the systems at different times of the day or season of the year [Heiselberg 1998]. However, better knowledge of natural ventilation is still fundamental for obtaining optimal implementation of hybrid ventilation strategies.

In general three approaches are available to study natural ventilation: empirical/semi-empirical, experimental and computational. The first two approaches do not provide sufficient information on natural ventilation and are limited to relatively simple geometry. CFD techniques offer detailed information about indoor flow patterns, air movement, temperature and local draught distribution in buildings, so that it has unique advantages as an efficient and cost-effective tool for optimum design in a complex built environment.

Recent development of CFD techniques in natural ventilation studies has been applied to modelling external flow around buildings and indoor thermal comfort simulation separately [Cook et al. 2003; Chen 2004]; simulating the combined indoor and outdoor airflows through large openings in wind tunnel models [Jiang et al. 2003a]; in a full-scale building placed in wind tunnel [Nishizawa et al. 2003] and in full-scale buildings located in the natural environment [Straw 2000].

Few experimental studies have been undertaken for cross ventilation in a full-scale cubic building with small openings in the natural environment. The present field data contributes to the small database of information on natural ventilation and is valuable for CFD model validations. Hence the key objective of this study is to evaluate the effectiveness with which CFD can capture the coupled external and internal flow fields under natural wind and buoyancy forces and predict the mean ventilation rate for design purposes.

### **1.1 Research objectives**

The project aimed to achieve a substantial improvement in the understanding of the natural ventilation process by utilisation of computational fluid dynamics (CFD), theoretical and experimental techniques. The overall objective was to assess natural

ventilation in a full-scale building induced by combined wind and buoyancy forces.

This project would:

- Verify and validate a CFD model for the study of natural ventilation in buildings
- Collect high quality full-scale experimental data for CFD validation
- Formulate guidelines for modelling natural ventilation in design practice

## **1.2 Structure of the thesis**

Chapter 2 contains a brief review of the techniques currently available for natural ventilation technologies and strategies. It also identifies the research problem, limitations and research gaps. In Chapter 3 the fundamental theories and study methods of natural ventilation in buildings are outlined. In particular, the basic principles and methods used in CFD techniques, such as the principles of numerical discretisation, descriptions of turbulence models, differencing schemes and accuracy control in CFD simulations are given in Section 3.3. The simple envelope flow models applied in design practice are presented in Section 3.5. The full-scale experimental technique and wind tunnel modelling principles are introduced in Section 3.6 and 3.7. Finally, the three methods for assessing mean ventilation rates in buildings considered in this project are summarised in Section 3.8.

Based on the published experimental data in a direct wind tunnel modelling [Carey and Etheridge 1999] study, the preliminary CFD simulations of wind induced ventilation in a 1/30 scale building model are presented in Chapter 4. Conclusions drawn from the comparison of CFD and wind tunnel test results provide the guidelines for the follow up CFD simulations on a full-scale cubic structure.

The verification and validation of the CFD model are performed in Chapter 5.

Firstly, the model is verified by reproducing the atmospheric boundary layer (ABL) with regard to freestream mean velocity profile and turbulence kinetic energy profile throughout the computational domain. Secondly, the simulation is validated by comparing with published full-scale data [Hoxey et al. 2002]. Further, external flow fields and surface pressure distributions induced by the wind around a cubic full-scale building are predicted. The simulation results for different wind directions ( $0^\circ$  and  $45^\circ$ ) are compared with published full-scale, wind tunnel data and other CFD studies [Richards et al. 2002]. Then the agreement and disagreement amongst the CFD results, full-scale and wind tunnel data are discussed. Finally, one of CFD models is chosen for further investigation into the cross ventilation effects on a cube with openings at two vertical levels.

The CFD investigations in Chapter 6 concentrate on the predictions of the surface pressure distribution on the ventilated cube, as well as the indoor and outdoor flow field patterns introduced by wind alone, and combined wind and buoyancy forces. The nondimensional mean ventilation rates estimated from the CFD results by the two calculation methods, i.e. the mean pressure field and velocity through individual opening for wind directions of  $0^\circ$ ,  $45^\circ$ ,  $90^\circ$  and  $180^\circ$  are shown in Section 6.3.6. CFD predictions of the cube with an indoor heater are presented in Section 6.3.7. The difference in the ventilation rates between the heated and unheated cube are also compared.

Chapter 7 explores the full-scale investigations on the test structure with openings under various natural conditions, i.e. summer, spring and winter seasons. It presents the details of the equipment used, the experimental techniques adopted and the results gained. Four methods have been used to measure the ventilation flow rates

simultaneously to ensure the quality of the experimental data. The methods are rated according to the error band associated with the recorded data.

In line with the recorded full-scale data, CFD simulations are performed and compared with field measurements in Chapter 8. Discussion is focused on the feasibility of the Reynolds Averaged Navier-Stokes (RANS) turbulence model approach to predict the total ventilation rates depending on whether the turbulent wind is dominant or not.

Finally, in Chapter 9 a summary of the research work is given and conclusions of the research are drawn. Suggestions for areas of improvement and perspectives for further research work are also presented.

## **Chapter 2    Literature Review**

## 2.1 Introduction

In **Chapter 1** the issue of economic and environmental impacts by energy use in buildings was discussed. Today, natural ventilation as a strategy for sustainable development in the construction industry is becoming more desired by clients (led by market forces and governmental regulations).

This chapter is a brief review of knowledge and techniques of natural ventilation studies in buildings. Of fundamental interest is the information that can be used to assist in the development of integrated design tools for naturally ventilated buildings.

## 2.2 Building ventilation design

Building ventilation plays an important role in providing good air quality and thermal comfort for the occupants. Ventilation is achieved by

- Natural ventilation;
- Mechanical ventilation;
- Hybrid (natural combined with mechanical) ventilation.

Natural ventilation systems rely on natural driving forces, such as wind and the temperature difference between a building and its environment, to supply fresh air to buildings interiors [BSI 1991].

Mechanical ventilation makes use of electrically powered fans or more complex ducting and control systems to supply and/or extract air to and from the building.

Air conditioning systems are based on mechanical ventilation systems with various levels of service to provide a fully controlled indoor environment within specified criteria, i.e. temperature, humidity, etc. [CIBSE AM 10 1997].

Hybrid ventilation systems can be described as systems providing a comfortable internal environment using both natural ventilation and mechanical ventilation systems. It operates according to the variation of the ambient conditions within individual days or the season, to use different features of the two systems optimally in response to the external environment [Heiselberg 1999]. To achieve energy efficiency demands the hybrid ventilation system is smartly controlled in natural ventilation system or mechanical ventilation system, which is using natural forces as long as possible and electric fans only if necessary.

### **2.2.1 Critical parameters in ventilation system design**

Ventilation systems, whether natural or mechanical, may be used for: indoor air quality control, air flow distribution patterns for thermal comfort, passive heating and cooling in various climate zones.

The appropriate design of a ventilation system can provide acceptable air quality and meet thermal comfort needs throughout the full range of climate conditions. In winter, design should minimise excess ventilation but ensure adequate indoor air quality to meet occupants' need for health, i.e. room temperatures, indoor air quality, and draught control are the critical parameters. In summer design, the main aim is to satisfy occupants' thermal comfort needs by avoiding overheating, i.e. control of room temperatures, solar and internal heat gain and provision of convective cooling.

Other important parameters in a natural ventilation system identified in the NatVent project [Kukadia et al. 1998] are the controllability by individuals, internal and external noise, internal air and external air pollution or odours, safety issues regarding fire regulations and security, and finally construction, operation and maintenance costs.

### 2.2.2 Natural ventilation versus mechanical ventilation

Throughout the world many traditional residential buildings are naturally ventilated, with unique building forms to suit the local climatic features, in moderate, cold and tropical climates.

Figure 2-1 shows three different climate zones in Europe:

1. Heating dominated zone – cool winter days
2. Intermediate zone – cool winter, hot summer days
3. Cooling dominated zone – hot summer days.

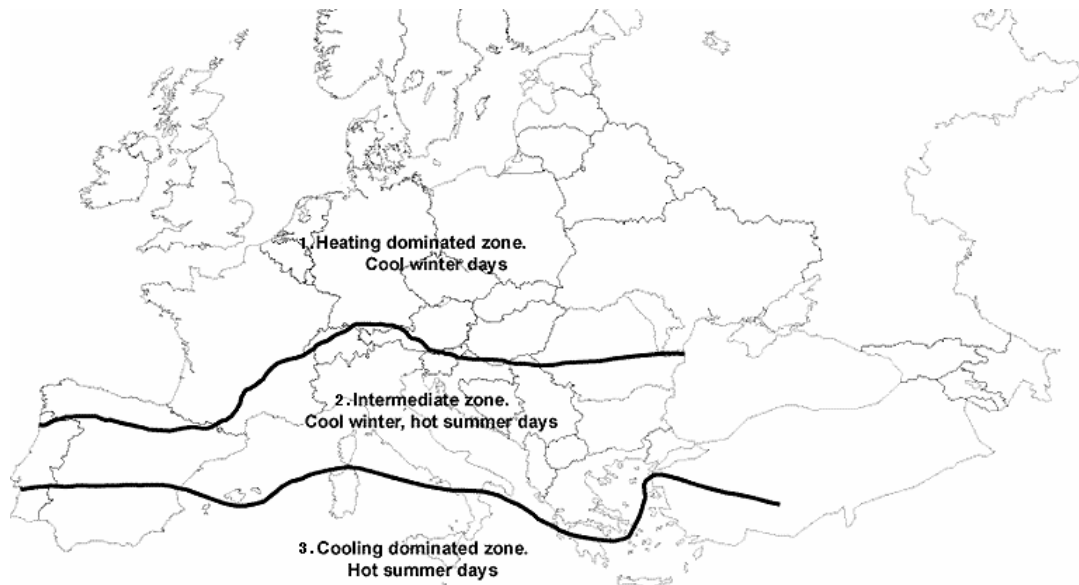


**Figure 2-1 European climate zones**

(<http://www.lema.ulg.ac.be/tools/rice/>)

Suited to the European climate zone 1, traditional British dwellings have been used for centuries, as shown in Figure 2-2. The high thermal capacity of the dwelling allows for a stable indoor temperature during cold spells in winter. On the other hand, the first floor open windows show convective ventilation at work, which

encourages hot air to rise from the house during the brief British summer, drawing in cooler air at lower levels to cool the building's mass.



**Figure 2-2 A traditional dwelling in Britain**

([http://www.greenhouse.gov.au/yourhome/technical/fs01\\_a.htm](http://www.greenhouse.gov.au/yourhome/technical/fs01_a.htm))

Achieving indoor thermal comfort in humid tropical climates is more difficult due to the combined effects of high temperatures and humidity, but cooling effects of indoor airflow from prevailing breezes is the principal technique used, as illustrated in Figure 2-3.

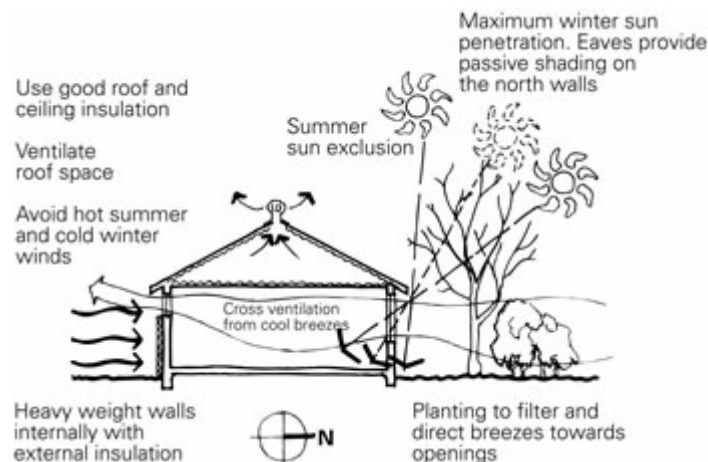


**Figure 2-3 Architecture responding to the tropical environment in Australia**

([http://www.greenhouse.gov.au/yourhome/technical/fs15\\_b.htm](http://www.greenhouse.gov.au/yourhome/technical/fs15_b.htm))

Cooling indoor space in locations with hot arid climates by evaporative cooling is also commonplace (see Figure 2-4). Solar assisted ventilation and heating are possible in locations with cooler climates, e.g. Les Pradettes in France and Carrigeen Park in Ireland [BRE 2003].

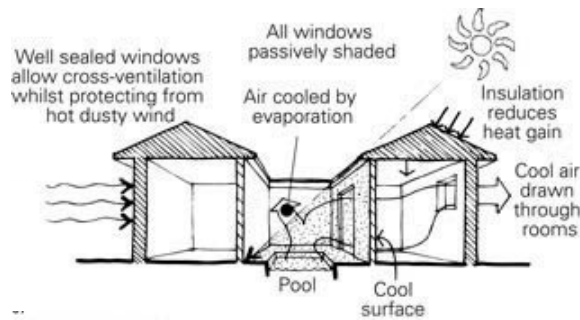


**Figure 2-4 Evaporative cooling in hot arid climate**

(<http://www.greenhouse.gov.au/yourhome/technical/fs14.htm>)

Typical cases of natural ventilation applications in non-domestic buildings have been reviewed by the Building Research Establishment [BRE 1994]. In particular, two projects in England – the Inland Revenue Centre in Nottingham (see Figure 2-5), and the Queen’s Building at De Montfort University in Leicester – are excellent examples of specially designed natural ventilation systems.

The Inland Revenue building complex is located in an urban area next to a railway station. Natural ventilation is driven by the stack effect from several ventilation towers (combined staircase and atrium spaces) located around the building. Solar gain in the ventilation tower enhances the stack effect. Fresh air is supplied through underfloor ducting and floor grills, which is fan assisted and can be controlled by the occupants.

Naturally ventilation contributes in the Inland Revenue Building energy saving to reduce the total energy demand by 25% than that consumed by a mechanical system. The Queen's Building also achieved impressive energy savings [BRE 1994].



**Figure 2-5 Inland Revenue Building, Nottingham**

(BRE Digest 399 [BRE 1994])

Kolokotroni and Aronis [1999] demonstrated the potential for applying natural night ventilation strategies in typical air conditioned office buildings in the UK and quantified the potential savings of cooling energy. Night cooling can affect internal conditions in an office building during the day in four ways:

- reducing peak air temperatures;
- reducing air temperatures throughout the day, and in particular during the morning hours;
- reducing slab temperatures; and
- creating a time lag between the occurrence of external and internal maximum temperatures.

Paassen et al. [1998] developed two design tools: a graphical chart and a set of simplified equations (to be used in spreadsheet) to determine the control strategies

and the required effective ventilation opening areas for night cooling with natural ventilation for an office building. Taking account of the variations in solar, internal heat gains, ventilation rates, occupancy patterns and external temperatures, they concluded that an optimal solution would be cross ventilation with an effective ventilation opening of 2% net floor area for a high or medium inertia office building.

Awbi [1991] also reports that naturally ventilated buildings have other benefits over mechanically ventilated ones, including reduced energy consumption, lower maintenance and capital costs, less space requirements, increased occupant satisfaction when given local control over indoor conditions, high productivity and fewer sick building syndrome (SBS) complaints.

Some potential problems associated with natural ventilation systems include: the reliability of the outdoor air ventilation rates, distribution pattern of the air within the building, control of moisture in naturally ventilated buildings, fire, safety or acoustics restrictions, building pressurisation concerns associated with chimney stacks and the entry of polluted air from outdoor without filtering. Therefore, a new legislative framework is needed for the better implementation of measures to improve the market penetration of solar assisted and natural ventilation in buildings [Niachou et al. 2000].

### **2.2.3 Key barriers for implementing a natural ventilation strategy**

For a successful energy-efficient natural ventilation scheme, the three issues of building tightness, good ventilation for occupants and natural ventilation design should be considered together in an integrated manner [BRE 1997].

The main barriers for implementing energy-efficient natural ventilation in the UK [Marmont 2003] are:

- Lack of powerful governmental regulations
- Little media interest and marketing promotion on successful cases to follow up the rapid innovative technology development
- Conservative national power generation and operation system
- Lack of off the shelf products for the potential users compared with the US market

Innovative design tools with adequate professional judgement are the keys to fulfil the “Build tight – ventilate right” mission. In particular, the advanced design technologies of computational fluid dynamics (detailed in Chapter 3) can demonstrate the performance of natural ventilation to the client early in the design process and also boost the market awareness.

### **2.3 Design procedure**

In naturally ventilated buildings, because wind and thermal buoyancy forces interact to produce the ventilation air flows, two distinct strategies have to be developed for winter and summer respectively.

The key issue for winter ventilation is the control of the indoor air quality (IAQ).

Etheridge [2002a] summarised the basic design procedure for the winter condition as:

- (i) decide a minimum ventilation rate for air quality (odour control)
- (ii) determine the “worst case” condition (wind speed, temperature, humidity, etc.)
- (iii) calculate the minimum area of the openings to meet the requirement at this condition.

For winter ventilation, Kolokotroni and Aronis [1999] reported that trickle ventilators can provide the necessary background ventilation (5 l/s per person criterion) to satisfy average office occupant densities (of 10 m<sup>2</sup> per person) for average external weather conditions in the UK.

Meanwhile, the summer condition design procedure is [Etheridge 2002a]:

- (i) determine the acceptable peak temperature rise
- (ii) calculate the ventilation rate using a thermal dynamic response model [Kendrick 1993] to ensure that this temperature rise is not exceeded
- (iii) choose the “worst case” as zero wind speed, so that the stack pressure provides the only natural force to drive a ventilation flow
- (iv) calculate the maximum area of the openings under this condition.

For example, the effect of wind on thermal comfort during summer has been evaluated by Aynsley [1999] for a preliminary house design in Australia based on readily available mean monthly local climatic data. This study indicates that indoor thermal comfort can be achieved from natural ventilation when the daytime wind speeds are higher, and relative humidity is lower, than night-time in warm humid tropical climates.

Furthermore, off-design conditions often occur between the basic summer and winter design conditions, such as the effects of:

- adventitious leakage
- wind speed and direction
- unsteadiness due to wind turbulence
- extreme conditions, e.g. fire breakout and gas explosion.

For instance, adventitious leakage has a number of important implications in relation to the performance of buildings. Ventilation arising from flow through adventitious

openings<sup>1</sup> is known as infiltration (or exfiltration) [Wilson 1961]. Night-time cooling in summer will rely on large openings normally neglecting adventitious openings.

#### **2.4 Analysis and design tools**

Suitable and valid analytical methods of natural ventilation system would give architects and engineers the necessary confidence in ventilation system performance, which is also the decisive factor for choice of system design.

The air passing through a building envelope<sup>2</sup> is called the envelope flow. Building envelope flowrate is the rate at which air enters and leaves the building [Etheridge and Standberg 1996]. This is the primary concern of natural ventilation design, where the basic aim is to ensure that openings are sized and sited such that maximum and minimum flowrates can be achieved under summer and winter conditions. It should also be noticed that occupants are expected to vary the opening sizes between these limits. Furthermore, predicting internal air motion requires detailed information of the indoor air supply distribution, such as airflow pattern, velocity, temperature, contaminant concentrations, and pressure.

A vast amount of publications [Liddament 1991; Allard 1998; Chen and Xu 1998; Li et al. 1998; Hunt and Linden 1999; Straw 2000; Etheridge 2002a; Jiang et al. 2003] cover the theoretical approaches, laboratory experiments, field studies, and numerical/computational simulations of the performance of natural ventilation

---

<sup>1</sup> Adventitious openings are the cracks, gaps and unknown openings in windows, doors, walls and roof, which are in opposite to the purpose-provided ventilation openings.

<sup>2</sup> Building envelope includes everything that separates the interior of a building from the outdoor environment, including the doors, windows, walls, foundation, basement slab, ceiling, roof and insulation.

systems. The advantages and disadvantages of the various methods are listed in Table 2-1. Wind tunnel modelling has been used for the generation of pressure coefficient ( $C_p$ ) data on conventional building shapes and for specific building designs. Experimental measurements are reliable but need large labour-effort and time. Therefore, the experimental approach is not feasible as a general design tool except for some prestigious buildings' design.

**Table 2-1 Approaches for natural ventilation design [Gan 1999]**

Approach		Advantages	Disadvantages
Theoretical	Envelope flow models	1. Simple, usually in formula or graphical form	1. Restricted to simple geometry 2. Assumptions are needed about the details of the flow to obtain simplified flow equations for bulk flow
	CFD models	1. Predict flow field in details 2. Resolve flow feature development with time 3. Greater flexibility	1. Numerical truncation errors 2. Boundary condition problems 3. Assumptions about turbulence structure and near wall treatment 4. Computer costs 5. Experienced user costs
Experimental		1. Capable of being most realistic	1. Equipment required 2. Scaling problems 3. Tunnel corrections 4. Measuring difficulties 5. Operating costs

Two types of envelope flow models are available for predicting natural ventilation:

- (i) single-zone models, e.g. British Standard Method [BSI 1991], nondimensional and graphical methods [Etheridge 2002a], and
- (ii) multi-zone models, e.g. BREEZE [Orme 1999] and COMIS [Allard et al. 1990].

Both single- and multi-zone models utilise the external pressure distribution to predict the bulk ventilation rates through indoor spaces. Since the external pressure

distribution depends on incoming wind speed and direction, local topography, building size and shape, and the size and location of ventilation openings, the accuracy of the zonal models depend mainly on the accuracy of the pressure distribution.

The other type of theoretical models, i.e. computational fluid dynamics (CFD), is based on the solution of the governing equations of the fluid flow combined with turbulence models. These tools can predict detailed flow field distribution patterns, flow rate and heat transfer through various components and the concentration of indoor pollutants. However, large computational and personnel costs are involved in implementing CFD. In practice, correct representation of the climatic boundary conditions and the coupling of the indoor and outdoor environment robustly in CFD are the main barriers to its use for the design of natural ventilation. Some well known CFD packages are CFX [AEA Technology 2001a], FLUENT [FLUENT 1992] and STAR-CD [Luu 2003].

#### **2.4.1 Natural ventilation system**

Buildings can use various types of natural ventilation and their combinations, namely displacement ventilation, cross ventilation, single-sided ventilation, night-time cooling, background ventilation, solar assisted and hybrid ventilation. A greater understanding of the relationship between the driving forces and indoor environmental conditions would increase designer confidence in generating natural ventilation design solutions.

Depending on the requirement, isolated spaces can alternatively be ventilated either by single-sided or cross ventilation.

### Single-sided ventilation

This occurs when large natural ventilation openings (such as windows and doors) are situated on only one external wall (Figure 2-6). Exchange of air takes place by wind turbulence, by outward openings interacting with the local external airstream and by local stack/buoyancy effects. Buoyancy effect can also introduce air flow into the space at low level and flow out at high level of a single opening.

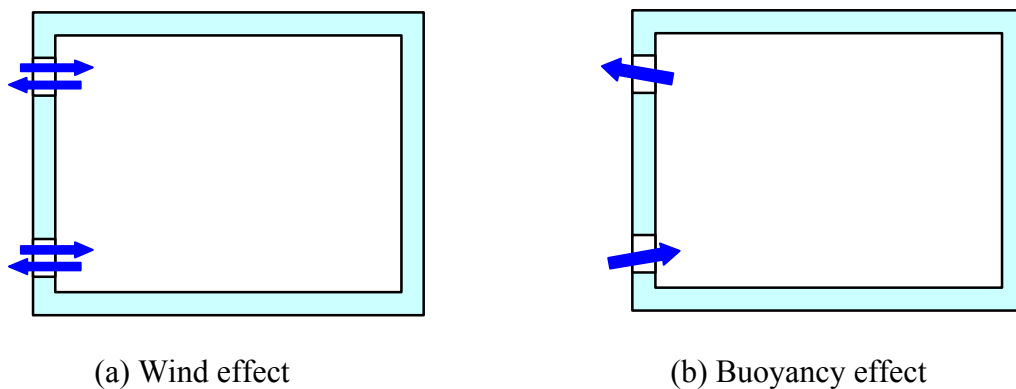


**Figure 2-6 Schematic of single-sided ventilation**

### Cross ventilation

This occurs when the inflow and outflow openings in external walls have a clear internal path between them (Figure 2-7). The effectiveness of cross ventilation is dependent on many factors including: building location with respect to predominant wind directions, interior plan layout, corridors, furniture, and other potential airflow obstructions, sizing of windows and other openings.

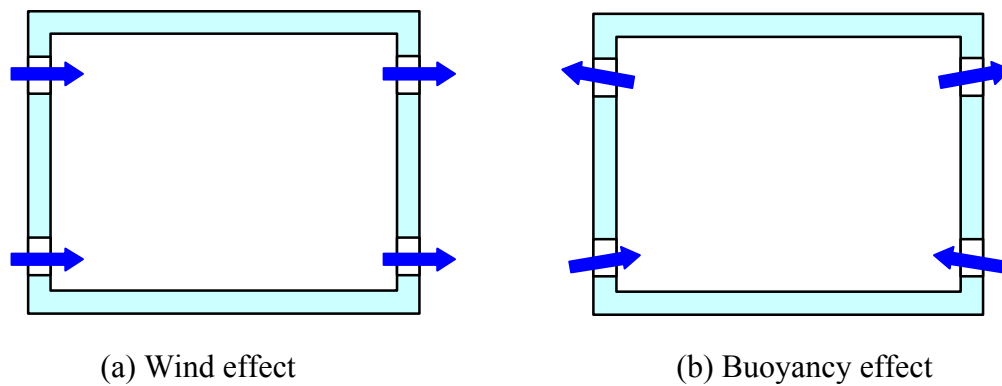


**Figure 2-7 Schematic of cross ventilation**

### 2.4.2 Envelope flow theories

Ventilation driven by natural wind and thermal forces varies with time. In the majority of cases the ventilation is more likely to be steady in the mean, rather than truly steady. Most theoretical models assume that the envelope flows behave as if the conditions are truly steady. The models for steady ventilation can be distinguished by whether they are empirical or theoretical and multi-zone or single-zone.

Empirical models are derived directly from field measurements of ventilation rates of a building, e.g. relating ventilation rate to wind speed by an empirical equation [Etheridge 1998]. These models should always be used within the limits of their applicability, i.e. within the range of parameters covered by the measurements.

Theoretical models are based on a much more fundamental approach involving the solution of the conservation equations, varying from the simple orifice flow equation for air movement through building openings to complicated CFD models for room air movement.

A single-zone model assumes that internal doors are open and neglects any internal resistance to flow. It predicts the total flow rate through a building.

A multi-zone airflow (or network) model divides the building into its component spaces (cells or zones). It is based on the mass flow balance of a space, combined with the effect of wind and buoyancy to calculate pressure difference across nodes in the airflows between building zones and the outside environment. It predicts the total flow rate through each cell, e.g. flow through a room and flow rate between cells.

Some of the multi-zone models also provide the ability to perform steady-state as well as transient (quasi-steady) analysis to quantify the impact of natural ventilation techniques on the thermal balance of the building [Kendrick 1993].

The limitations of airflow network models are well known. While network models can predict the air flow rates between the zones of a building and the outdoors, they are not able to give any information about airflow patterns and the velocity field within the rooms. However, these data are obviously necessary when dealing with comfort prediction or natural ventilation efficiency. Also, values of the external pressure coefficient,  $C_p$ , are available for a limited number of geometrical configurations and wind incidence angles, as they are derived either by wind tunnel tests or by parametric analysis. Finally, it should be noted that most of the models do not account for wind turbulence. Dascalaki et al. [1999] applied COMIS model to model single-sided and cross ventilation through large openings in two zones of a full-scale building. The turbulence effects were considered by an equivalent pressure difference profile and effects of reduction of the effective area of the aperture were represented by a single coefficient. For single-sided ventilation tests with relatively

high wind speeds and small temperature differences between the indoor and outdoor environment, a correction factor was incorporated into the COMIS model in order to have good agreement between the simulated data and measured data. For cross ventilation experiments with low prevailing outdoor wind speeds, the global flows were found to be reasonably well estimated by COMIS. However, inaccuracies in pressure and discharge coefficients could cause significant errors in estimating the specific air flows at each opening between the indoor zones and the outdoors.

For flow in real buildings, the effect of wind turbulence causes turbulent pressure fluctuations. The calculation of pressure fluctuations involves statistics and the effect is normally neglected or handled by simple coefficients in mathematical modelling. More sophisticated computational fluid dynamics (CFD) techniques could be used for modelling the mean flow field whilst taking account of turbulent effects.

## **2.5 CFD application in ventilation studies**

CFD methods solve the time dependent or time-averaged Navier-Stokes equations together with the continuity equation for fluid flow. Within the capacity and speed of present computers, direct numerical simulation (DNS) for any realistic situation is still not practical [Stathopoulos 2002]. Consequently, air flow simulations use turbulence models to resolve the time-averaged equations of motion. The most common turbulence models are called Reynolds Averaged Navier-Stokes (RANS) models which are named for the extra terms generated by the averaging process of the modelling assumptions. To tackle the unsteady flow problem associated with natural ventilation more effectively, large eddy simulation (LES) calculates large-scale flow motion while simulating small-scale flow motion by subgrid-scale models

in transient form. The computing cost of utilising LES is between DNS and RANS models.

The performance of CFD prediction of flow around a basic shape building or building models in wind tunnel based on various turbulence models has been investigated by many researchers [Murakami et al. 1992; Mochida et al. 2002; Richards et al. 2002; Wright and Easom 2003]. In general, RANS models can produce data for the mean surface pressures and the near wake flow which are in reasonable agreement with experiment in most places. The differences between wind tunnel data and field measurements have been highlighted in the comparison study of flows around a cubic building [Richards et al. 2002].

The mechanism of single-sided ventilation driven by wind forces has been investigated by Jiang et al. [2003a] using large eddy simulation (LES). Detailed airflow fields, such as mean and fluctuating velocity and pressure distribution inside and around a cubic, building-like model were measured by wind tunnel tests and compared to LES results for model validation. With an opening area to wall area ratio of 16.8%, the opening size on the building-like model is relatively large compared to a real building. However, the numerical results from LES are in good agreement with the experimental data with regard to the predicted internal and external airflow patterns and velocity field, and the surface pressure over the models. For buoyancy driven, single-sided ventilation, the steady RANS model predicts much higher ventilation rates than LES results [Jiang et al. 2003b].

Nishizawa et al. [2003] placed a full-scale building model (5.56 m × 5.56 m × 3 m) in a wind tunnel. The obtained air flow pattern was expected to be different from a conventional boundary layer wind tunnel. In wind directions of  $0^\circ \sim 165^\circ$ , the

predicted cross ventilation rates through the two diagonally located large openings (9% wall area) using the standard  $k-\varepsilon$  model was generally in good agreement with measured value. However, at high ventilation rates the predicted value was approximately 10% above the measured value.

Straw [2000] studied wind induced cross ventilation in a 6m cubic full-scale building with two large openings (7.7% wall area) at the same level on two opposite walls. Ventilation rate was determined by integrating the velocity at measuring points by area at wind directions of  $0^\circ$ ,  $45^\circ$  and  $90^\circ$  to the wall with opening. The author concluded that RANS turbulence models could provide reliable mean flow when the mean flow component was high relative to fluctuating mechanisms. However, when the mean flow component was low, RANS models were incapable of modelling the turbulence driven ventilation.

Prianto and Depecker [2002] numerically investigated the effects of balcony, opening design and internal division on the indoor airflow patterns of a living zone located on the second floor of a two storey building in a tropical humid region. The authors concluded from the numerical experiments on the 2D building model that the location of balcony, the arrangement of window and the internal division had great influence on the flow inside the building, especially the indoor velocity distribution. CFD modelling of a 3D full-scale building was considered to be a more feasible and effective design tool for studying the local architectural features' effects on the indoor flow patterns than a scaled building model in a wind tunnel.

Holmes and Davies [2003] demonstrated the interaction between CFD and thermal analysis for predicting air flows in a  $6\text{ m} \times 6\text{ m} \times 3\text{ m}$  room with a large window on one wall. The room was ventilated by a displacement system with constant air

supply. Data from the thermal analysis program were transferred into the CFD using a user-defined subroutine. The variation of the assumptions made for the thermal boundary conditions had little influence on the air speed predictions, but caused significant differences in temperature distributions. The coupling of air flow and thermal analysis models offers great challenges to design engineers.

Zhai and Chen [2003] integrated an Energy Simulation (ES)<sup>3</sup> program with CFD and studied the existence, uniqueness, convergence, and stability of the numerical solutions from the coupled program. The simple zero-equation turbulence models had been used. The authors concluded from both the theoretical analysis and numerical experiments that the iteration between ES and CFD programs can lead to a correct and converged solution. Their further study [Zhai and Chen 2004] on the numerical determination and treatment of convective heat transfer coefficient found that the first grid near a wall in CFD was crucial for the correct prediction of the convective heat. Their theoretical studies showed that the convective heat transfer coefficients for room with strong temperature stratification might cause divergence and instability in energy simulation.

Well established experimental technologies for natural ventilation in buildings can be utilised to validate the theoretical CFD simulations.

## **2.6 Experimental technology**

Ventilation measurement includes the determination of air exchange rates, interzonal airflow rates, air-tightness/leakage and leakage distribution. Methods for the measurement include tracer gas techniques and scale modelling techniques

---

<sup>3</sup> Energy simulation (ES) program is an analysis program to predict building thermal performance.

### **2.6.1 Tracer gas techniques**

Air exchange rate measurement is carried out using, predominantly, tracer gas techniques. More detailed explanations can be found in Chapter 3 (Section 3.6.2).

Although full-scale testing of building ventilation systems promises to provide the most accurate and reliable information, its feasibility is still very limited due to the high construction costs, operation costs and time duration involved. Consequently, laboratory small-scale visualisation and modelling systems have been widely used for understanding and evaluating natural ventilation in buildings. Achievement of geometric, thermal and dynamic similarities mean that quantitative information can be obtained from small-scale models and extrapolated to full-sized buildings. Over the past decade our understanding of natural ventilation has been significantly advanced and improved by new research using laboratory models [Linden et al. 1990; Carey and Etheridge 1999; Li and Delsante 2001; Etheridge 2002b; Chiu and Etheridge 2004].

### **2.6.2 Scale (physical) modelling**

Currently, there are essentially three laboratory-scale modelling techniques: wind tunnel modelling, salt-bath modelling and fine-bubble technique.

#### **2.6.2.1 Wind tunnel technique**

Wind tunnel scale models are often used for (a) the determination of wind pressure coefficients, from which ventilation rates are obtained indirectly by means of a mathematical model and (b) for the direct determination of ventilation rates [Carey and Etheridge 1999].

The potential advantage offered by the direct approach is that wind effects are more accurately accounted for than they are by the indirect/mathematical model approach or by the salt-bath technique (see Section 2.6.2.2).

The wind tunnel modelling system uses air or other gases as the flow media, while the buoyancy flows are generated by embedded heating elements.

There are basically two wind effects, namely the generation of the surface pressures and the velocity field local to the opening. In general, both the pressure and velocity fields are unsteady. Current theoretical design procedures take into account the time-averaged surface pressures by making use of pressure coefficients determined from wind tunnel models [BSI 1991]. The effects of unsteady pressures and the local velocity field are ignored, which can be significant. For example, Jozwiak et al. [1995] presented the investigation of the aerodynamic interference effects on the pressure distribution on a building adjacent to another one in a wind tunnel. It was found that for some wind directions local values of the external pressure coefficient on the leeward wall, close to the gap between buildings, was 2.5 times higher than on an isolated building. This led to a reverse draught in the natural ventilation system of the apartment buildings.

Design for buoyancy effect only is relatively straightforward, and most natural ventilation systems are designed for this force alone. The boundary conditions for temperature i.e.  $dT/T$  in the model should be the same as that at full-scale.

Considering combined wind and buoyancy effects, it is generally necessary to invoke the Boussinesq approximation, so that the required Archimedes number can be achieved by using much higher temperature difference for the model while still operating at a wind speed exceeds the critical Reynolds number  $Re$  [Carey and

Etheridge 1999]. In the design of naturally ventilated buildings with stacks, the stack Reynolds number should be above a critical value to ensure the stack flow being turbulent at model scale [White 2001].

#### **2.6.2.2 Salt-bath technique**

Salt-bath (saline) modelling utilises the density difference between salt solution and fresh water to generate buoyancy forces which represent those found in naturally ventilated buildings. Salt-bath techniques have been used to consider building ventilation under the combined buoyancy and wind effects [Hunt and Linden 1999]. The ventilation performance was assessed by measuring density and velocity within the model; the corresponding air temperatures and ventilation flow rates within the test building were predicted.

#### **2.6.2.3 Fine-bubble technique**

The fine-bubble modelling system uses electrolytically generated fine hydrogen bubbles to simulate the buoyancy-driven ventilation airflows in buildings. Experiments for displacement natural ventilation [Chen et al. 2001] in a single-zone building induced by two types of buoyancy sources, a point source and a line source, showed that the ventilation and stratification phenomena were successfully modelled by the fine-bubble technique. The experimental results for stratification were in good agreement with both the experimental data and theoretical predictions available in the literature.

#### **2.6.2.4 Pros and cons of scale-modelling techniques**

One advantage of the salt-bath technique is that there is no real problem about achieving high Reynolds numbers with prototype Archimedes numbers. Another

potential advantage is that the technique attempts to model the internal flow such that the internal pressure distribution reflects temperature stratification arising from buoyancy sources.

The main advantage of the wind tunnel technique is that the atmospheric boundary layer can be more accurately modelled in an environmental wind tunnel than in a water channel. The volumes of water required in an equivalent channel would be difficult to handle.

Including buoyancy effects in wind tunnel modelling offers the best way of determining the interaction between wind and buoyancy. This is particularly important for devices such as chimney stacks, where adverse wind effects may overcome buoyancy forces and lead to flow reversal [Chiu and Etheridge 2004]. To achieve the dynamic similarity for wind and buoyancy forces at the same time, compromises need to be made by using a much higher temperature difference for the model and hence using a sufficiently high wind speed to exceed the critical Reynolds number [Carey and Etheridge 1999].

The fine bubble technique is less bulky and costly than the salt-bath technique for buoyancy driven flow modelling. One of the few limitations for the fine bubble technique is that when the top opening is lower than the ceiling level, bubbles will accumulate at the top of the building, which gives rise to unrealistic flow fields. Furthermore, it can only be used for buoyancy effect simulation.

Scale modelling has often been used as a complementary tool to numerical modelling and been proved especially useful in model development and validation [Richards et al. 2002]. Nevertheless, differences between wind tunnel and full-scale experimental data should be carefully considered when validating numerical models.

The use of CFD for predicting the air flow and air quality makes it possible to include the effect of room geometry, equipment and occupants in the design of ventilation systems.

## **2.7 Summary**

Ventilation strategy should be chosen to ensure that the optimum design is produced that delivers the required comfort conditions whilst also achieving the minimum environmental impact.

Suitable theoretical models [Allard et al. 1990; BSI 1991; Etheridge 2002a] can be chosen to solve the fundamental design problems at different complexity levels to take account of major effects by the natural driving wind and buoyancy forces.

Innovative experimental techniques provide a powerful tool for examining the performance of naturally ventilated buildings at design stage as it may be used to predict quantitatively ventilation flow rates and temperature stratification under a wide range of climatic conditions.

CFD modelling is a valuable tool for evaluation and optimal design of room air distribution systems based on the predicted thermal comfort, air quality and overall ventilation effectiveness. CFD analysis tools can be very beneficial in analysing temperature, airflow and contaminant fields within individual zones of a building, particularly with large spaces such as atria. However, the uncertainty in the definition of boundary conditions as well as their spatial and temporal variation limits the accuracy of results.

## 2.8 Unresolved issues

This brief review of the existing design methods and tools covers a wide range of different analytical and experimental tools to address the complex interaction between the coupled natural wind and buoyancy driving forces for natural ventilation systems. Moreover, the new trend of ventilation systems is hybrid systems which are intelligent with control systems that can automatically switch between natural and mechanical modes in order to minimise the energy consumption.

The significant unresolved issues identified in the literature review are:

- (i) There is little formal guidance about CFD techniques for assessing and predicting coupled internal and external ventilation flows in the natural/built environment, which are driven by combined wind and buoyancy forces.
- (ii) There are few field studies where data has been collected for CFD modelling validation in real buildings.

This work involves quantitative investigation into the natural ventilation rates in a cube structure under various weather conditions using field measurements, simple envelope methods and CFD.

## **Chapter 3    Methodology**

### **3.1 Introduction**

This chapter discusses the available modelling techniques and assessment methods for studying natural ventilation in buildings. The background information includes the computational fluid dynamic (CFD) modelling techniques, the conventional envelope flow theories of natural ventilation applied in design practice, the full-scale experimental measurement methods and wind tunnel modelling techniques.

### **3.2 Wind Engineering**

The assessment of wind effects on building structures requires knowledge of the complex interactions that involve meteorology, aerodynamics and building structures. The great majority of buildings and structures in the field of wind engineering are considered as bluff bodies. A body is referred to as bluff, when the aerodynamic flow streamlines are detached from the surface of the body. This is encountered with the formation of separated flow around the body, creating a wide trailing turbulent wake [Cook 1985]. Proper understanding and precise wind profile simulation in an atmospheric boundary layer is essential in pursuing further studies of the air flow around a building and the flow fields inside the building.

#### **3.2.1 The atmospheric boundary layer (ABL)**

The atmospheric boundary layer (ABL) is the layer of turbulent flow between the Earth's surface and the undisturbed wind, with thickness varying from hundreds to thousands of meters. The thickness is determined by the gradient height at which surface friction of the ground no longer affects the general flow of wind.

The ABL is identified as surface and outer layers. The surface (or inner) layer just above the ground is divided into the roughness sublayer and inertial sublayer

respectively. The outer (or Ekman) layer continues from the surface layer to the top of the boundary layer.

The bottom 5 to 10 % of the ABL is considered as the roughness sublayer. This layer is affected by the frictional forces exerted by the ground, i.e. fences, trees, buildings, etc. The average wind speed increases with the height above the ground, while the intensity of the turbulence or gusting decreases. The difference in terrain conditions directly affects the magnitude of the frictional force and also causes the mean wind speed variations, which are illustrated in Figure 3-1.

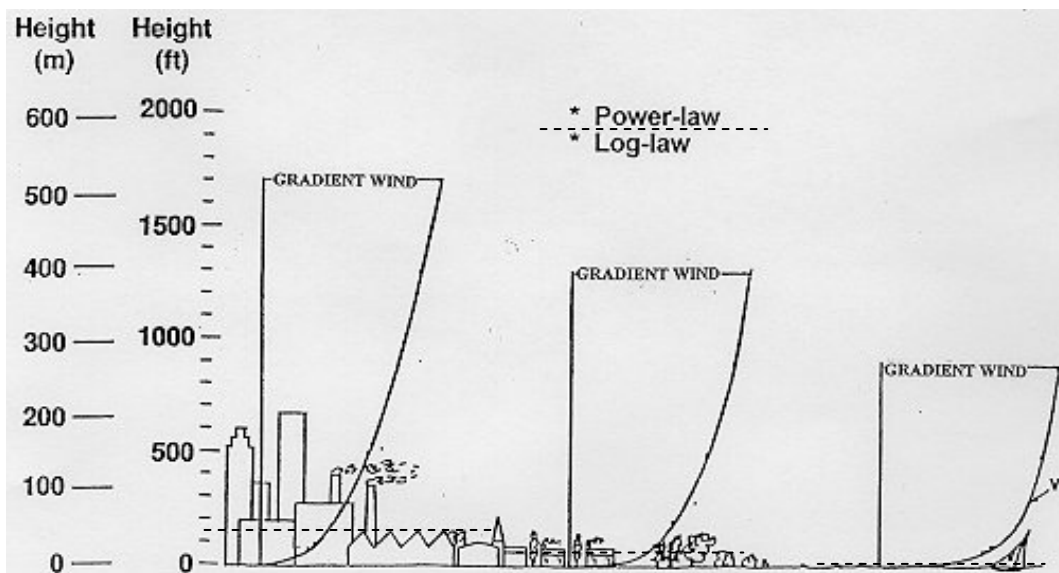


**Figure 3-1 Wind speed variation with height and terrain conditions**

(<http://www.wind.ttu.edu/>)

In this roughness sublayer region the vertical variation of shear stress can be neglected without significant loss of accuracy with regards to the development of the mean velocity profile.

Above the roughness sublayer is the inertial sublayer. In this region the averaged turbulent fluxes are constant with height.

The logarithmic law representing the variation of the mean wind speed with height above the ground surface can be expressed as:

$$U(z) = \frac{u_*}{\kappa} \ln\left(\frac{z}{z_0}\right) \quad (3.1)$$

where

$U(z)$  is the mean wind speed at height  $z$ ,

$u_*$  is the friction velocity

$\kappa$  is the von Karman constant ( $\kappa = 0.41$ )

$z_0$  is the roughness height determined by the surface condition.

In the outer region the airflow shows little dependence on the nature of the surface, and the Coriolis force due to the Earth's rotation becomes important. The increase of the height leads to the increase of the Coriolis force and the reduction of the shear stress. An empirical power law representation of the mean velocity profile in the outer layer can be given by the following relation:

$$\frac{U(z)}{U_{ref}} = \left(\frac{z}{z_{ref}}\right)^\alpha \quad (3.2)$$

where  $U_{ref}$  is the mean wind speed at reference height  $z_{ref}$ , and the exponent,  $\alpha$ , depends on the range of height being covered and the surface roughness.

### 3.2.2 Wind effects on buildings

Most flows encountered in nature and engineering practice are turbulent. In the ABL, the complex terrain increases the roughness of the surface and therefore

increases the turbulence as well. Turbulent flows are unsteady and contain fluctuations that are chaotic in space and time.

### 3.2.2.1 Turbulent flow

Formation of turbulence depends on surface roughness (of a solid boundary) and the ratio of speed to Reynolds number of two fluid layers. In turbulent flow, the flow and fluid variables – especially velocity – vary with time and position. The time-averaged velocity is the main factor for describing bulk flow, but does not precisely account for the instantaneous behaviour. The instantaneous quantities can be expressed as the summation of the average value and their instantaneous deviation from the average.

The instantaneous velocity components in x-, y- and z- Cartesian coordinates are then:

$$u = U + u' \quad v = V + v' \quad w = W + w' \quad (3.3)$$

where capital letter denotes the time average and prime represents the instantaneous deviation from the mean.

The intensity of the turbulence,  $I$ , is calculated as the “root mean square” of the instantaneous deviation velocity divided by the time-averaged velocity:

$$I = \frac{\sqrt{\frac{\overline{(u')^2} + \overline{(v')^2} + \overline{(w')^2}}{3}}}{U} \quad \text{or} \quad I_u = \frac{\sqrt{\overline{(u')^2}}}{U} \quad (3.4)$$

Boundary layer transition and separation, heat and mass transfer rates at the surface all depend on the intensity of the turbulence amongst other things.

Two significant parameters used to describe the turbulence are the turbulence Reynolds number  $Re$  and its length scale  $L$ .

$$R_e \equiv \frac{\sqrt{k}}{\nu} L = \frac{k^2}{\varepsilon \nu} \quad (3.5)$$

$$L \equiv \frac{k^{3/2}}{\varepsilon} \quad (3.6)$$

where

$k$  is the turbulence kinetic energy, its dissipation rate is  $\varepsilon$  and

$\nu$  is the kinematic viscosity of the fluid  $\nu \equiv \frac{\mu}{\rho}$ .

Turbulence is a decisive practical phenomenon that has therefore been extensively studied in the context of its applications by engineers and applied scientists. The outcomes of these studies have also been combined with modern numerical computing techniques.

### 3.3 Computational Fluid Dynamics (CFD)

Computational Fluid Dynamics (CFD), numerical analysis and simulation of fluid flow processes, are relevant to many mechanical, aeronautical, automotive, power, environmental, medical and process engineering applications. CFD simulations are used to design, investigate the operation of the different engineering systems and to determine their performance under various conditions.

### 3.3.1 Overview of CFD applications

CFD techniques combine the classical branches of theoretical and experimental science with the power of modern numerical computation. They are used to improve the understanding of fluid physics and chemistry.

In principle CFD can deal with problems including compressible and incompressible flow, steady and unsteady flow, turbulent and laminar flow with and without heat transfer, single-phase and multi-phase flows, flows with radiation, non-Newtonian flows, supersonic and hypersonic flows with strong shocks and many other more complex flows.

CFD solutions are the numerical approximation of the governing equations of fluid flow in space and time. A CFD code works by dividing the region of interest into a large number of cells or control volumes (the mesh or grid). In each of these cells, the partial differential equations describing the fluid flow (the Navier-Stokes equations) are replaced by algebraic approximations that relate the pressure, velocity, temperature and other variables, to the values in the neighbouring cells. These equations are then solved numerically yielding a complete profile of the flow to the grid resolution.

The three main components of a CFD code are:

- a pre-processor
- a solver
- a post-processor

At the first stage, a computational domain is created to represent the geometry of the object being modelled. Then the mesh divides the solution domain into a finite

number of cells or control volumes. This is followed by the definition of fluid properties and specification of appropriate boundary conditions.

The numerical solver solves the equations of state for each cell until an acceptable convergence is achieved. According to the way in which the flow variables are approximated with the discretisation process, five numerical solution techniques are defined: finite difference method, finite element method, finite volume method, spectral method and gridless method [Versteeg and Malalasekera 1995; Blazek 2001]. In theory, each type of method yields the same solution if the grid is very fine.

In the post-processing stage, the modelled results are analysed both numerically and graphically. This provides visualisation ranging from 2-D graphs to 3-D representations of vectors, particle tracks and gradients.

### **3.3.2 Governing Equations**

The fundamental governing equations of fluid dynamics, i.e. the continuity, momentum and energy equations, are the mathematical statements of three fundamental physical principles, which can be regarded as follows:

- Conservation of mass (Continuity Equation)
- Newton's Second Law (Momentum Equation)
- Conservation of energy (First law of thermodynamics)

Utilising the finite volume method, the equation for the conservation of mass (also referred to as the continuity equation) is discretised by means of a mass balance for a

finite (control) volume. Thus for a steady incompressible fluid with uniform temperature, the incoming mass flow is equal to the outgoing mass flow.

By applying Newton's Second Law of Motion, the relationship between the forces on a control volume of fluid and the acceleration of the fluid gives an expression for the conservation of momentum (or Navier-Stokes equations).

The First Law of Thermodynamics states that energy is conserved in a fluid. It ensures the rate of change of energy of the fluid particle is equal to the sum of the net rate of work done on the fluid particle and the net rate of heat addition to the fluid and the rate of increase of energy due to sources [Versteeg and Malalasekera 1995]. This would therefore allow the definitions of changes in fluid temperature within a control volume.

These fundamental principles can be expressed in terms of a set of partial differential equations (PDEs) and in solving these equations the velocity, temperature and pressure are predicted throughout the flow field.

In the flow of compressible fluids, the equations of state (Eqn.3.10) provide the linkage amongst the energy equation (Eqn.3.9), mass conservation (Eqn.3.7) and the momentum equations (Eqn.3.8).

$$\frac{\partial \rho}{\partial t} + \frac{\partial}{\partial x_i}(\rho u_i) = 0 \quad (3.7)$$

$$\frac{\partial}{\partial t}(\rho u_i) + \frac{\partial}{\partial x_i}(\rho u_i u_j + p \delta_{ij} - \tau_{ij}) = 0 \quad (3.8)$$

$$\frac{\partial}{\partial t}(\rho e_{tot}) + \frac{\partial}{\partial x_i}(\rho_i e_{tot} + u_i p + q_i - u_i \tau_{ij}) = 0 \quad (3.9)$$

$$f(p, \rho, T) = 0 \quad (3.10)$$

where

$\rho$	density
$p$	pressure
$u$	instantaneous velocity
$\tau_{ij}$	viscous stresses
$\delta_{ij}$	Kronecker delta function, ( $i=j, \delta_{ij}=1$ or $i \neq j, \delta_{ij}=0$ )
$x_i, x_j$	coordinate variable
$T$	thermodynamic temperature
$e_{tot}$	total energy is defined by $e_{tot} = e + u_i u_i / 2$
$q_i$	heat-flux

The functional form of the equation of state (Eqn. 3.10) depends on the nature of the fluid.

The flow of constant-property Newtonian fluids is governed by the Navier-Stokes (N-S) equations together with the mass conservation equation only. Liquids and gases flowing at low speeds behave as incompressible fluids.

The simplified N-S equations for an incompressible Newtonian fluid in the notation of Cartesian tensors can be written as:

$$\frac{\partial u_i}{\partial t} + \partial u_j \frac{\partial u_i}{\partial x_j} = -\frac{1}{\rho} \frac{\partial p}{\partial x_i} + \nu \frac{\partial^2 u_i}{\partial x_j^2} \quad (3.11)$$

where  $\nu \equiv \frac{\mu}{\rho}$  is the kinematic viscosity.

Considering the hypothetical case of an ideal (inviscid) fluid, the isotropic stress tensor is

$$\tau_{ij} = -P\delta_{ij} \quad (3.12)$$

The physical interpretation of the eddy Reynolds stresses is the effect of turbulent transport of momentum across the main flow direction, which influences the flow in the same way as increased shear stress. The stress tensor is given by:

$$\tau_{ij} = -P\delta_{ij} + \mu\left(\frac{\partial U_i}{\partial x_j} + \frac{\partial U_j}{\partial x_i}\right) \quad (3.13)$$

This plays an important role in the numerical treatment of turbulence which is discussed in Section 3.3.4.2.

### 3.3.3 Numerical grid

Three types of numerical grids can be used in CFD code: structured grids, unstructured grids and combined grids.

In the structured grids, the number of cells that share a common vertex is uniform in the interior of the domain. The geometric domain is decomposed into subdomain blocks, within which a structured grid is generated. Special treatment is applied at block interfaces, mapped by a boundary-fitted coordinate leading to multiblock block-structured grids. Overlapping blocks may be applied locally. For structured grids, algorithms can be formulated that run fast on vector computers with less computer memory required, and coarse grid generation for multigrid and the implementation of transfer operators between blocks is straightforward [Blazek 2001]. However, the generation of the domain decomposition into blocks requires much time and effort from the user.

Unstructured grids apply a mixture of tetrahedral, pyramidal, prismatic and hexahedral computational cells. They are more flexible and easier to generate than a structured grid, and better for adaptive discretisation (i.e. local refinement). The disadvantage of unstructured grids is the irregularity of the data structure, which means that the development of accurate discretisations and efficient solution methods is more difficult than for structured grids [Blazek 2001].

A third type of grid consists of the union of locally overlapping grids that cover the domain. The flexibility of this kind of grid is especially useful for flows in which boundary parts move relatively to each other [Lomax and Pulliam 2001].

The fundamental problem of CFD simulations lies in the prediction of the effects of turbulence, which is three dimensional, unsteady and chaotic.

### **3.3.4 Turbulence modelling**

In practical engineering flows turbulence and turbulent mixing usually dominate the behaviour of the flow. Turbulence plays a crucial part in the determination of many relevant engineering parameters, such as frictional drag, heat transfer, flow separation, transition from laminar to turbulent flow, thickness of boundary layers, extent of secondary flows, and spreading of jets and wakes [Versteeg and Malalasekera 1995].

Turbulent flows contain turbulent eddies with a wide range of length scales, from the energy-carrying large scales to the small dissipative scales. These spatial scales are typically  $10^{-5}$  to  $10^{-6}$  of the size of computational domain in each co-ordinate direction [ERCOFTAC 2000]. By solving the complete, time-dependent Navier-Stokes equations, the direct numerical simulation (DNS) captures the time and length

scales of all the characteristic structure of the turbulent flows. However, the computational cost of DNS increases as the cube of the Reynolds number ( $Re^3$ ), so that the high cost limits its application to high Reynolds number flows [Blazek 2001].

In most engineering applications, emphasis is placed on the effects of the turbulence on the mean flow rather than resolving the details of the turbulent fluctuations. Thus, a turbulent flow can be described by the mean values of flow properties and the statistical properties of their fluctuations. By performing the time-averaging operation on the momentum equations, we can obtain the time-averaged momentum equations (Reynolds equations) and six additional unknowns, the so-called Reynolds stresses, which represent the velocity fluctuating effects on the flow. In order to close the system of mean flow equations, assumptions are needed for the extra unknown terms generated by the averaging process. This procedure of solving closure problems is called turbulence modelling [Versteeg and Malalasekera 1995].

#### **3.3.4.1 Overview of turbulence models**

Turbulence is one of the great unsolved physical problems of fluid dynamics. One flow is distinguished from another solely by the specification of material properties and of initial and boundary conditions. Intensive theoretical and experimental research states that turbulent flows are so complex and varied that no generally valid universal model of turbulence exists.

Broad ranges of turbulence models are available, that vary in complexity, accuracy and range of applicability. They are classified into four principle classes:

- Zero-equation models
- Two-equations models

- Second-order closures
- Large eddy simulation (LES)

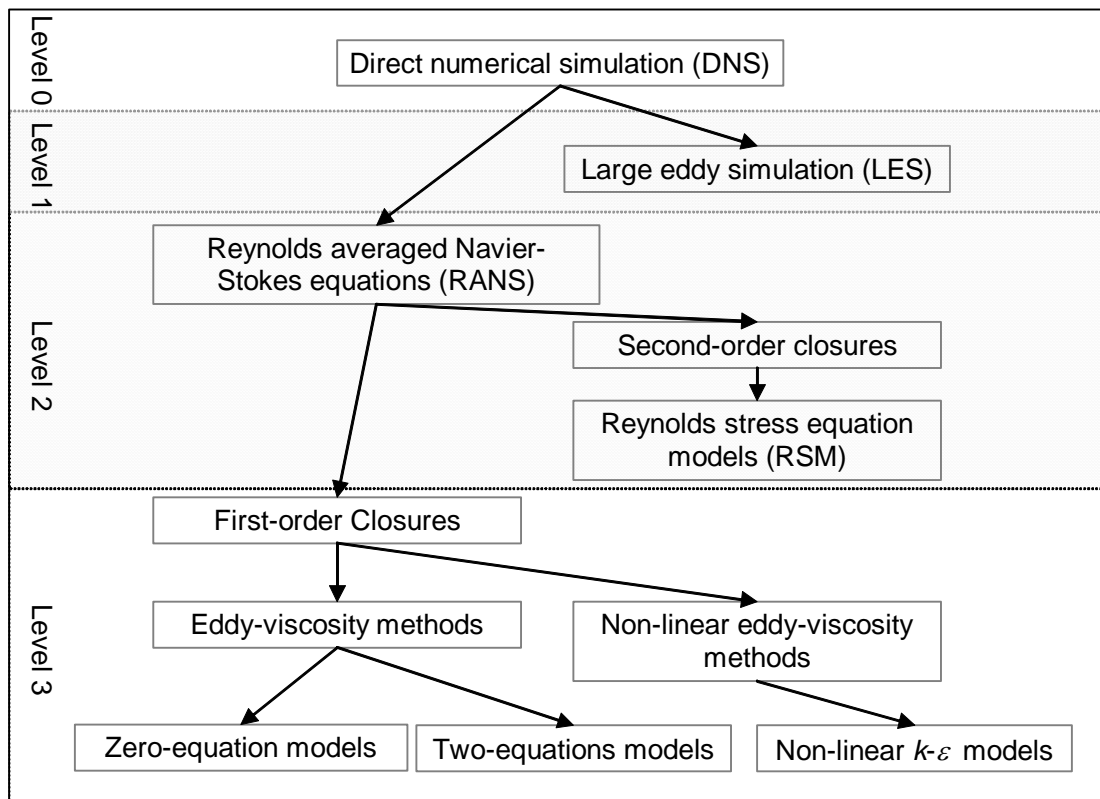


**Figure 3-2 Hierarchy of turbulence models**

(after Blazek, 2001)

Among them, the zero-equation/mixing length model (see Section 3.3.4.2) and DNS are at the extremes of the range of approaches. Figure 3-2 shows the overview of the turbulence models displayed according to their decreasing level of complexity.

The first two models belong to the so-called first-order closures, which are based mostly on the eddy viscosity hypothesis. The eddy viscosity concept (proposed by Boussinesq in 1877) assumes that the turbulent stresses are linearly related to the mean rate of strain by a scalar turbulent (eddy) viscosity. However, for certain applications the isotropic eddy viscosity assumption used in the majority of

turbulence models is not valid. The non-linear eddy viscosity models proposed by Lumley [1978] offer a substantially improved prediction capabilities for complex turbulent flow with a slightly more expensive computational requirement than the linear approach.

### 3.3.4.2 Reynolds Averaged Navier-Stokes (RANS) models

Reynolds Averaged Navier-Stokes equations (RANS) are developed from the time-dependent three-dimensional Navier-Stokes equations, which describe the unsteady eddies by their mean effects on the flow, through the Reynolds stresses.

The mixing length model (zero-equation model) uses an algebraic equation to calculate the viscous contribution from turbulent eddies. The flow description is at the mean flow level, apart from the specified mixing length,  $l_m(x,y)$ , which is described as a function of position by means of a simple algebraic formula. The turbulent viscosity ( $\nu_t$ ) is then:

$$\nu_t = l_m^2 \left| \frac{\partial U}{\partial y} \right| \quad (3.14)$$

In simple two-dimensional turbulent flows, the only significant Reynolds (turbulent) stress is linearly related to the mean velocity gradients and described by:

$$\tau_{xy} = \tau_{yx} = -\overline{\rho u'v'} = \rho l_m^2 \left| \frac{\partial U}{\partial y} \right| \frac{\partial U}{\partial y} \quad (3.15)$$

This simple model is only capable of calculating the mean flow properties and turbulent shear stress. It is incapable of describing flows with separation and recirculation, which are the flow features found in wind engineering.

The  $k$ - $\varepsilon$  type models calculate a mean, steady state velocity and pressure field and account for the velocity and pressure fluctuations through modelled variables, which are the kinetic energy ( $k$ ) and its rate of dissipation ( $\varepsilon$ ).

**(a) Standard  $k$ - $\varepsilon$  model**

The three dimensional incompressible turbulent flow of a Newtonian fluid is governed by the mass conservation and the Navier-Stokes equations. By introducing the Reynolds averaging procedure, the set of equations expressed in Cartesian tensor notation is [Versteeg & Malalasekera 1995]:

$$\frac{\partial U_i}{\partial x_i} = 0 \quad (3.16)$$

$$\frac{\partial U_i}{\partial t} + \frac{\partial(U_i U_j)}{\partial x_j} = -\frac{1}{\rho} \frac{\partial P}{\partial x_i} + \frac{\partial}{\partial x_j} (-\overline{u_i u_j}) \quad (3.17)$$

where  $P$  stands for mean pressure and  $\rho$  for fluid density. The Reynolds stress tensor  $-\overline{u_i u_j}$  is modelled using the eddy viscosity concept:

$$-\overline{u_i u_j} = \nu_t \left( \frac{\partial U_i}{\partial x_j} + \frac{\partial U_j}{\partial x_i} \right) - \frac{2}{3} \delta_{ij} k \quad (3.18)$$

The isotropic eddy viscosity  $\nu_t$  is determined using the following expression

$$\nu_t = C_\mu k^2 / \varepsilon \quad (3.19)$$

which requires the distribution of  $k$  and its rate of dissipation  $\varepsilon$ .

In the standard  $k$ - $\varepsilon$  model [Launder and Spalding 1974], the distributions of  $k$  and  $\varepsilon$  are determined from the following model transport equations:

$$\frac{\partial k}{\partial t} + U_i \frac{\partial k}{\partial x_i} = \frac{\partial}{\partial x_i} \left( \frac{\nu_t}{\sigma_k} \frac{\partial k}{\partial x_i} \right) + \nu_t \frac{\partial U_i}{\partial x_j} \left( \frac{\partial U_i}{\partial x_j} + \frac{\partial U_j}{\partial x_i} \right) - \varepsilon \quad (3.20)$$

$$\frac{\partial \varepsilon}{\partial t} + U_i \frac{\partial \varepsilon}{\partial x_i} = \frac{\partial}{\partial x_i} \left( \frac{\nu_t}{\sigma_\varepsilon} \frac{\partial \varepsilon}{\partial x_i} \right) + C_{\varepsilon 1} \frac{\varepsilon}{k} \nu_t \frac{\partial U_i}{\partial x_j} \left( \frac{\partial U_i}{\partial x_j} + \frac{\partial U_j}{\partial x_i} \right) - C_{\varepsilon 2} \frac{\varepsilon^2}{k} \quad (3.21)$$

For the standard model the model coefficients are:

$$C_\mu = 0.09; C_{\varepsilon 1} = 1.44; C_{\varepsilon 2} = 1.92; \sigma_k = 1.0 \text{ and } \sigma_\varepsilon = 1.3.$$

The standard  $k$ - $\varepsilon$  model is the most commonly used and validated turbulence model in engineering applications. The popularity of this model is due to its robustness in a wide range of industrially relevant flows, relatively low computational costs and generally better numerical stability than more complex turbulence models [Versteeg and Malalasekera 1995]. However, the weaknesses of this model affect its overall performance in wind engineering field:

- The turbulent kinetic energy is over-predicted in regions of flow impingement and re-attachment leading to poor prediction of heat transfer and the development of boundary layer flow around leading edges and bluff bodies. The RNG  $k$ - $\varepsilon$  model proposes a modification to the transport equation for  $\varepsilon$  and may also improve predictions in this area [ERCOFTAC 2000].
- Highly swirling flows are often poorly predicted due to the complex strain fields and regions of recirculation in a swirling flow are often underestimated. A non-linear  $k$ - $\varepsilon$  model or an algebraic Reynolds stress model would improve the performance [ERCOFTAC 2000].
- Flow separation from surfaces under the action of adverse pressure

gradients is often poorly predicted. The real flow is likely to be much closer to separation (or more separated) than the calculations suggest.

There are several modifications from the standard  $k$ - $\varepsilon$  model which have been proposed to improve the performance for special applications.

### **(b) Low Reynolds Number $k$ - $\varepsilon$ model**

This model uses a different treatment in the near wall region from the standard  $k$ - $\varepsilon$  model. The high Reynolds number standard  $k$ - $\varepsilon$  model uses the universal law of the wall to give special treatment near the wall. This so-called “wall function” is introduced and depends on the unit distance normal to the wall (see Section 3.3.5). The low Reynolds number model [Patel et al. 1985] does not apply this method and effectively integrates to the wall surface in the low Reynolds number region of the flow. It therefore requires additional grid cells in this region and significant additional computational effort.

### **(c) RNG $k$ - $\varepsilon$ model**

In the Re-Normalization Group (RNG)  $k$ - $\varepsilon$  model, the transport equation for turbulence generation is the same as that for the standard  $k$ - $\varepsilon$  model, but the model constants are different, and the extra term in the  $\varepsilon$  equation represented by extra coefficient  $C_{IRNG}$ , makes this model perform differently from the standard  $k$ - $\varepsilon$  model.

$$C_{\mu} = 0.085; C_{\varepsilon 1} = 1.42; C_{\varepsilon 2} = 1.68; \sigma_k = \sigma_{\varepsilon} = 0.72.$$

Further details can be found in [Yakhot et al. 1992].

**(d) MMK  $k$ - $\varepsilon$  model**

The MMK (Murakami-Mochida-Kondo) model is also a revision to the standard  $k$ - $\varepsilon$  model to improve its performance. It was developed to tackle the specific problems of flows with separations and reattachments as found in wind engineering flow fields [Tsuchiya et al. 1997]. The standard model constant  $C_\mu$  becomes a function of the ratio of vorticity to shear. Therefore, when this ratio is less than one (e.g. flow stagnation point) the eddy viscosity is reduced. Although the MMK model was found to improve the results in some areas of the flow it had the opposite effect in other areas [Wright and Easom 1999]. Therefore, this model is limited by the general accuracy in different cases.

**(e)  $k$ - $\omega$  model**

The  $k$ - $\omega$  model introduced by Wilcox [1993] performs very well close to the wall in boundary layer flows, particularly under strong adverse pressure gradients (i.e. in aerospace applications). However, it is very sensitive to the free stream value of  $\omega$  ( $\omega \equiv \varepsilon/k$ ).

The  $k$ - $\omega$  model is superior near the wall, due to its simple low Reynolds number formulation and its ability to compute flows with weak adverse pressure gradients accurately. The  $k$ - $\varepsilon$  model is the better model near the boundary layer edge and for flows away from walls, due to its insensitivity to the free stream values. A few models have been developed to blend the advantages of the  $k$ - $\varepsilon$  and the  $k$ - $\omega$  model, i.e. Shear Stress Transport (SST) model of Menter [1994]. This model has performed well for flows with adverse pressure gradients, which can be found in many applications in the aeronautics industry, e.g. airfoils and heat exchangers.

**(f) Reynolds stress model (RSM)**

When modelling the complex strain field arising from the action of swirl, body forces such as buoyancy or extreme geometrical complexity, the eddy viscosity models with the simple strain field assumption are found to be inadequate [ERCOFTAC 2000]. A more subtle relationship between stress and strain is invoked in the RSM model, also called the second-order or second-moment closure model, in that six Reynolds stresses and the rate of dissipation of turbulent kinetic energy are determined by the solution of six additional coupled equations, together with an equation for  $\varepsilon$ . This model gives better predictions for flows with distinct anisotropic quantities, but the computational cost and lack of numerical stability are practical drawbacks with RSM compared with other RANS models.

**3.3.4.3 Non-linear  $k$ - $\varepsilon$  model**

The non-linear  $k$ - $\varepsilon$  model [Speziale 1987; Craft et al. 1996] solves only two transport equations, which is the same number solved by its standard (linear) counterpart. On the other hand, due to the non-linear constitutive relation between the stress and rate of strain tensors, this model is theoretically capable of simulating the anisotropy of turbulence. It is therefore an economical way of accounting for the anisotropy of Reynolds stresses without solving the whole Reynolds stress transport equations. However, further development work is still required to improve the numerical stability in wind engineering applications [Wright and Easom 1999].

### 3.3.4.4 Large Eddy Simulation (LES)

In large eddy simulation (LES) the larger three-dimensional unsteady turbulent motions are directly represented, whereas the effects of the smaller scale motions are modelled.

Compared with RANS models, LES has the advantage of describing the unsteady, large scale turbulent structures, and hence can be used to study phenomena such as unsteady aerodynamic loads on structures and the generation of sound. LES can be expected to be more accurate and reliable than Reynolds stress models (RSM), in the prediction of the flows over bluff bodies, which involve unsteady separation and vortex shedding [Murakami 1997]. However, LES models require large computing resources and therefore they are still research tools rather than general purpose tools in engineering applications.

### 3.3.5 Wall functions

In a turbulent flow, the presence of a wall causes a number of different effects. Near the walls, the turbulence Reynolds number approaches zero, and the mean shear normal gradients in the boundary layer flow variables become large.

At high Reynolds number the standard  $k$ - $\varepsilon$  turbulence model does not seek to directly reproduce logarithmic profiles of turbulent boundary layers, instead it applies the law of the wall in the adjacent layer (so-called log-layer). The law of wall is characterised in terms of dimensionless variables with respect to boundary conditions at the wall.

The wall friction velocity  $u_\tau$  is defined as  $(\tau_w/\rho)^{1/2}$  where  $\tau_w$  is the wall shear stress.

Assume  $U$  is the time-averaged velocity parallel to the wall and let  $y$  be the normal

distance from the wall. Then the dimensionless velocity,  $U^+$  and dimensionless wall distance,  $y^+$  are defined as

$$U^+ = \frac{U}{u_\tau} \quad (3.22)$$

and  $y^+ = \rho \frac{u_\tau}{\mu} y$  (3.23)

When using this model the value of  $y^+$  at the first mesh point must be within the limit of validity of the wall functions,  $30 < y^+ < 500$  [Versteeg and Malalasekera 1995]. The universal wall functions are valid for smooth walls. For rough walls, the wall functions can be modified by scaling with an equivalent roughness length. However, the wall function methods are not valid in the presence of separated regions and/or strong three dimensional flows. When a low Reynolds number turbulence model is used, the first node points from walls of the computational grids must be carefully allocated within the unity distance normal to the wall.

### 3.3.6 Discretisation scheme

The accuracy of the numerical solution of a CFD model is dependent on the quality of discretisation applied to the governing equations. The general differential form of all the governing equations can be written as follows [Versteeg and Malalasekera 1995]:

$$\frac{\partial}{\partial t}(\rho\phi) + \frac{\partial(\rho u_i \phi)}{\partial x_i} = \frac{\partial}{\partial x_i} \left( \Gamma \frac{\partial \phi}{\partial x_i} \right) + S_\phi \quad (3.24)$$

where

$\Gamma$  is the diffusivity of a variable  $\phi$ ,

$S_\phi$  is the source term.

Based upon a Finite Volume Method by application of Gauss' divergence theorem, the integration of Eqn.3.24 over a three-dimensional control volume yields:

Time-dependent	Convection	Diffusion	Source
----------------	------------	-----------	--------

$$\int_V \frac{\partial \rho \phi}{\partial t} dV + \int_A \rho u_j \hat{n}_j \phi dA = \int_A \Gamma \frac{\partial \phi}{\partial x_j} \hat{n}_j dA + \int_V S_\phi dV \quad (3.25)$$

where

$\hat{n}_j$  is the surface outward normal vector

$A$  and  $V$  are the outer surface area and volume of the control volume respectively.

The main consideration in deriving the discrete equations in this way is that it accounts for the convection and diffusion terms explicitly. The fundamental properties of a discretisation scheme are conservativeness, boundedness and transportiveness, which are necessary to produce physically realistic results.

#### Conservativeness:

To ensure the conservation of a quantity  $\phi$  for the whole solution domain, the flux of  $\phi$  across a certain face of a control volume must be the same as that entering the adjacent volume through the same face. Inconsistent flux interpolation formulae could cause unsuitable schemes that do not satisfy the overall conservation.

#### Boundedness:

Within the solution domain, the iterative numerical techniques are used to solve the set of algebraic equations at each nodal point. The calculated quantities should fit in the physical bounded maximum and minimum boundary values of the flow variables.

Undershoots and overshoots results are typically associated with higher order schemes or too coarse grids.

Transportiveness:

The relative strength of convection and diffusion terms defines the directionality of influence in the discretisation scheme. In a highly diffusive situation, the diffusion term affects the distribution of a transported quantity along its gradients in all directions, i.e. the influence of the source at all neighbouring nodes would be equal. However, in the case of pure convective conditions, only the adjacent node would be strongly influenced by the upstream/downstream source depending on the flow direction.

The order of the discretisation scheme is named in terms of Taylor series truncation error. The following differencing schemes are discussed in terms of their suitability in dealing with the convection term.

The first order schemes such as “upwind” and “hybrid” produce bounded solutions within the physical limitations, but they involve significant false diffusion, smearing sharp gradients. The Quadratic Upstream Interpolation for Convective Kinetic (QUICK) scheme [Leonard 1979] is a third order accurate approximation, which has many benefits as it satisfies the requirements of conservativeness and transportiveness, but introduces unphysical over- or under-shoot problems due to the lack of the boundedness property. It has been shown to sometimes lead to negative turbulence quantities [Wright 2000]. A modified version of QUICK gives the Curvature Compensated Convective Transport scheme (CCCT) second order accuracy and provides boundedness and hence computational stability. The CCCT

scheme [Gaskell and Lau 1988] uses a blending factor to improve the QUICK scheme's interpolation performance near the boundaries.

To choose a discretisation scheme, a compromise between simplicity, ease of implementation, accuracy and computational efficiency has to be made.

### **3.3.7 Credibility of CFD simulation**

The confidence and trust in CFD simulation results are obtained from the verification and validation of the code.

Verification is the process of determining the accuracy of a given computational solution with respect to the underlying model, while validation is the process of assessing the relevance of the computational results with respect to physical reality [AIAA 1998]. The fundamental strategy of verification is the identification and quantification of error in the computational model and its solution.

There are four predominant sources of errors in CFD simulations: insufficient spatial (grid) discretisation convergence, insufficient temporal discretisation convergence, lack of iterative convergence, and computer programming.

Grid sensitivity studies are crucial for all turbulent flow computations. Time-step convergence tests make sure the results are taken from the fully developed flow. Generally as a minimum requirement, the second-order accurate differencing schemes should be employed in any computational procedure [AIAA 1998].

The discretised Navier-Stokes equations are solved iteratively. The residual for each equation gives a measure of how far the latest solution is from the exact (converged) solution to the discretised equations.

Usually, there are two levels of iterations: the inner iterations, within which the linear equations are solved, and the outer iterations, that deal with the non-linearity and coupling of the equations.

The convergence criteria for CFD simulations are essentially problem dependent.

Generally if the root-mean-squared (RMS) residuals are all below  $10^{-4}$  (a fourth order of magnitude reduction in residuals) and the global imbalances are less than 1%, then that solution can be assumed converged.

To validate CFD predictions, the CFD results should be compared with the analytical solution, benchmark solution and full-scale experiment of the same problem. The discrepancies between full-scale measured and CFD calculated flow quantities arise from the following factors [Roache 1998]:

- inaccuracies of the model
- numerical error
- measurement error, and
- discrepancies in the boundary conditions

### **3.3.8 Unstructured grid CFD code – CFX5**

All simulations in the present investigation use the commercial general purpose CFD software, CFX5. CFX5 is a second order, pressure/velocity coupled, finite element based control volume method that uses an unstructured grid [Blazek 2001] and a coupled algebraic multi-grid solver [Raw 1996]. A comprehensive description of the relevant theory can be found in CFX5 User Manual [AEA Technology 2001a]. The overview of the numerical prediction techniques within this code is presented in the following sections.

### 3.3.8.1 Turbulence models

The built-in turbulence models are mixing length model, standard  $k$ - $\varepsilon$  model, RNG  $k$ - $\varepsilon$  model, shear stress transport (SST) model, low Reynolds number  $k$ - $\varepsilon$  model and Reynolds stress models. Other turbulence models which are more suitable for wind engineering studies, i.e. non-linear  $k$ - $\varepsilon$  model, large eddy simulation (LES) have not been fully tested and released by the code vendor at present.

### 3.3.8.2 Numerical scheme

The discretisation schemes used by CFX5 are based on conventional upwind differencing scheme for the advection terms in the discrete finite volume equations. The scheme can be run with a 'blend factor' between 0.0 and 1.0 to achieve 1<sup>st</sup> and 2<sup>nd</sup> order accuracy, respectively.

### 3.3.8.3 Coupled solver

The overall solution process consists of linearising the non-linear equations (coefficient iteration) and solving the linearised equations (equation solution iteration). The same general solution system is used for all the coupled 3D mass-momentum equation set and scalar equations. However, this coupled solution algorithm needs more storage spaces for all the coefficients than a non-coupled or segregated approach.

The process of multigridding involves carrying out early iterations on a fine mesh and later iterations on progressively coarser virtual ones. The results are then transferred back from the coarsest mesh to the original mesh. Applying the Algebraic Multigrid technique improves the iterative solver's performance as the

number of computational mesh elements increases, or if large element aspect ratios are present.

#### **3.3.8.4 Near wall treatment methods**

In CFD simulation close to solid structures or walls, it is often difficult for the user to generate a mesh that is fine enough to resolve the boundary layer and simultaneously place the first grid node within the flow region where the logarithmic scaling law (standard wall functions) is valid. The scalable wall function in CFX5 forces all grid nodes to be outside the viscous sublayer and allows the user to apply arbitrarily fine grids without a violation of the underlying logarithmic profile assumptions.

Applying a low Reynolds number model requires a very fine grid resolution near the wall. The automatic near-wall treatment in CFX5 switches automatically from a low-Reynolds number formulation to a standard wall function treatment based on the grid density on the walls.

### **3.4 Building Envelope Flows**

In all cases of natural ventilation, the basic driving forces of an envelope flow are the internal and external pressures, which lead to flows through all kinds of openings in the building structure. Pressure differences result from the combined action of two mechanisms, the wind and temperature differences.

#### **3.4.1 Wind effect**

The wind effect is transient, creating local areas of positive pressure (on the windward side) and negative pressure (on the leeward side) on buildings. This introduces flows through the building openings. The wind velocity and pressure

fields around buildings are greatly affected by the form of the building envelope, i.e. the shape, the location and surroundings of the building.

The surface pressure coefficient  $C_p$  on buildings is defined by

$$C_p \equiv \frac{(p - p_{ref})}{\frac{1}{2} \rho U_{ref}^2} \quad (3.26)$$

where

$p_{ref}$  is the reference static pressure

$\frac{1}{2} \rho U_{ref}^2$  is reference dynamic pressure associated with the flow.

Mean pressure differences are determined primarily by the wind speed, the wind direction, the geometry of the building and the geometry of the building environment. In ventilation studies, for a given building in a specific environment, the difference of pressure coefficients can merely be taken as a function of the wind direction. The fluctuating surface pressures are caused by the turbulence in the wind, meanwhile the building also affects the airflow in its immediate vicinity.

### 3.4.2 Buoyancy effect

Air movement by the buoyancy (stack) effect occurs as a result of pressure differences generated by the different variations of temperature with height inside and outside the building envelope. The buoyancy effect exists whenever there is a temperature difference between the adjacent internal zones or indoor and outdoor. This effect becomes stronger as the temperature difference increases. As heated air escapes from the upper openings of the building, replacement outdoor air is drawn into the openings at the lower level of the building.

### 3.4.3 Combined wind and buoyancy effects

In practice, wind and thermal effects are often combined to drive the ventilation in buildings. The physical processes which govern natural ventilation are outlined by the following equations which are known as building envelope flow theories.

## 3.5 Mathematical Models of Envelope Flows

Building envelope flows are often considered independent of internal flows, and one can then apply a set of simplified mathematical relationships to calculate the required envelope flows from knowledge of certain properties of the building and prevailing meteorological conditions.

The common conventional mathematical models can be classified as purely-empirical or semi-empirical. The first ones represent the correlations of field data. The second ones solve the mass conservation equation for the building either in its multi-cell or single-cell form. Semi-empirical models often contain many simplifying assumptions themselves.

### 3.5.1 Air leakage

Air leakage is the airtightness of a building envelope and is independent of weather conditions and ventilation operation systems. The air leakage is usually expressed as the building air change rate at a reference pressure difference across the building envelope or as an effective leakage area that accounts for all the leaks in the building.

In normal weather conditions, the ventilation rate due to adventitious leakage can be measured by the tracer gas decay technique (see Section 3.6.2.1). The tracer gas decay history gives the average infiltration rate of the buildings  $Q_{inf}$ , which is calculated by using the equation:

$$Q_{inf} = Vol \frac{\ln \frac{C(t_1)}{C(t_2)}}{t_2 - t_1} \quad (3.27)$$

where

$Q_{inf}$  is infiltration rate in  $m^3/h$

$Vol$  is the effective volume of the building in  $m^3$

$C(t_1)$  and  $C(t_2)$  are the concentration of the gas at time  $t_1$  and  $t_2$  respectively.

### 3.5.2 Envelope flow models

For a single-zone building model, with two sharp-edged openings (where the diameter is very much greater than the depth of the opening) the flow parameters used in ventilation study are shown in Figure 3-3 and outlined as follows:

- Mean wind speed and direction ( $U$  and  $Dir$ )
- Indoor and outdoor temperatures and densities ( $T_i, \rho_i$  and  $T_e, \rho_e$ )
- Surface pressure coefficient at each opening ( $C_{p1}, C_{p2}$ )
- Relative height difference of two openings ( $h$ )
- Mean volume flow rate through each opening ( $q_1, q_2$ )

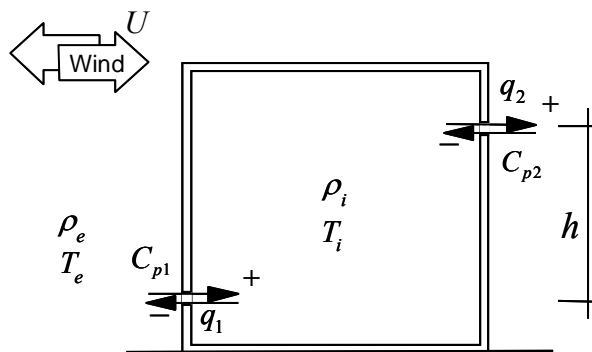


Figure 3-3 Flow parameters in ventilation studies

Most ventilation flows are unsteady, due to the presence of wind turbulence. When the bulk flow through the opening is unsteady (i.e. it varies with time), analytic solutions to the equations of motion are very rare even for the simplest openings and boundary conditions. However, the main interest in practice is the relationship between the bulk mean flow rate and the differences between the mean external static pressures on the inlet and outlet sides. The flow characteristics can be described by  $q = f\{\Delta p\}$  or in nondimensional terms by  $C_d = f(Re_o)$ , where  $Re_o$  represents the opening Reynolds number.

In the presence of wind, ventilation is most likely to be steady in the mean, rather than truly steady. The steady ventilation rate then indicates that which is due to the mean values of internal and external pressure averaged over a sufficiently long period of time (usually 10 to 15 minutes), and hence they can be treated as independent of time. For any ventilation opening with given steady external conditions,  $C_d$  is a function of the shape of the opening and its opening Reynolds number  $Re_o$ , which is defined in terms of the average velocity within the opening and the diameter of the opening.

Theoretical models contain assumptions and approximations made about the flow equation and the continuity equation [Etheridge 2000a]:

#### The flow equation assumptions

- (i) the pseudo-steady flow assumption forms the basis of most mathematical models of envelope flows. It states that the time-averaged flow characteristic of each opening is the same as it would be if the pressure and flow fluctuations were not present.

- (ii) the quasi-steady flow assumption states that at each instant of time the flow behaves as if it were truly steady. Truly steady ventilation occurs when the pressure differences due to temperature differences are much greater than those caused by the wind.

#### The continuity equation assumption for two different cases

- (i) It is sometimes assumed that the Boussinesq approximation is valid, that is the difference between the internal and external densities can be neglected in the continuity equation.
- (ii) The Boussinesq approximation is not used.

#### **3.5.2.1 Pseudo-steady model with Boussinesq approximation**

The pseudo-steady model assumes that the time-averaged quantities follow the same relationship as for truly steady flow. By applying the Boussinesq approximation, the continuity (mass conservation) equation for the envelope of a building becomes:

$$q_1 + q_2 = 0 \quad (3.28)$$

The ventilation of the building may be induced by wind effects alone, buoyancy effects alone and combined wind and buoyancy effects.

##### **(a) Ventilation due to wind effect**

The wind-driven ventilation consists of two components – a mean component driven by the mean pressure difference across the ventilation openings, and a fluctuating component driven by the fluctuating pressures and unsteady flows around the openings. Most envelope flow models only take account of mean pressures.

To predict the wind-induced ventilation for a building, we need to know:

- the surface distribution of the pressure coefficients and how this distribution varies with wind direction.
- the steady flow characteristics of the openings and
- the positions of the openings.

The steady flow characteristic of an opening is the relationship between the flow rate through the opening and the pressure difference across it. In the simple case of a building with two small, sharp-edged openings ( $C_d = \text{constant}$ ) as shown in Figure 3-2 (p.64), the ventilation rate due to wind alone is proportional to wind speed and pressure coefficient difference  $dC_p$  across the two openings, which is mainly influenced by wind direction. The openings are assumed to be identical with the same flow characteristic, so that the wind-driven ventilation rate is defined by

$$Q = C_d A U_{ref} \sqrt{\frac{dC_p}{2}} = C_d A \sqrt{\frac{dP}{\rho}} \quad (3.29)$$

where

$C_d$  is the opening discharge coefficient (independent of  $Re_o$  for sharp-edged openings)

$dP$  is the mean static pressure difference across the openings (Pa)

$\rho$  is the air density ( $\text{kg/m}^3$ ).

### (b) Ventilation due to buoyancy effect

For the same case, the ventilation rate due to temperature difference is proportional to the square root of  $dT$  and  $h$ .

The average density is defined as:

$$\rho_a = \frac{\rho_e + \rho_i}{2} \quad (3.30)$$

and density difference is:

$$d\rho = \rho_e - \rho_i \quad (3.31)$$

then the ventilation rate is given as:

$$Q = C_d A \sqrt{\frac{(d\rho)gh}{\rho_a}} = C_d A \sqrt{\frac{(dT)gh}{T_e}} \quad (3.32)$$

where

$T_e$  is the external/outdoor temperature (K)

$dT$  is the temperature difference,  $T_e - T_i$  (K)

$h$  is the vertical distance between the two openings (m)

$g$  is the gravitational acceleration ( $m/s^2$ )

### (c) Combined effects of wind and buoyancy forces

The volume flow rate introduced by combined wind and buoyancy effects is described as:

$$Q = C_d A U \sqrt{\left| \frac{dC_p}{2} + \frac{(d\rho)gh}{\rho_a U^2} \right|} \quad \text{or} \quad Q = C_d A U \sqrt{\left| \frac{dC_p}{2} - \frac{(d\rho)gh}{\rho_a U^2} \right|} \quad (3.33)$$

where the “+” or “-” sign indicates that the wind force complements or counteracts the buoyancy effect.

#### 3.5.2.2 Pseudo-steady model without Boussinesq approximation

The continuity equation without the Boussinesq approximation is expressed as:

$$\rho_1 q_1 + \rho_2 q_2 = 0 \quad (3.34)$$

Eqn.3.29 is also applied for the wind effect alone case, but Eqn 3.32 for buoyancy alone case becomes:

$$q_1 = C_d A \sqrt{\frac{2(d\rho)^* gh}{\rho_e} \frac{\rho_i}{(\rho_e + \rho_i)}} \quad (3.35)$$

$$q_2 = C_d A \sqrt{\frac{2(d\rho)^* gh}{\rho_i} \frac{\rho_e}{(\rho_e + \rho_i)}} \quad (3.36)$$

More complicated quasi-steady models can be found in [Etheridge 2000b].

The pseudo-steady model is adopted for practical design procedures [BSI 1991].

Therefore, this model has also been used in the current investigation.

### 3.6 Experimental Technology

For the present investigation, the tracer gas and the ultrasonic technique are used. As shown in Figure 3-4, the ultrasonic anemometer was chosen to measure the instantaneous wind velocity.



**Figure 3-4 Ultrasonic anemometer (Gill Instrument Research R3)**

<http://www.gill.co.uk/products/anemometer/anemometer.htm>

### **3.6.1 Ultrasonic technique**

At standard atmospheric temperature and pressure, the velocity of sound, often designated “ $c$ ”, is 340.3 m/s in air. As the working environment changes, the temperature, moisture and air density will affect the speed of sound locally. The ultrasonic technique enables the anemometer to overcome this problem, so that the measurement is relatively independent of the flow properties (e.g. spatial and time variations, density, and temperature).

#### **3.6.1.1 Principle of operation**

The ultrasonic anemometer (pulse based) measures air speed by measuring the influence of this air movement on the time of flight of ultrasound pulses that travel between pairs of transmitters and receivers.

For optimum undisturbed airflow, three pairs of transceivers set in a non-orthogonal arrangement are employed to measure the air speed and direction. The ultrasonic anemometer records a true vector, with a correction for misalignment (yaw) of the probe from the direction of flow, therefore it can be used to make measurements across the vast spectrum of normally occurring work conditions.

The Solent Research R3 anemometer [Gill Instruments Ltd 2000] has a sampling rate of up to 100 samples per second and resolution of 0.01m/s with accuracy of 1%.

Once the anemometer is calibrated by the manufacturer, its accuracy will last for its life-time.

### **3.6.2 Tracer Gas Techniques**

Tracer gas techniques are the most popular and important techniques for ventilation measurements in buildings. According to the method of injection and the form of

mass balance equation these techniques are classified into four types [Cheong 2001]: concentration decay, constant injection, pulse injection, and constant concentration.

### 3.6.2.1 Concentration-decay technique

The concentration-decay technique involves an initial injection of tracer gas into the test building. In order to produce a well-mixed and evenly distributed sample in the test space, a portable mixing fan can be used. The decay of tracer gas is monitored over a given time interval.

The tracer decay history can be expressed by

$$C(t) = C(0)e^{-It} \quad (3.37)$$

$C(t)$ ,  $C(0)$  represents the tracer gas concentration at any time point and the beginning of the record time period respectively. The slope of the natural logarithm plot of this tracer concentration,  $I$ , gives the volume flow rate in air change per hour. So that, the ventilation rate in  $\text{m}^3/\text{s}$  is given by  $\frac{IV}{3600}$ , where  $V$  is the volume of the building.

This technique can provide a precise measurement of ventilation rate in buildings because the air change rate is low and good mixing of tracer gas and air can be achieved by using portable fans [Etheridge and Standberg 1996].

### 3.6.2.2 Constant injection technique

Applying the constant injection technique, the tracer gas is continuously injected into the building, while the concentration of tracer is measured at an indoor point. The constant injection rate is controlled by a mass flow meter/controller. The sampling and analysis of the tracer gas is carried out continuously using a gas analyser. If the change of the indoor tracer concentration is small, both the injection of tracer gas

into the building and the air exchange rate is close to equilibrium. Therefore the ventilation rate would simply be given by the ratio of injection rate to indoor concentration (Eqn 3.38).

$$Q = \frac{q_{gas}}{C(t)} \times 10^6 \quad (3.38)$$

where

$q_{gas}$  is the injection volume flow rate in  $m^3/s$

$Q$  ( $m^3/s$ ) is the total ventilation rate of the cube

$C(t)$  is the indoor tracer gas concentration in ppm.

A schematic of the constant-injection equipment is shown in Figure 3-5.

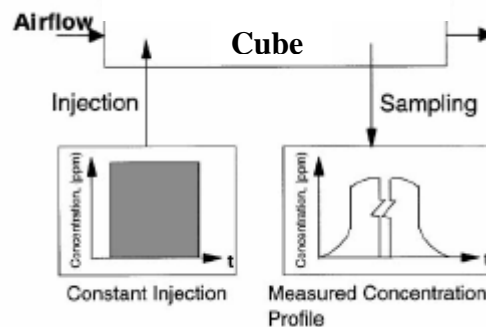


**Figure 3-5 Schematic diagram of constant injection technique**

(after Cheong, 2001)

The advantage of this method is that it provides continuous information. During one measurement period a range of wind speeds and directions can be recorded [Baptista et al. 1999]. However, under natural conditions, the equilibrium state is difficult to reach and this technique requires excessive tracer gas consumption compared to the decay technique. It also relies on the assumption that all the air flows out of only one opening. Normally it is used with running fans to overcome this limitation.

The assessment details of the other two techniques, i.e. pulse injection and constant concentration, can be found in [Cheong 2001].

Comparing the tracer gas techniques for building ventilation studies, tracer gas decay technique requires less tracer gas consumption, less equipment involved than the other techniques. It is more suitable to measure ventilation associated with turbulence in the external flow [Carey and Etheridge 1999]. Therefore, the tracer gas decay technique is chosen for the current investigation.

### **3.7 Wind Tunnel Modelling**

As mentioned in Section 2.6.2, wind tunnel modelling is one of the physical modelling techniques which simulates the flow field in and around buildings at reduced scale. The essential concepts relevant to wind tunnel investigations of natural ventilation are discussed below.

#### **3.7.1 Similarity requirements**

The fundamental consideration in wind tunnel modelling is the issue of similarity. If the similarity requirements are satisfied, the full-scale (prototype) quantities can be obtained from measurements at the model scale by applying known scale factors.

Similarity of the boundary conditions takes two forms: geometric similarity and dynamic similarity. Geometric similarity states that the size of the model buildings should be scaled down geometrically to the prototype as well as the other boundary conditions. Dynamic similarity means that fluid elements that are initially at corresponding points in the two systems follow corresponding paths.

Typically wind tunnel modelling simulates only the lower region of the atmospheric boundary layer (ABL), which is up to one-third of the full depth [Kaimal and Finnigan 1994]. Ideally all of the following parameters of the natural wind in the ABL should be reproduced at model scale:

- (i) mean velocity profile
- (ii) turbulence intensity profile
- (iii) turbulence length scale ( $z_0/H$ ) or turbulent spectrum

Requirement (i) accounts for the simple combinations of the principal dimensions length and time. Incorporating it with requirement (ii) ensures the achievement of upstream flow conditions and flow over the building environment. Requirement (iii) relates to simulating the pressure distribution on buildings in atmospheric wind, the ratio of the surface roughness ( $z_0$ ) to the building height ( $H$ ) in the wind tunnel must be equal to that of the ABL.

The Reynolds number ( $Re$ ) represents the ratio of inertial to viscous forces. The scale reduction diminishes the magnitude of a Reynolds number by several orders from that in full-scale. Consequently, this indicates the potential domination of the viscous forces in the model. Fortunately, sharp-edged structures are generally insensitive to Reynolds number, and therefore the scaled model flow will be dynamically similar to the full-scale case if Reynolds number is larger than a minimum critical value.

### **3.7.2 Similarity parameters in building ventilation studies**

The similarity requirements in the wind tunnel studies of building ventilation can be explained in terms of nondimensional parameters (Reynolds and Archimedes numbers) and boundary conditions as follows:

### 3.7.2.1 Wind effect alone - Reynolds numbers

For natural ventilation design purpose-provided openings often have flow characteristics which are not sensitive to Reynolds number [Etheridge 2000a]. There are two types of Reynolds number that should be considered in wind tunnel tests, namely the opening Reynolds number and the building Reynolds number.

With sharp-edged openings and building, there are values of the Reynolds numbers ( $Re$ ), above which the discharge coefficient and the external flow are independent of  $Re$  (the so-called critical  $Re$ ). Reynolds number independence can justify the use of smaller  $Re$  (which exceeds the critical  $Re$ ) in a model than in a prototype.

#### (a) Opening Reynolds number

$$Re_o \equiv \frac{q}{A} \cdot \frac{d}{\nu} \quad (3.39)$$

where

$q$  is the mean volume flow rate through the opening ( $m^3/s$ )

$A$  is the opening area ( $m^2$ )

$d$  is the diameter of the opening (m)

$\nu$  is the kinematic viscosity ( $m^2/s$ ).

#### (b) Building Reynolds number

$$Re_b \equiv \frac{U_{ref} H}{\nu} \quad (3.40)$$

where

$U_{ref}$  is the reference wind speed (m/s)

$H$  is the building height (m).

### 3.7.2.2 Combined wind and buoyancy effects - Archimedes number

If buoyancy is also involved, extra parameters relating to the temperature boundary conditions and the Archimedes number ( $Ar$ ) are required. Depending on whether the Boussinesq approximation can be invoked or not, these requirements vary.

The Boussinesq approximation states that the density differences can be neglected in the inertia terms but retained in the buoyancy terms [Turner 1973]. If the Boussinesq approximation is valid, the density differences can be neglected in the mass conservation equation (Eqn. 3.28), then it is allowable to use higher values of  $dT/T$  in the model [Etheridge 2000a]. If the Boussinesq approximation cannot be applied, the ratio of temperature difference ( $dT$ ) to ambient temperature ( $T$ ) in the model should be the same as in the prototype.

The Archimedes number which should be maintained in the scaled model, is defined as:

$$Ar \equiv \frac{(d\rho) \cdot gh}{\rho_a U_{ref}^2} \equiv \frac{(dT) \cdot gh}{TU_{ref}^2} \quad (3.41)$$

where

$h$  is the relative height distance of two openings (m)

$\rho_a$  is the average density ( $\text{kg/m}^3$ )

$T$  is the absolute temperature (Kelvin) of the air.

In addition to satisfying the Reynolds number requirement, the Archimedes number ( $Ar$ ) of the prototype should be achieved, which gives the required ratio between buoyancy and wind forces. In this case, the  $dT/T$  value should be kept as small as possible to ensure exceeding the critical Reynolds numbers.

The wind tunnel technique is preferable when wind effects are important. It is desirable to include buoyancy effects at the same time to model the interaction between wind and buoyancy. This is important when adverse wind effects may overcome buoyancy forces, such as for chimney stacks, it may lead to significant departures from design conditions [Chiu and Etheridge 2004].

In wind tunnel modelling it is difficult to achieve prototype  $Re$  and  $Ar$  at the same time. The achievement of  $Ar$  requires low wind speeds, which is in conflict with the requirement for achieving high  $Re$ . This can be overcome by using higher temperature differences  $dT$ . For example, the ratio of  $dT/T$  should be kept as small as possible with the selections of  $dT$  and the wind speed  $U$  to give the full-scale range of  $Ar$  [Etheridge 2002b].

### 3.8 Summary

In this chapter different methods of studying building ventilation and the measurement techniques have been introduced. The information includes the simple pseudo-steady model with Boussinesq approximation (Section 3.5.2.2) and the tracer gas decay method (detailed in Chapter 7) employed in the current field investigations.

The fundamental aspects of CFD techniques have been discussed, e.g. governing equations, numerical grids, turbulence models, wall functions, discretisation schemes, and the quality and trust in CFD results. Meanwhile, the similarity parameters required in wind tunnel modelling have been outlined.

Current theoretical design procedures do not take into account the effects of unsteady pressures and local velocity field. CFD techniques predict the mean flow field

combined with turbulence models to consider the turbulence effects. The performance of CFD application is discussed in the following Chapters 4, 5 & 6.

# **Chapter 4    Preliminary CFD Study of Ventilation in a Building Model**

#### 4.1 Introduction

This chapter is a preliminary study comparing the results of CFD simulations and the experimental results of wind induced ventilation flows for a building model. The building model is a 1/30 scaled model with two identical circular openings, as illustrated in Figure 4-1.

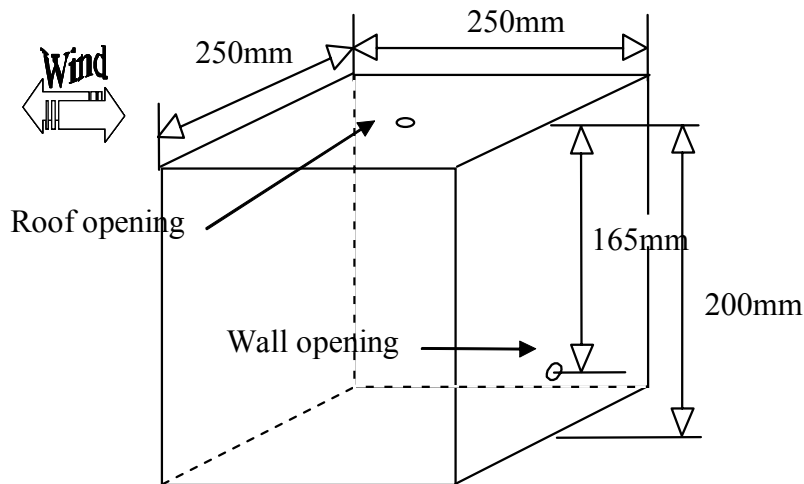


**Figure 4-1 The 1/30 scale building model with two identical circular openings (diameter = 10.9mm)**

This model was used by Carey and Etheridge [1999] for direct determination of ventilation rates in a wind tunnel. Nevertheless, there is an indirect technique widely used in the design codes where pressure coefficients are measured in a wind tunnel, then used in a mathematical model to determine the ventilation rates. Carey and Etheridge contrasted the two techniques and concluded that:

“... It (the direct technique) offers more accuracy in the determination of wind effects than ... the indirect use of wind tunnels ...”.

In accordance with these experiments, the experimental conditions of wind-alone tests were chosen to perform the subsequent CFD simulations.

## 4.2 CFD predictions

To prefigure the wind tunnel results on the building model, steady-state CFD simulations have been performed using an unstructured grid CFD code, CFX5 [AEATechnology 2001a]. The CFX5 computation adopts a finite-volume approach to solve the conservation form of the governing flow equations on unstructured meshes (see Section 3.3.8 in Chapter 3).

In the CFD simulation, the same 1/30 scale building model with the dimensions of 250 mm × 250 mm × 200 mm was used as in the wind tunnel (see Figure 4-1). With the guidance of previous studies of a cube structure in the atmospheric boundary layer [Straw 2000], the dimensions of the computational domain were set as  $5L$  ( $L$ =model building width) upstream and  $10L$  downstream of the model;  $5L$  either side of the model and  $5L$  above the model as illustrated in Figure 4-2.

The unstructured mesh uses a mixture of tetrahedral and prismatic cells. This enables the code to be run at high resolution along the boundary layers and in the vicinity of the building and lower resolution elsewhere (Figure 4-3). The computational domain was divided into 600,000 cells. The resolution on the model surfaces was taken as 1/16 of the model building height, that is 12.5 mm, and the cell size was 2 mm approximately 1/5 of the opening diameter with an expansion factor of 1.2 around the openings.

The popular standard  $k$ - $\varepsilon$  model [Launder and Spalding 1974] was applied with the 2<sup>nd</sup> order upwind discretisation scheme in combination with the standard wall-function (Section 3.3.8). The log-law velocity profile was imposed at the inlet boundary, no-slip rough wall surface on the ground (roughness height  $z_0=0.33$  mm),

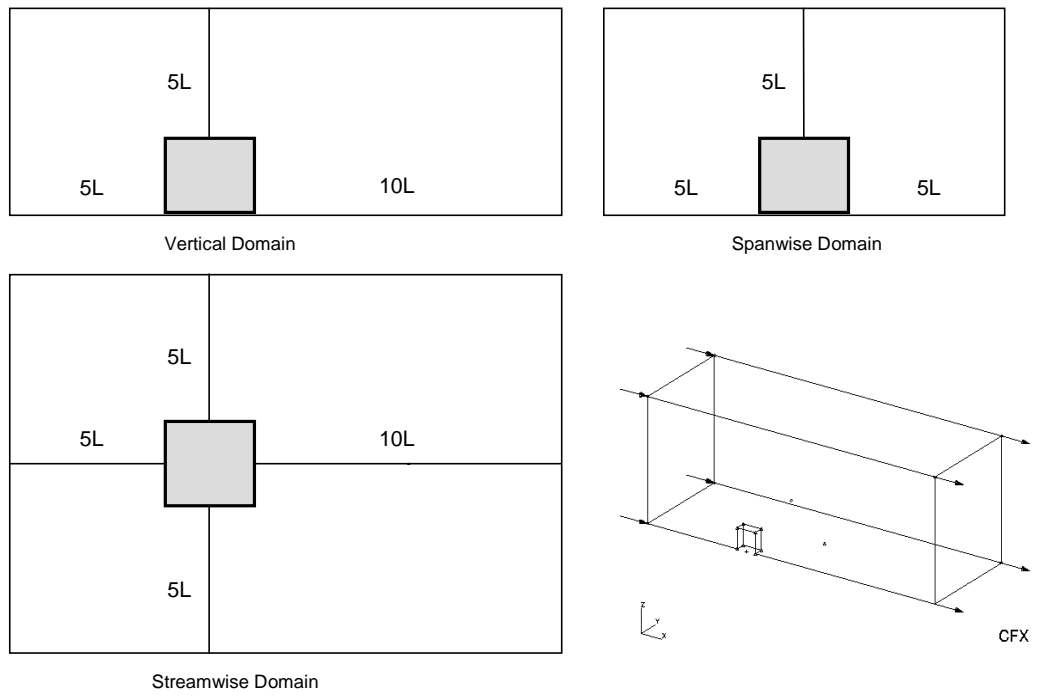


**Figure 4-2 CFD computational domain for the 1/30 scale building model**

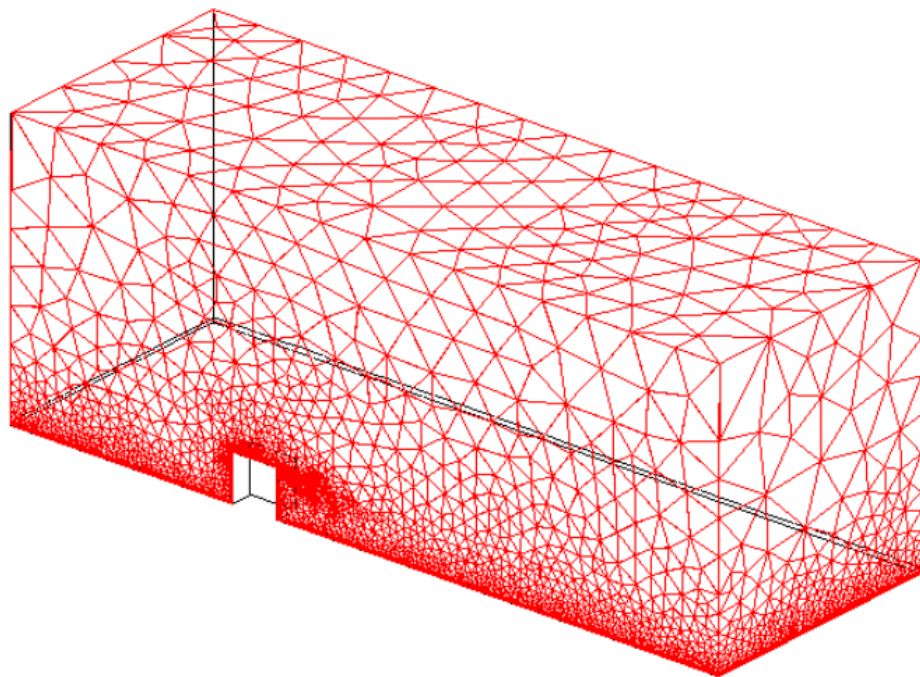


**Figure 4-3 The unstructured surface mesh around the 1/30 model**

and zero static pressure boundary condition at the outlet. A symmetry boundary condition was applied at the geometric symmetry x-z plane. This implies only half of the flow field variables were calculated in this preliminary study.

Under wind effect alone, the wind tunnel tests [Carey and Etheridge 1999] considered a  $0^\circ$  case, for which the wind direction blew perpendicularly to the building wall containing a lower level opening, i.e. windward wall. Another wind direction, i.e. the  $180^\circ$  case, which is opposite to the previous case, was also examined. In the wind tunnel the measured wind speeds were 1.1 ~ 3.9 m/s for the  $0^\circ$  cases and 0.8 ~ 2.9 m/s for the  $180^\circ$  cases, which were classified as low to medium wind speeds.

Three cases were selected to cover the low, medium and high wind speed range under each wind direction to test the sensitivity of the CFD results to the building Reynolds number. Moreover, slightly different wind speeds for  $0^\circ$  and  $180^\circ$  cases have been chosen in order to test the sensitivity of the CFD simulation regarding the opening Reynolds number. For the  $0^\circ$  cases, the reference wind speeds ( $U_{ref} = 0.2, 4$  and  $10$  m/s) at the building height (200 mm) were investigated. For the  $180^\circ$  cases, the lower opening was located on the leeward wall; the reference wind speeds of 0.3, 5 and 10 m/s were studied respectively.

### **4.3 Comparison of CFD and wind tunnel test results**

The flow patterns through the 1/30 model building at wind directions of  $0^\circ$  and  $180^\circ$  were investigated at various wind speeds in the CFD simulations.

Figures 4-4 & 4-5 show the surface pressure distributions on the model at reference wind speed 4 m/s for the wind directions of  $0^\circ$  and 5 m/s for the  $180^\circ$  cases.

Comparing the pressure contours on the windward wall, the roof and the leeward wall, it can be seen that in both cases the openings only have minor effects on the pressure distribution locally very close to the openings.

The indoor and outdoor velocity vectors pattern predicted by CFD for both cases are shown in Figures 4-6 & 4-7 (section view at model vertical centre plane). The outflow speed from the roof opening in  $0^\circ$  case is obviously higher than the  $180^\circ$  case, although the latter case has higher reference wind speed. In the  $0^\circ$  case the lower opening at windward wall introduces local downward current reaching the  $2/5$  width of the building. It encourages indoor recirculation vertically. In contrast, the lower opening on the leeward wall in the  $180^\circ$  case has much less effect on the indoor flow distribution pattern.

The CFD simulations gave the pressure distribution, velocity flow fields and turbulence parameters both around and within the  $1/30$  model building. Utilising the CFD results and applying the simple envelope flow model (Section 3.5.2.1), the methods summarised in Table 4-1, were used to calculate the discharge coefficient of each opening, the pressure coefficient differences and the mean ventilation rates through the building. The comparison of the wind tunnel experimental measurements [Carey and Etheridge 1999] on the  $1/30$  building model (named as *tunnelmodel*) with the CFD results (named as *CFDmodel*) are shown in Figures 4-8 to Figure 4-12.

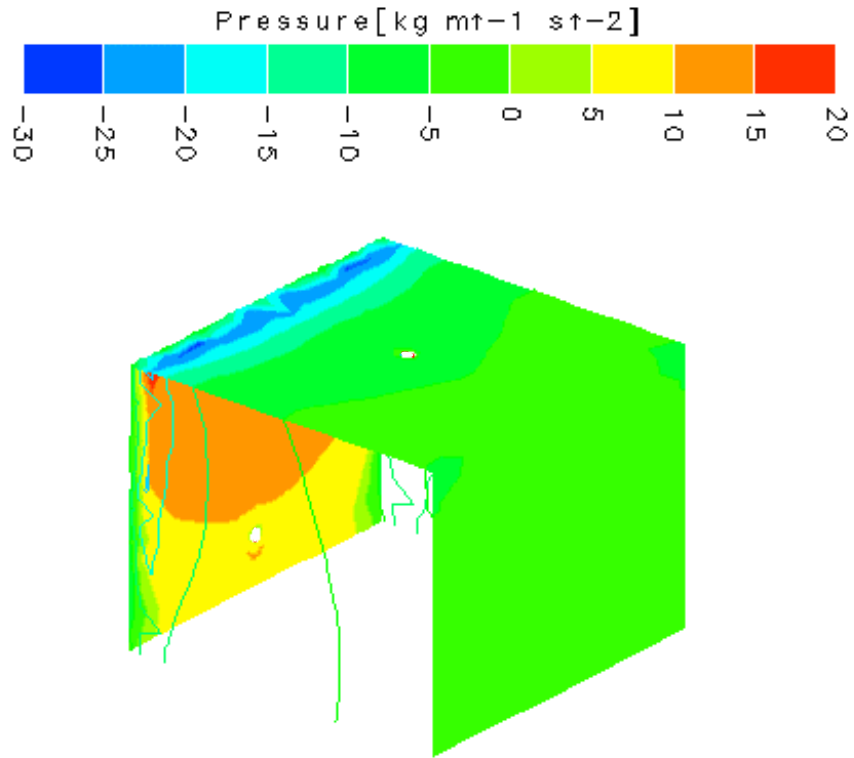


**Figure 4-4** CFD prediction of the surface pressure distribution on 1/30 model for 0° case ( $U_{ref}=4\text{m/s}$ )

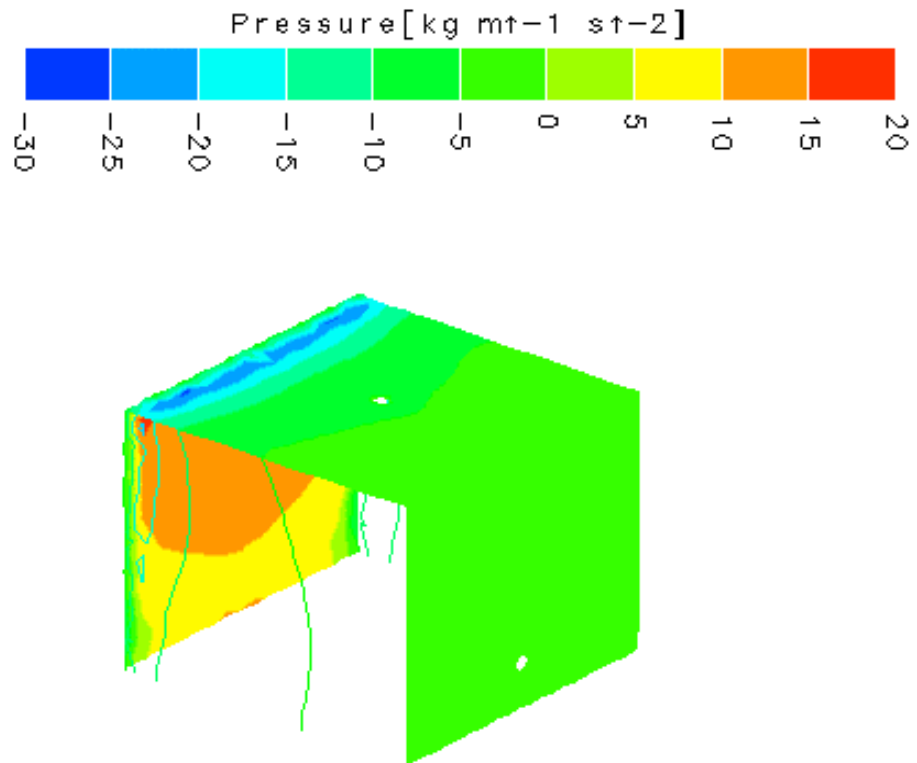


**Figure 4-5** CFD prediction of the surface pressure distribution on 1/30 model for 180° case ( $U_{ref}=5\text{m/s}$ )

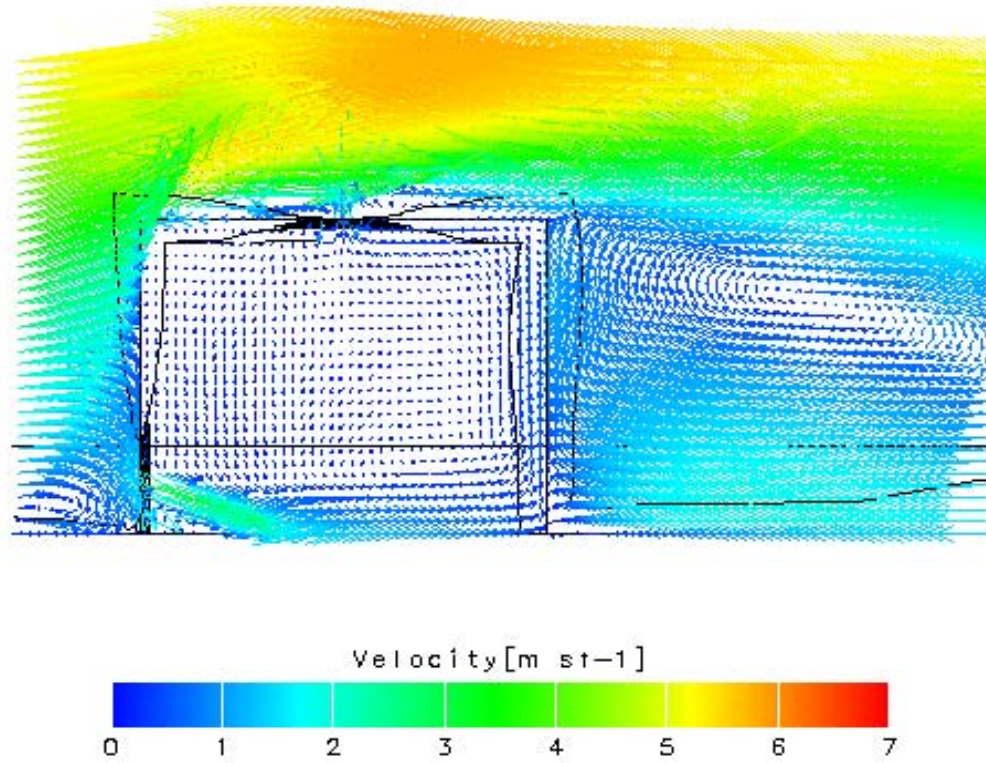


**Figure 4-6** CFD prediction of the velocity vector plot around 1/30 model for 0° case – central section view ( $U_{ref}=4\text{m/s}$ )

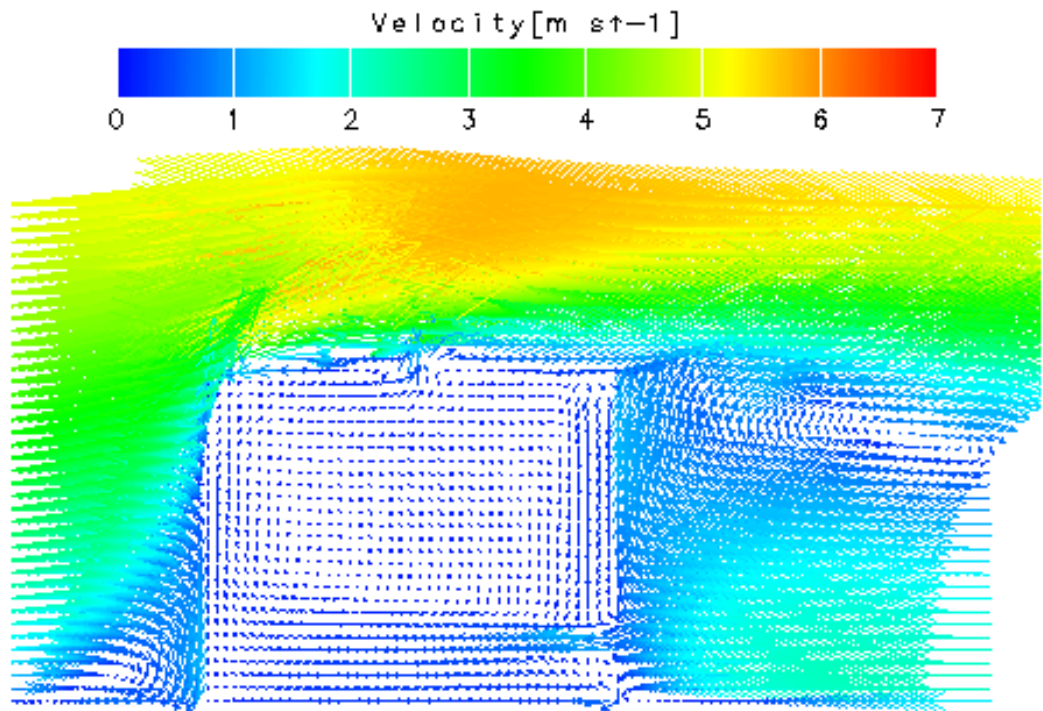


**Figure 4-7** CFD prediction of the velocity vector plot around 1/30 model for 180° case – central section view ( $U_{ref}=5\text{m/s}$ )

**Table 4-1 Assessment of ventilation rates from CFD simulation**

Method	Equation	Variable	Illustration
Integrating the streamwise velocity component $u$ over lower opening	$C_{z1} = \frac{\overline{uA}}{U_{ref} A \sqrt{\frac{dP}{\rho}}}$	Lower opening discharge coefficient	Figure 4-8
Integrating the vertical velocity component $v$ over roof opening	$C_{z2} = \frac{\overline{vA}}{U_{ref} A \sqrt{\frac{dP}{\rho}}}$	Roof opening discharge coefficient	Figure 4-9
Abstracting the pressure coefficient difference between the two ventilation openings	$\sqrt{\Delta C_p} = \sqrt{\frac{dP}{0.5 \rho U_{ref}^2}}$	Pressure coefficient difference	Figure 4-10
Utilising the pseudo-steady model with Boussinesq approximation	$\frac{Q}{AU_{ref}} = C_d \sqrt{\frac{dP}{\rho}}$	Non-dimensional mean ventilation rate	Figure 4-11 & 4-12

From Figures 4-8 & 4-9 it can be seen that the CFD predicted opening discharge coefficients were close to the envelope flow theoretical value of 0.6. Higher values were found at the lower opening for  $180^\circ$  cases than the  $0^\circ$  ones in Figure 4-8. At the roof opening  $0^\circ$  wind introduced more outflow than  $180^\circ$  wind. In the wind tunnel measurements, the opening discharge coefficients required to give good agreement between the envelope flow model and measurement varied between 0.75 and 0.85.

Experiments conducted on a Fan Test Rig [Shea and Robertson 2004] have shown that a sharp-edged circular opening (zero depth as in CFD simulation), has a  $C_d$  value of 0.6. As the aspect ratio of the opening diameter to depth increases above zero, the  $C_d$  value rises sharply. This value varied from 0.6 to 0.9, with a maximum at an aspect ratio of 3 and staying high up to an aspect ratio of 7. Due to friction, the  $C_d$  value began to fall again after exceeding an aspect ratio of 7.

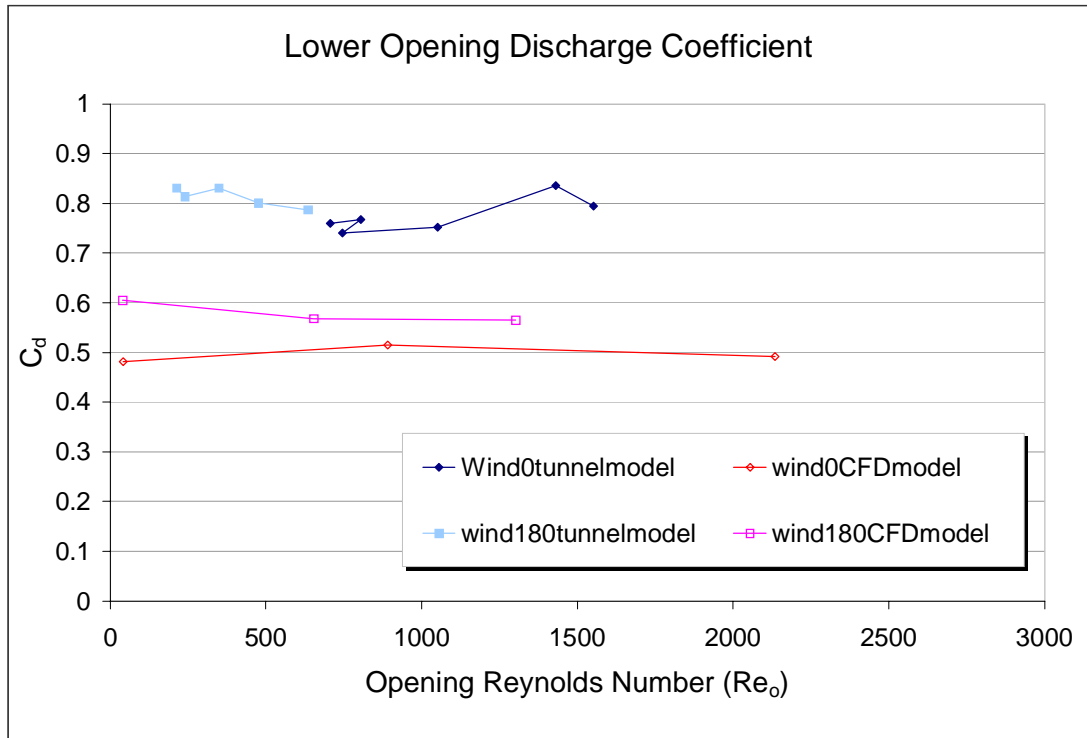


Figure 4-8 CFD and wind tunnel tests results comparison – lower opening discharge coefficient vs opening Reynolds number

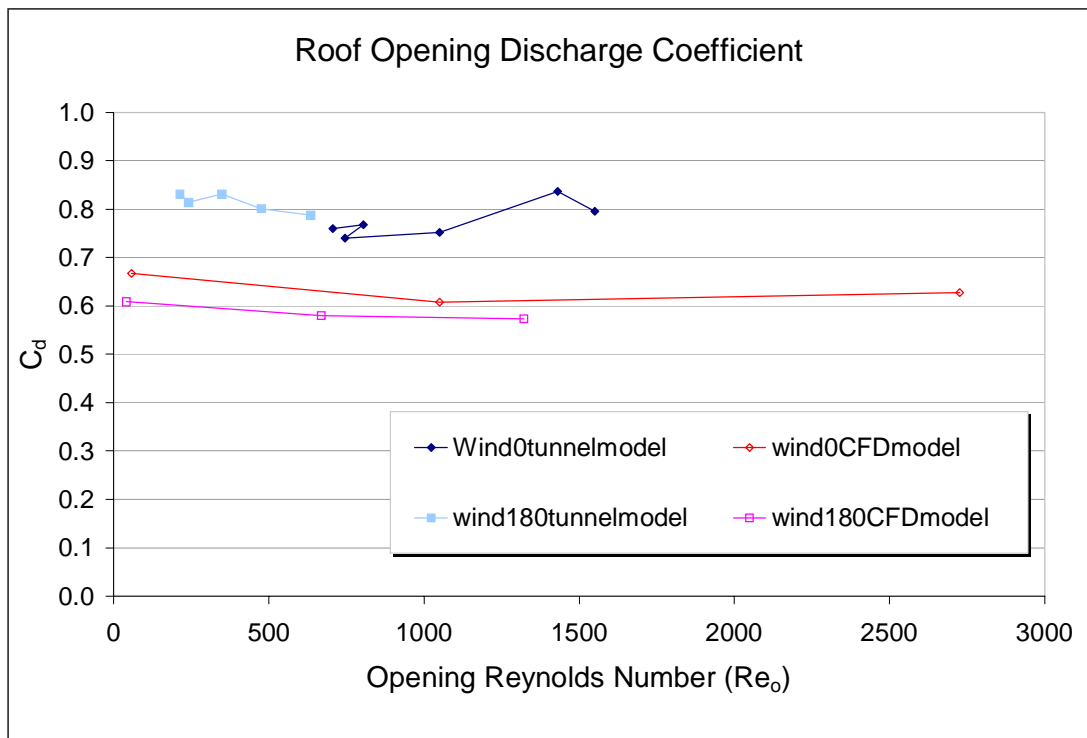
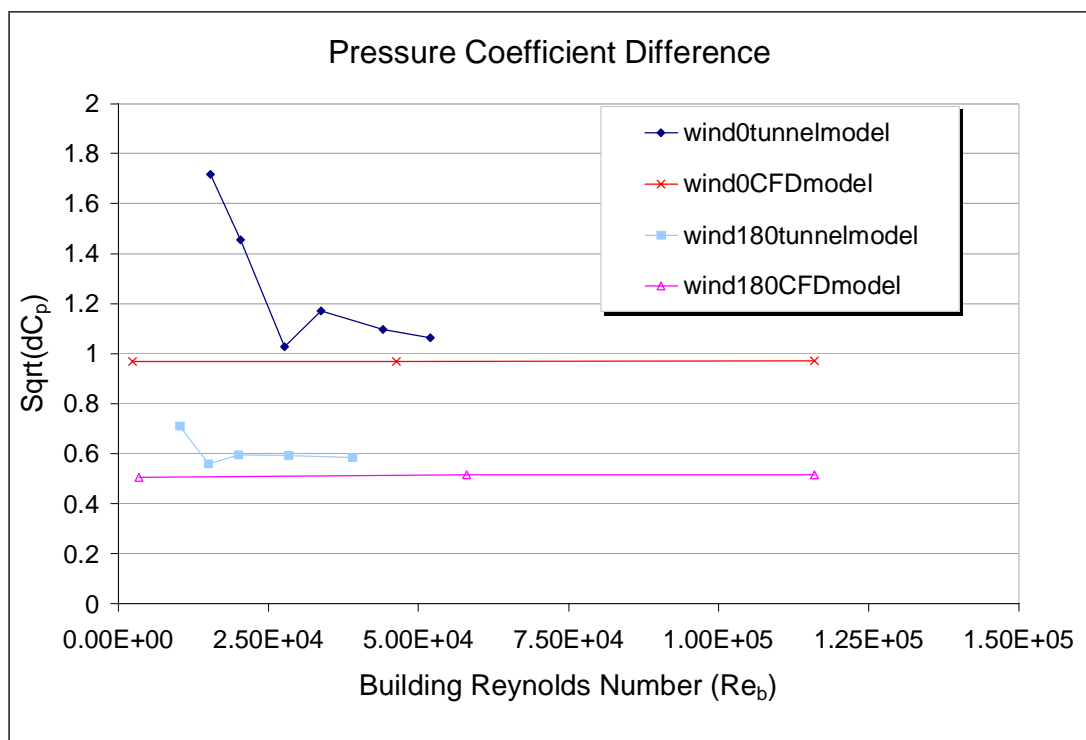


Figure 4-9 CFD and wind tunnel tests results comparison – roof opening discharge coefficient vs opening Reynolds number

Clearly seen in Figure 4-10, the CFD results of pressure coefficient difference were less sensitive to the building Reynolds number than the experimental measurements. The wind tunnel data for the  $0^\circ$  cases show higher fluctuations than the  $180^\circ$  cases, which can be caused by the vortex formation in front of the building interacting with the flow through the lower opening on windward face. CFD results present the time averaged pressure field, which is close to the lowest measured data for both wind directions.



**Figure 4-10 CFD and wind tunnel tests results comparison - square root of pressure coefficient difference vs building Reynolds number**

Consequently it is shown in Figure 4-11 that the CFD simulation underpredicted the total effective ventilation rates, because of the lack of consideration of the unsteadiness of the flow around the openings. However, allowing for the non-circular opening depth effect [Shea and Robertson 2004], if one was to choose a

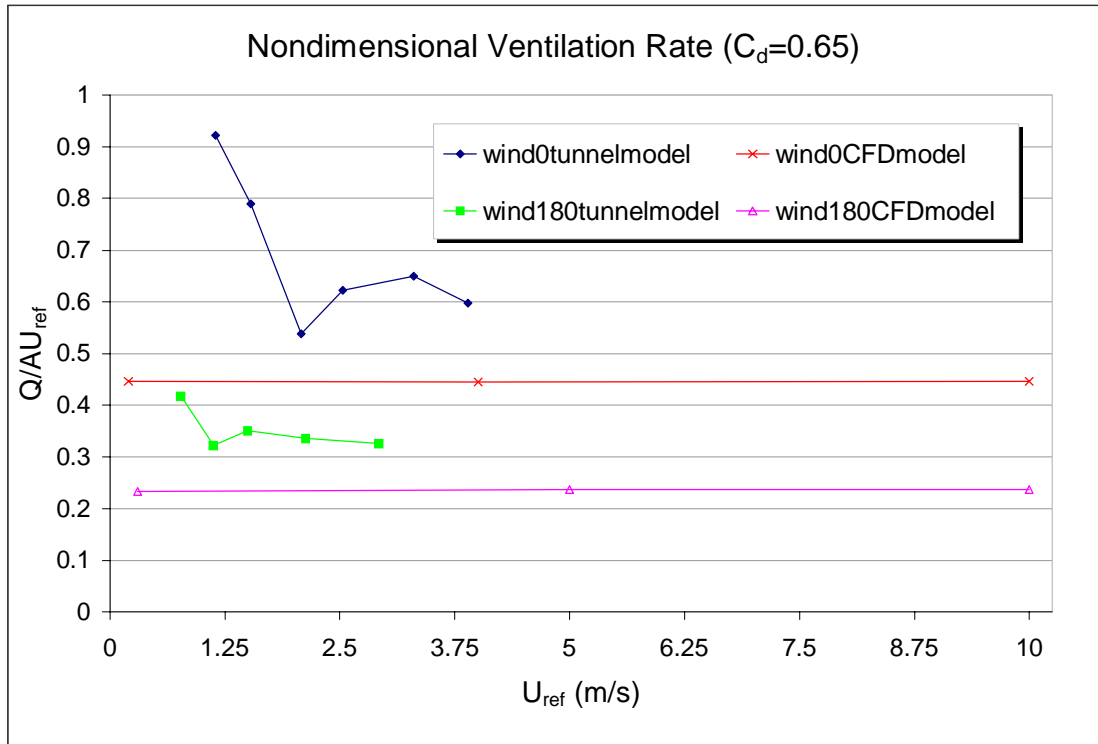


**Figure 4-11 Ventilation rates comparison between CFD and wind tunnel tests (discharge coefficient = 0.65)**

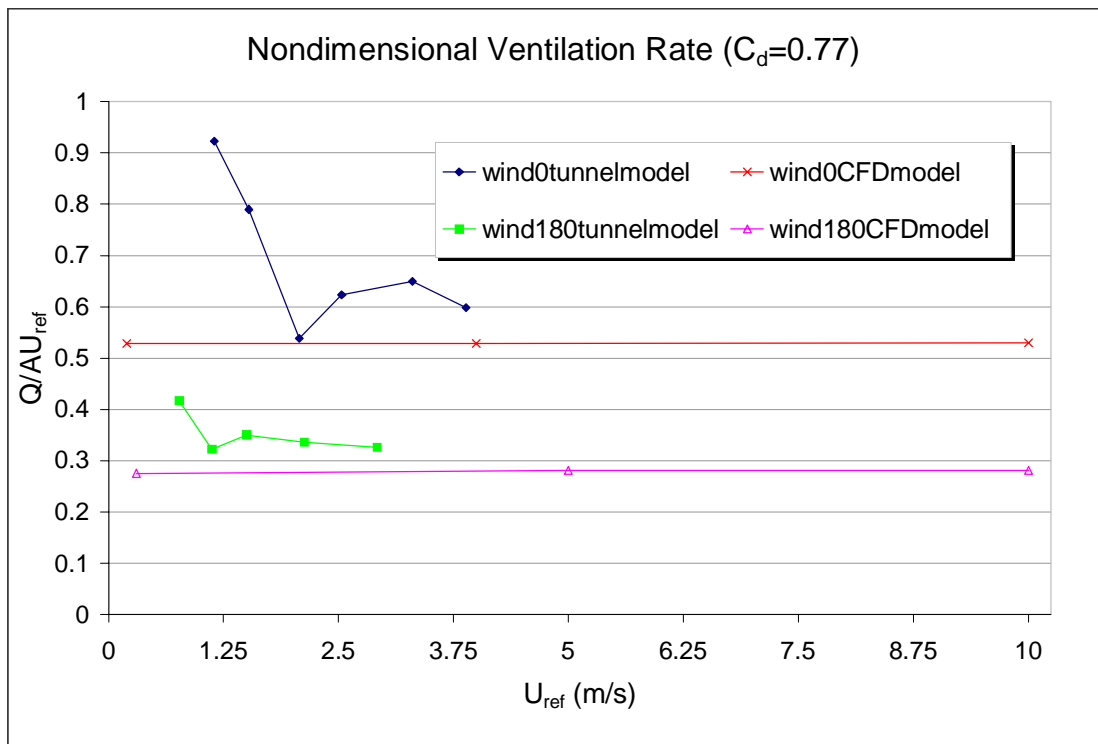


**Figure 4-12 Ventilation rates comparison between CFD and wind tunnel tests (discharge coefficient = 0.77)**

higher value for the discharge coefficient  $C_d$ , such as 0.77 (Figure 4-12), the calculated flow rate from CFD would be a closer prediction of the experimental measurements. This is consistent with the findings of Carey and Etheridge [1999].

Under the condition of low wind speed in particular, the fluctuating ventilation component driven by the fluctuating pressures and unsteady flows around the openings is dominant over the mean components driven by the mean pressure field. At low wind speed, the instantaneous velocity at an opening changes direction frequently due to strong interaction between outdoor and indoor flows. In this case, the standard  $k$ - $\varepsilon$  model showed its weakness at representing the total ventilation flow through the openings, because it is unable to represent this flow reversal.

#### 4.4 Discussion

In this preliminary CFD investigation of the ventilated cube with lower level and roof openings, the ventilation flow rates were evaluated by integrating the flow speed through the openings and by applying the simple envelope flow model (Section 3.5.2.1) combined with the CFD results of the mean pressure difference.

From the preliminary CFD modelling experience, the following actions are necessary for the next step. To ensure the quality of the CFD results, additional simulations are needed in order to test the sensitivity of the solutions to various modelling aspects (i.e. boundary conditions, mesh independence, discretisation scheme, convergence levels, etc.).

Without taking account of the unsteadiness of the wind around the openings, the steady-state time-averaged CFD results under-predict the total pressure differences between openings. The calculated mean ventilation rate according to the mean

pressure difference does not include the instantaneous turbulent air exchange between the indoor and the outdoor airflows. More sophisticated envelope flow models taking account of the turbulent term in the flow equation [Etheridge and Standberg 1996; Etheridge 2000b] or more advanced turbulence models should be implemented to tackle the complex turbulent features of the wind.

However, it should be noted from the literature that various turbulence models have been unable to accurately calculate the pressure distribution over the roof of a bluff body for wind engineering applications [Murakami et al. 1992; Richards et al. 2002; Wright and Easom 2003]. These studies found that most RANS models had difficulties in generating the separation region on the roof, which was observed in the full-scale and wind tunnel experiments. Therefore, in order to utilize available built-in turbulence models in the CFX5 package and bypass the weakness of inaccurate CFD predictions of the flow reattachment on the roof, the high level opening was relocated onto the leeward wall in the full-scale experiment (Chapter 7) and CFD simulations (Chapter 6).

# **Chapter 5 Verification & Validation of the CFD Model**

## **5.1 Introduction**

This chapter examines the reproduction of the atmospheric boundary layer (ABL) and the prediction of the flow around a low-rise building by an unstructured CFD code, CFX5 [AEA Technology 2001a]. CFX5 results are then compared to the published Computational Wind Engineering 2000 Conference (CWE2000) competition data [Hoxey et al. 2002]. In the CWE2000 competition, a detailed set of full-scale measurements for a cube structure with well defined boundary conditions was provided in order to validate three RANS solutions for the flow around a cube. The CFX5 simulations and the CFD results from the competition [Richards et al. 2002] using different approaches within commercial codes, are compared in order to clarify the major factors which affect the prediction accuracy and to verify the CFX5 models for further natural ventilation study.

## **5.2 Atmospheric boundary layer (ABL) reproduction in CFD**

To study the time-averaged natural air flow characteristics in the built environment, correct reproduction of the ABL profile in CFD is very important. It is also required to achieve consistent numerically-generated mean wind flow fields within the computational domain.

### **5.2.1 ABL boundary condition specification**

Computational problems associated with wind engineering simulations within the ABL had been investigated by Richards and Hoxey [1993], who stated that the specified boundary conditions should produce a horizontally homogeneous boundary layer flow in the absence of any obstructions. Furthermore, detailed measurements for the basic boundary layer at Silsoe wind engineering site, including pressure,

velocity components and turbulence profiles were reported in the CWE2000 Competition [Hoxey et al. 2002].

Based on the results of Richards and Hoxey [1993] and using the standard  $k$ - $\varepsilon$  turbulence model, the profile of inflow velocity, associated turbulent kinetic energy  $k$  and its dissipation rate  $\varepsilon$ , are expressed as the following equations:

$$U(z) = \frac{u_*}{\kappa} \ln(z/z_0) \quad (5.1)$$

$$k = \frac{u_*^2}{\sqrt{C_\mu}} \quad (5.2)$$

$$\varepsilon = \frac{u_*^3}{\kappa z} \quad (5.3)$$

where  $z_0$  is the ground roughness height and the von Karman constant is  $\kappa = 0.41$ .

The friction velocity  $u_*$  is determined by the reference velocity  $U_{ref}$  at a reference height  $z_{ref}$  as

$$u_* = \frac{\kappa U_{ref}}{\ln(z_{ref}/z_0)} \quad (5.4)$$

Boundary conditions for the ABL simulation in CFX5 are summarised in Table 5-1. Simulations of the ABL were carried out for steady and isothermal conditions. The wind direction was perpendicular to the calculation domain, and the reference wind velocity was 10 m/s at a reference height of 6 m.

**Table 5-1 Boundary conditions in CFX5.5.1**

Boundary	Settings	Comments
Inlet	Empirical log-law profile with specified $k$ & $\varepsilon$	See Eqns. 5.1 ~ 5.3
Outlet	Relative static pressure is zero; normal gradient of other variables is zero, i.e. $\partial/\partial x = 0$	
Ground	No-slip rough wall (roughness length $z_0 = 0.01\text{m}$ )	*
Top	Symmetry (vertical velocity component $w=0$ & $\partial/\partial x, \partial/\partial y = 0$ )	
Sides	Symmetry (spanwise velocity component $v=0$ & $\partial/\partial x, \partial/\partial z = 0$ )	

\* The equivalent sand grain roughness height, the accepted value for representing a rough wall in CFX5, was treated as 7.5 times the measured roughness length  $z_0$  [Stangroom and Wright 2003].

### 5.2.2 Grid sensitivity tests results

The simulation results are based on the standard  $k$ - $\varepsilon$  turbulence model using the 2<sup>nd</sup> order discretisation scheme in CFX5 (Section 3.3.8). The convergence criterion is that the root-mean-square (RMS) of the normalised residual for all variables is less than  $1 \times 10^{-6}$ .

Table 5-2 details the global and local refinement grid settings, and the computational domain size in streamwise ( $x$ ), transverse ( $y$ ) and vertical ( $z$ ) directions respectively. The grid sizes on the ground were the smallest; then expanded out away from the ground surface towards the rest of the domain with an overall expansion factor equal to 1.2 in all directions. Along the vertical direction the ABL profile changes dramatically near the ground because of the friction effect from the ground. CFX 5 has the capability of ‘inflating’ surface triangular elements into structured prismatic elements, which is used to improve boundary layer representation [AEA Technology

2001a]. Therefore, 10 layers of grid cells with the specified vertical expansion factor of cell height were defined above the ground.

Considering both the accuracy and the efficiency of CFD simulations, various sizes of computational domain were selected (see Table 5-2) in order to reproduce the relevant two-dimensional ABL profile.

**Table 5-2 Mesh types for ABL simulation**

Mesh Name		Grid_coarse	Grid_medium1	Grid_medium2	Grid_fine
Domain size x(m)×y(m)×z(m)		96×10×60	96×20×36	192×20×36	96×20×36
Mesh length scale on the ground (m)		0.8	0.6	0.6	0.25
Global cell expansion factor		1.2	1.2	1.2	1.2
Horizontal	Resolution on the ground	120×13	137×15	274×15	384×80
	Resolution on the top domain	16×2	16×4	32×4	20×4
Vertical	1 <sup>st</sup> cell height above the ground (m)	0.02	0.015	0.015	0.015
	Vertical expansion factor above the ground	1.1	1.05	1.05	1.2
Total number of cells		63,900	86,300	177,500	964,200

The mean free stream velocity and turbulent kinetic energy profiles at the inlet and the outlet from the CFX5 simulation were compared in Figures 5-1, 5-2 & 5-3 (pp 99, 100 & 101). The velocity is non-dimensionalised with respect to the reference wind speed ( $U_{ref}$ ) expressed as  $u/U_{ref}$ , and the non-dimensional turbulent kinetic

energy is expressed by  $k/U_{ref}^2$ . The distance above the ground was measured by the reference building height  $z_{ref}=6$  m.

Table 5-3 summarises the percentage differences of the velocity and kinetic energy profile for the four grid settings defined in Table 5-2.

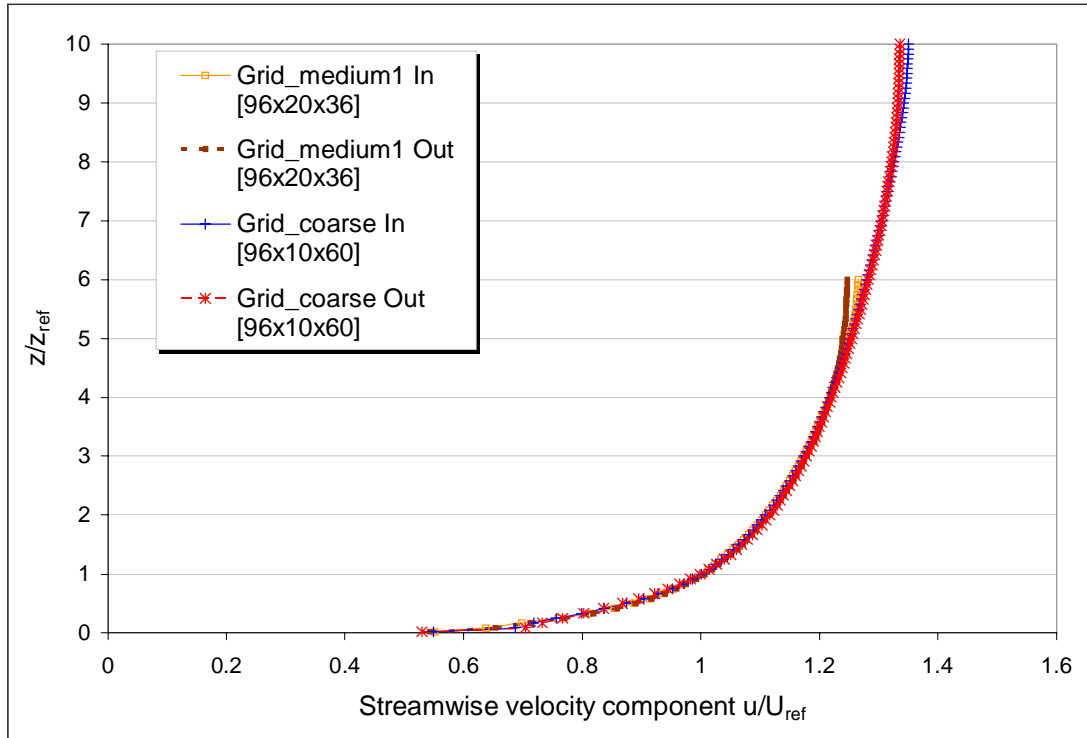
**Table 5-3 The ABL profile differences on four types of grids (%)**

Grid			Difference (%)	Inlet	Inlet vs. Outlet		Outlet	Illustration
					$u/U_{ref}$	$k/U_{ref}^2$		
Grid_medium1			Avg.	-	0.8	0.2	-	Figures 5-1~ 5-3
			Max.	-	1.9	0.4	-	
				Inlet		Outlet		
				$u/U_{ref}$	$k/U_{ref}^2$	$u/U_{ref}$	$k/U_{ref}^2$	
Grid_coarse	vs.	Grid_medium1	Avg.	0.3	0	0.9	0	Figure 5-1
			Max.	4.9	0.2	5.2	0.2	
Grid_medium2	vs.	Grid_medium1	Avg.	0.1	0.2	0.5	0.2	Figure 5-2
			Max.	0.3	0.4	2.6	0.3	
Grid_fine	vs.	Grid_medium1	Avg.	0.2	0	0.4	0	Figure 5-3
			Max.	3.9	0.3	4.1	0.3	

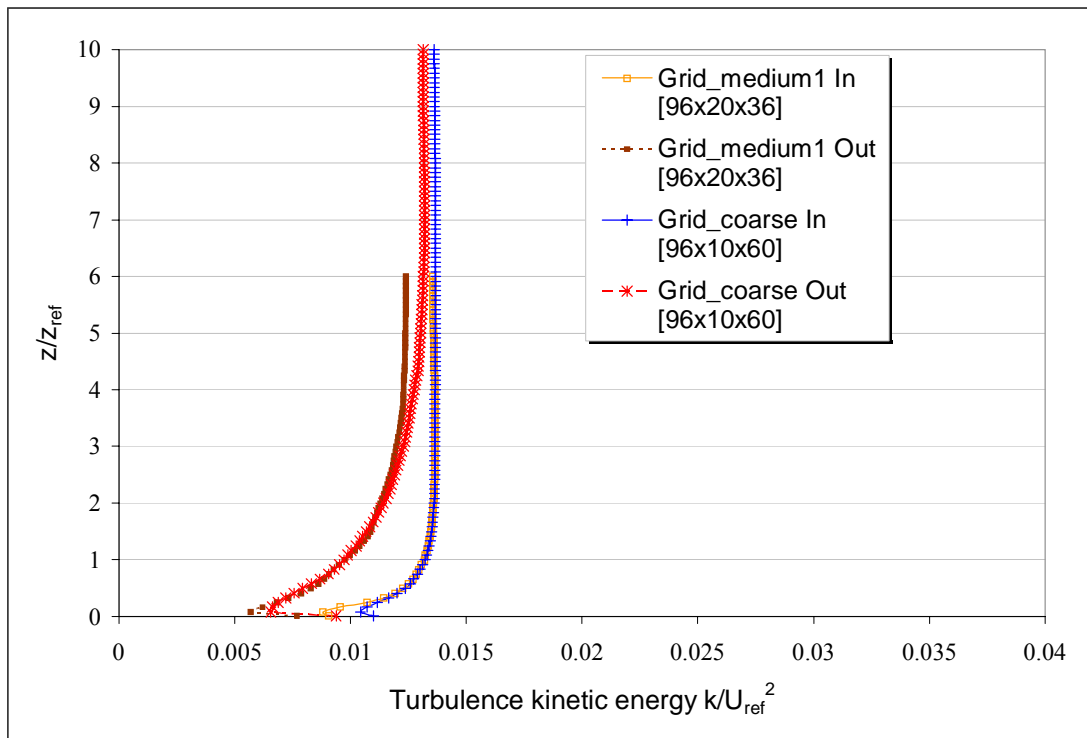
On the medium grid (Grid\_medium1) the average velocity difference between the inlet and outlet is 0.8%, including the maximum value of 1.9%. Meanwhile the differences of the turbulent kinetic energy between the inlet and outlet were an average of 0.2% and 0.4% at maximum.

Inlet and outlet profiles from the Grid\_medium1's were considered as references on which the other grids, namely Grid\_coarse, Grid\_medium2 & Grid\_fine, were evaluated.

It can be seen from Figures 5-1a, 5-2a & 5-3a that the outlet velocity profiles are very similar to the inlet profile with only small differences showing at positions close to the ground or near the top of the domain. For instance, the predicted velocity

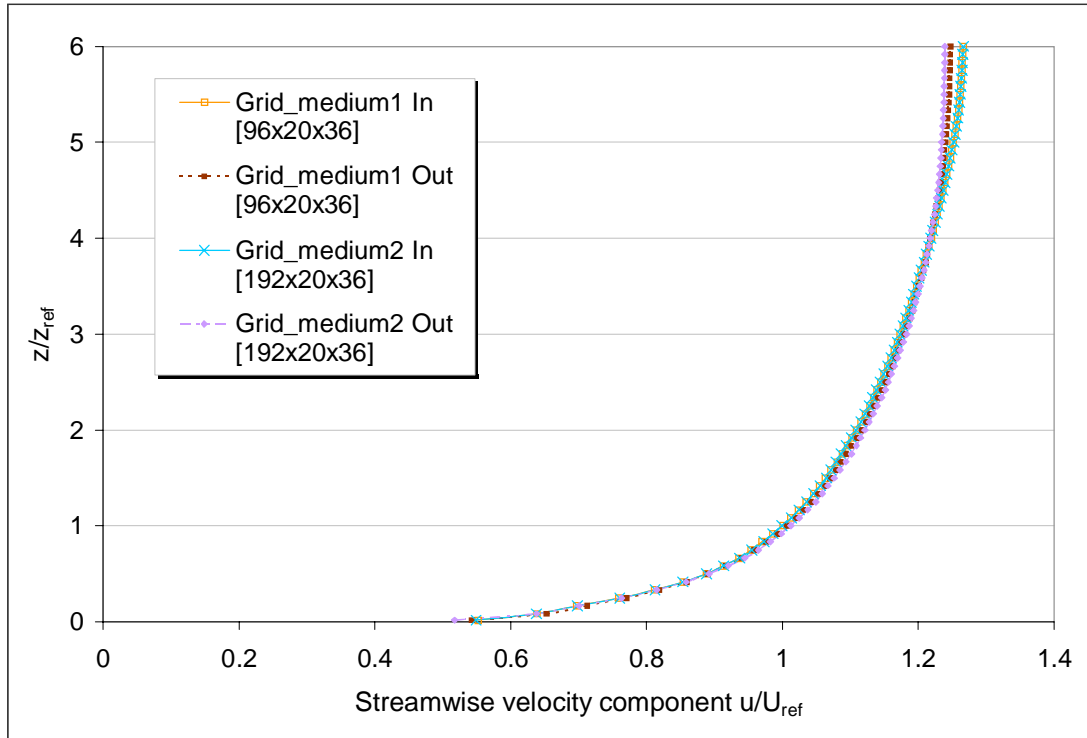


(a) Mean streamwise velocity

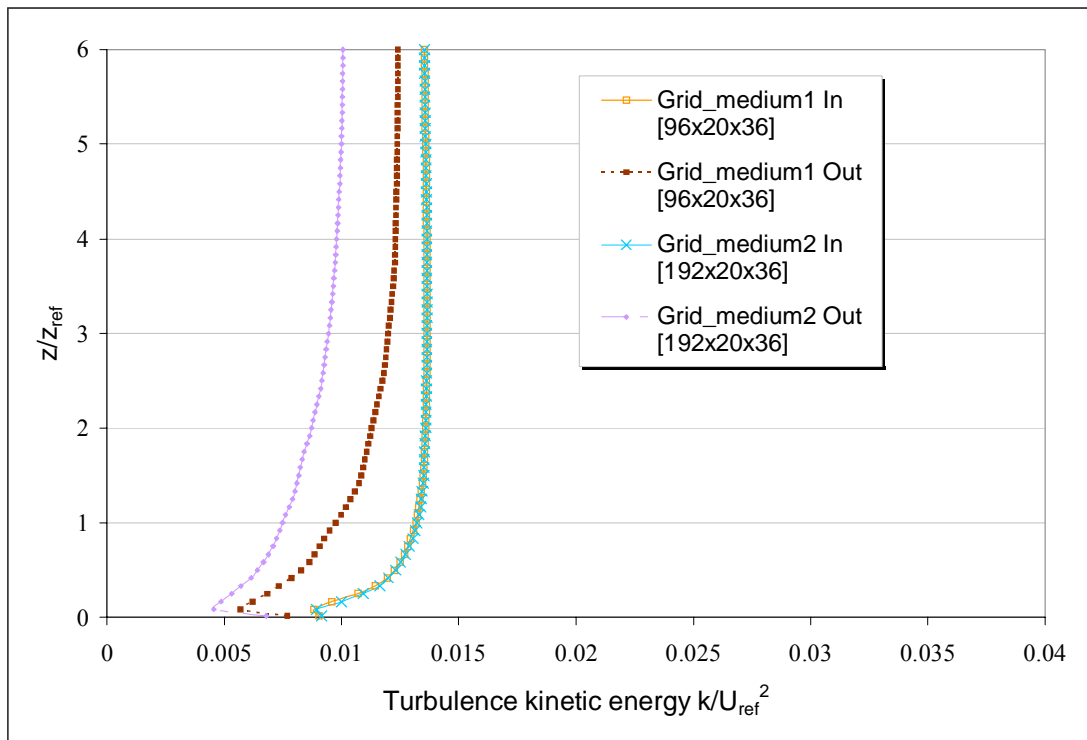


(b) Turbulent kinetic energy

Figure 5-1 Grid sensitivity tests – inlet & outlet profiles on coarse & medium grids

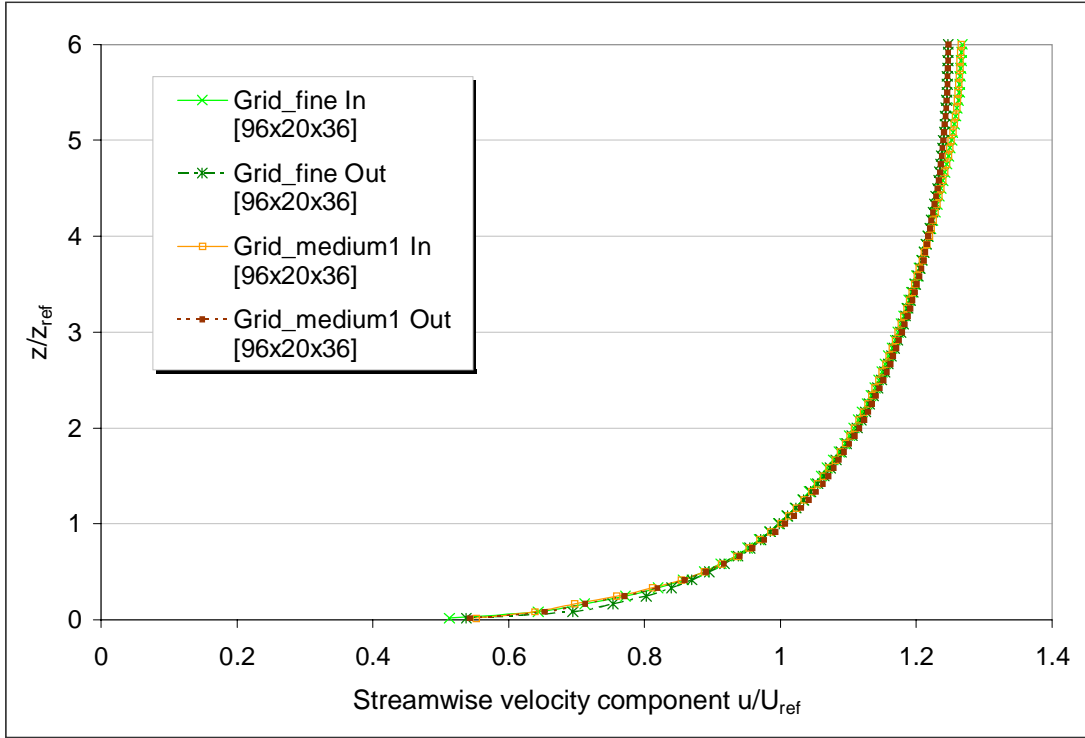


(a) Mean streamwise velocity

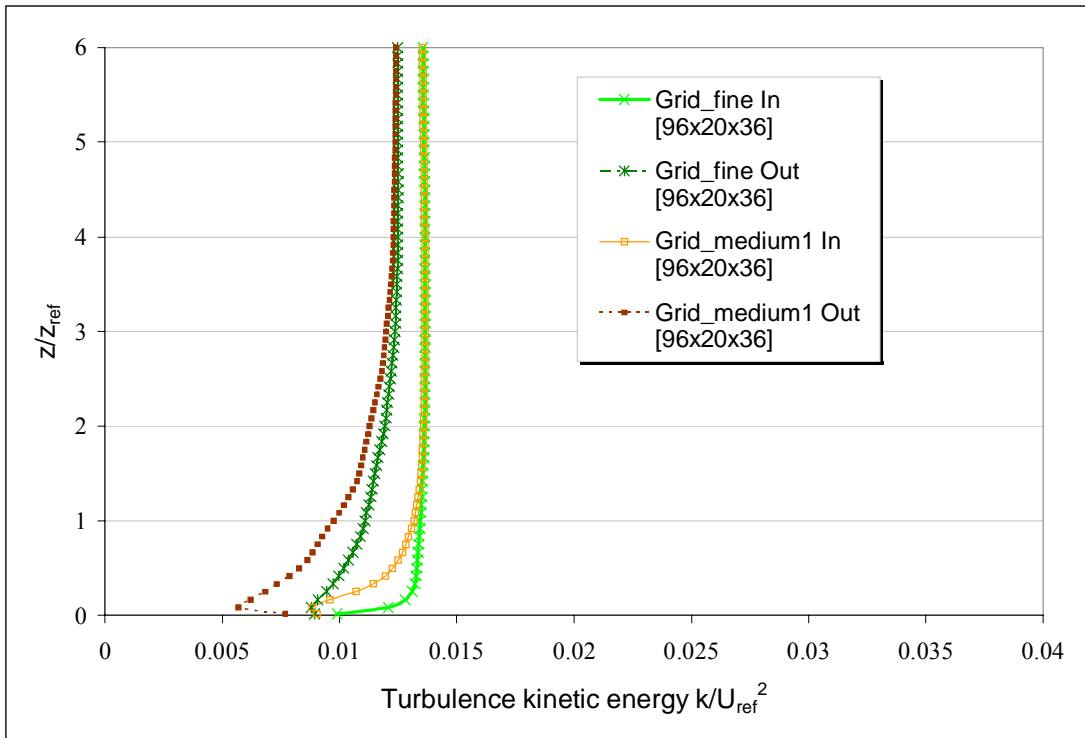


(b) Turbulent kinetic energy

Figure 5-2 Grid sensitivity tests – inlet & outlet profiles on two medium grids



(a) Mean streamwise velocity



(b) Turbulent kinetic energy

Figure 5-3 Grid sensitivity tests – inlet & outlet profiles on fine & medium grids

difference was in the order of 5% maximum due to increasing the domain height (Figure 5-1a), doubling the upstream fetch length (Figure 5-2a) and refining the resolution on the ground (Figure 5-3a).

The difference of the turbulent kinetic energy profile due to the change of above three parameters is more visible than that of the velocity profile as shown in Figure 5-1b, 5-2b & 5-3b. However, the overall difference of the turbulence kinetic energy was less than 0.4%.

Increasing the domain height (Figure 5-1b) gave the same level of turbulence near the ground, however at the height  $6H$  it showed slightly higher level of turbulence. Doubling the domain length (Figure 5-2b) caused the turbulent kinetic energy level to decrease both near the ground and at the domain top. It is shown in Figure 5-3b that on the fine grid (Grid\_fine) the turbulence level at the inlet and the outlet has less difference than on the other grid settings. With the exception of the  $k$  profile on the fine grid, all the kinetic energy values at the inlet had decreased rather sharply at 0.1m above the ground. This is possibly caused by the artefact of the ‘rough wall’ simulation used in CFX5, which is represented by the equivalent sand grain roughness height rather than the roughness length of the surface [Stangroom and Wright 2003].

It has been noted that, as illustrated in Figure 5-3, the ABL simulation results on the fine grid (Grid\_fine) shows the most consistent performance. On the other hand, within the same computational domain, the total grid cells of the fine grid had been set 10 times more than the medium one (Grid\_medium1). The maximum difference of the ABL profile generated on both grids was 4.1% for the velocity and 0.3% for

the kinetic energy. This is very much within the error range experienced in full-scale measurements, i.e. 10-15%.

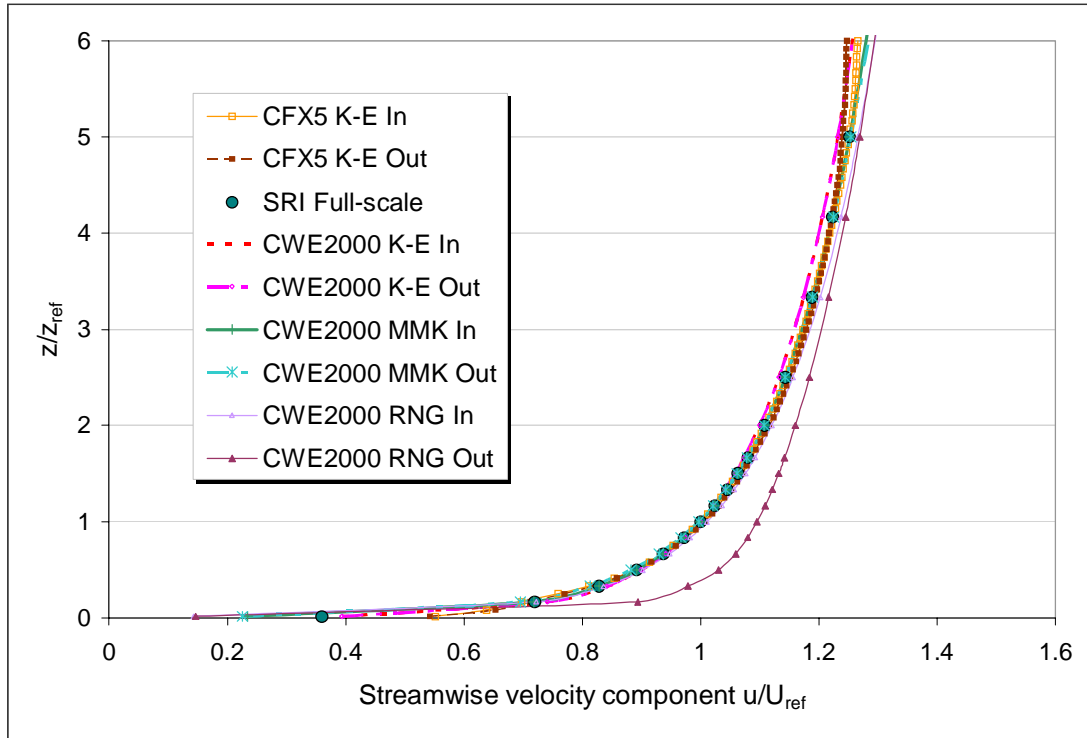
Moreover, for a building to be put into this ABL domain, more grid cells are needed to define the building surfaces for ventilation studies, and so using the fine grid is not a practical choice due to the computational resource limitation (up to 2 million cells). Therefore the medium grid (Grid\_medium1) was selected for the following ABL profile comparisons with other published data in the literature.

### 5.2.3 Comparison of CFX5 and CWE2000 competition results

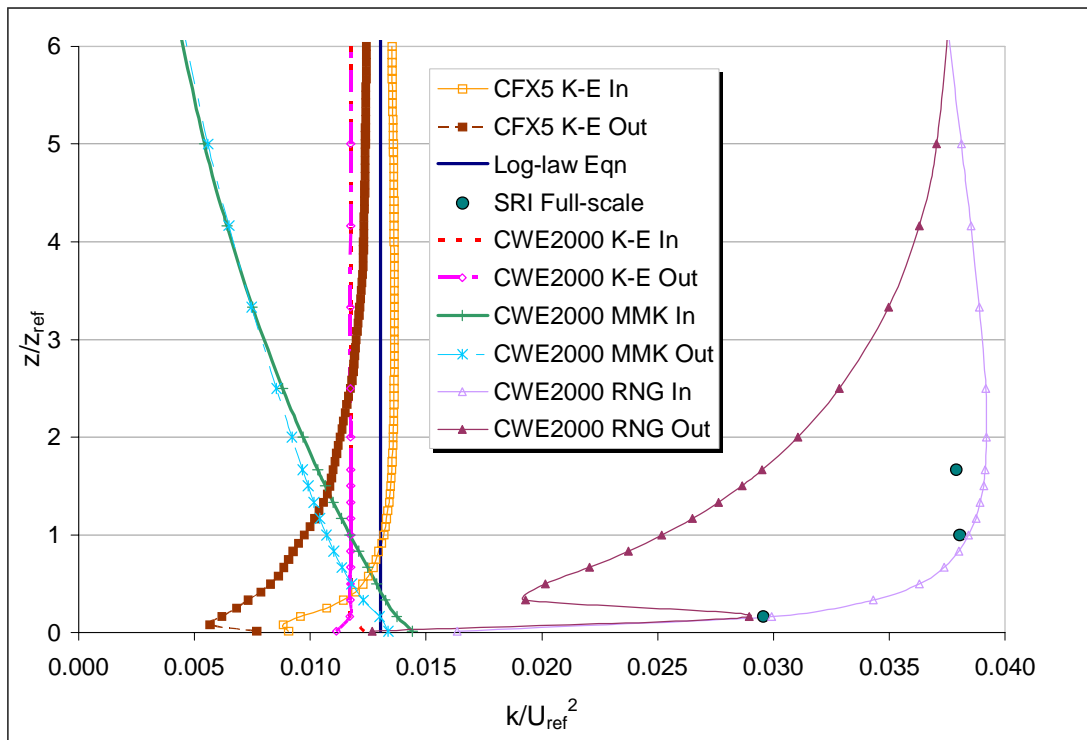
The ABL simulation results obtained in CFX5 are compared with the CWE2000 competition solutions [Richards et al. 2002] as well as the full-scale data collected for this competition. The modelling details of the CFX5 simulations and the three CWE2000 competition solutions are listed in Table 5-4. Following the notation in this paper, CFX5 simulation is named as ‘CFX5 K-E’, and the results from three CWE2000 computational models are quoted as ‘CWE2000 K-E’, ‘CWE2000 MMK’ and ‘CWE2000 RNG’. Meanwhile the full-scale data is plotted as ‘SRI Full-scale’ in Figure 5-4.

**Table 5-4 ABL Modelling details**

Model Name	CFX5 K-E	CWE2000 K-E	CWE2000 MMK	CWE2000 RNG
Code	CFX v5.5.1	PHOENICS v3.2	CFX v4.3	Fluent v5
Turbulence model	$k-\varepsilon$	$k-\varepsilon$	MMK $k-\varepsilon$	RNG $k-\varepsilon$
Domain size x(m)×y(m)×z(m)	96×20×36	96×96×48	150×60×60	240×210×100
Mesh type	Unstructured	Structured	Structured	Structured
Convective differencing scheme	Higher-order upwind differencing (2 <sup>nd</sup> order)	Hybrid differencing (1 <sup>st</sup> / 2 <sup>nd</sup> order)	CCCT (2 <sup>nd</sup> order)	Higher-order upwind differencing (2 <sup>nd</sup> order)



(a) Mean streamwise velocity



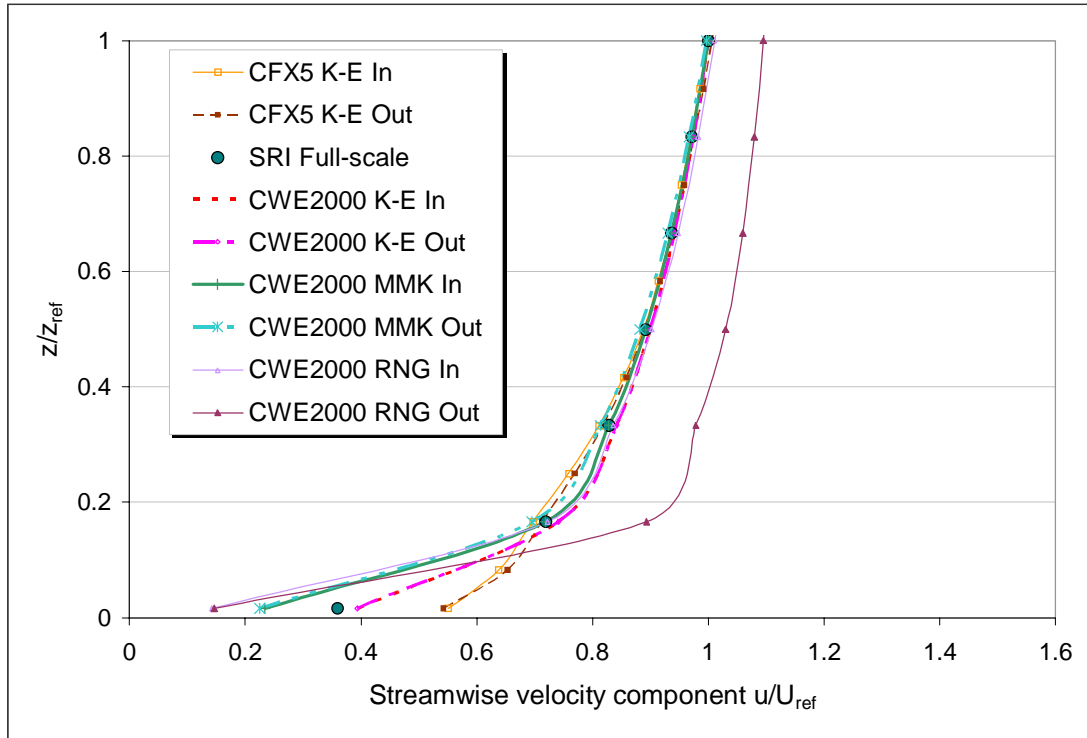
(b) Turbulent kinetic energy

Figure 5-4 ABL comparisons – inlet & outlet profiles

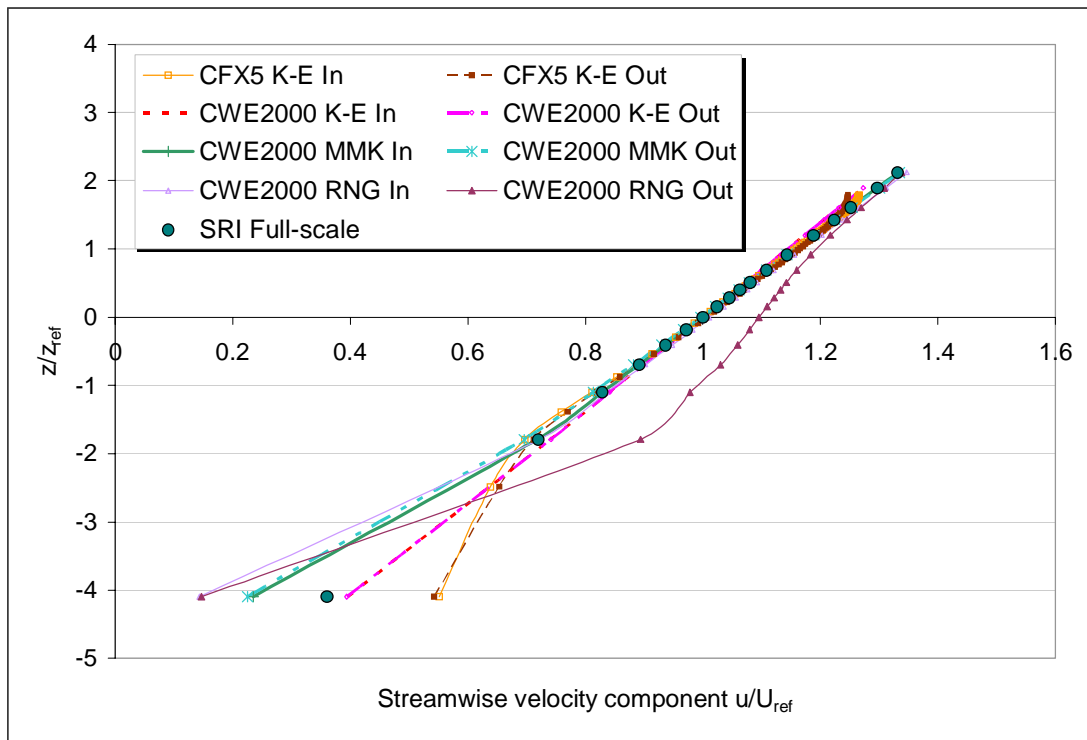
It is observed in Figure 5-4a that apart from the CWE2000 RNG solution, the other three solutions' outlet profiles are very similar to the inlet ones, and agree well with the full-scale mean velocity profile.

On closer inspection near the ground (Figures 5-5a and the log-plot of the velocity shown in Figure 5-5b), it can be seen that above 0.5m, all CFD results match the field measurement except the CWE2000 RNG result at the outlet. In the region between 0.1m and 0.5m above the ground, CFX5 K-E solution presents better agreement with the SRI field data than CWE2000 RNG model. Apparently CWE2000 K-E & MMK models give the closest matching ABL profile in this region. Their advantages could be associated with defining the rough ground surface, particularly by the user FORTRAN subroutine on structured grids.

CFX5 K-E, CWE2000 K-E & CWE2000 MMK simulations all produce the kinetic energy profile close to the empirical log-law profile (Figure 5-4b). The CWE2000 RNG solution imposed the turbulence levels matching the full-scale measurements at the inlet, but the outlet profile changes significantly especially near the ground. This phenomenon is explained by the contribution of low frequency turbulence [Richards et al. 2002]. It was found that the CFX5 results were consistent with the other CWE2000 CFD models. They all represent the high frequency turbulence that is approximately expressed by Equation 5.2 (p95) and filtered out the low frequency turbulence. This was consequently considered a good indicator for representing the mean flow field of the ABL. Therefore the CFX5 results were considered acceptable to undertake further studies involving the building structure.



(a) Zoom-in view of Figure 5-4 (a)



(b) Mean streamwise velocity log-plot

Figure 5-5 Mean streamwise velocity profile near the ground

### 5.3 Flow field modelling around a cube

To undertake the second challenge in the CWE2000 competition, a 6m cube (without openings) was placed into the computational domain to model the flow around this cube in the ABL.

#### 5.3.1 Computational domain and boundary conditions

The computational domain size was set with the dimensions of  $96\text{ m} \times 66\text{ m} \times 36\text{ m}$ , which was  $5H$  ( $H$ =building height) upstream and  $10H$  downstream, and  $5H$  away from each side and above the roof of the cube as illustrated in Figure 5-6. The domain size independency has been tested in previous studies [Easom 2000; Straw 2000].

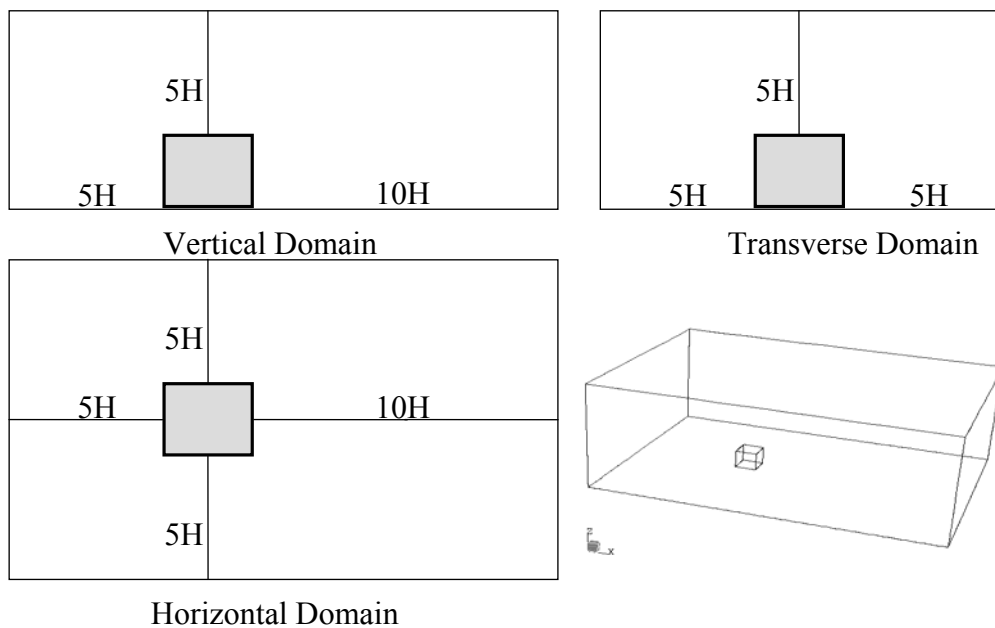


**Figure 5-6 CFD simulation domain for a 6m cube**

In addition to the boundary conditions listed in Table 5-1 (Section 5.2.1), the cube surfaces were treated as no-slip walls with the roughness length  $z_0$  equal to 0.005 m

[Easom 2000]. The reference wind speed was 10 m/s at cube height corresponding to the field data in the CWE2000 competition [Hoxey et al. 2002].

### 5.3.2 Grid independence tests

Steady state simulations have been performed using the standard  $k-\varepsilon$  model with the scalable wall function (Section 3.3.8). The residual target (convergence criteria) used was  $1 \times 10^{-4}$  (RMS). Table 5-5 shows the key parameters in the grid independence studies. A typical surface mesh in Figure 5-7 shows the finer mesh distribution on the surface, edges and around the cube.

**Table 5-5 Mesh settings for a 6m cube in the ABL**

Mesh Name	Grid15	Grid30	Grid40	Grid60
Mesh length scale on the ground (m)	0.6	0.6	0.6	0.5
Global cell expansion factor	1.2	1.2	1.2	1.2
Mesh length scale on the cube surface (m)	0.4	0.2	0.15	0.1
Resolution on the cube surface	15	30	40	60
1 <sup>st</sup> cell height from surface (m)	0.02	0.015	0.015	0.015
Vertical expansion factor near surface	1.1	1.05	1.05	1.05
Total number of cells	780,300	1,013,700	1,146,400	1,675,400

In addition to the four meshes listed in Table 5-5, a mesh named Grid15adapt was also used. This mesh consisted of a total of 1.75 million cells which was automatically adapted by CFX5 solver from Grid15 based on the calculated velocity and pressure gradients.

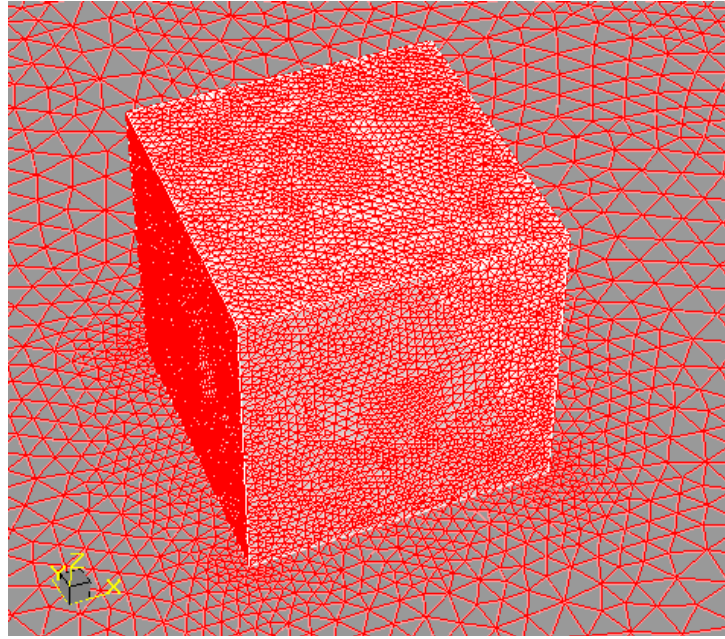


**Figure 5-7 Unstructured mesh around the cube**

Considering the wind direction  $0^\circ$  (which is normal to the cube face), Figures 5-8, 9 & 10 illustrate the pressure coefficient distribution along streamwise, transverse and horizontal centrelines of the cube predicted by the standard  $k-\varepsilon$  model on each grid.

Figure 5-8 shows the pressure distribution streamwise along the centreline of the cube. There is little difference on the windward wall on these grids. More significant differences occur on the roof in terms of the peak pressure. The weakest suction on the roof with a pressure coefficient  $C_p$  value of -1.1 is sensibly predicted on Grid15adapt (which shows the closest agreement with field data in CWE2000 competition). The highest value of -1.59 is predicted on Grid30 with  $1/18H$  distance from the front leading edge. On other grids it shows a  $C_p$  value of -1.4 on average.

Although Grid30 gives the highest negative pressure on the roof, it agrees well with Grid15adapt on leeward wall, and predict 0.1 less negative peak suction pressures than on the finer grids (Grid40 & Grid60).

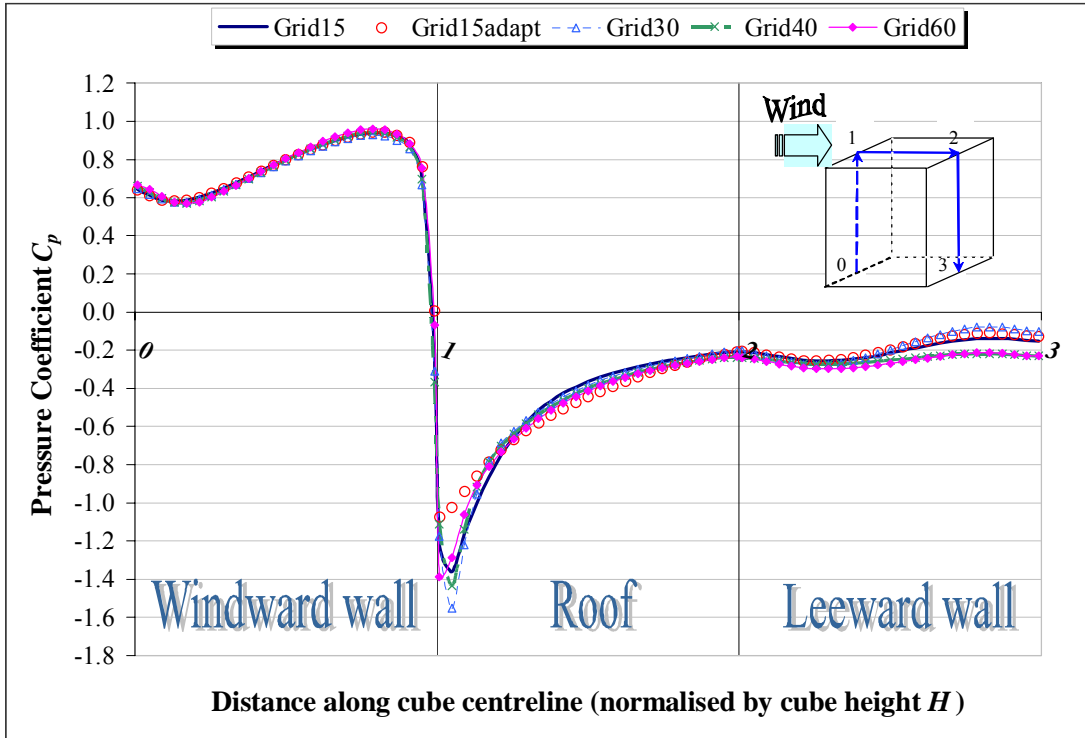


Figure 5-8 Grid independence tests - pressure coefficients along the streamwise vertical centreline of the cube

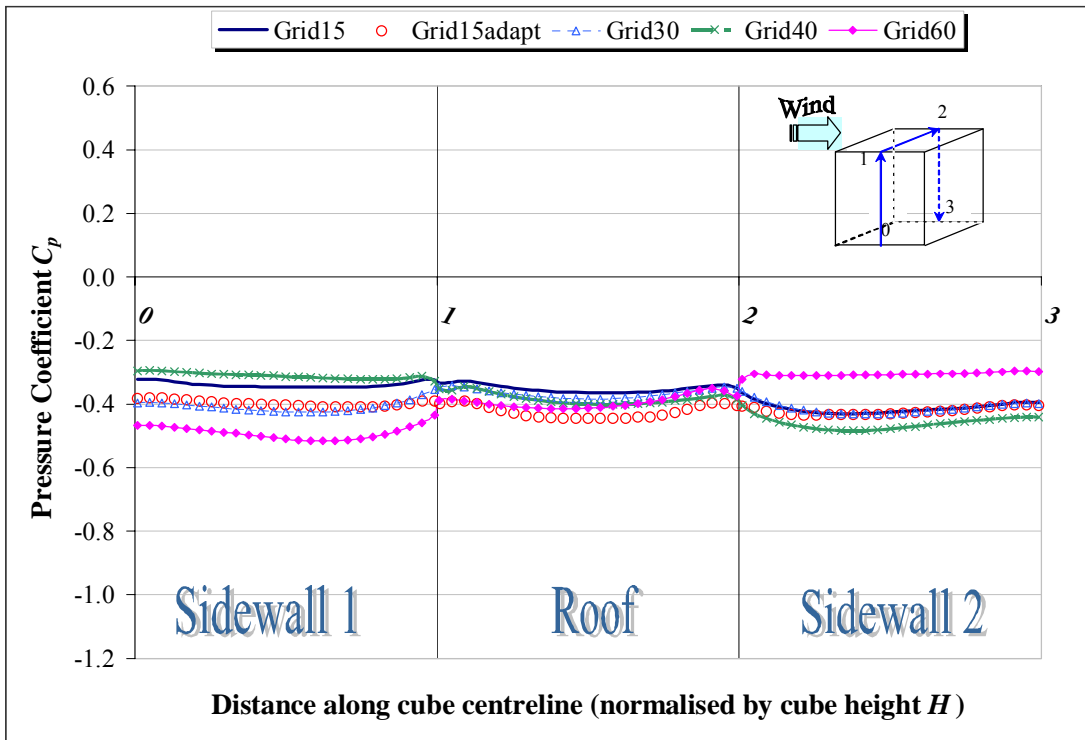
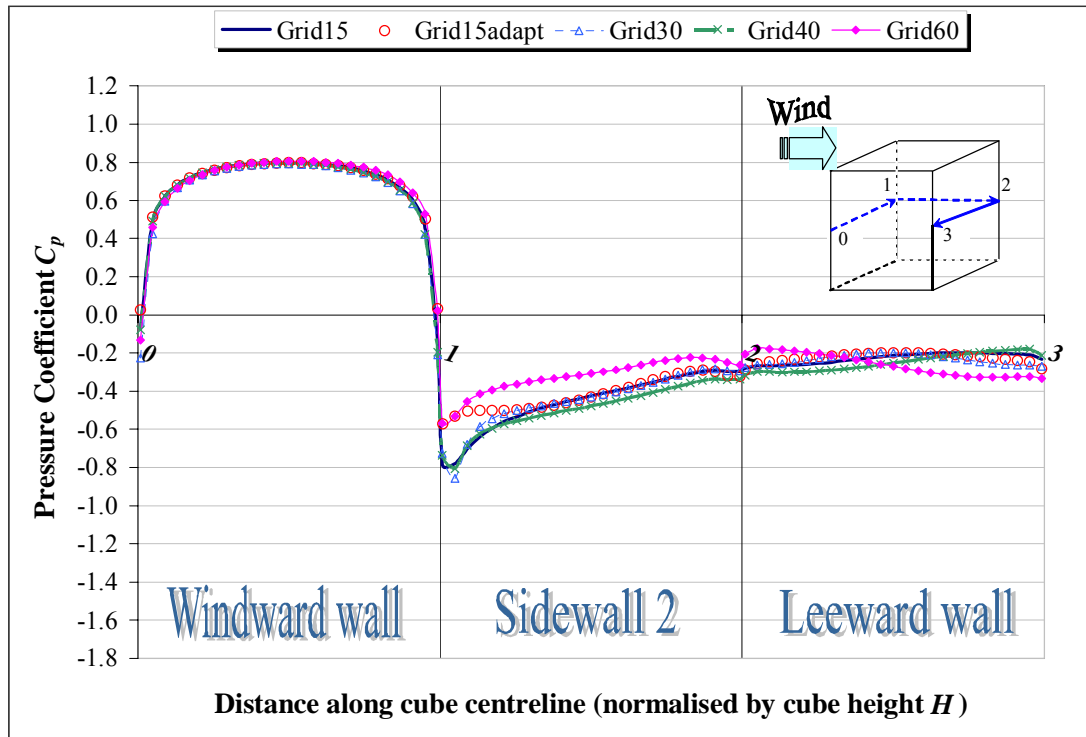


Figure 5-9 Grid independent tests - pressure coefficients along the transverse vertical centreline of the cube



**Figure 5-10 Grid independent tests - pressure coefficients along the horizontal mid-height centreline of the cube**

Along the transverse vertical centreline in Figure 5-9, Grid30 had the closest solutions to Grid15adapt results. Grid40 & Grid60 show asymmetric results on the two sidewalls. Meanwhile all models performed very similarly on the roof.

In Figure 5-10 windward wall results are almost the same along the horizontal centreline, close agreement was found on the leeward wall, with a maximum difference value of 0.2 amongst the models on the sidewall.

Referring to the CWE2000 data [Richards et al. 2002] in Figure 5-12, 5-14 & 5-15 (pp 117 & 120), the CFD results using the same/different turbulence models on structured grids, with the same/different methods of discretisation showed more scatter than was found in Figures 5-8 ~ 5-10, in particular on the roof. As shown in Figure 5-9, there were also asymmetric flow features found on side walls in other

CWE2000 simulations (except the CWE MMK model which imposed a central symmetry plane).

In order to clarify whether the asymmetric flow phenomenon on a bluff body is physically present or just an artefact imposed by CFD solvers, Prevezer and Holding [2002] investigated the flow over the front face of a bluff cab lorry. Their findings suggest that the flow asymmetry does physically exist, which was supported by wind tunnel experimental evidence and various CFD simulations using different commercial codes, mesh criteria, turbulence models and solver schemes. They also concluded that the asymmetry may be dependent on the aspect ratio of the bluff body and the asymmetry of the flow increased as the turbulence model increased in accuracy.

The flow on the side of the cube has a highly turbulent and unsteady nature [Richards and Hoxey 2002], in theory the asymmetric (in both an instantaneous and time-averaged sense) flow structure should also be identified numerically. However, the standard  $k-\varepsilon$  model has a well known weakness when solving flows associated with separation and recirculation. Therefore, more sophisticated turbulence models, such as the RNG  $k-\varepsilon$  and RSM models are needed to provide more accurate solutions and more flow details [Wright and Easom 1999].

It is concluded in the studies by Easom [2000] that the RNG  $k-\varepsilon$  model was able to predict flow separation and reattachment on the roof of the cube with an improved roof pressure distribution than the standard  $k-\varepsilon$  model. The Reynolds stress models (RSM) are based on transport equations for all components of the Reynolds stress tensor and the dissipation rate. The two Reynolds stress models used in the present study, one with isotropisation of production assumption [Launder et al. 1975]

(hereafter denoted RSM) and the other with a quadratic approximation for the pressure-strain correlation [Speziale et al. 1991] (hereafter denoted SSG).

The automatic mesh adaptation by the CFD solver can provide a more accurate solutions without excessive overall mesh refinement [Meroney et al. 1999]. Grid30 showed the overall better agreement with the adaptation results Grid15adpt and reasonable computing time. In order to conduct further simulations for more wind directions other than  $0^\circ$  on the same grid, and based on the overall performance among the four grids in Table 5-5, consequently Grid30 was chosen for further investigation using the RNG  $k-\varepsilon$  model and two versions of Reynolds stress turbulence models in Figure 5-11.

It is noted that applying the more accurate 2<sup>nd</sup> order differencing scheme with the RNG  $k-\varepsilon$  model, the solutions appeared to converge only to the level of  $2 \times 10^{-4}$  RMS. Modifications of computing timesteps, mesh settings and extended runtime up to one week, did not improve the convergence level. The fluctuation of the solution has been investigated by others [Knapp et al. 2003] using transient simulations with the RNG  $k-\varepsilon$  model. The instantaneous results have shown unsteadiness varying with time with a number of distinct frequencies, and the asymmetry was also present in the solutions.

More complicated RSM and SSG turbulence models for steady-state simulation have been achieved only with 1<sup>st</sup> order accuracy solver. Convergence difficulties were encountered in the RNG  $k-\varepsilon$  model simulations when trying to use a blend factor of 0.5 or higher. The convergence levels are discussed further in next section.

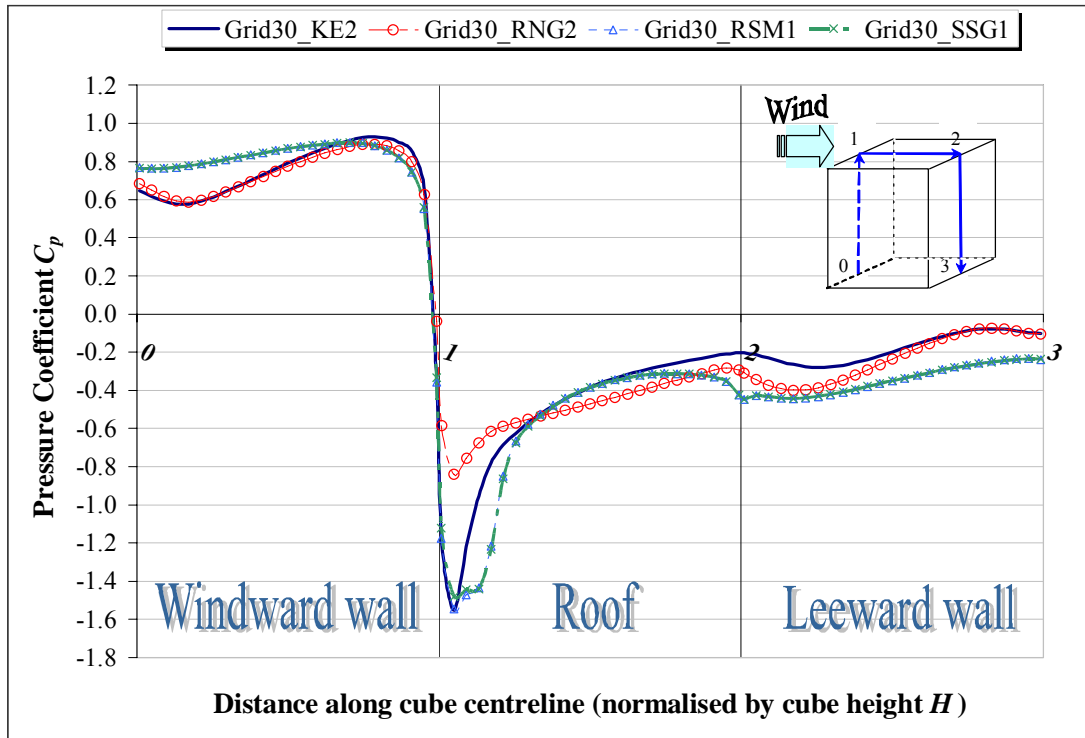


**Figure 5-11 Turbulence models effects on the streamwise pressure distribution**

### 5.3.3 Convergence criteria

Using the standard  $k-\varepsilon$  model further solutions converged to  $1 \times 10^{-5}$  (RMS) (one more order of magnitude than the original solution  $1 \times 10^{-4}$  (RMS)) on Grid15 adapt and Grid30, have shown no differences in the surface pressure coefficient results on the cube. It was therefore concluded that the original criterion  $1 \times 10^{-4}$  (RMS) was sufficient.

In terms of convergence, the RNG  $k-\varepsilon$  model using 2<sup>nd</sup> order differencing scheme reached the residual target of  $2 \times 10^{-4}$  RMS, and the CPU time needed was two days more than the standard  $k-\varepsilon$  model on a 1GHz Pentium III PC. Both RSM and SSG models were converged to  $5 \times 10^{-4}$  RMS by using 1<sup>st</sup> order upwind differencing scheme (UDS), which consumed about one-day CPU time on the PC.

Figure 5-11 shows the behaviour of the two Reynolds stress models is almost identical, but small pressure changes along the windward & leeward walls are found on comparing the RNG & standard  $k-\varepsilon$  models. On the roof, RNG model predicts 50% less negative pressure near the leading edge. RSM results are similar to  $k-\varepsilon$  model on the roof but closer to RNG model on the leeward wall. On the leeward wall, RNG results are shifted between RSM and standard  $k-\varepsilon$  model.

Unfortunately, it was not possible to obtain sufficiently converged results with both RSM models when using this geometry. Chen [1995] compared the performance of three RSM models and the  $k-\varepsilon$  model in the investigation of room air motion with heat transfer. The convergence criterion used was the sum of the absolute normalised residuals less than  $10^{-3}$ . The computing effort with the RSMs was 5~20 times greater than that with the standard  $k-\varepsilon$  model. The study concluded that RSMs can predict typical airflows encountered in the room airflows better than the standard  $k-\varepsilon$  model but the improvement was not significant.

Currently, the rapid development of computer power and decreasing costs make the use of complicated turbulence models more applicable not only in the research community but also in the industry. However, the robustness and accuracy of using RSMs are the main barriers of their wider use [Stangroom and Wright 2003]. In this natural ventilation study with the coupling external and internal flow simulations, the solution accuracy level should be kept close to  $1 \times 10^{-4}$ . The reason is due to the size of ventilation openings which are relatively small compared with the computational domain inlet or outlet section. Tight convergence levels can minimise the relative errors of the solutions at the openings. As such the RSM models will not be tested further in current project.

The non-linear  $k-\varepsilon$  model needs less computational effort than RSM and proved to be the most accurate model in some wind engineering applications [Wright et al. 2001].

However, it is not currently available on the unstructured grid solver in CFX 5.5.1.

Therefore, the CFX5 solutions with the standard and RNG  $k-\varepsilon$  models on Grid 30 were selected for further comparison studies with the CWE2000 competition data.

### 5.3.4 Surface pressure distribution for the $0^\circ$ case

Details of the computational settings in CFX5 and the information abstracted from the CWE2000 competition are listed in Table 5-6.

**Table 5-6 Modelling details for the cube**

Model Name	CFX5 K-E & CFX5 RNG	CWE2000 K-E	CWE2000 MMK	CWE2000 RNG
Code	CFX v5.5.1	PHOENICS v3.2	CFX v4.3	Fluent v5
Turbulence model	$k-\varepsilon$ & RNG $k-\varepsilon$	$k-\varepsilon$	MMK $k-\varepsilon$	RNG $k-\varepsilon$
Domain size x(m)×y(m)×z(m)	96×66×36	96×96×48	150×60×60	240×210×100
Mesh type	Unstructured	Structured	Structured	Unstructured & structured
Convective differencing scheme	Higher-order upwind differencing (2 <sup>nd</sup> order)	Hybrid differencing (1 <sup>st</sup> / 2 <sup>nd</sup> order)	CCCT (2 <sup>nd</sup> order)	Higher-order upwind differencing (2 <sup>nd</sup> order)
Resolution on the cube surface	0.2 m ( $H/30$ )	0.09 m ( $H/69$ )	0.3 m ( $H/20$ )	0.5 m × 0.38 m ( $H/12 \times H/16$ )
Global cell expansion factor	1.2	1.41	1.1 to 1.41	1.21
Total number of cells	1,013,700	611,585	93,700	127,783

Figures 5-12, 5-14 & 5-15 show the distribution of pressure for wind flowing normal to the cube wall ( $0^\circ$  case) as predicted by standard  $k-\varepsilon$  and RNG  $k-\varepsilon$  models using CFX5. The Silsoe full-scale data and CWE2000 computational results are also presented for comparison.

As can be seen from Figures 5-12, 5-14 & 5-15, in general the windward wall pressures are in good agreement with the full-scale measurements. In terms of the stagnation point, where flow is brought to rest on the windward wall of the building which corresponds to the maximum peak pressure, all the models except CWE2000 MMK model predict a higher stagnation position than measured (Figure 5-12).

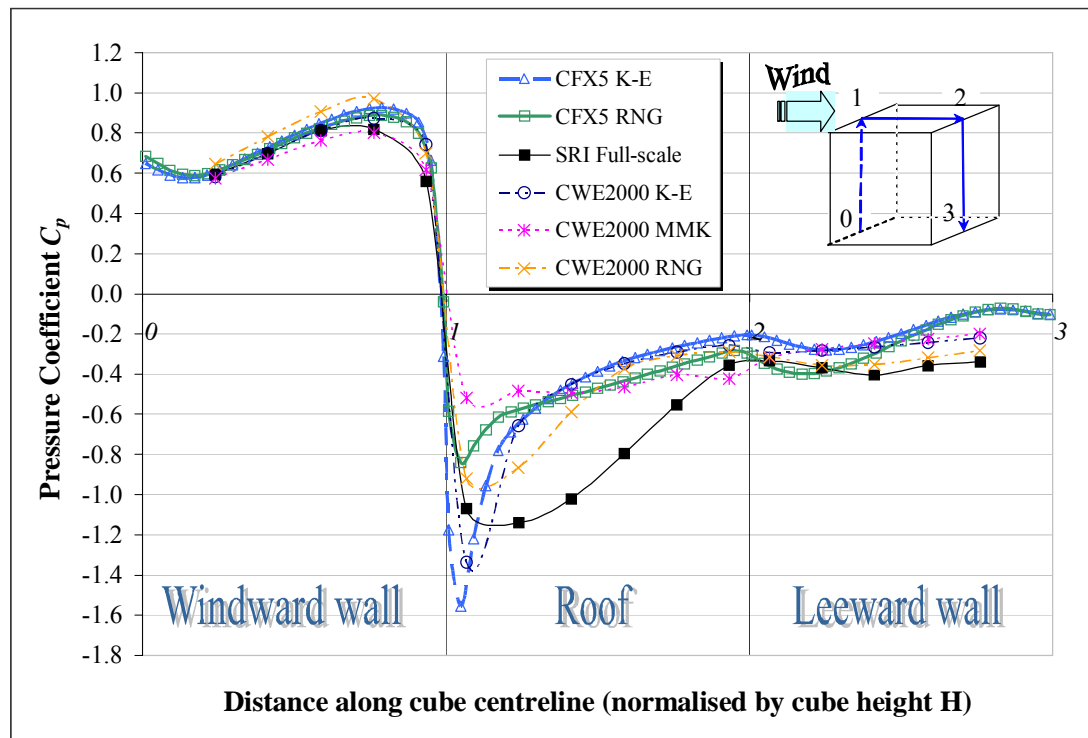


**Figure 5-12 Pressure coefficients comparison for the cube - streamwise vertical centreline section [0° case]**

On the leeward wall, both CFX5 models show similar negative pressures near the ground. The CFX5 RNG model gives values closer to the field measurement than CFX5 K-E model towards the roof level.

Both standard  $k-\varepsilon$  models, CFX5 K-E and CWE2000 K-E, significantly overpredict the negative peak pressure around the leading edge of the roof. The peak value is -1.58, which is almost 37% more than the measured value (-1.15). The overall

discrepancy decreases from the leading edge towards the leeward edge. But numerical results are all lower than the full-scale measurement elsewhere on the roof.

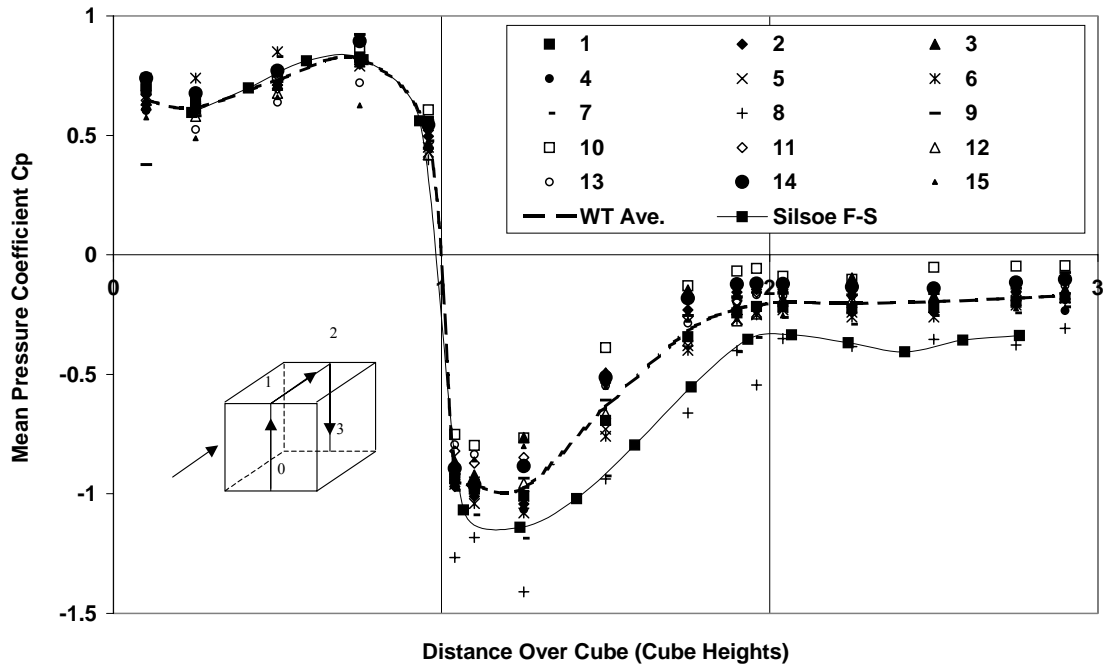


**Figure 5-13 Streamwise vertical centreline section pressure coefficients from the Silsoe full-scale test and 15 wind tunnel tests ( $0^\circ$  case) by Richards et al. [2002]**

Figure 5-13 after Richards et al. [2002] shows pressure coefficient distribution data along the vertical centreline section from the Silsoe full-scale data and 15 individual wind tunnel tests along with the average of the 15 tests. In general, there is good agreement on the windward wall. The wind tunnel data spread considerably on the roof and the leeward wall, but the majority of the wind tunnel tests have a trend of under-prediction. The average of the 15 tests has the similar shape to the Silsoe full-scale data. Comparison of Figure 5-12 and 5-13 shows that the computational models have more significant spread in the leading edge roof pressure than the wind tunnel tests. None of the computational models predicted the trend correctly on the roof.

In Figure 5-14, the RNG models show the asymmetry effect more than the K-E models. The CFX5 RNG result especially is significantly different on either side wall. The CWE2000 MMK solution imposed symmetry by only modelling half of the domain. The possible reasons for the asymmetry have been discussed in Section 5.3.2 (p112). On the roof, all the modelled negative pressures have about the same value at around -0.42 on average. All the numerical solutions show the least agreement (less than 1/3) with the field data around the centre of the roof. All models also under-estimate the measured suctions on side walls by least 30% to 50%.

On the horizontal mid-height plane in Figure 5-15, all models show close agreement with measured data on windward and leeward walls. On the sidewall, only the CFX5 RNG model captured the sudden pressure drop near the leeward edge as indicated in the field data. The CWE2000 RNG results show the closest match with measurement on the sidewall.

In terms of the pressure distribution on the roof, Figure 5-16 shows that the CWE2000 K-E & CWE2000 RNG solutions are close to the field measurement near the windward edges in row 1 (points 11-14). The CFX5 K-E solution overpredicts the suction in row 1 but under-predicts the suction away from the leading edge in rows 2 to 4. The CFX5 RNG solution shows similar behaviour as the CWE2000 MMK model with 50% under-estimation of the suction on the roof corner.

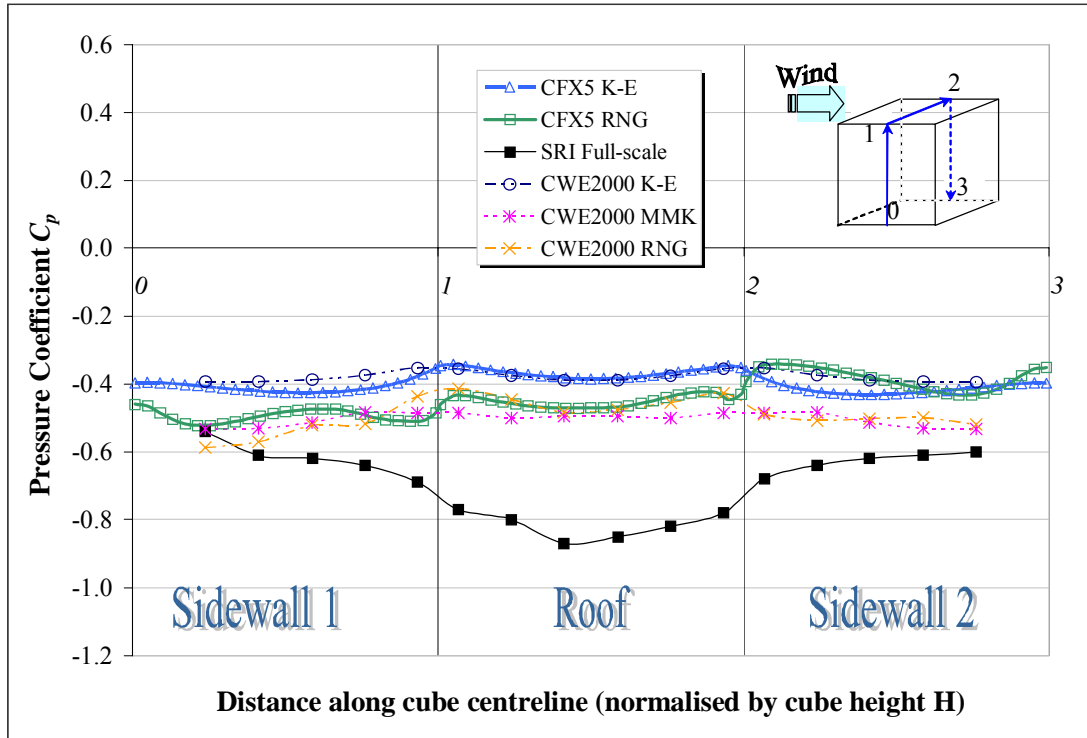


Figure 5-14 Pressure coefficients comparison for the cube - transverse vertical centreline section [0° case]

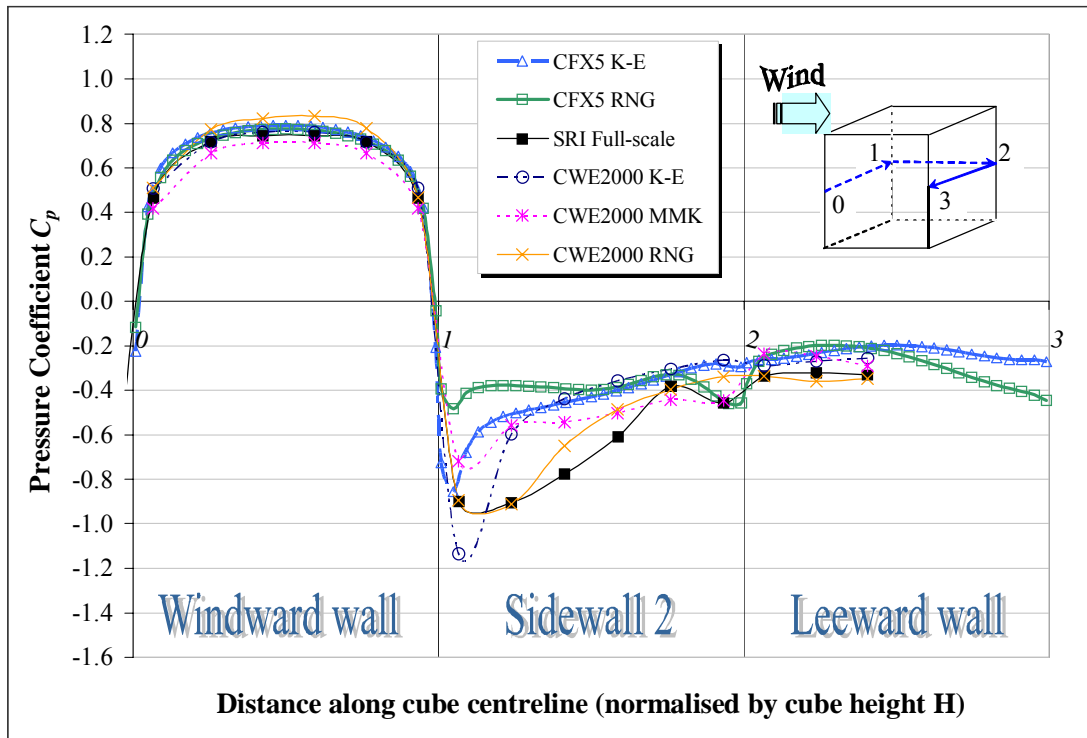
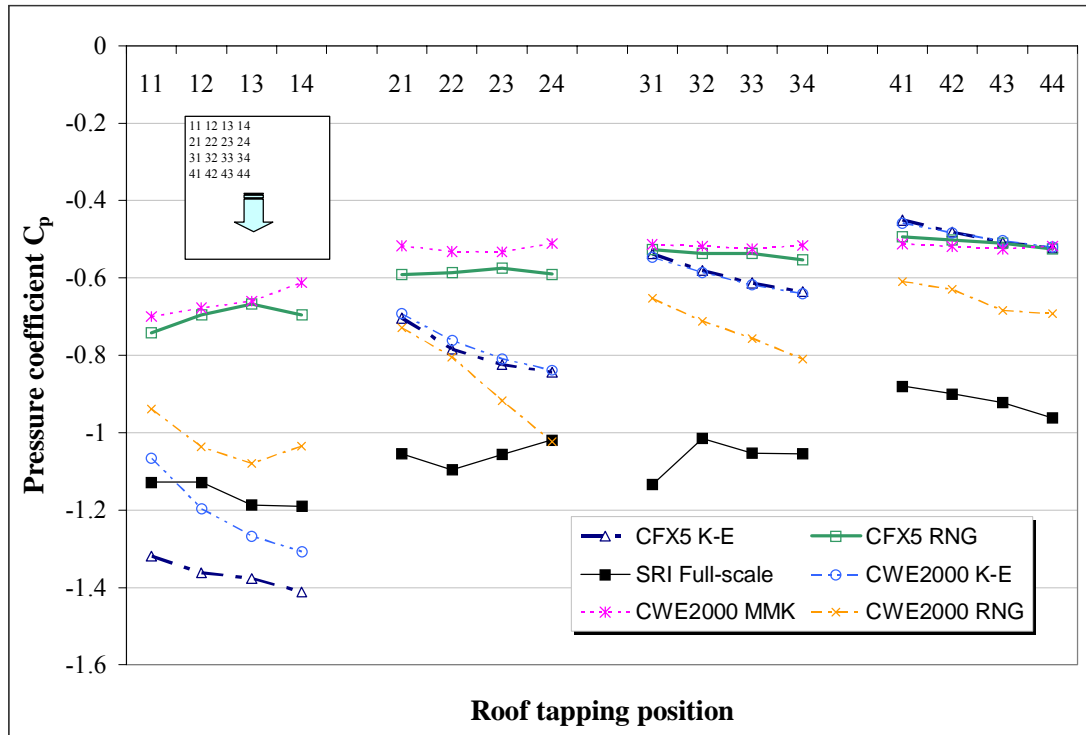


Figure 5-15 Pressure coefficients comparison for the cube - horizontal mid-height section [0° case]



**Figure 5-16 Pressure coefficients comparison for the cube - roof corner tapping points [ $0^\circ$  case]**

### 5.3.5 Velocity field and turbulence intensity for the $0^\circ$ case

Several locations (illustrated in Figure 5-17) were selected to compare the performance of the CFD models with the field measurements in terms of velocity and turbulence intensity.

In Figure 5-17a plan view has been plotted to illustrate the different locations from the windward wall, side wall and leeward wall, marked as (5, 1) (2, 6) and (3, 7) respectively. Each adjacent point is positioned 0.6 m from the wall, while the far point is located 6 m away from the wall. For each location as illustrated on the plan view, data was taken at three different heights. This is demonstrated in the section view of Figure 5-17b, where the vertical positions of each point had been

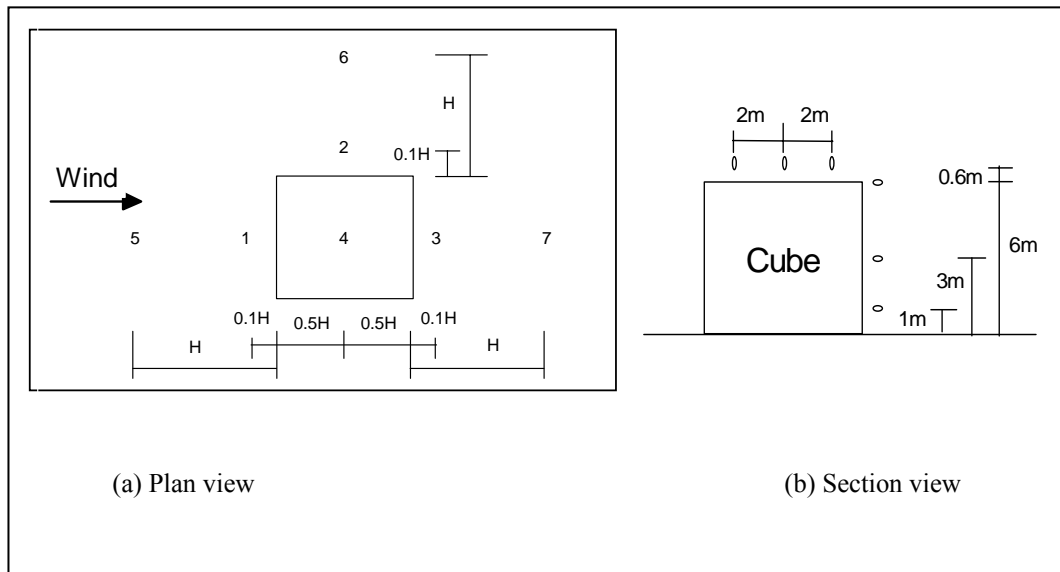


**Figure 5-17 Illustration of measurement points around the cube**

indicated at the heights 1 m, 3 m and 6 m above the ground level. Three more points were positioned 0.6 m above the roof along the streamwise centreline. One of which was placed on the centre of the roof, the other two to be separated 2 m upwind and downwind. The velocity components and the turbulent kinetic energy at all points are compared in Figures 5-18 ~ 5-21.

Good agreement between the full-scale measurement and CFD solutions for the velocities are shown in Figures 5-18, 19 & 20, at the points upstream of the cube (points 1 & 5) and 6 m beside the cube (Point 6). On the roof, predictions by numerical models on the streamwise velocity component  $u$  are more widely varied than other directions (Point 4).

In Figure 5-18, close to the leeward wall, the streamwise velocity component  $u$  at the heights 1m and 3m is well predicted by the CFX5 K-E & CFX5 RNG turbulence models. However at the height 6m both models under-predict the  $u$  value by 40% compared to field data. In the cube wake particularly at point 7, both models have

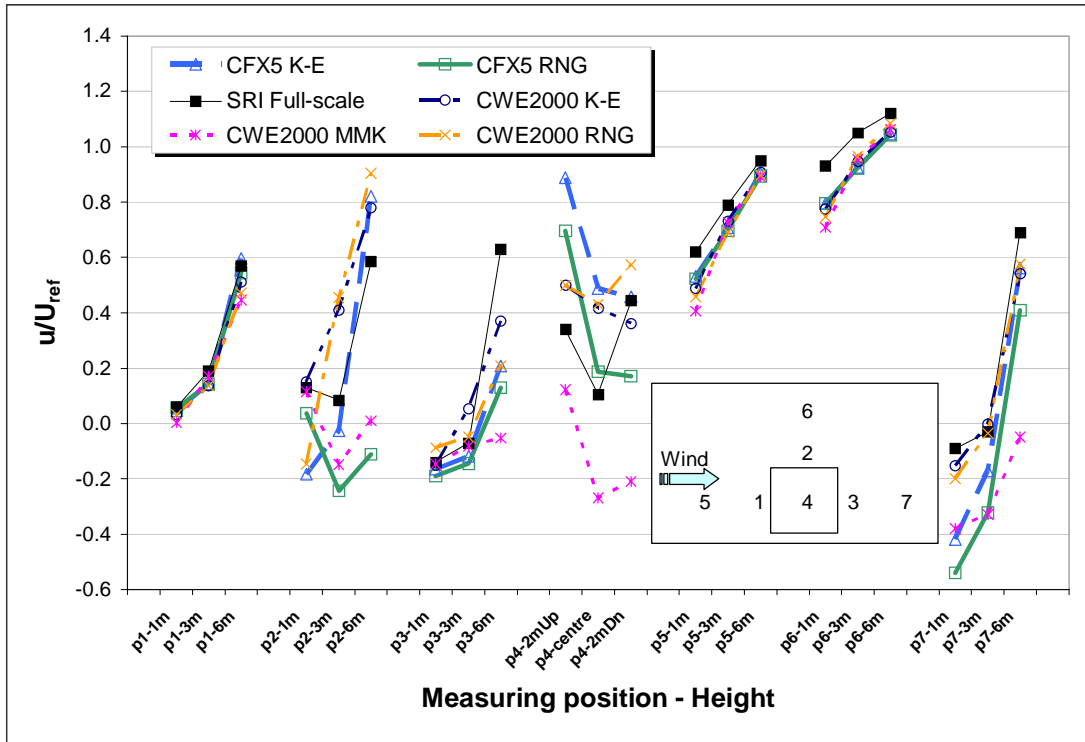


Figure 5-18 Velocity coefficients comparison around the cube - streamwise component  $u/U_{ref}$  [ $0^\circ$  case]

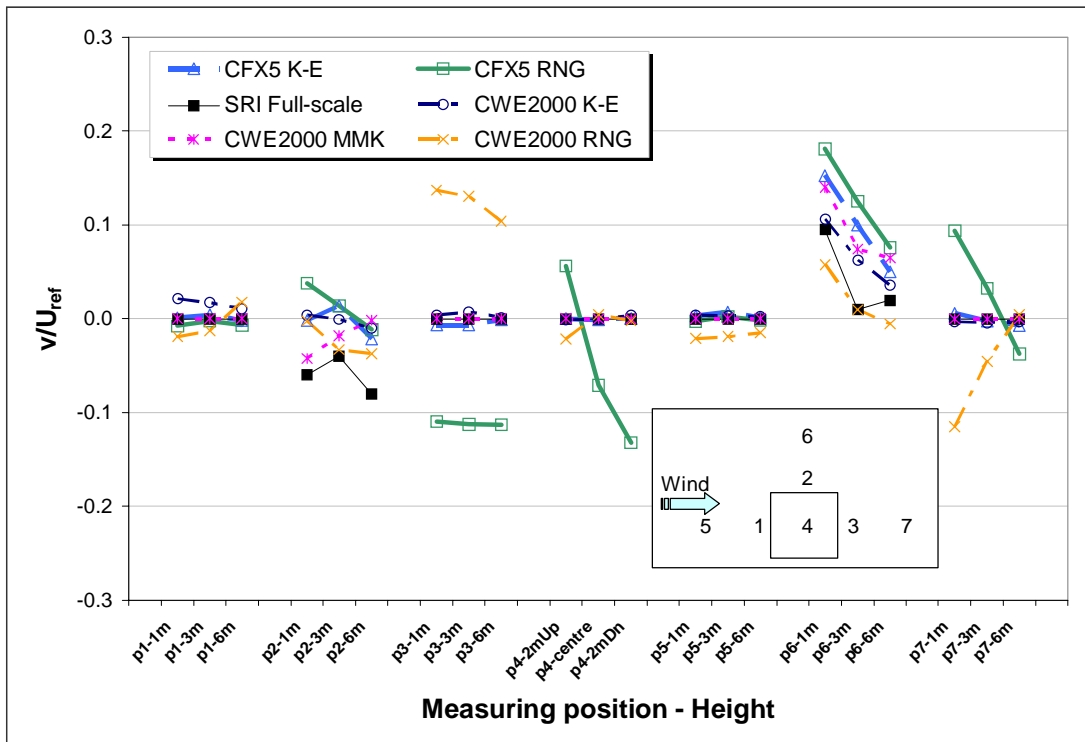


Figure 5-19 Velocity coefficients comparison around the cube - transverse component  $v/U_{ref}$  [ $0^\circ$  case]

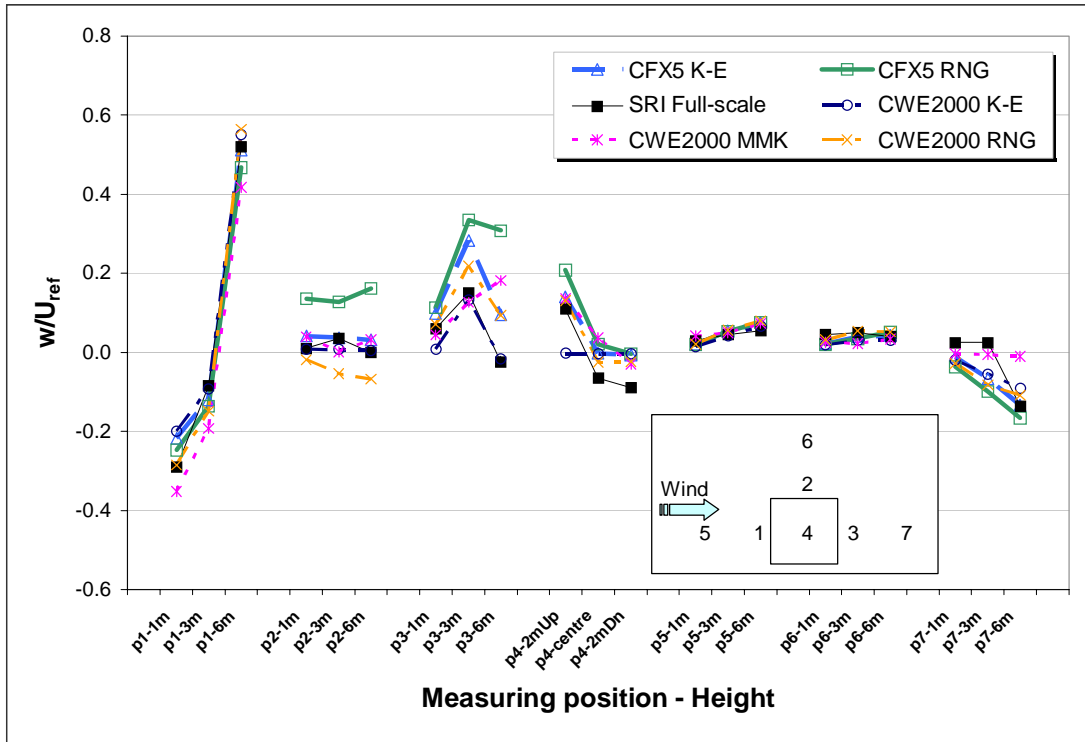


Figure 5-20 Velocity coefficients comparison around the cube - vertical component  $w/U_{ref}$  [ $0^\circ$  case]

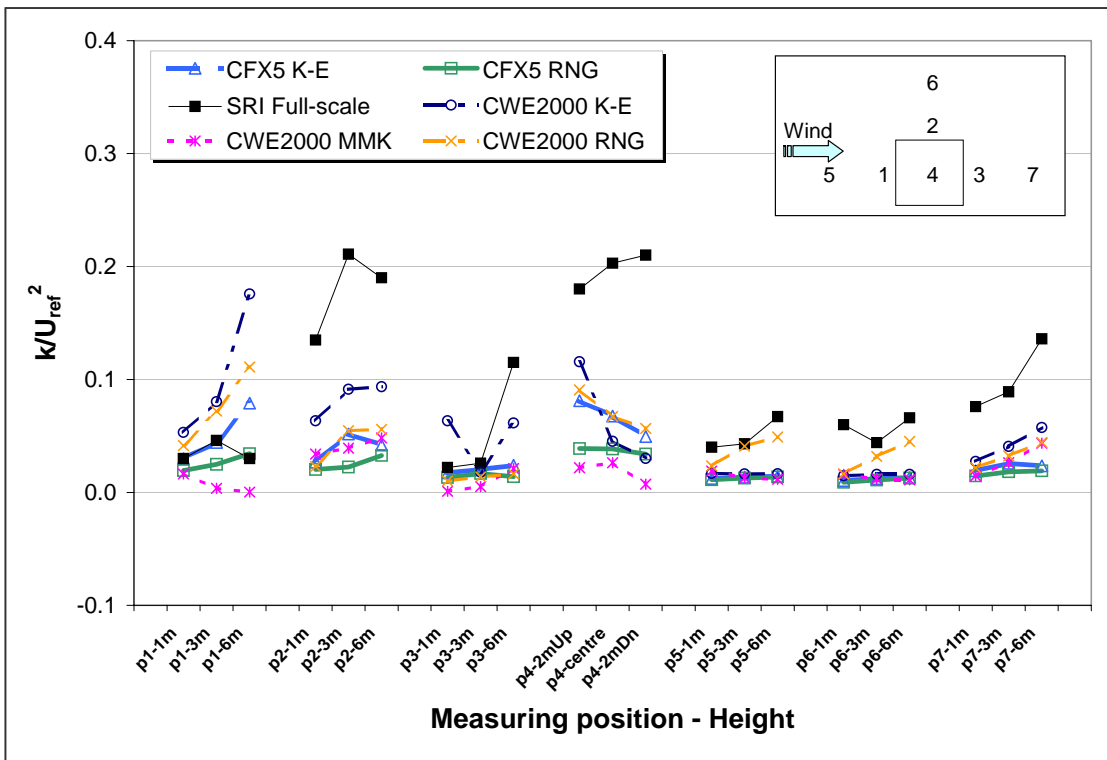


Figure 5-21 Turbulence level comparison around the cube - turbulent kinetic energy  $k/U_{ref}^2$  [ $0^\circ$  case]

predicted higher reversed velocity ( $<0$ ) at the heights 1 m and 3 m. Nonetheless, at 6m height the prediction agreed well with the measurement. Knapp et al. [2003] has demonstrated that the initial transient simulations have no benefit over the steady-state RANS solution in CFX5.

For the transverse component  $v$  in Figure 5-19, the CWE2000 RNG and CFX5 RNG solutions at the points 3 and 7 are opposite. This is probably caused by the asymmetry effect in the wake. Near the side wall, a higher value of the horizontal component was measured in the tests than in all models (Point 2). On the roof, CFX5 RNG shows the worse prediction than all other models and field data (Point 4). General agreement can be found between field data and other CFD models, i.e. CFX5 K-E, etc.

Moreover, good agreement with the vertical velocity component  $w$  is shown in Figure 5-20. Both the CFX5 K-E & CFX5 RNG models show upward components at 1 m downstream of the windward leading edge (p4-2mUp), and almost no vertical component at roof centre (p4-centre) and downstream (p4-2mDn). The CFX5 K-E solution presents closer agreement with full-scale measurement than the CFX5 RNG solution for the  $w$  component in Figure 5-20.

The turbulent kinetic energy predictions in Figure 5-21 show that in general all models under-predicted the turbulence level compared to the measurements. In particular on the roof and around the side wall the discrepancies are quite significant at 70%~100%. This originates from the choice of low frequency turbulence contribution at the inlet boundary conditions and the turbulence models in CFD simulations.

### 5.3.6 Surface pressure distribution for the 45° case

Measured and predicted pressure distributions on the cube for the 45° case are shown in Figures 5-22, 23 & 24.

In general better agreements are found between the CFD solutions and the full-scale measurements for the 45° case than the 0° case. In Figure 5-22 the strong suction measured along the windward edges of the roof appear to be significantly higher than those obtained for the 0° case in Figure 5-12 (p117). When wind blows diagonally onto the cube, the flow separating at the upwind corner will tend to be displaced under the flow separating immediately downwind of the corner. The net effect is that the vorticity of the flow is increased until a strong conical vortex is formed resulting in very high negative pressure [Cook 1985]. However, all CFD solutions under-predict this high level suction. The peak negative pressure predicted by the CFX5 RNG is -0.7, approximately 53% under-estimation of the measured peak value (-1.5). The CFX5 K-E results show no difference with the CFX5 RNG on the windward wall, better prediction on the roof and the closest agreement on the leeward wall amongst all the other CFX5 RNG and CWE2000 solutions.

In Figure 5-23, the CWE2000 RNG solution gives slightly higher positive pressure than the other solutions on the windward wall. The measured data has lower pressure around the front corner of the cube, which is caused by the horseshoe vortex formation. However, all CFD results overpredict the positive pressure close to the leading corner. Both CFX5 solutions have shown a small peak around the corner to the sidewall. Other models and field data did not have the data points as close as CFX5 models, therefore this phenomenon can not be verified.

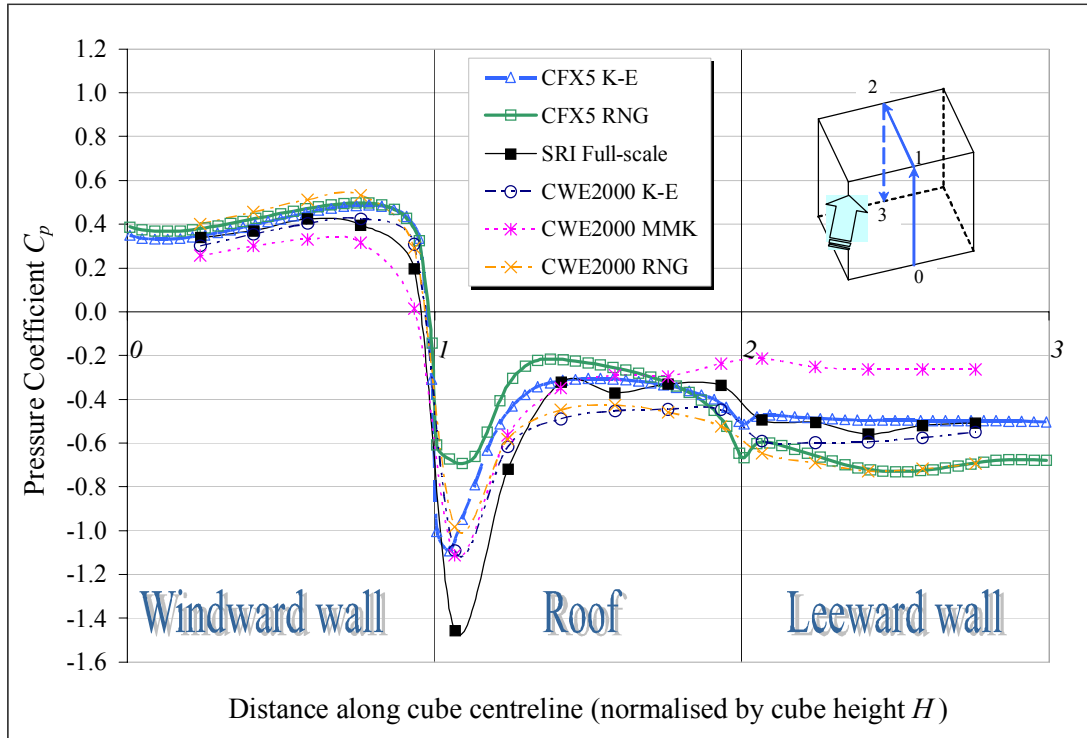


**Figure 5-22 Pressure coefficients comparison on the cube - vertical centreline section [45° case]**

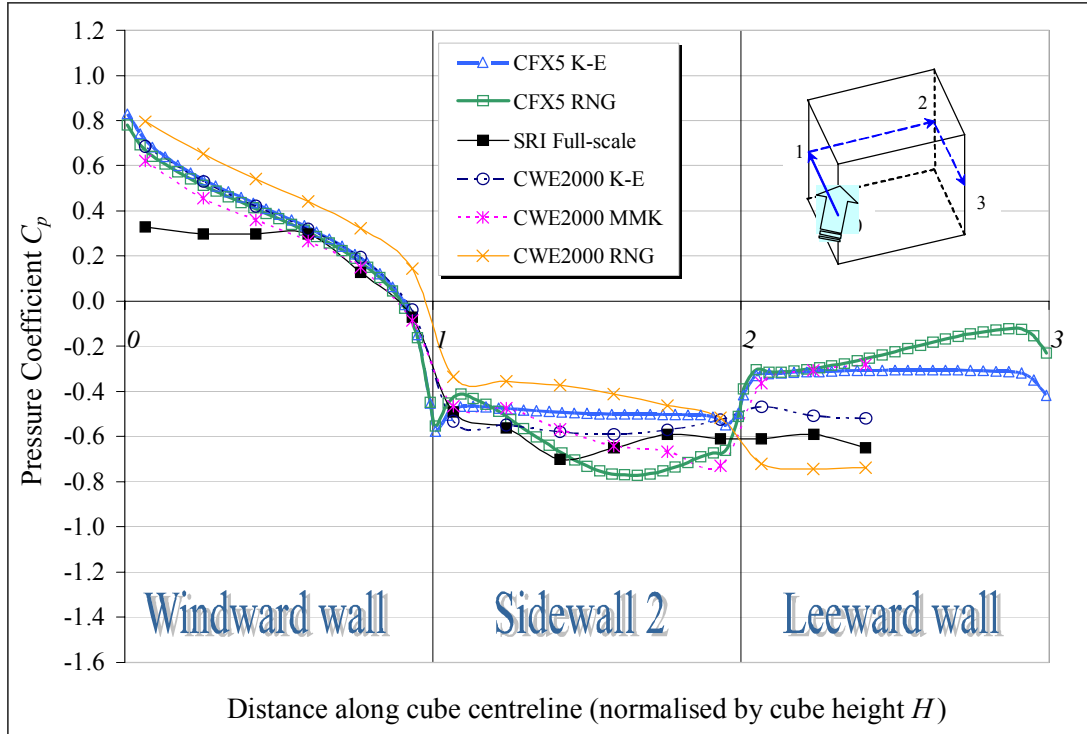


**Figure 5-23 Pressure coefficients comparison on the cube - horizontal mid-height section [45° case]**

All models show closer agreement near both the windward and leeward corner on the sidewall, but a spread of predictions between the corners. The CWE2000 K-E and RNG models present better agreement with the field data than other models on half of the leeward wall.

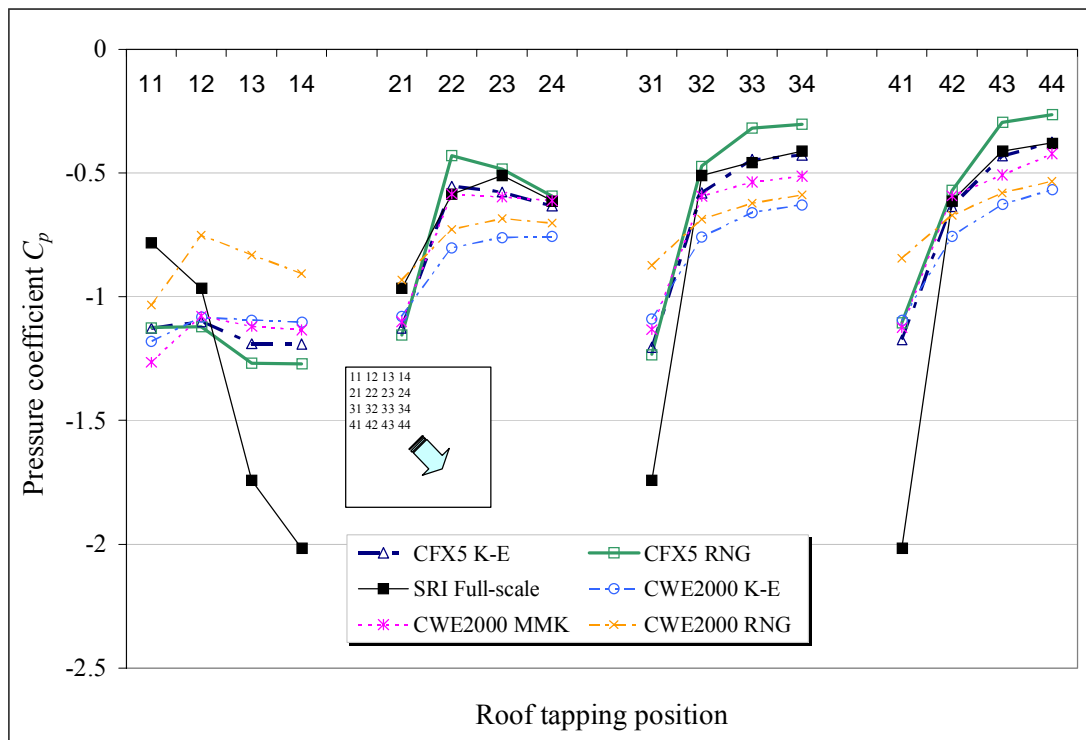


**Figure 5-24 Pressure coefficients comparison on the cube - roof corner tapping points [45° case]**

All CFD solutions show general agreement with the full-scale measurement on the roof corner in row 2-4 (Figure 5-24). Amongst these, the CFX5 K-E solution gives the closest estimation. Near the leading corner, all CFD results have failed to model the pressure changing trend in row 1(11-14). The rapid pressure change along row 1 in full-scale measurement is believed to be associated with the conical vortex formation.

### 5.3.7 Velocity field and turbulence intensity for the 45° case

The CFD predictions for streamwise velocity component around the cube for the 45° case are in good agreement with the experiments in Figure 5-25. The CFX5 K-E solution shows closer agreement with field data than the CFX5 RNG result.

Highly divergent solutions are found for the transverse velocity component except at Points 5 & 6 in Figure 5-26. Particularly in the wake (Points 2, 3 and 7), the CFD solutions show varying degrees of asymmetry.

All CFD results of vertical velocity component in Figure 5-27 match the upstream full-scale measurement at Point 1, 5 and 6. At all locations, good agreement is present with the CWE2000 K-E and the CFX5 K-E solutions. An asymmetric solution is shown by the CFX5 RNG results more obviously than the other models on Point 2 and 3.

All CFD models underpredict the high levels of turbulence measured at 6m height, across the roof (Point 4) and in the wake (Points 2, 3 and 7) by various degrees (see Figure 5-28). The CFX5 K-E and CFX5 RNG models perform very similarly for turbulence level predictions. Both models predict the same low level turbulence as CWE2000 MMK at all positions around the cube. It should be noted that the CWE2000 K-E solution shows the closest match to the measured turbulence levels.

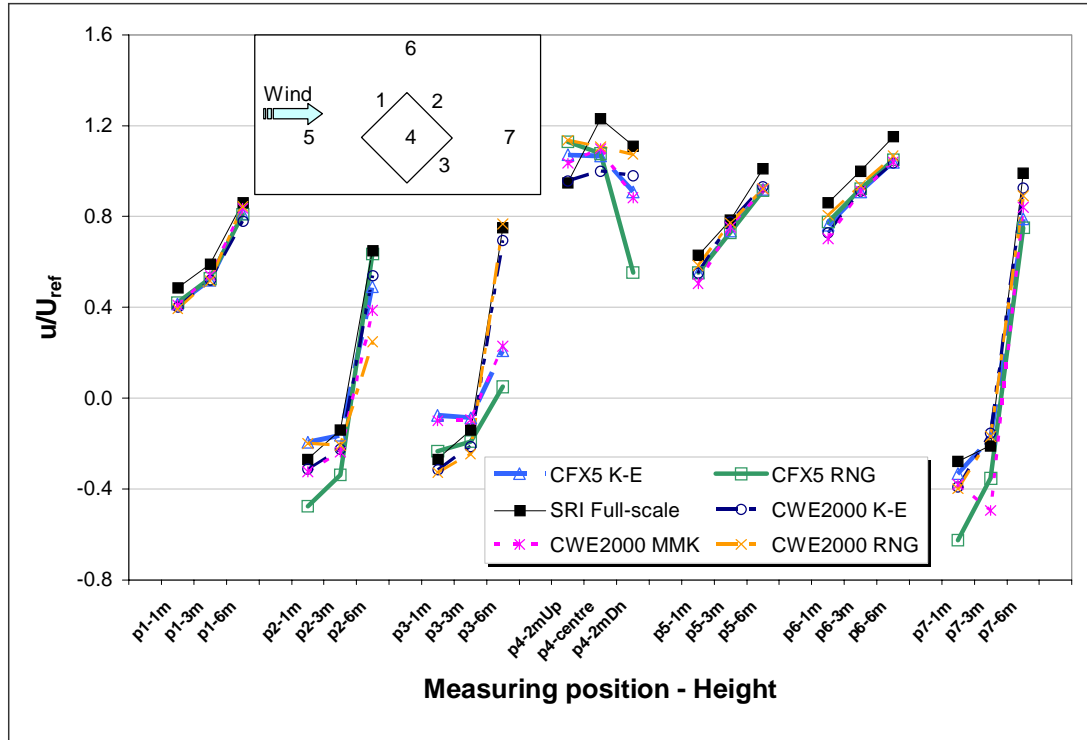


Figure 5-25 Velocity coefficients comparison around the cube - streamwise component  $u/U_{ref}$  [45° case]

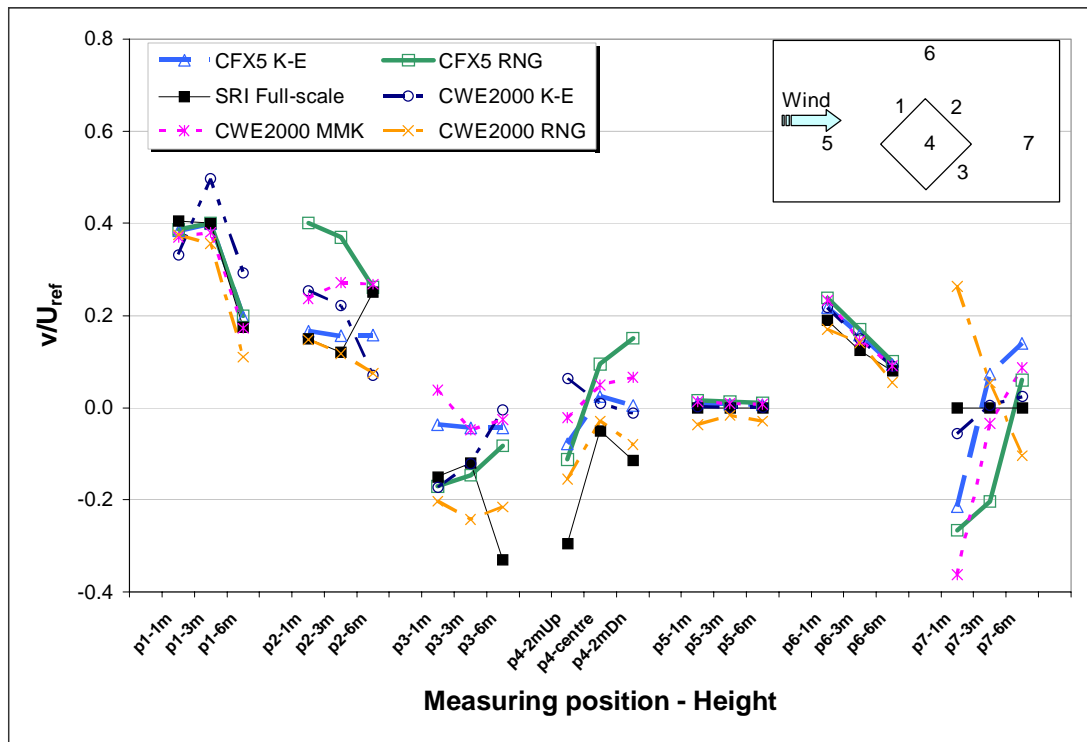


Figure 5-26 Velocity coefficients comparison around the cube - transverse component  $v/U_{ref}$  [45° case]

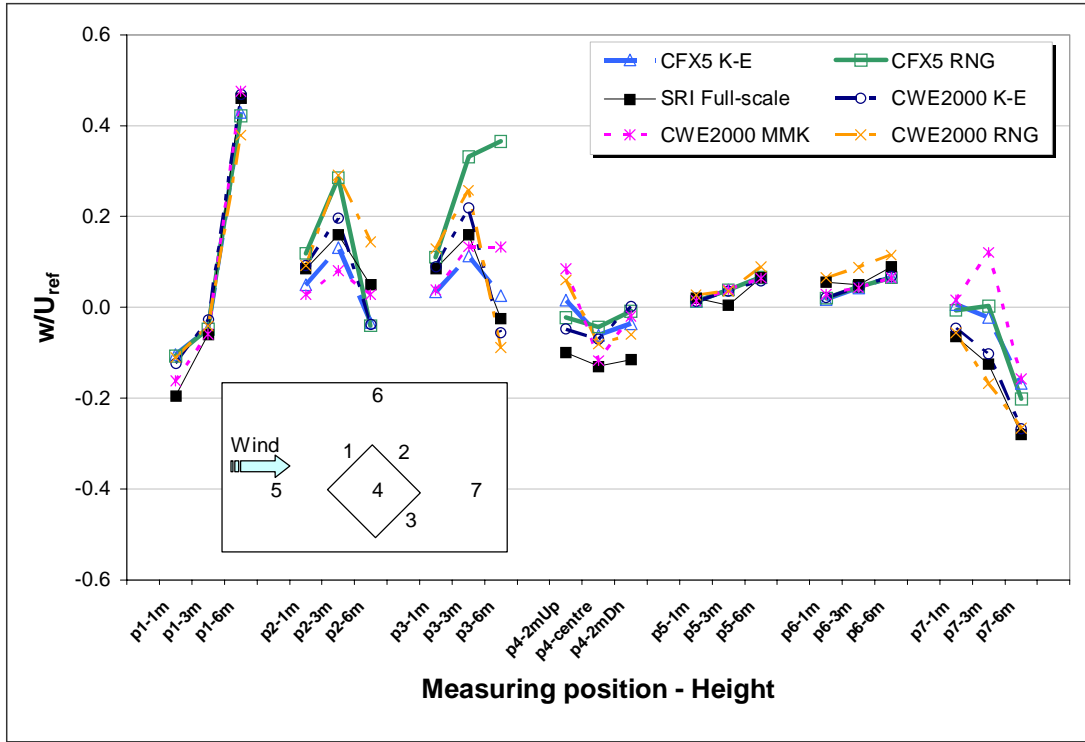


Figure 5-27 Velocity coefficients comparison around the cube - vertical component  $w/U_{ref}$  [45° case]

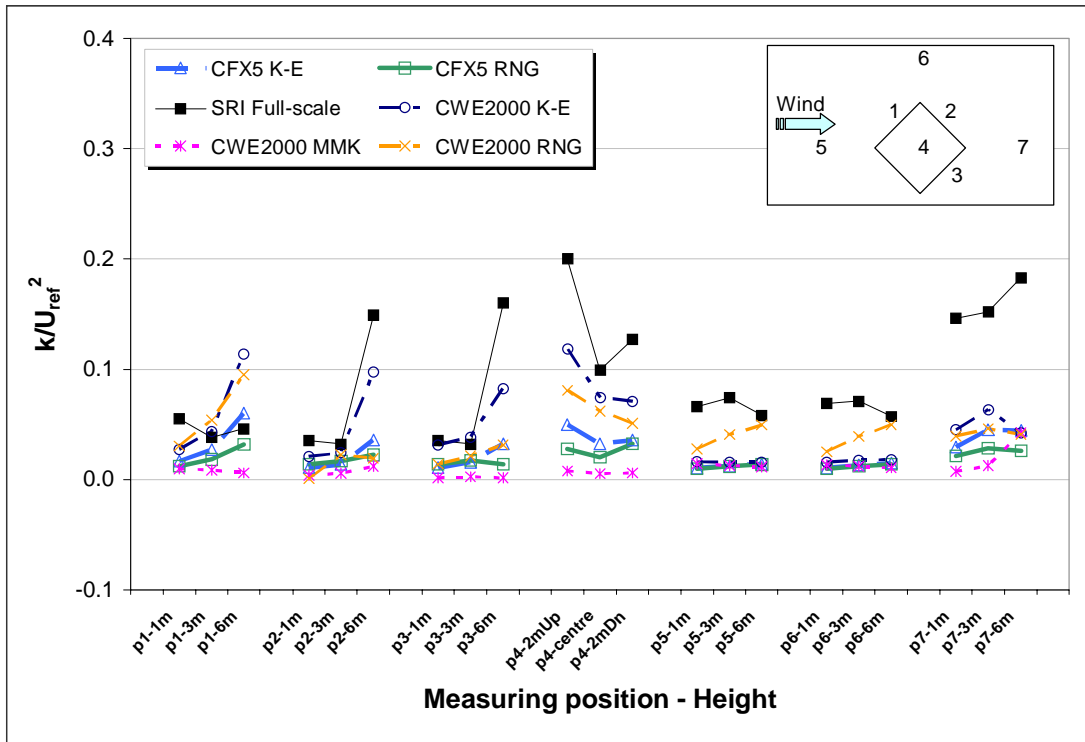


Figure 5-28 Turbulence level comparison around the cube - turbulent kinetic energy  $k/U_{ref}^2$  [45° case]

## 5.4 Discussion

The performance of CFD prediction of the freestream ABL and mean flow field around a surface mounted cube based on various RANS turbulence models has been investigated. In addition to three CWE2000 competition models, the standard  $k-\varepsilon$ , the MMK  $k-\varepsilon$  and the RNG  $k-\varepsilon$  turbulence models, two CFX5 models using the standard  $k-\varepsilon$  and RNG  $k-\varepsilon$  turbulence models have been included in the evaluation.

The major differences in the CFD solutions compared with the CWE2000 full-scale measurements appear to be related to the use of different turbulence models, and different grid systems (structured or unstructured grid).

The inlet conditions chosen by the author specify lower inlet turbulent kinetic energy levels than measured, in order to generate a homogeneous boundary layer which is consistent with the standard  $k-\varepsilon$  turbulence model.

To ensure the accuracy of the solutions, local grid refinement and evaluation of sensitivity to domain height and length have been carefully performed. The simulation results showed good agreement with full-scale measurement of the freestream ABL flow.

Two wind directions  $0^\circ$  and  $45^\circ$  to the surface mounted cube are examined and compared to the CWE2000 competition full-scale data and CFD solutions.

Generally CFD results give good predictions of pressure coefficients on windward and leeward walls for both  $0^\circ$  and  $45^\circ$  cases with typical errors being below 5-10%.

Mostly the CFX5 K-E solution is much closer to full-scale measurement than the CFX5 RNG solution.

On the roof the separation of flow and vortex shedding effects generate more turbulence leading to the fluctuating surface pressure. Sharma and Richards [1999] developed the quasi-steady theory further with wind tunnel experimental evidence to include the effect of  $\overline{uw}$  Reynolds stress on building surface pressures. They concluded that:

“ $\overline{uw}$  Reynolds stress are responsible for shear layer instabilities which cause

- (i) the very severe suction pressures near the leading edge and the corner of roofs,
- (ii) the apparent asymmetry in roof pressure records about their mean values, and
- (iii) consistent observation of momentary positive pressures on the roof despite the mean pressures being highly negative.”

Therefore, without taking account of the individual Reynolds stress effect, all RANS simulations failed to predict the high suctions in the centre of the roof for the  $0^\circ$  case, and along the windward edges for the  $45^\circ$  case.

Overall velocity predictions by RANS models are better than the pressure coefficients results. The velocity results show good agreement at positions upstream of the cube and over one building height distance to the sidewalls. Widely varying results in the separation and recirculation zones above the cube and in the wake have shown that the choice of turbulence model affects the CFD solutions. The highly turbulent and unsteady nature of the flow around the cube causes the asymmetric flow structure. More complicated turbulence models can provide accurate solutions and more flow details, therefore more asymmetric results. In this investigation, the RNG  $k-\varepsilon$  model shows more asymmetric features than the standard  $k-\varepsilon$  model. Only

MMK  $k-\varepsilon$  model from the CWE2000 competition avoided the asymmetry problem by only modelling half of the domain for the  $0^\circ$  case.

The CFX5 RNG model performed differently from the CWE2000 RNG model, the possible reasons for that are:

- (i) inlet condition with lower kinetic energy level
- (ii) fully unstructured and much finer grid on cube surface and within the domain in CFX5 simulation
- (iii) different near wall treatment in different CFD code.

The more promising turbulence models for wind engineering application, e.g. the non-linear  $k-\varepsilon$  model [Wright and Easom 2003] and LES model are not currently available in CFX5. Recently Cheng et al. [2003] compared the performance of large eddy simulation (LES) with the standard  $k-\varepsilon$  model for a fully developed turbulent flow over a matrix of cubes. Based on the detailed comparisons between the CFD predictions and the corresponding wind tunnel experimental data, the authors concluded that both the LES and standard  $k-\varepsilon$  model were able to predict the main characteristics of the mean flow in the array of cubes reasonably well. The flow structures in the vicinity of a cube, such as separation at the sharp leading top and side edges of the cube, recirculation in front of the cube, and the arch-type vortex in the wake are captured by both models. Nevertheless, LES was able to give a better overall quantitative agreement with the experimental data than the standard  $k-\varepsilon$  model. The computational cost associated with LES is about 100 times greater than that with the standard  $k-\varepsilon$  model.

Attempts to simulate with two versions of Reynolds stress models were not successful due to the numerical stability and the accuracy level of results. The overall performance of the CFX5 K-E and CFX5 RNG models showed little difference. For the  $0^\circ$  case, CFX5 RNG solution was closer to the full-scale data except for the turbulent kinetic energy prediction in the wake. For the  $45^\circ$  case, CFX5 K-E performed better than CFX5 RNG. In particular on the windward wall and leeward wall, CFX5 K-E results are closer to the field data than CFX5 RNG.

Therefore, for the further investigation on the time-averaged cross ventilation effects on the cube with openings at two vertical levels, only the CFX5 K-E and CFX5 RNG models were chosen as appropriate in terms of the overall accuracy and computational resource and time factors.

# **Chapter 6    CFD Simulations of Cube Envelope**

## 6.1 Introduction

The external pressure and flow field for the sealed cube have been validated with published experimental data in Chapter 5. In this chapter, wind alone and combined wind & buoyancy induced ventilation in the 6m cube at a number of incident wind directions are investigated by CFD.

## 6.2 CFD Test Configuration

Two identical rectangular openings were located along the cube vertical centreline in opposite walls. They were positioned 1m above the ground and 1m below the roof as illustrated in Figure 6-1. Each vent had an opening size of  $0.35 \text{ m} \times 0.25 \text{ m}$ , with a ratio of the opening area to wall area at 0.24%. This ratio is the same as the test model in Chapter 4.

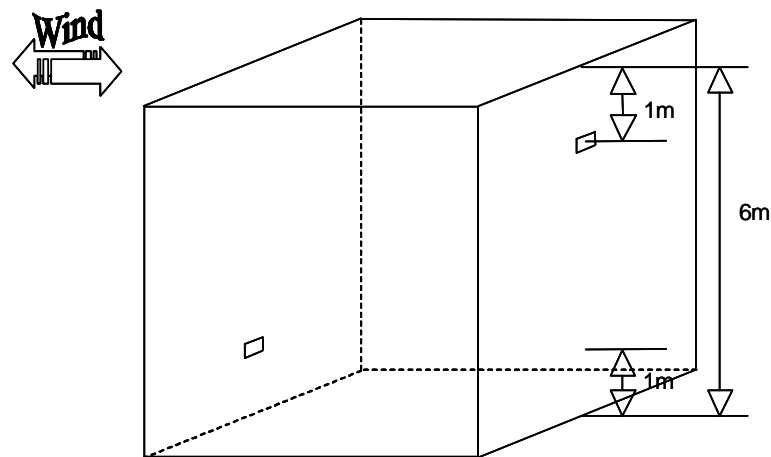


**Figure 6-1 Schematic diagram of the 6m cube with two rectangular openings**

The computational domain and boundary conditions were the same as for the sealed cube described in Section 5.3.1.

### 6.3 CFD Simulations of Wind Induced Ventilation

This section presents the CFD predictions of the wind induced mean ventilation rates through the cube and the indoor airflow patterns under various wind directions.

#### 6.3.1 Grid settings

In order to assess the accuracy of different mesh sizes and capture detailed flow feature through the openings, three types of meshes were used and named according to the resolution on the cube surface (the ratio of the cube height to the length scale of the mesh element). These settings are listed in Table 6-1 and a typical mesh is shown in Figure 6-2.

**Table 6-1 Mesh types for the cube with ventilation openings**

Mesh Name	Grid15	Grid20	Grid40	Notes
Mesh length scale on cube surface (m)	0.4	0.3	0.15	
Mesh resolution on cube surface	15	20	40	Cube height /Mesh length scale
Mesh resolution at openings	5	6.25	12.5	Opening height /Mesh length scale
1 <sup>st</sup> cell height above surfaces (m)	0.02	0.02	0.015	
Vertical expansion factor	1.1	1.1	1.05	
Mesh length scale in indoor space (m)	0.4	0.3	0.3	
Total number of cells	927,500	1,172,000	1,449,300	
No. of iterations	44	68	124	
Total CPU time	4hr51m	8hr14m	18hr13m	

The convergence criteria used on the coarse, medium and fine grids (Grid15, Grid20 and Grid40) were the root-mean-square of normalised residual for all variables to be less than  $1 \times 10^{-4}$  (RMS).

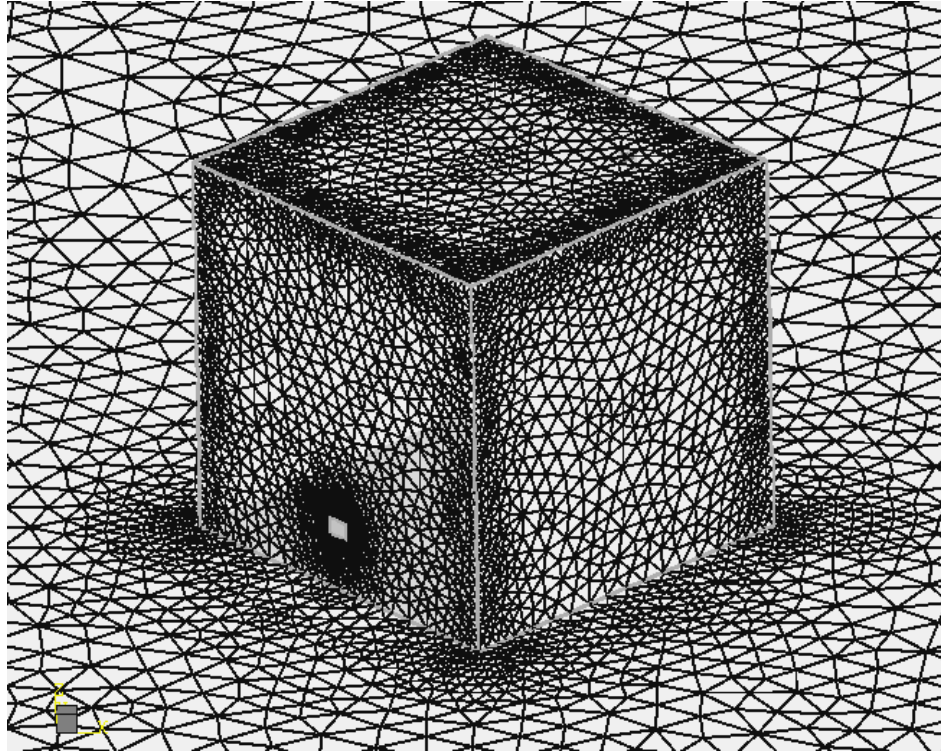


**Figure 6-2 Unstructured mesh around the cube with openings**

The CFD simulations on the three grids were performed for the normal ( $0^\circ$ ) wind direction using the standard  $k-\varepsilon$  model. Two points 0.5m away from the centre of each opening along the vertical centreline were selected to compare the predicted pressure coefficients  $C_p$  (Figure 6-3) with those measured on the full-scale building. In Figure 6-4 at these points on the fine grid (Grid40), the  $C_p$  value had 3% (or 5%) difference from the other two grids around the lower (or higher) level opening. Amongst the three grids the maximum value of  $C_p$  difference was 0.07 on the leeward wall. The variations occurred on the leeward wall halfway down toward the ground. There was almost identical  $C_p$  distribution along the windward wall. Along

the roof a slightly less peak negative value occurred on the fine grid (Grid 40) than on other grids.

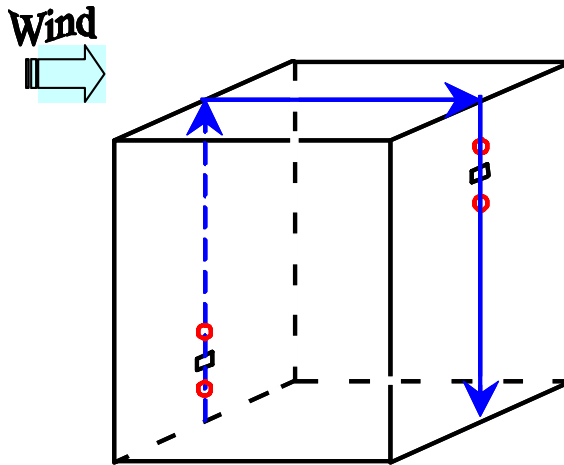


Figure 6-3 Two pressure tapping points located 0.5m apart from each opening centre vertically

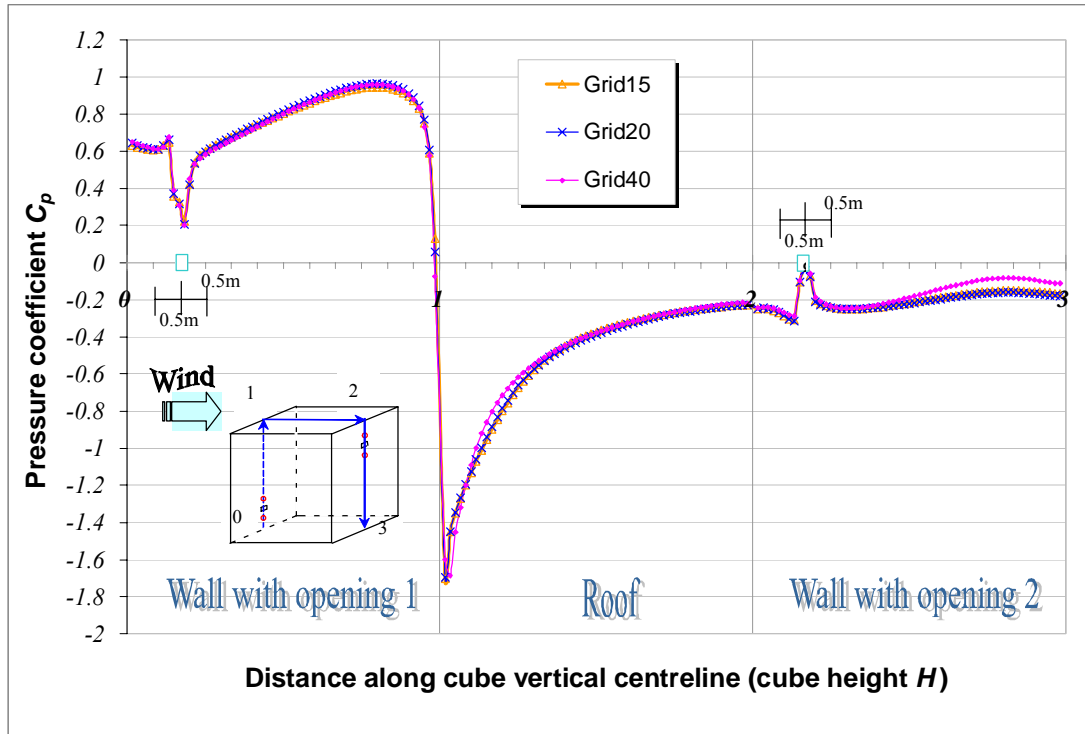


Figure 6-4 Grid sensitivity tests – pressure coefficients along vertical centreline on coarse, medium and fine grids

### 6.3.2 Convergence tests and solution accuracy

All the three meshes (Grid15, Grid20 and Grid40) were used to obtain solutions using the 2<sup>nd</sup> order discretisation scheme with a convergence criteria of two more orders of magnitude than the original solution. Table 6-2 lists all the residual levels achieved on all grids, the total CPU time, and the number of the iterations.

**Table 6-2 Convergence tests criteria for the cube with openings**

Tests	Convergence level	RMS residual value	Total CPU time	No. of iterations
Grid15	A	$1 \times 10^{-4}$	4hr51m	44
	B	$1 \times 10^{-5}$	13hr15m	94
	C	$1 \times 10^{-6}$	1day4hr10m	227
Grid20	A	$1 \times 10^{-4}$	8hr14m	68
	B	$1 \times 10^{-5}$	16hr10m	80
	C	$1 \times 10^{-6}$	1day9hr03m	239
Grid40	A	$1 \times 10^{-4}$	18hr13m	124
	B	$1 \times 10^{-5}$	2day10hr26m	327
	C	$4 \times 10^{-6}$	4day0hr03m	538

There are three convergence levels listed in Table 6-2 & 6-3: the RMS residual value of the order of  $10^{-4}$  was labelled as the convergence level A. Consequently, the RMS value of  $10^{-5}$  and  $10^{-6}$  were named as level B and level C.

Comparison of the resulting quantities, such as the mean speed and the mass flow rate through ventilation openings, showed that the solutions had less than 1% difference between the results obtained at level B and level C (see Table 6-3).

Detailed variations of these two parameters are illustrated in Figure 6-5.

**Table 6-3 CFD solutions accuracy for the cube with openings**

Tests		Mean speed (m/s)		Imbalance (In-Out)/In (%)	Mean speed (%)	
		In	Out		In	Out
Grid15	(A) $1 \times 10^{-4}$	3.55	3.70	-4	-3	2
	<i>(C-A)/C (%)</i>	0	1			
	(B) $1 \times 10^{-5}$	3.55	3.74	-5	-2	4
	<i>(B-A)/B (%)</i>	0	1			
	(C) $1 \times 10^{-6}$	3.57	3.73	-5	-2	3
	<i>(C-B)/C (%)</i>	0	0			
Grid20	(A) $1 \times 10^{-4}$	3.54	3.64	-3	-3	1
	<i>(C-A)/C (%)</i>	2	-1			
	(B) $1 \times 10^{-5}$	3.55	3.64	-2	-2	1
	<i>(B-A)/B (%)</i>	1	0			
	(C) $1 \times 10^{-6}$	3.59	3.59	0	-1	-1
	<i>(C-B)/C (%)</i>	1	-1			
Grid40	(A) $1 \times 10^{-4}$	3.44	3.64	-6	-5	1
	<i>(C-A)/C (%)</i>	5	-1			
	(B) $1 \times 10^{-5}$	3.62	3.65	-1	-1	1
	<i>(B-A)/B (%)</i>	5	0			
	(C) $4 \times 10^{-6}$	3.64	3.61	1	-	-
	<i>(C-B)/C (%)</i>	1	-1			
Tests		Mass flowrate (kg/s)		Imbalance (In-Out)/In (%)	Mass flowrate (%)	
		In	Out		In	Out
Grid15	(A) $1 \times 10^{-4}$	0.69	0.70	-1	-1	0
	<i>(C-A)/C (%)</i>	1	0			
	(B) $1 \times 10^{-5}$	0.69	0.70	-1	0	0
	<i>(B-A)/B (%)</i>	0	1			
	(C) $1 \times 10^{-6}$	0.70	0.70	-1	-	-
	<i>(C-B)/C (%)</i>	0	0			
Grid20	(A) $1 \times 10^{-4}$	0.58	0.60	-4	-2	2
	<i>(C-A)/C (%)</i>	2	-2			
	(B) $1 \times 10^{-5}$	0.58	0.60	-3	-1	1
	<i>(B-A)/B (%)</i>	1	0			
	(C) $1 \times 10^{-6}$	0.60	0.59	-1	-	-
	<i>(C-B)/C (%)</i>	1	-1			
Grid40	(A) $1 \times 10^{-4}$	0.48	0.51	-6	-5	1
	<i>(C-A)/C (%)</i>	5	-1			
	(B) $1 \times 10^{-5}$	0.50	0.51	-2	-1	1
	<i>(B-A)/B (%)</i>	5	0			
	(C) $4 \times 10^{-6}$	0.51	0.51	0	-	-
	<i>(C-B)/C (%)</i>	1	-1			

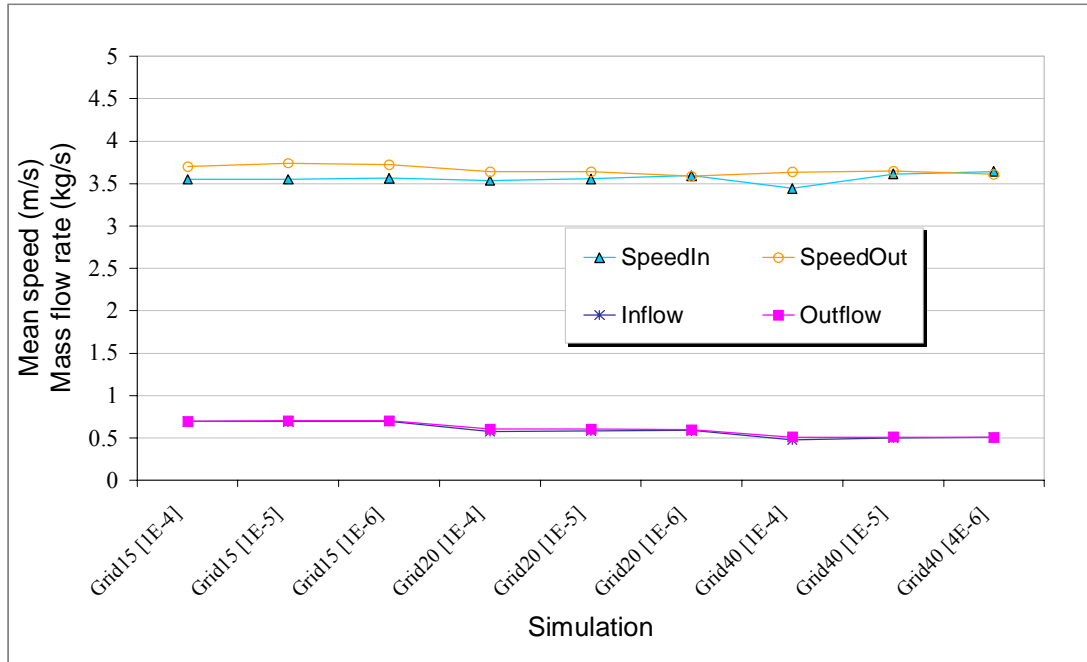


**Figure 6-5 Solution accuracy tests – mean speed & mass flowrate through the lower & higher level openings**

The total number of cells at each opening on the coarse grid (Grid15) and the fine grid (Grid40) are shown in Figure 6-6. The mean speed through each opening was calculated as an area-weighted average velocity through the opening within the CFD code. The mass flowrate was obtained by adding the mass flow of air at each cell through the surface of the lower or the higher opening accordingly.

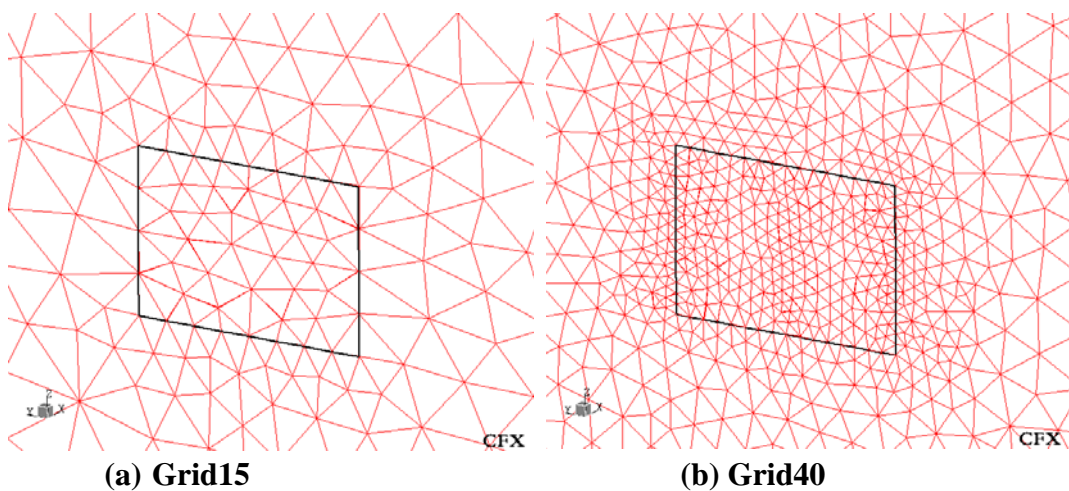


**Figure 6-6 Mesh details at the ventilation opening**

For the continuity equation to be satisfied by the ventilation, the mass flow entering the lower opening should be equal to the flow leaving the building at the higher opening. In terms of the numerical accuracy of the area-weighted average velocity in CFX 5, the finer mesh the more accurate is the mean velocity value. The best agreement of CFD solutions between the lower and higher openings was found on the fine grid (Grid40) at the convergence level C. In this case, there was equal mass flowrate through each opening and 1% difference for the mean speed estimation between the two openings (Table 6-3, p142). Therefore, these solutions were taken as the reference values to compare to the other simulations.

With regard to the mean speed estimation, the solutions obtained by the standard  $k-\varepsilon$  turbulence model on the coarse, medium and fine grid (Grid15, Grid20 and Grid40) at the convergence level A had less than 3%, 3% and 5% differences from the reference values respectively. On Grid20 and Grid40, the difference of the predicted mean speed between convergence level B and C was less than 1%.

At convergence level A, the mass flowrate between the lower and higher openings had the least disagreement on the coarse grid (Grid15). At convergence level B the least difference was shown on the coarse grid (Grid15) and the fine grid (Grid40). At level C, the mass flowrate obtained on Grid15 and the medium grid (Grid20) had 1% difference from the reference values.

Furthermore, in Figure 6-7 on the fine grid (Grid40) the pressure coefficients ( $C_p$ ) produced at different convergence levels, namely level A ( $1 \times 10^{-4}$ ), level B ( $1 \times 10^{-5}$ ) and level C ( $4 \times 10^{-6}$ ), show almost no change on the windward wall and the roof and only a small difference around the higher opening on the leeward wall.

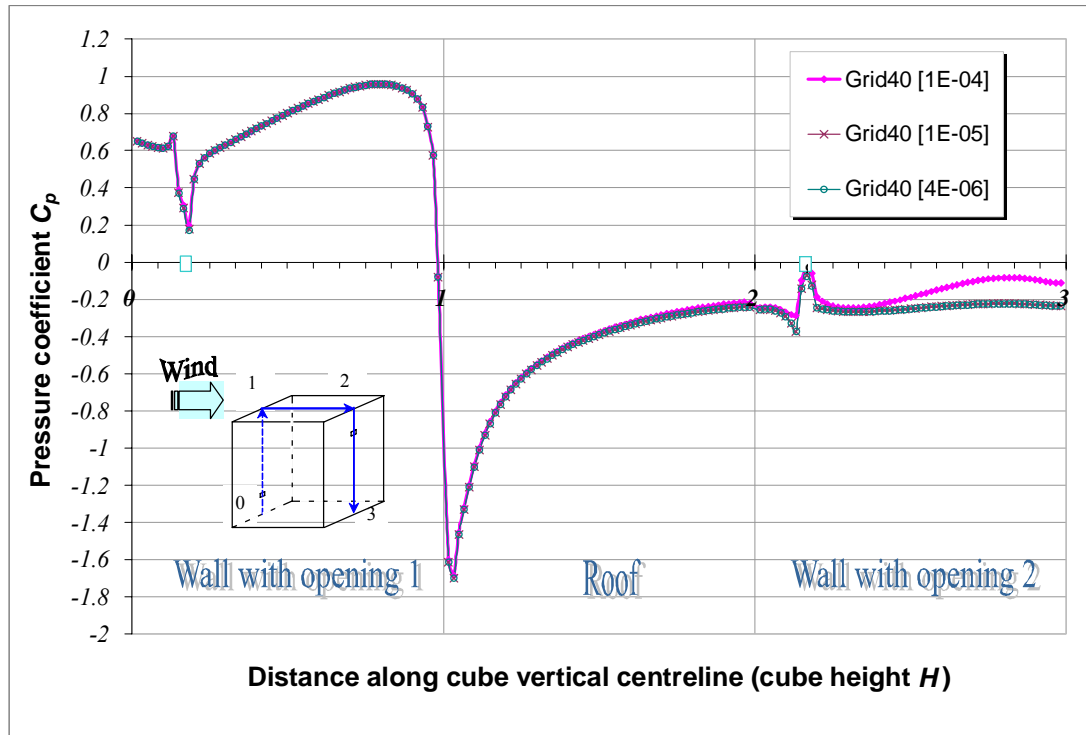


**Figure 6-7 Convergence sensitivity tests – pressure coefficients on the fine grid**

Reaching the convergence level C the pressure distribution on Grid40 showed little difference from the solution at level B. The pressure coefficient  $C_p$  obtained at level A showed less suction on the leeward wall than that at the other two convergence levels. In order to achieve higher convergence level on the fine grid (Grid40), i.e. from level A to B or level B to C, two days more CPU time was needed (see Table 6-2, p141). On the leeward wall,  $C_p$  values obtained at level A on the coarse grid (Grid15) showed closer agreement with the reference value than that on Grid40 (see Figures 6-4 & 6-7).

In summary, the solutions obtained on the fine mesh (Grid40) at the convergence level C ( $4 \times 10^{-6}$ ) were considered as the reference values. In this case, equal mass flowrate through each opening was predicted, and the mean speed through the lower and higher openings had 1% difference.

In terms of the pressure prediction around the opening, i.e. 0.5 m higher and lower from the centre of the opening, only negligible difference was found amongst the three grids (Grid15, Grid20 and Grid 40) and also as that at different convergence levels (level A, B and C). In the case of obtaining the mean flow rate through opening by the integration of velocity components, the solution on Grid40 at convergence level C is required. In other cases concerning only the pressure distribution around the opening, the result on Grid15 at level A has shown to be adequate.

### 6.3.3 Turbulence model effect

Solutions by the RNG  $k-\varepsilon$  turbulence model have also been investigated. The obtained results on the coarse, medium and fine grids had all converged to level A (Table 6-4). Obviously it can be seen in Figure 6-8 that the RNG  $k-\varepsilon$  model predicted higher mean speeds than the standard  $k-\varepsilon$  model. Comparing the results by the RNG  $k-\varepsilon$  model to the same reference case by the standard  $k-\varepsilon$  model in Section 6.3.2, there was about 5% (or 13%) increase of the mean speed through the lower (or higher) opening on Grid20 and Grid40. Less than 5% increase of the mean speed was predicted on Grid15.

As it was not possible to obtain further converged results, all the results acquired by the RNG  $k-\varepsilon$  model were only converged to level A of the order of  $10^{-4}$  (RMS). The mass flow rate through the lower opening was different from the upper openings by 7%, 11% and 8% on Grid15, Grid20 and Grid40 respectively.

**Table 6-4 CFD solutions by different turbulence models**

Tests		Mean speed (m/s)		Difference (In-Out)/In (%)	Mean speed (%)		Turbulence model
		In	Out		In	Out	
Grid40	(C) $4 \times 10^{-6}$	3.64	3.61	1	-	-	Standard <i>k-ε</i>
Grid15	(A) $2 \times 10^{-4}$	3.82	3.74	2	5	3	RNG <i>k-ε</i>
Grid20	(A) $2 \times 10^{-4}$	3.82	4.09	-7	5	13	
Grid40	(A) $6 \times 10^{-4}$	3.83	4.07	-6	5	13	
Tests		Mass flowrate (kg/s)		Difference (In-Out)/In (%)	Mass flowrate (%)		Turbulence model
		In	Out		In-Out		
Grid40	(C) $4 \times 10^{-6}$	0.51	0.51	0	-		Standard <i>k-ε</i>
Grid15	(A) $2 \times 10^{-4}$	0.75	0.71	5	7		RNG <i>k-ε</i>
Grid20	(A) $2 \times 10^{-4}$	0.63	0.68	-9	-11		
Grid40	(A) $6 \times 10^{-4}$	0.53	0.57	-7	-8		

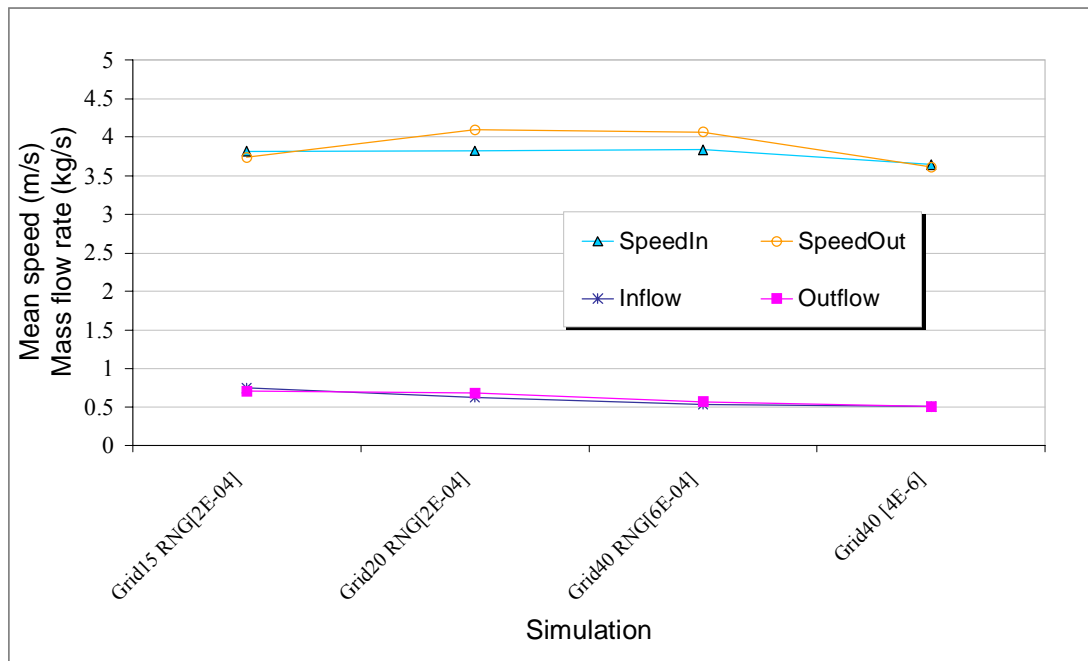


**Figure 6-8 Turbulence model effects – mean speed & mass flowrate through the lower & higher level openings**

On average, applying the RNG  $k-\varepsilon$  model consumed about 1 day more CPU time than the standard  $k-\varepsilon$  model to achieve the convergence level of  $10^{-4}$  (RMS) on the three types of grids.

In Figure 6-9, both turbulence models produced similar pressure distributions on the windward wall. Significant differences occurred on the roof especially near the leading edge, and some discrepancies were shown around the higher opening. This is expected because flow separation off an edge of a bluff body creates a detached shear layer whose character depends strongly on the separation location. Wakes change accordingly in their overall form and general nature [Sharma and Richards 1999; Richards and Hoxey 2002].

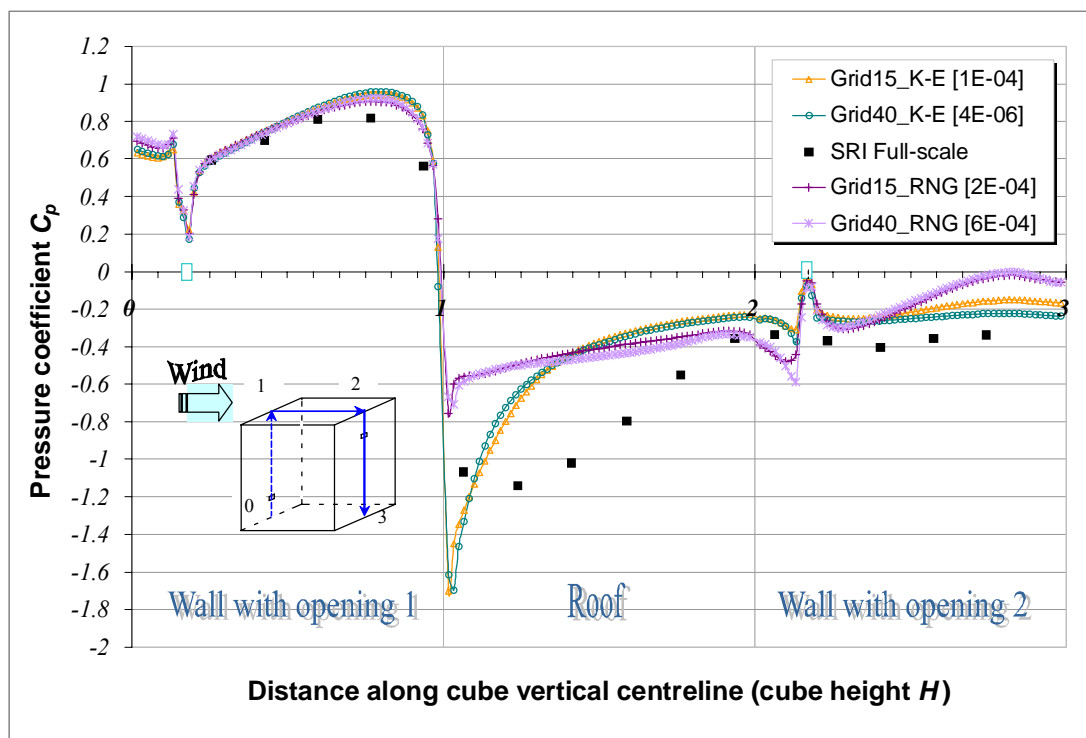
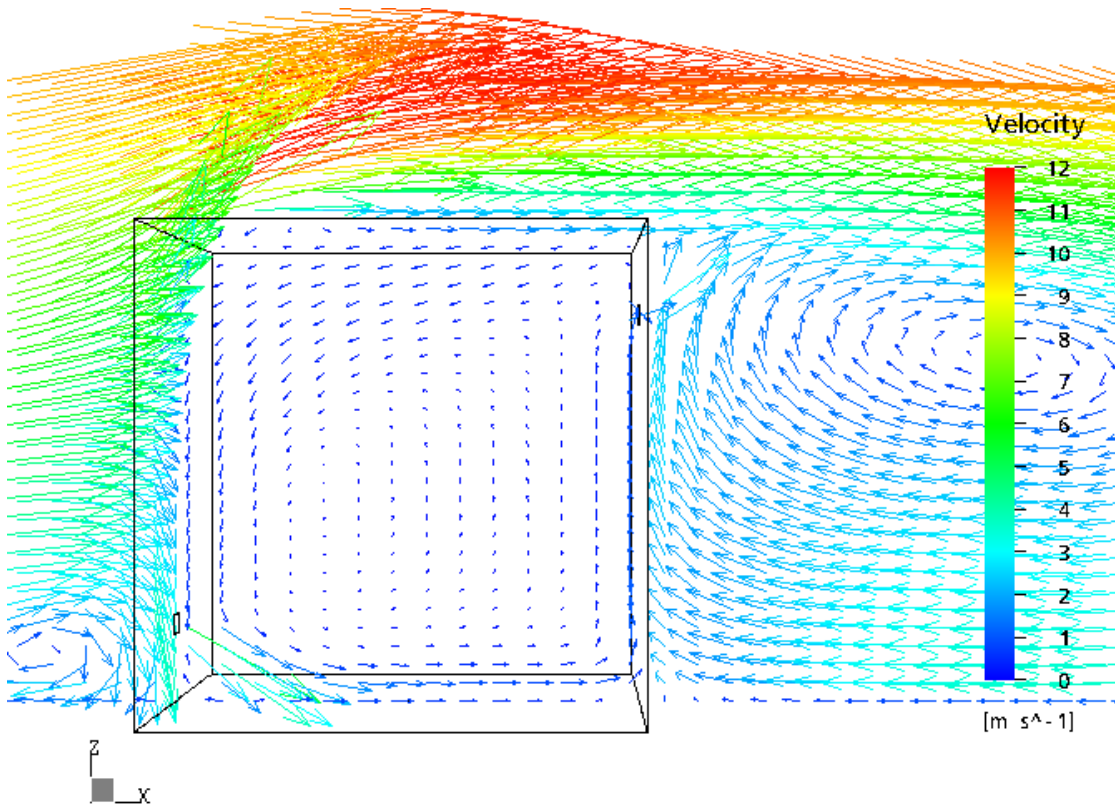


**Figure 6-9 Turbulence model effects - pressure coefficients along vertical centreline**

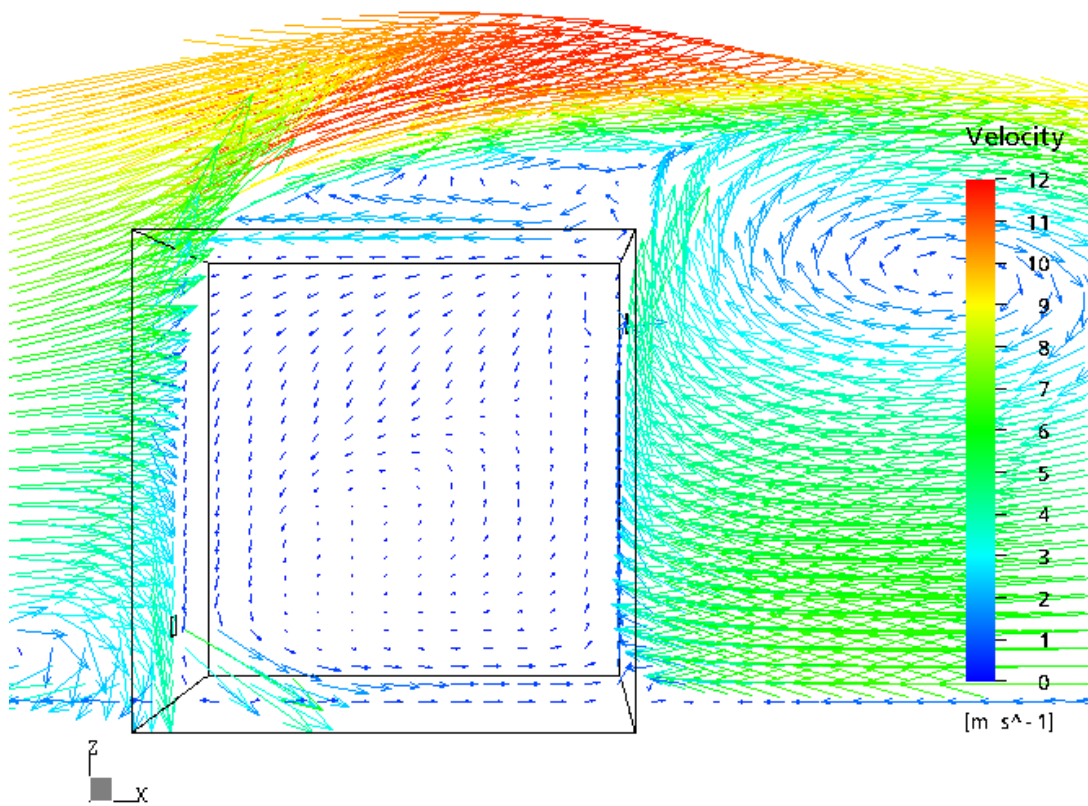
In order to identify the opening effects on the pressure distribution, the full-scale data on the sealed cube from the CWE2000 competition (as SRI Full-scale) were also plotted in Figure 6-9. It can be seen that on the windward wall, the lower opening had local effects only around the opening. On the leeward wall, the RNG  $k-\varepsilon$  model predicted more negative pressure above the opening and more or less the same pressure just below the opening as the standard  $k-\varepsilon$  model. In addition, when the flow is approaching close to the ground the RNG  $k-\varepsilon$  model simulated a lower value of negative pressure field than the standard  $k-\varepsilon$  model. Around each opening, the maximum value of 0.20 and minimum of 0.01 were the  $C_p$  difference between these two turbulence models results.

Figure 6-10 & 6-11, show the flow field patterns around the cube obtained by the standard  $k-\varepsilon$  model and the RNG  $k-\varepsilon$  model. The standard  $k-\varepsilon$  model predicted the flow remaining attached on the roof. In contrast, the RNG  $k-\varepsilon$  model results showed weak roof vortex reattachment at  $0.933H$  (cube height) along the roof. In the wake recirculation region the standard  $k-\varepsilon$  model predicted a bigger wake vortex than the RNG  $k-\varepsilon$  model. Unlike the RNG  $k-\varepsilon$  model results, the centre of the vortex predicted by the standard  $k-\varepsilon$  model was located lower than the high level opening height (5m) and further away from the leeward wall.

The ground level vortex close to the windward wall predicted by the RNG  $k-\varepsilon$  model is slightly bigger in size and faster in velocity than that with the standard  $k-\varepsilon$  model. For both models the indoor velocity vectors produced similar patterns while the RNG  $k-\varepsilon$  model had slightly higher velocities around the interior.



**Figure 6-10** Velocity vector plot around the cube predicted by the standard  $k-\varepsilon$  model



**Figure 6-11** Velocity vector plot around the cube predicted by the RNG  $k-\varepsilon$  model

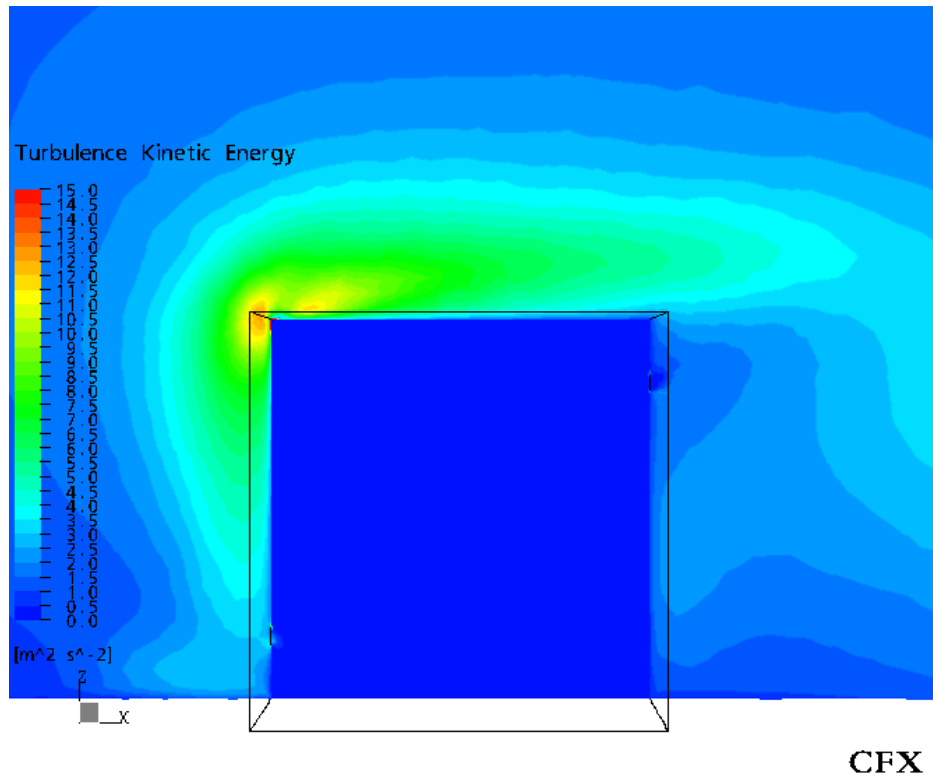


**Figure 6-12** Turbulent kinetic energy distribution around the ventilated cube predicted by the standard  $k-\varepsilon$  model

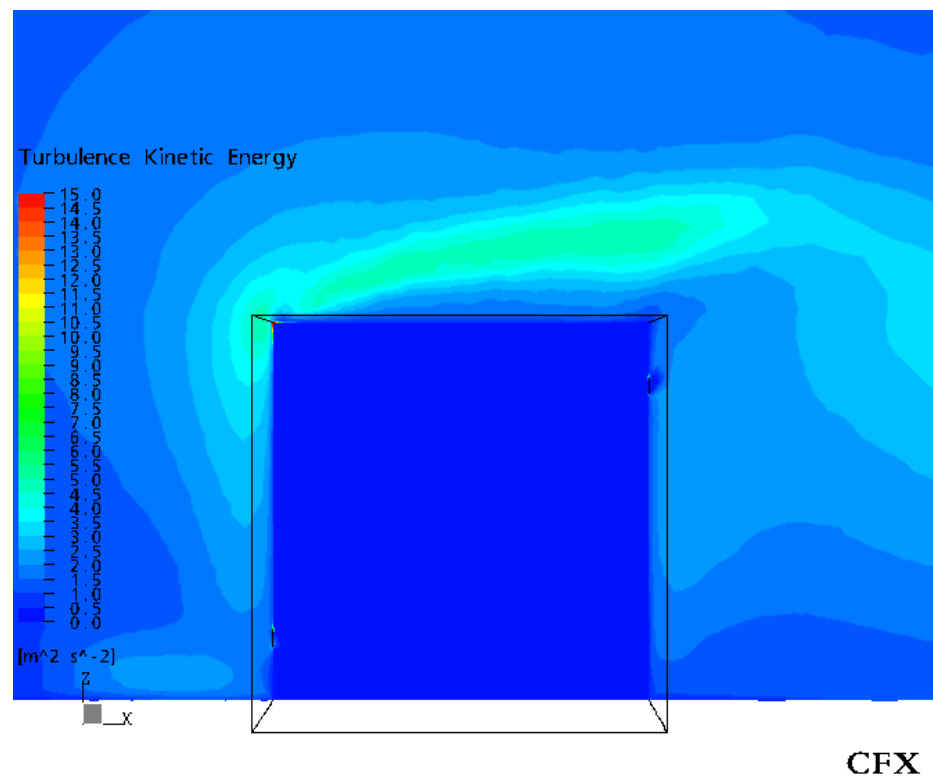


**Figure 6-13** Turbulent kinetic energy distribution around the ventilated cube predicted by the RNG  $k-\varepsilon$  model

It can be seen in Figures 6-12 & 6-13 that at the front corner of the cube the standard  $k-\varepsilon$  model predicted excessive levels of turbulent kinetic energy compared with the RNG  $k-\varepsilon$  model. Consequently, higher eddy viscosity indicates the flow pattern superposed along the roof by the standard  $k-\varepsilon$  model.

The total CPU time for simulation by standard  $k-\varepsilon$  model on the fine grid (Grid40) was 18 hour & 13 minutes (see Table 6-2, p141) to reach  $4 \times 10^{-6}$  (RMS) convergence level on a 1 GHz Pentium III PC with 1GB RAM. To implement RNG  $k-\varepsilon$  model using the same computer, more than 1-day CPU time was needed to reach accuracy level at  $6 \times 10^{-4}$  (RMS).

To sum up, the resulting flow field parameter differences between the two turbulence models were below 7% for the mean speed, 9% for the mass flowrate through openings, and a maximum value of 0.2 for the pressure coefficients difference on the windward and leeward walls. This accuracy level is acceptable in full-scale and wind tunnel experiments.

Hence, the compromise of numerical accuracy and computational time leads to the choice of the standard  $k-\varepsilon$  turbulence model on the fine grid of around 1,450,000 cells (Grid40) with a convergence level of  $1 \times 10^{-4}$  (RMS), for the follow-up parametric studies of wind induced ventilation under various wind directions. In this case, the fine resolution mesh at the opening is needed to obtain the integrated mean flow rate through the opening.

Overall the best agreement with the reference case was found on the coarse grid (Grid15) at the convergence level A ( $1 \times 10^{-4}$ ) with the standard  $k-\varepsilon$  model: i.e.

- (i) the predictions of the mean speed through the lower and higher openings, showed less than 3% difference,
- (ii) the evaluation of the mass flowrate through the two openings had 1% imbalance,
- (iii) the pressure coefficient  $C_p$  at 0.5m from each opening centre had 3% (or 8%) difference at the lower (or higher) opening from the reference case.

Therefore, for the cases where only the surface pressure coefficients are the important and decisive parameters, Grid15 at level A is chosen to perform the CFD simulations.

### **6.3.4 Surface pressure distribution on the ventilated cube**

Pressure distribution contour plots on cube surfaces for four different wind directions, referred as the  $0^\circ$ ,  $180^\circ$ ,  $90^\circ$  and  $45^\circ$  cases, can be found in Figures A-1 to A-8 in Appendix A. Generally speaking, the two ventilation openings only affect the surface pressure distribution locally.

### **6.3.5 Mean airflow pattern inside the cube**

Figures 6-14, 6-15, 6-16 & 6-17 show the velocity vector plots on the cube vertical central plane for wind directions of  $0^\circ$ ,  $180^\circ$ ,  $90^\circ$  and  $45^\circ$ . The heights of the lower and higher openings are above the ground 1 m and 5 m respectively. Therefore, the plan views of the velocity vector plots have been plotted at 1 m and 5 m for these four cases in Figures A-9 to A-16 in Appendix A.

Although the reference wind speed at the cube height (6m) was 10 m/s, the indoor velocity could be maintained under 1.5 m/s at 1m and 5m height above the ground. Outdoor airflow was only introduced near the lower opening for  $0^\circ$ ,  $45^\circ$  and  $90^\circ$  cases. At the 1m height comfort zone level,  $180^\circ$  and  $45^\circ$  cases had relatively higher

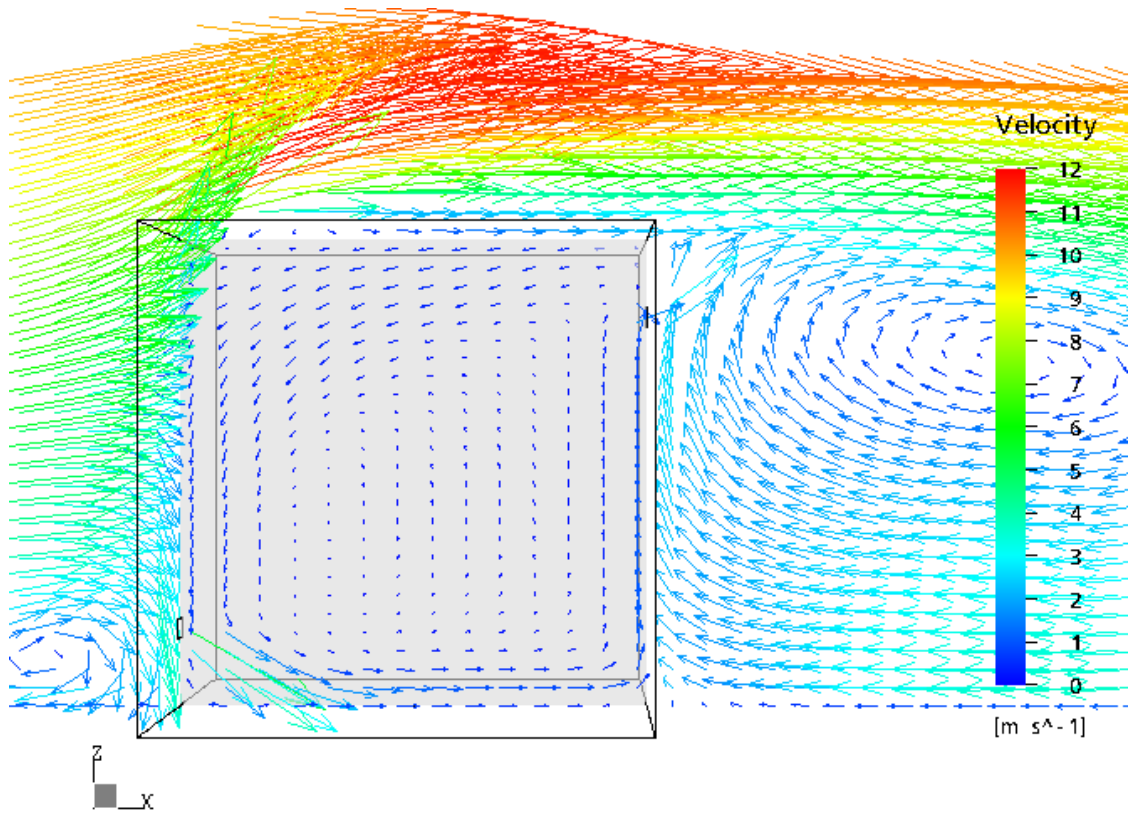


Figure 6-14 Velocity vector plot around the cube [0° case]

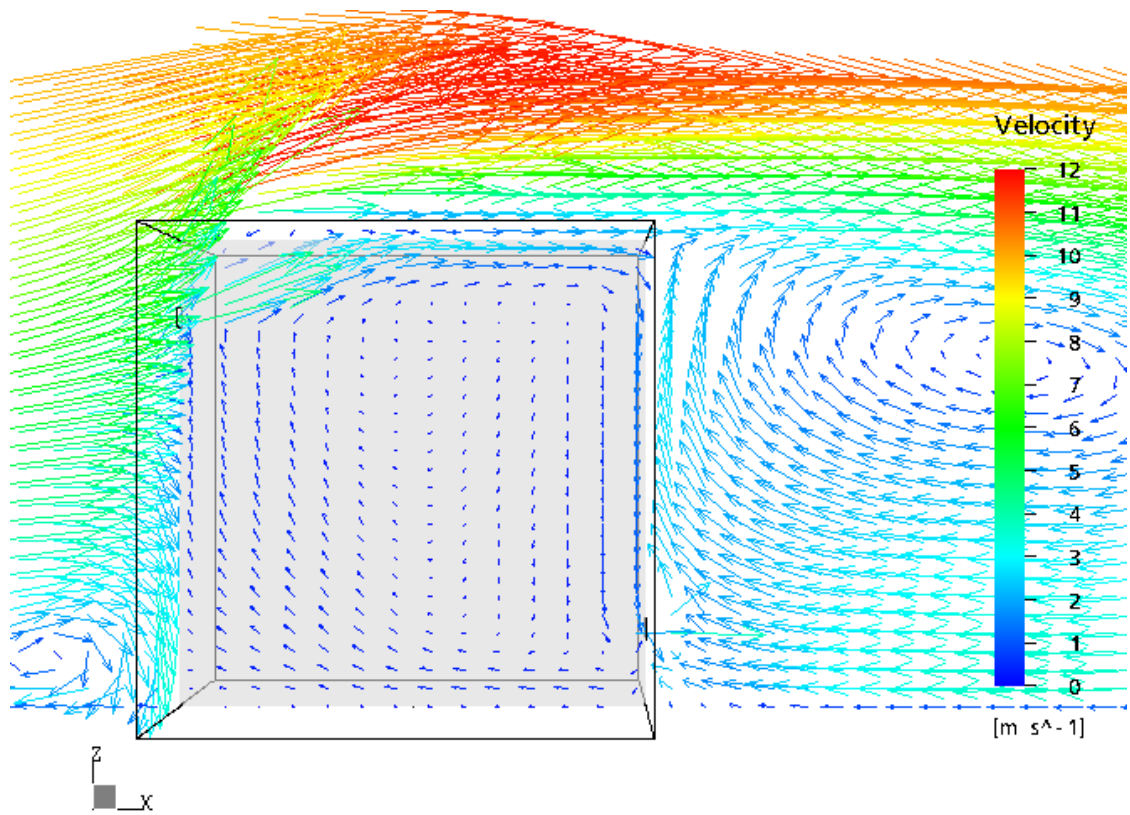


Figure 6-15 Velocity vector plot around the cube [180° case]

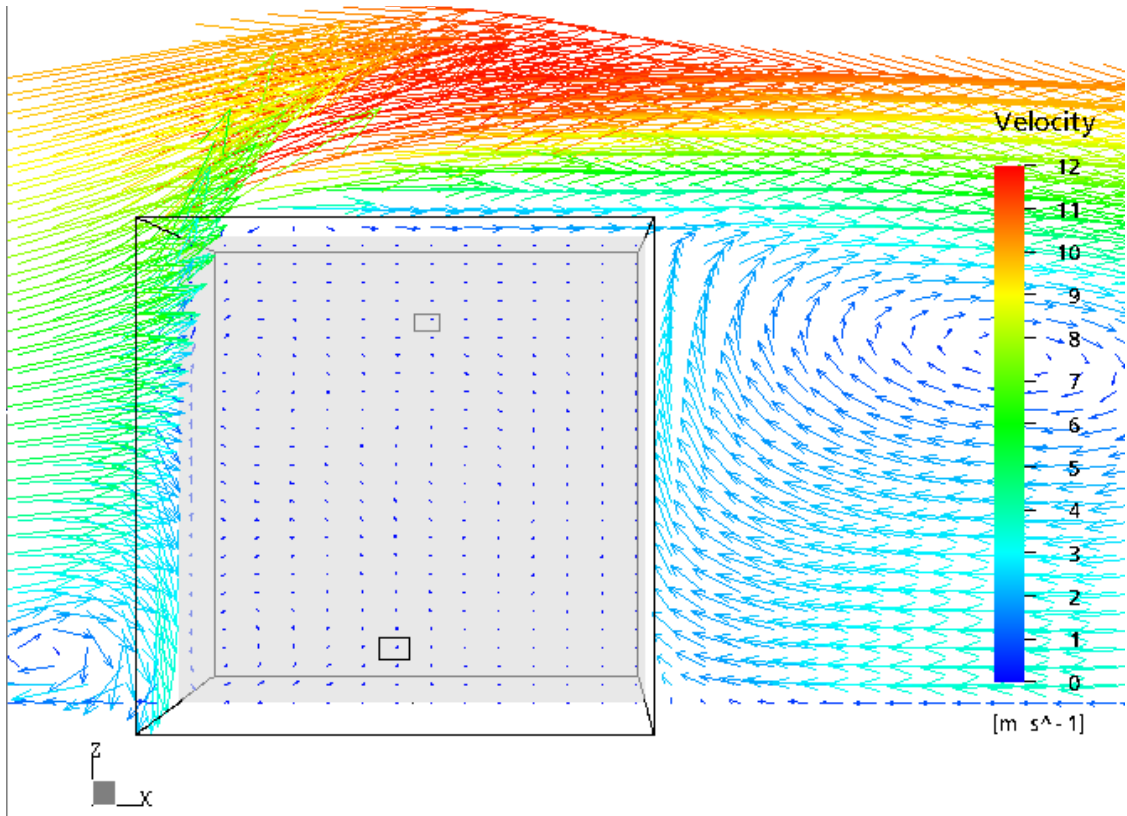


Figure 6-16 Velocity vector plot around the cube [90° case]

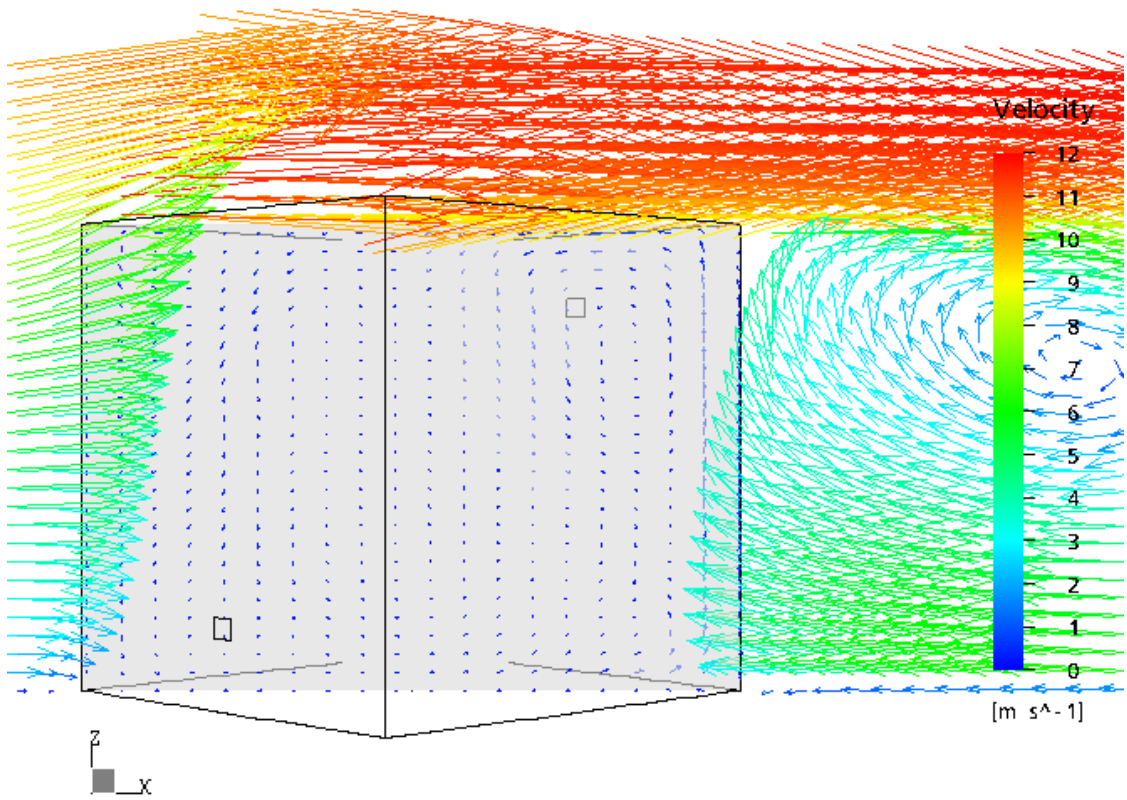


Figure 6-17 Velocity vector plot around the cube [45° case]

speed and better mixing than the 0° and the 90° cases. Particularly for the 90° case, the majority indoor area had slow air movement of about 0.2 m/s.

### 6.3.6 CFD predictions of wind induced ventilation rates

To calculate the ventilation rates from the CFD simulation results, the following methods have been used:

- (i) extract the mean pressure coefficient difference between the two openings at the locations 0.5m away from the opening centre, then apply pseudo steady model (Eqn.3.29) to obtain the non-dimensional ventilation rate,

$$Q\{dC_p\} = C_d A U_{ref} \sqrt{\frac{dC_p}{2}} = C_d A U_{ref} \sqrt{\frac{|C_p(in) - C_p(out)|}{2}} \quad (\text{Eqn.3.29, p67})$$

where  $A=0.35 \times 0.25=0.0875 \text{ m}^2$  and  $U_{ref}=10 \text{ m/s}$ .

- (ii) integrate the velocities over all cells in the plane of the inlet and outlet openings in CFX5.

Table 6-5 lists the calculated ventilation rates for wind directions of 0°, 45°, 90° and 180°. The results of Method (i) shows that the non-dimensional mean ventilation rates decreases with the wind incident angles from 0° to 90° and increases when wind blows into the cube from the upper opening at 180°. Because the incoming mean air speed has larger value at higher level opening than at low level opening, the resulting ventilation rate at 180° is higher than at 0° wind direction. Method (ii) shows the same trend of calculated mean speeds at the openings as Method (i). The percentage of the relative difference (%) is compared with Method (i) in Table 6-5. When wind

blows parallel to the openings, i.e. 90° case, the absolute value of the flow rate is small, therefore large % difference was found between method (i) and method (ii).

**Table 6-5 Wind induced nondimensional mean ventilation rates in CFX5**

Wind direction	Method (i)				Method (ii)			
	$C_d$	$C_p(in)$	$C_p(out)$	$\frac{Q\{dC_p\}}{(A*U_{ref})}$	$\frac{U(in)}{U_{ref}}$	% Diff. from (i)	$\frac{U(out)}{U_{ref}}$	% Diff. from (i)
0°	0.6	0.60	-0.27	<b>0.39</b>	0.36	-8	0.36	-8
45°	0.6	0.28	-0.23	<b>0.30</b>	0.27	-12	0.26	-13
90°	0.6	-0.31	-0.46	<b>0.16</b>	0.12	-27	0.14	-12
180°	0.6	0.92	-0.25	<b>0.46</b>	0.44	-4	0.44	-4

The possible contributions of the discrepancy between the inflow and outflow at 45° and 90° are as follow:

- (1) RANS model cannot capture the unsteadiness caused by the wind at the directions of 45° and 90°, which is where the fluctuating components play a more dominant role than the mean velocity components at the openings.
- (2) The achievable convergence level for 45° and 90° cases was  $10^{-4}$  (RMS). The relative error on the velocity components through the opening cells can be expected as big as 0.5% if the normalised residual is  $10^{-4}$  (RMS) or 0.01% for the convergence level of  $10^{-6}$  (RMS).
- (3) In CFX5.5.1 the 2D locator to extract the velocity data is placed manually according to the opening coordinates. The global geometry tolerance of the computational model was set as 0.002 m. The possible error of the area due to slight dislocating will introduce the error of the opening placement as 0.09%.
- (4) Therefore the error of the velocity integration method (2)\*(3) is 0.5%.
- (5) The area-weighted average function calculates the mean cancelling out the flow from opposite directions, i.e. reverse flow.

Higher convergence levels and more sophisticated turbulence models could reduce this difference; however for the time being it is not a practical solution in terms of computational power and time in the parametric studies or practiced in building design industry.

### **6.3.7 CFD predictions of wind and thermal effects**

This section presents the numerical trial results for the indoor distribution of air temperature and velocity under combined wind and thermal effects.

#### **6.3.7.1 Geometry set-up for coupled external and internal flows**

Unlike the structured code CFX4, the thermal effect facility in CFX5 was still under ongoing development, no FORTRAN user subroutine could be easily added to enhance the CFX5 code for specific application [AEA Technology 2001b; Morvan 2002; Wright 2002]. Therefore, attempts to build up the computational models including a heat source inside the cube had failed using CFX5.5.1.

It was not possible to create a heat source as a subdomain inside another existing subdomain, the cube. To overcome this geometry set-up problem, the following cases have been investigated alternatively, i.e. creating a collection of subdomains within the whole computational domain to form the interior of the cube.

Figure 6-18 shows the close-up view of the cube containing four subdomains as four walls, one subdomain as the roof and two small subdomains as the two openings.

The heat source was defined as a patch (0.6 m × 0.6 m) at the centre of the floor with heat generation. The resulting temperature pattern for this case is shown in Figure 6-19.

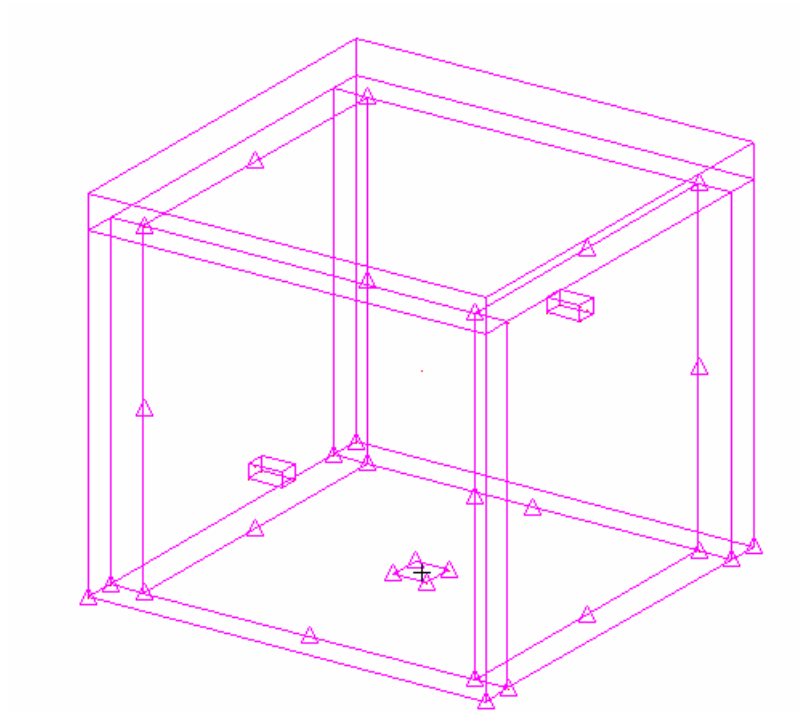
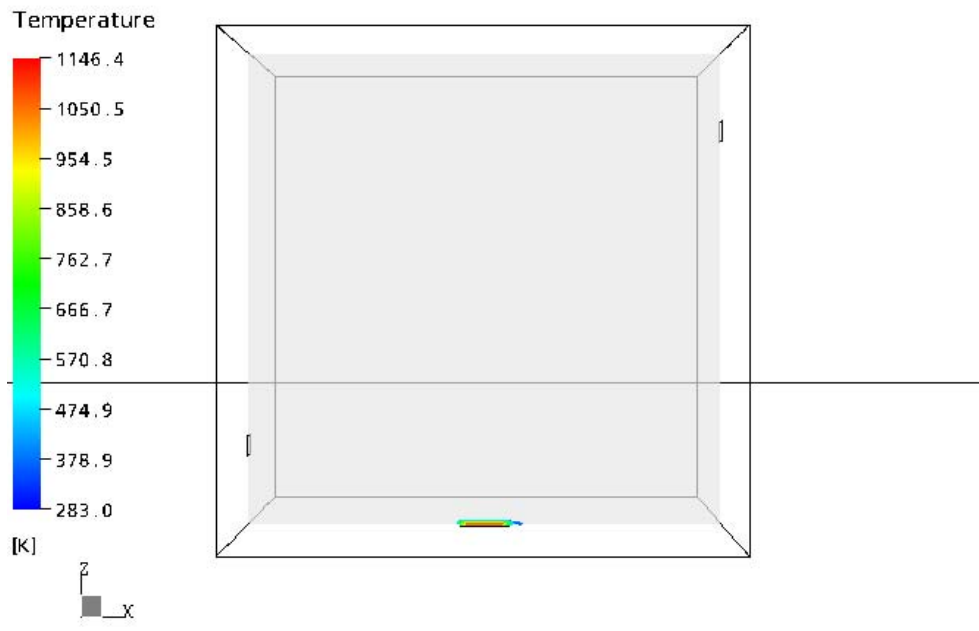


**Figure 6-18 Geometry set-up1 (cube with a heating patch at floor level)**

Extremely high temperature appeared just above the heat source whether it was defined as a hot surface with a specified temperature or with a heat flux. The CFD prediction was unrealistic.

Another type of geometry was also tested as shown in Figure 6-20. The potential heat source was defined as a small box located above the centre of the floor. The CFD run has included thermal simulation but only wind speed at domain inlet was defined, no heat or momentum sources were specified at the inner 0.6 m box.

Unexpected leakages were found around the cube edges despite several smaller global model tolerance values than the default one (0.005 m) being selected from 0.004 m, 0.002 m down to 0.001 m. Consequently, the simulation diverged after several iterations.



CFX

**Figure 6-19 Temperature contour plot on centre plane (cube with a heating patch at floor level)**

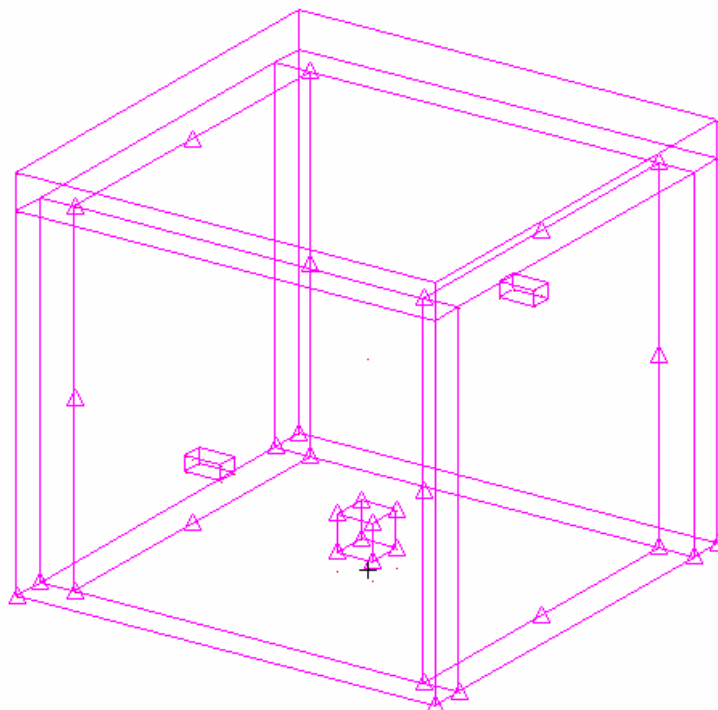


**Figure 6-20 Geometry set-up2 (cube with a 0.6m cubic box above the floor)**

From the above experience, the following simulations were conducted to simulate the combined wind and forced or natural convection effects, in which the heat source has to be introduced as another inlet boundary condition from the location of the heater. The combined wind and thermal influence on the ventilation rate and indoor flow pattern is given in the following section.

### **6.3.7.2 Combined wind and forced (or natural) convection scenario**

To predict the scenario of winter conditions, a heater was placed inside the CFD model cube. The reference wind speed was taken as 4 m/s, which is the annual mean wind speed in the UK [BSI 1991]. Assuming that the outdoor temperature was 5°C, the heating power selected for the heater to provide indoor thermal comfort was 8.6kW. It had dimensions of 0.3 m × 1.2 m × 0.6 m with a hot air volume flow rate of 0.36 m<sup>3</sup>/s at 25°C. Because of the subdomain set-up problem stated in section 6.3.7.1, the hot air flow from the heater could only be defined as a second inlet boundary condition (BC) to the computational domain along with the first inlet BC of ABL wind profile.

Initially, the heater was placed in the centre of the cube. Figure 6-21 shows the hot air plume generated above the heater, reaching the roof level before circulating downwards. As the hot air generated convection force was stronger than the wind driven flow, air exited through both the lower opening and the higher opening.

The temperature distribution pattern in the indoor space is shown in Figure 6-22. It is evenly distribution at lower level but there is a clear stratification above the heater level. In the 0 ~ 1.8m comfort zone the air temperature rose 3 ~ 4°C above the outdoor air.

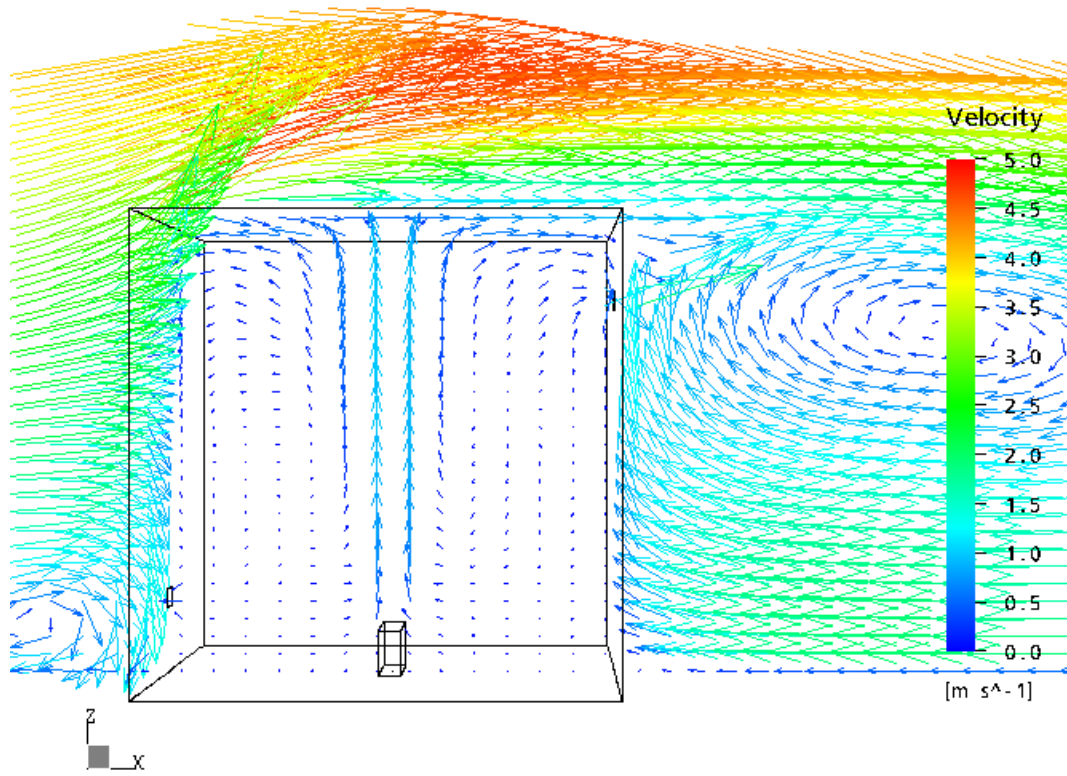


Figure 6-21 Velocity vector plot in the cube with a centre heater

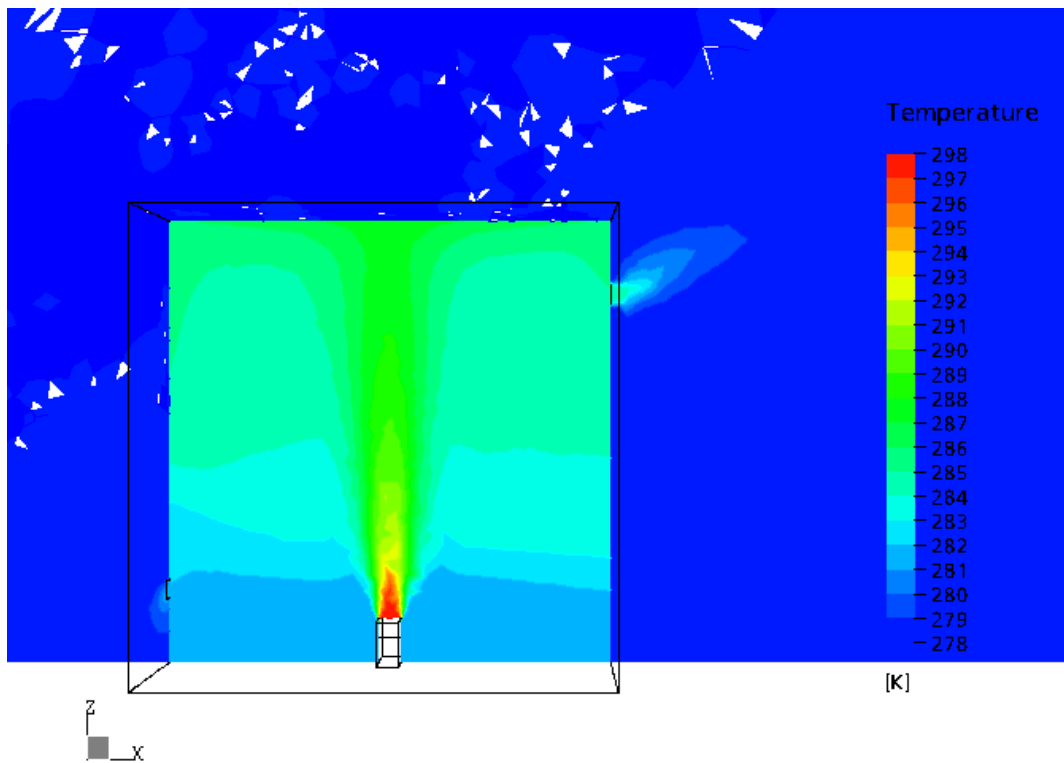
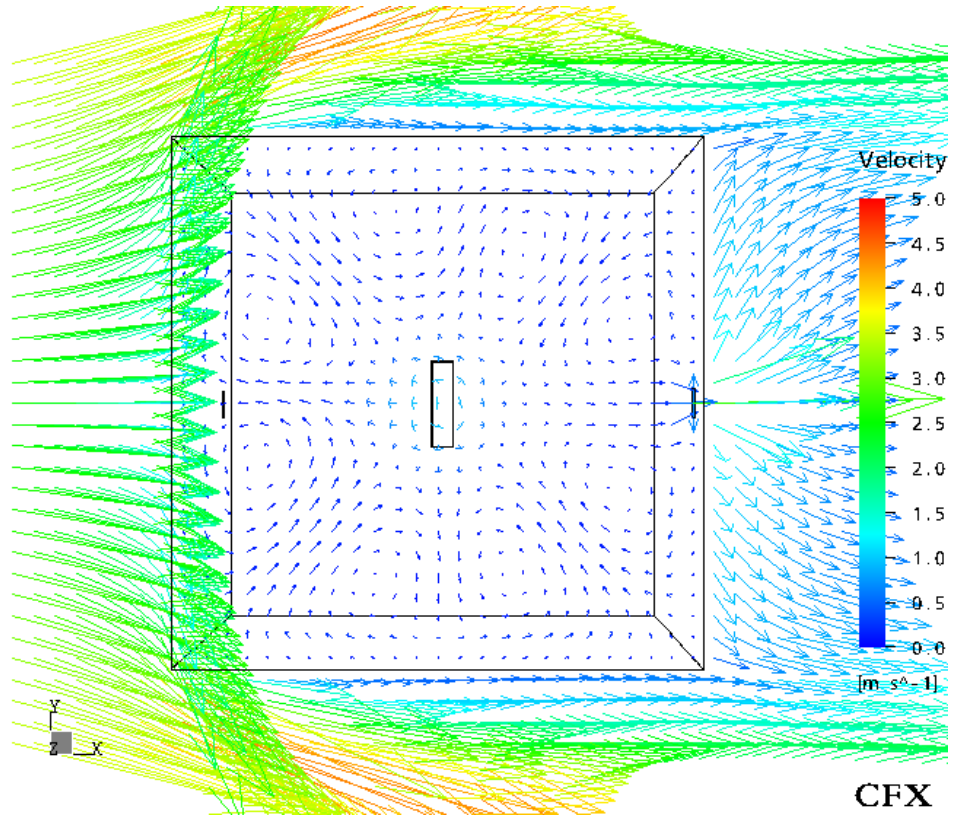
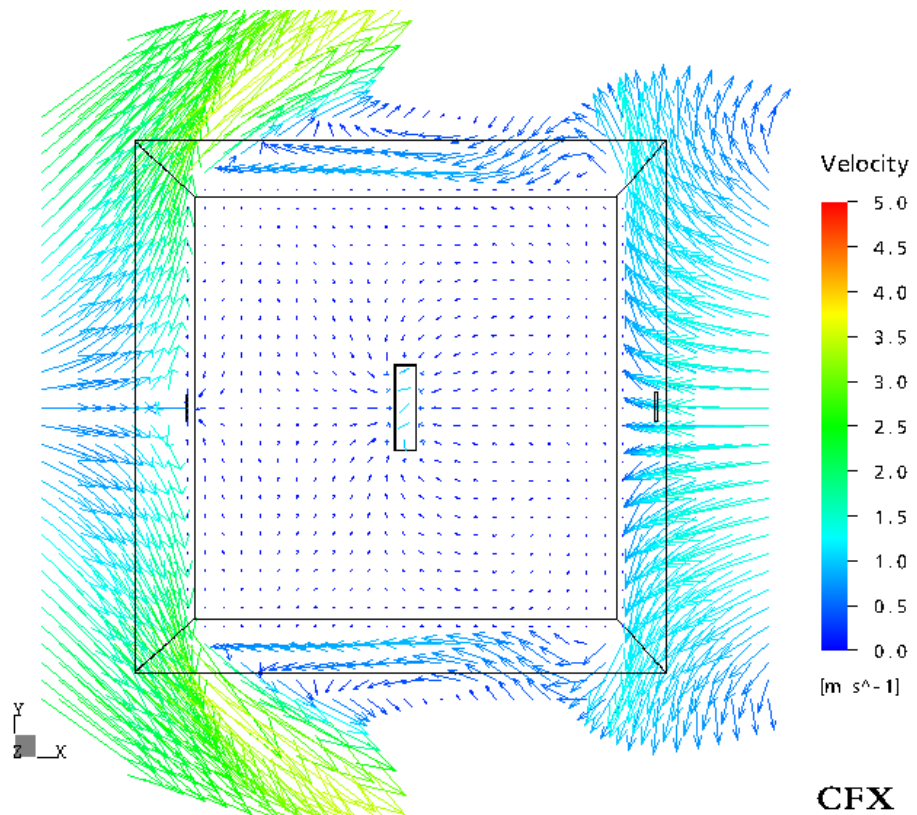


Figure 6-22 Temperature stratification in the cube with a centre heater



**Figure 6-23 Velocity vector plot above the ground 5m in the cube with a centre heater**



**Figure 6-24 Velocity vector plot above the ground 1m in the cube with a centre heater**

Meanwhile, the heat source generated eight secondary horizontal recirculation zones at 5 m height, resulting in good indoor air mixing (Fig.6-23). There was no localised draughty region at 1 m level (Fig.6-24).

Another investigation (Figures 6-25 & 6-26) in which the same heater was placed near the lower opening, showed a temperature increases of about  $6^{\circ} \sim 7^{\circ} \text{C}$  within the 1.8m height comfort zone. The temperature stratification is not as even as the previous centre heater case. The hot plume rises along the wall above the heater and encourages air circulation in the upper region of the building. Figure 6-27 shows that horizontally there are only two vortices formed at the upper opening region compared with eight for the previous case and slight air movement at the lower opening level is shown in Figure 6-28.

The indoor temperature distribution with the centre and side placed heater are compared in Figures 6-29 & 6-31. In order to predict the natural convection scenario, only a hot surface was defined at the top of the heater places in another two simulations. The resulting indoor temperature distributions are shown in Figures 6-30 & 6-32. The temperature contour plots are located at the vertical planes of -2.5, -1.5, -0.5, 0.5, 1.5 & 2.5 m from the centre plane for these cases. In general these distributions show good symmetry as expected.

The calculated non-dimensional ventilation rates using Eqn.3.33 for above cases are listed in Table 6-6. The temperature differences were calculated from the difference between the mean temperature of the outgoing flow at the higher level opening and the ambient temperature.

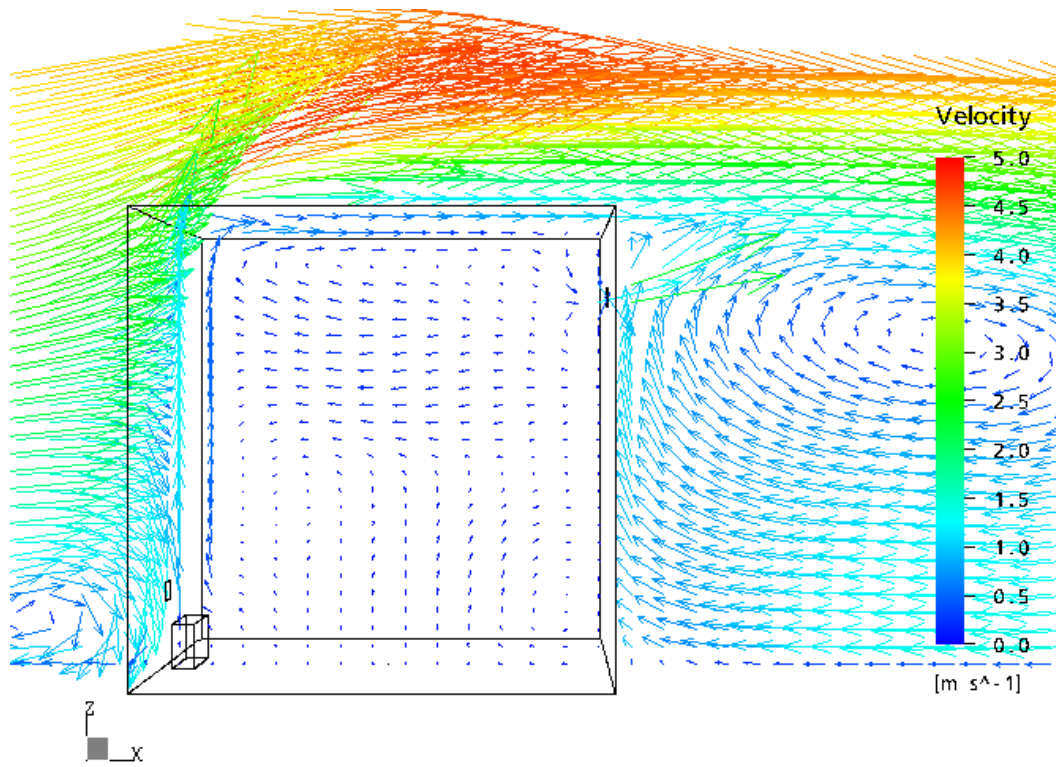


Figure 6-25 Velocity vector plot in the cube with a side heater

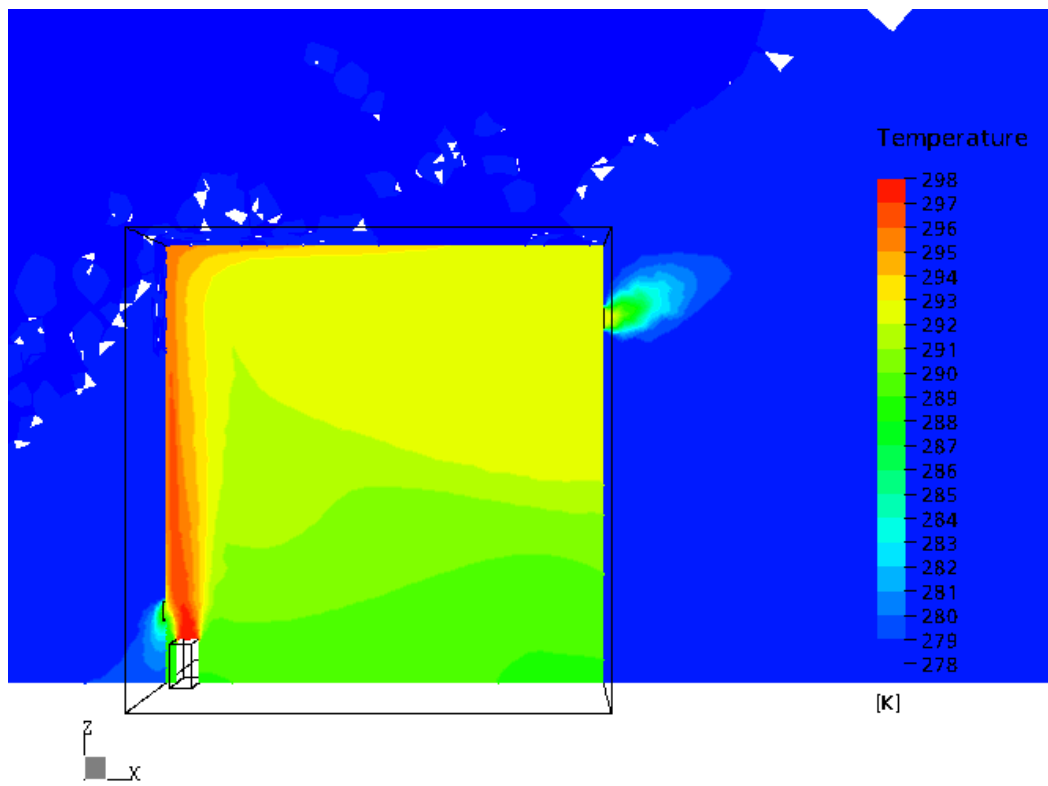


Figure 6-26 Temperature stratification in the cube with a side heater

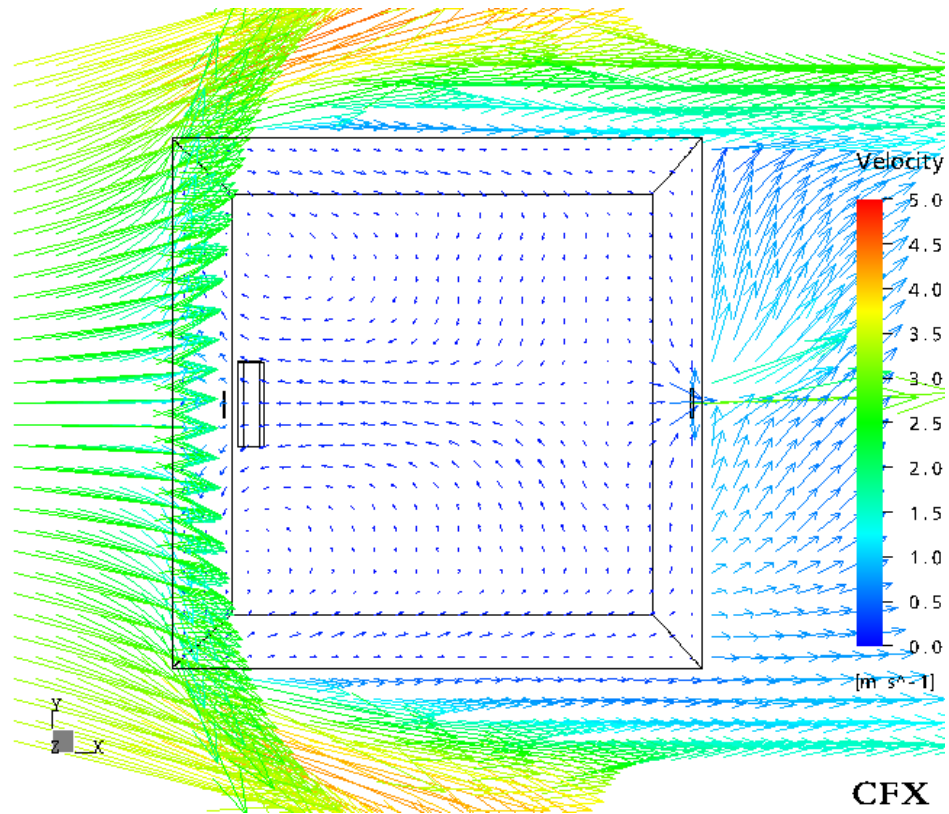


Figure 6-27 Velocity vector plot above the ground 5m in the cube with a side heater

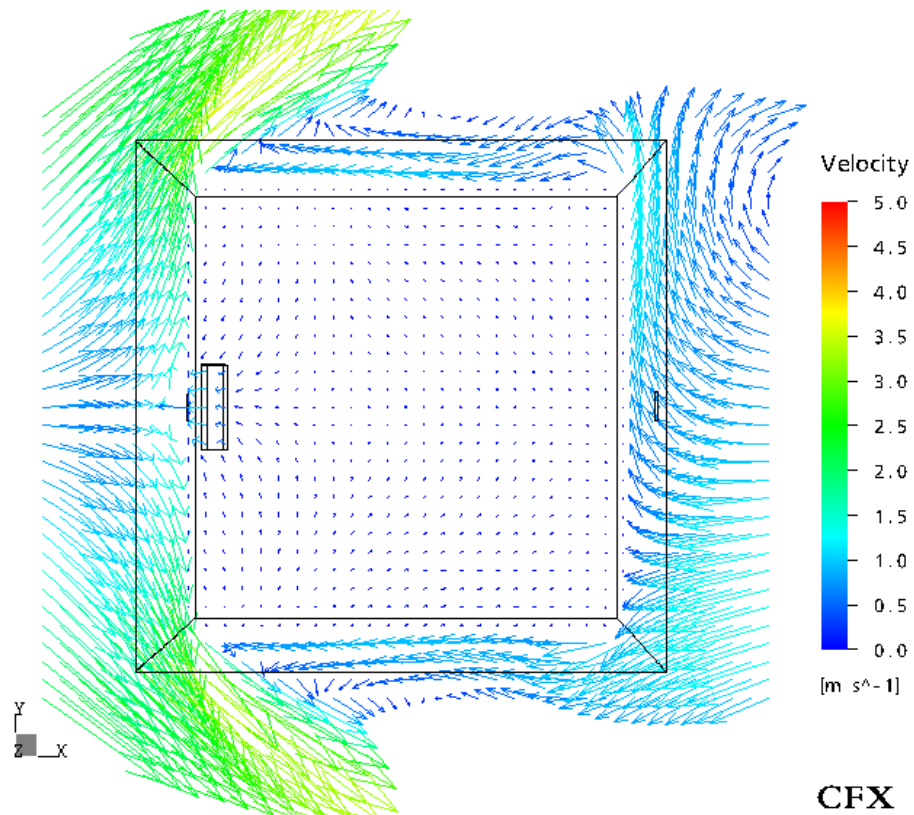


Figure 6-28 Velocity vector plot above the ground 1m in the cube with a side heater

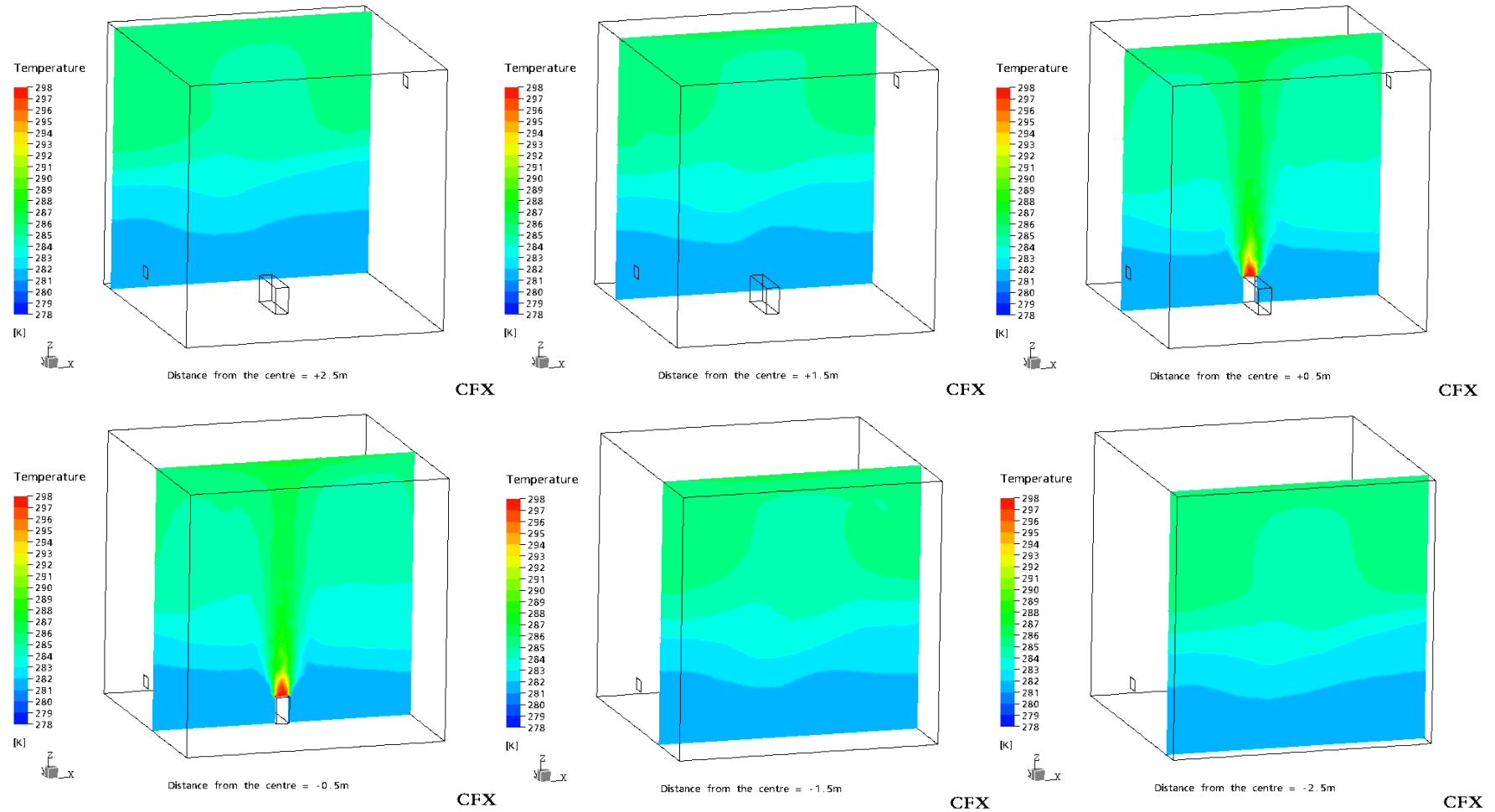
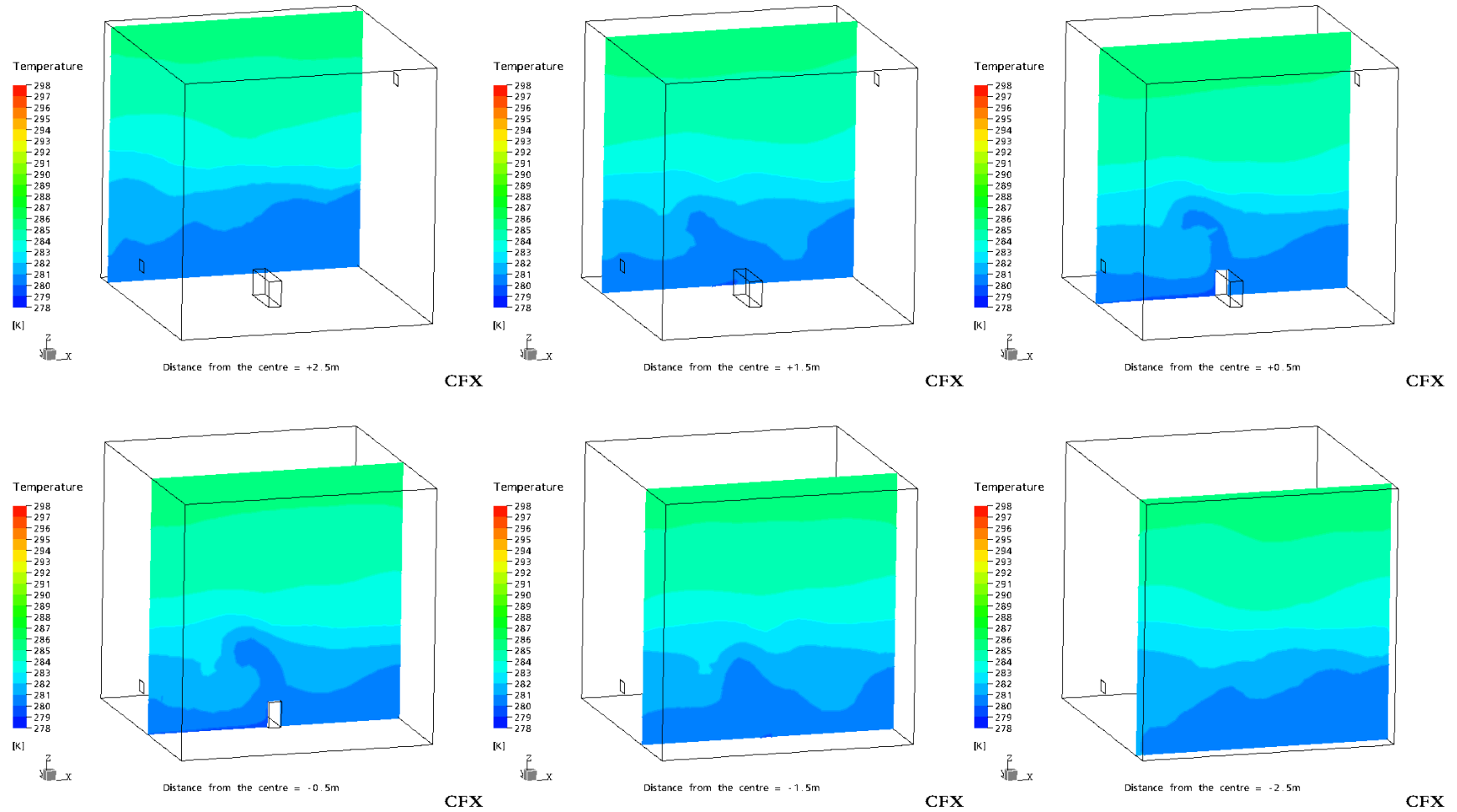


Figure 6-29 Temperature contour plots in the cube with a centre heater ( $y=-2.5,-1.5,-0.5,0.5,1.5$  &  $2.5$ m)



**Figure 6-30 Temperature contour plots in the cube with a centre located hot surface ( $y=-2.5,-1.5,-0.5,0.5,1.5\&2.5m$ )**

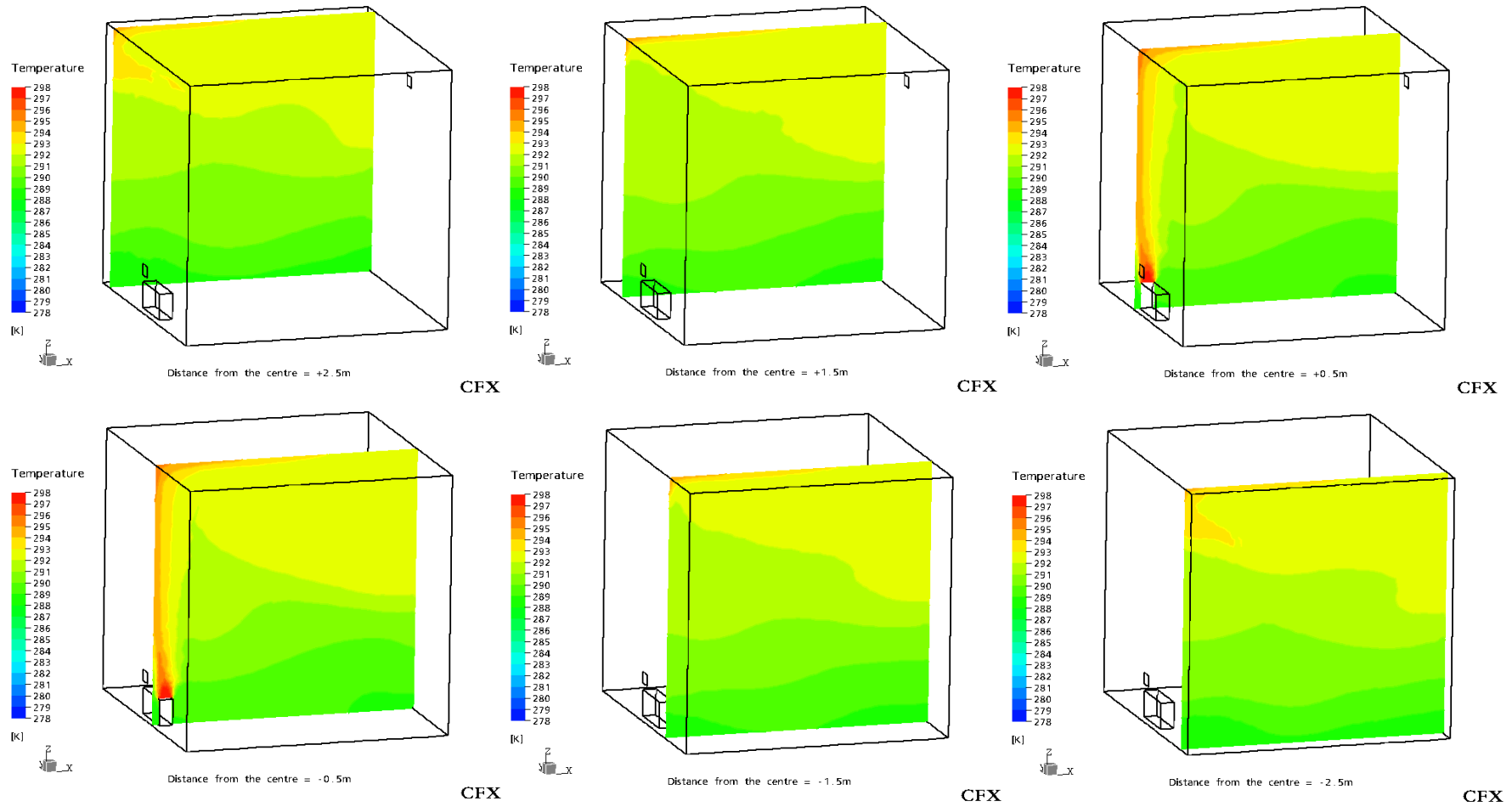


Figure 6-31 Temperature contour plots in the cube with a side heater ( $y=-2.5,-1.5,-0.5,0.5,1.5\&2.5m$ )

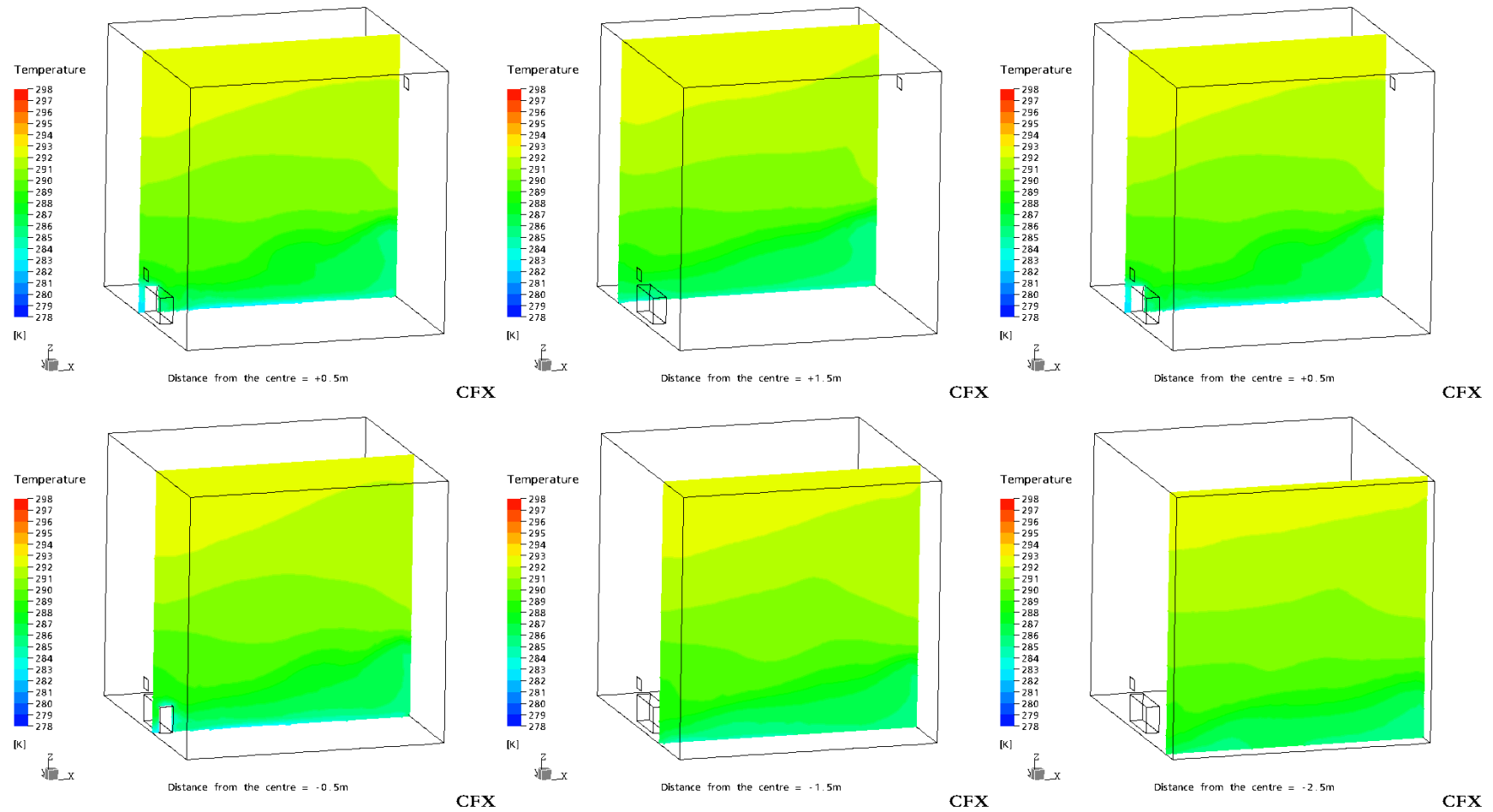


Figure 6-32 Temperature contour plots in the cube with a side located hot surface ( $y=-2.5,-1.5,-0.5,0.5,1.5$  &  $2.5$ m)

$$Q\{dC_p + dT\} = C_d A U_{ref} \sqrt{\frac{|C_p(in) - C_p(out)|}{2} + \frac{dT}{T(out)} \frac{gh}{U_{ref}^2}} \quad (\text{Eqn. 3.33, p68})$$

where  $A=0.35 \times 0.25=0.0875 \text{ m}^2$ ,  $U_{ref}=4 \text{ m/s}$  and  $C_d=0.6$ .

**Table 6-6 Mean ventilation rates introduced by combined wind and forced (or natural) convection [0° case]**

Cases	(i) Centre heater	(ii) Centre hot surface	(iii) Lower opening side heater	(iv) Lower opening side hot surface
$dT$ (°C)	6.8	5.1	14.5	12.0
$\frac{Q\{dC_p+dT\}}{A*(U_{ref}+U_b)}$	0.43	0.34	0.41	0.33

In Table 6-6 with the same amount of hot air input in the forced convection cases (i) & (iii), the centre located heater generated about 4% higher ventilation than the side placed heater. Wind effect was more dominant 93%(or 91%) than thermal effect in case (i) (or case (iii)). Better indoor air mixing and more levelled stratification could be achieved using the centre heater case (i). On the other hand, case (iii) increased the indoor temperature about 7°C higher than case (i).

In comparison of the forced convection case (i) (Figure 6-29) with the corresponding natural convection case (ii) (Figure 6-30), better air mixing occurred in case (i) than case (ii) within 1.8m above the ground. For the side placed heat source cases (ii) & (iv), the difference of temperature stratification occurred near the roof region (Figure 6-31 & 6-32).

Although the driving thermal forces were the same in above cases, the predicted overall ventilation rates in the forced convection cases (i & iii) were about 20% more

than the natural convection cases (ii & iv), but detailed indoor flow and temperature distribution patterns differed from one to another.

### **6.3.7.3 Possible improvement in the CFX5 software**

From above experiments for simulation of combined wind and buoyancy effects in CFX5, the following improvement in the software can be suggested:

- (1) Enable to define internal momentum and/or heat sources as subdomains within any other subdomains.
- (2) Predefine the user interested 2D surface within pre-processor to increase the accuracy for output data.
- (3) Extend the User FORTRAN functions and include the example of CFX expression language (CEL) function of defining the thermal wall boundary condition of the combination of heat flux and temperature.
- (4) Enable to visualise boundary condition profiles in pre-processor.
- (5) Enable to choose a default view of z-direction align vertically in post-processor and easily to select views of buildings.

Following up the feedback on possible improvements provided to CFX technical support team, the latest version CFX5.7 is able to solve buoyancy related problems effectively and the geometry generation tool has improved to handle source definition easily, etc. [Sinai 2004].

## 6.4 Summary and Discussion

CFD simulations have been used to investigate the mean ventilation flow rates through the cube structure by wind effect alone and combined wind and forced/natural convection effects.

The performance of CFD predictions of flow around a surface mounted cube based on the standard and RNG  $k-\varepsilon$  turbulence models has been investigated. Other attempts with more complicated models i.e. RSM and SST turbulence models, were not successful because of the limitation of computer power.

To minimise the inaccuracies of the CFD solutions associated with the spatial discretisation errors, and convergence (iteration errors and precision errors) in all of the solutions, three mesh densities of grid have been investigated, namely the coarse (Grid15), medium (Grid20) and fine grid (Grid40).

Using the standard  $k-\varepsilon$  model on a 1GHz Pentium III PC with 1Gb RAM, the total CPU time used on the fine grid (Grid40) at the convergence level of the root-mean-square residual of  $4 \times 10^{-6}$  was 4days 3minutes and 7hours 20minutes on the coarse grid (Grid15) at the level of  $1 \times 10^{-4}$ (RMS) respectively. Applying the RNG  $k-\varepsilon$  model to achieve the level of  $2 \times 10^{-4}$ (RMS) consumed at least 1 day more CPU time than the standard model.

The differences of flow field variables from the grid and turbulence model sensitivity tests were all below 10%. It is common to accept a tolerance of  $\pm 10\%$  error band in full-scale and wind tunnel measurements. Therefore, a compromise of the accuracy and the computational cost was made to investigate more scenarios under various

wind directions on the fine grid at the convergence level of  $1 \times 10^{-4}$  (RMS) with the standard  $k-\varepsilon$  model.

The CFD assessments utilising the pressure difference between the two openings showed that the mean ventilation rates decreased when the wind direction changed from  $0^\circ$ ,  $45^\circ$  to  $90^\circ$ . At  $180^\circ$  the ventilation rate was larger than the value at  $0^\circ$  because of the higher speed of incoming flow from the higher opening.

Ventilation rate results predicted by integrating velocities through each opening are more sensitive than the pressure coefficients to the convergence level and normally demands much more computing time to reach a higher level of convergence.

Therefore velocities are less reliable results than the pressure coefficients obtained in CFD simulations for calculating ventilation rates. Also the method of placing the locator manually to extract the output flowfield data within the CFX5.5.1 software can introduce errors into the integration of results.

To sum up, the mean pressure difference results should be chosen for obtaining the mean ventilation rate in CFD simulations (for CFX5.5.1 package only). The velocity and temperature patterns in CFD can be used to visualise the details of indoor and outdoor flow distributions and treated as guidance for placing probes in field measurements. In the following chapter, the CFD predictions are to be validated by field measurements.

# **Chapter 7    Field Study of Ventilation Rates in the 6m Cube**

## 7.1 Introduction

As discussed in Chapter 4, one method of validating CFD simulations is full-scale measurements. In this chapter the building and measurement techniques used in the current full-scale investigations are introduced. The accuracy levels of different measurement methods are also discussed.

## 7.2 Description of the Cube Structure

The building studied is the full-scale 6m cube positioned on an open field site at the Silsoe Research Institute (see Figure 7-1). An effective roughness height of 0.01m is derived from the surrounding flat ground with regularly cut grass.



**Figure 7-1 The full-scale 6m cube on the SRI wind engineering site**

The cube is constructed with a double-layer metal sheet, which is usually used as the typical external wall of standard low-rise industrial building. It is mounted on an internal turntable so that it can be rotated through  $360^{\circ}$  to suit the prevailing wind direction.

The configuration of the two ventilation openings was shown in Figure 5-1 in Chapter 5. The ratio of the opening area to wall area is 0.24%.

### 7.3 Leakage Test

With natural ventilation a building is usually ventilated via purpose-provided and adventitious openings. Air leakage is a measure of the airtightness of a building envelope and is independent of weather conditions. The leakage test is a preliminary investigation into the building's leakage characteristic carried out before conducting any ventilation measurement. In this case the aim is to measure the leakage rate through adventitious openings.

#### 7.3.1 Leakage tester

The nozzle type flow measuring device shown in Figure 7-2 is used for testing the leakage characteristic of the cube. It employs airflow measuring grids (AMGs) near the inlet in a relatively short duct (Length/Diameter  $\approx 3$ ) with a honeycomb element in front of the fan. Here, the AMGs are utilised as the metering element, which offer low flow resistance with relative insensitivity to installation effects [Etheridge and Standberg 1996].

AMGs will transmit a comparable and repeatable differential pressure proportional to the average airflow. Some of the tubes in the grid are perforated with small holes facing upstream which sense total pressure, whilst other tubes have holes on the downstream side to sense static pressure. The upstream and downstream tubes are connected to separate manifolds which thus provide two average pressure signals. The output readings are converted from the differential pressure signal into a voltage.

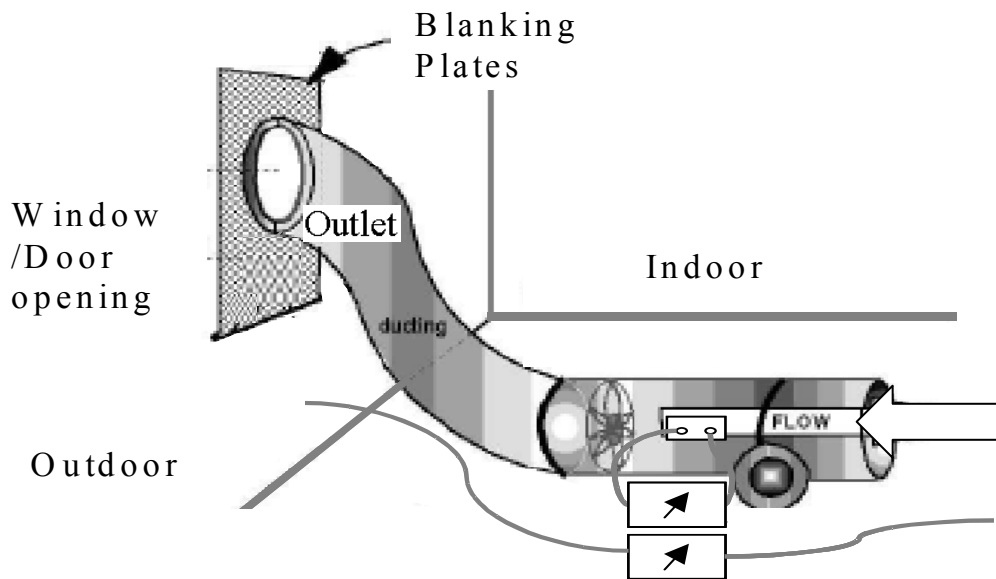


**Figure 7-2 Schematic of leakage measurement (after Green, 1999)**

Two manometers were used to measure the pressure difference across the fan ( $\Delta P_{fan}$ ) and the internal and external pressure difference of the building ( $\Delta P_{cube}$ ) respectively. By adjusting the speed of the fan, it was therefore possible to increase  $\Delta P_{fan}$ , from 10Pa up to 60Pa in 5Pa increments.

The average dynamic pressure of the flow in the fan unit has previously been calibrated against the flow rate ( $Q_{fan}$ ) through the fan inlet. Therefore, the value of  $\Delta P_{cube}$  with regards to the set of  $\Delta P_{fan}$  associated with the flow rate could be found.

### 7.3.2 Leakage rate measurements

It is advisable that building leakage tests should only be carried out under weather conditions of low wind speed and low temperature difference between outdoors and indoors. The reference wind data were recorded at the reference mast 18m upstream of the cube and at building height of 6m (see Figure 7-3). The wind velocity was measured by an ultrasonic anemometer sampled at 20.8 samples per second. During

the two experiment periods, the mean wind speed was 3.72 and 4.08 m/s respectively.

The correlation of leakage rate and pressure difference across the building ( $\Delta P_{building}$ ) can be fitted by a quadratic equation [Etheridge 1998].

$$\Delta P_{building} = a_T Q_L^2 + b_T Q_L \quad (7.1)$$

where  $a_T$ ,  $b_T$  are leakage coefficients, and  $Q_L$  represents the leakage flow rate.

In Figure 7-4 the best fit curve of two sets of test data indicated the leakage parameter  $Q_{50}^b$ , to be 0.30 m<sup>3</sup>/s, which equates to 5.0 air changes per hour (ACH) for the cube. This leakage characteristic is within the range of domestic houses in the UK [Etheridge and Standberg 1996], which represents moderate leakage. Therefore infiltration through adventitious cracks should not be neglected in the ventilation measurements.

#### 7.4 Infiltration test

The adventitious leakage of the building can be found in a pressurisation test as described in the previous section (Section 7.3.2). The infiltration flow rate through the adventitious openings can be measured under normal ventilation conditions by a tracer gas technique.

---

<sup>b</sup>  $Q_{50}$ : the leakage rate at a pressure difference of 50Pa as defined in BSI [1991].



Figure 7-3 Reference mast located 18m upstream of the cube

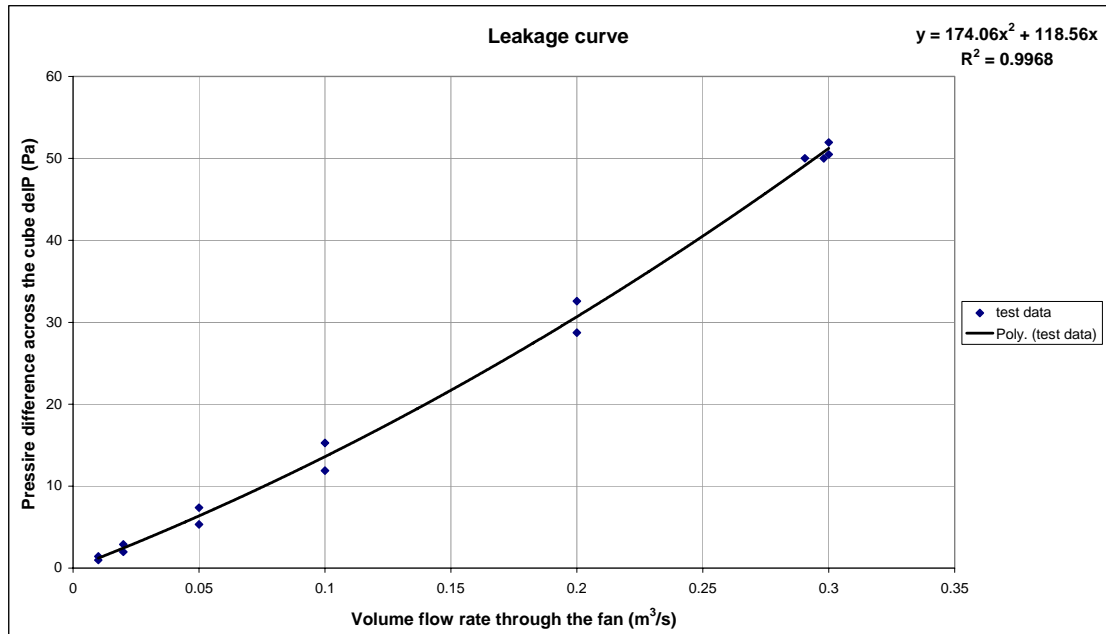


Figure 7-4 Leakage rate against pressure difference across the cube

### 7.4.1 Experiment apparatus

The schematic diagram of the test rig is shown in Figure 7-5. The tracer gas supply/injection system consists of the following components:

- Carbon monoxide (CO) gas cylinder (pure CO gas)
- N<sub>2</sub> purge gas (zero CO concentration)
- Pressure reduction valve for each gas cylinder
- Calibrated low pressure mass flow rate controller (max.5liter/sec)
- Distribution tubes consisting of non-absorbent material

The tracer gas sampling system consists of:

- CO concentration analyser (Fullscale range, 20ppm & time response, 10sec averaging)
- CO calibration gas (17ppm CO concentration)
- Data logger
- Data recording PC
- Distribution tubes consisting of non-absorbent material
- Portable Fans (mixing up tracer gas and indoor air)

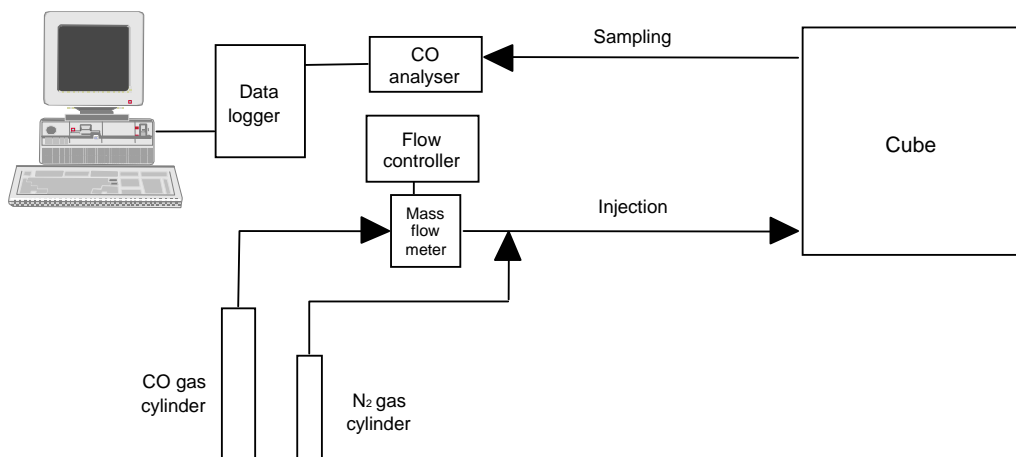


**Figure 7-5 Schematic of experiment rig**

### **7.4.2 Infiltration rates test**

The tracer gas decay technique was used in the tests. The air change rate through the cube with the large openings sealed was tracked by the tracer gas CO released at the interior release point. First, the tracer gas was injected until the indoor concentration had built up to certain level (nominally 20ppm). Then, the tracer gas concentration and its time series were recorded, which was used to assess the infiltration flow rates.

In order to produce a well-mixed and evenly distributed sample in the test space, a mixing fan was used. The sampling point should be located to measure a representative concentration of the tracer gas. In this investigation, the sampling point was located at the centre of the cube.

#### **7.4.2.1 CO analyser calibration**

To verify the accuracy of the sampling system it was necessary to calibrate the CO analyser. The calibration of both zero and span point was facilitated using the CO calibration gas before and after each data recording period. This procedure would minimise the noise and error of the recorded data.

The measurement of reference wind speed and direction was carried out simultaneously using a three axis ultrasonic anemometer (Figure 3-4, p69) mounted at the reference mast. Wind data were collected by a PC based data acquisition system sampled at 20 samples per second and the value of the velocity components was averaged every minute.

#### **7.4.2.2 Infiltration rates measurements**

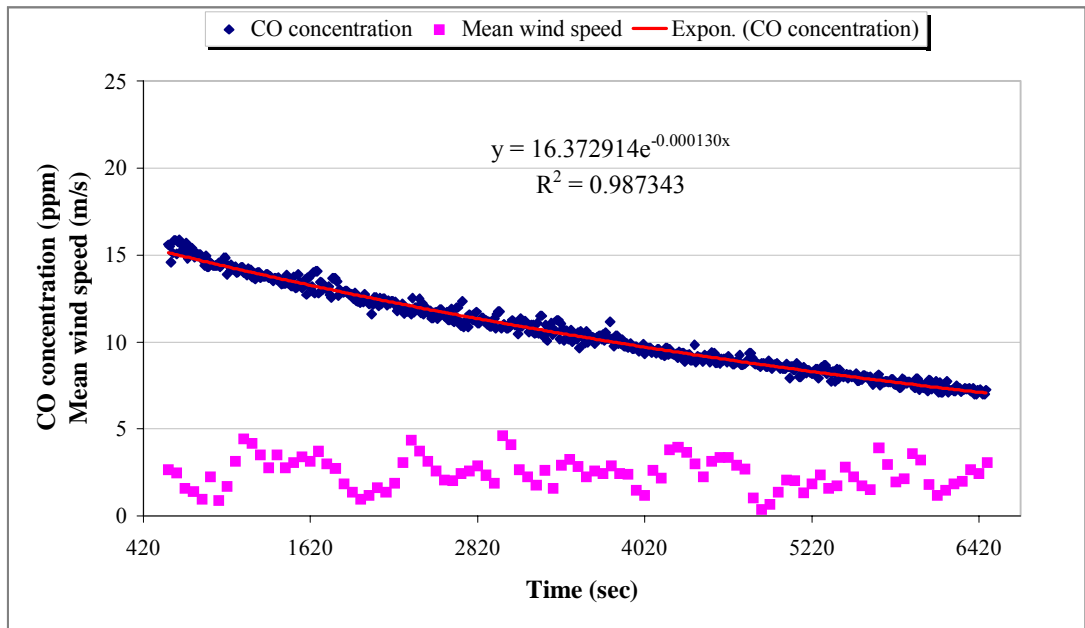
The duration of the data collection for the three experiments covered two daytime and one nighttime periods. During the two daytime tests, the mean wind speed was

2.47 and 2.34 m/s, and the mean indoor temperature was higher than outdoor by 18.8°C and 19.4°C respectively. During the night, the mean wind speed reduced to 0.51 m/s.

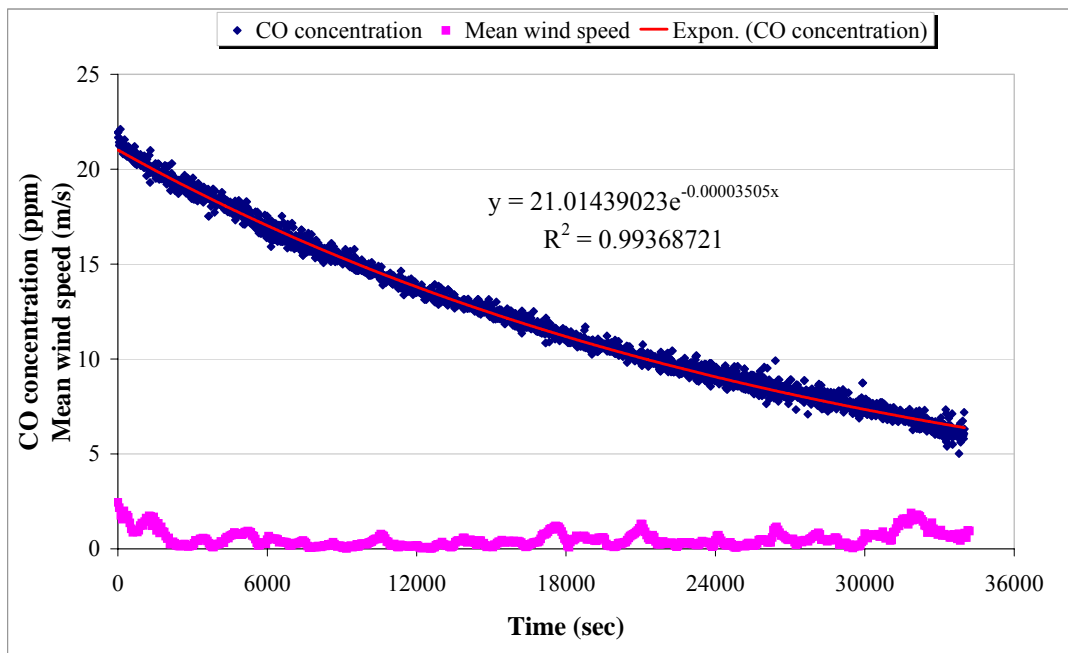
The concentration data recorded are shown in Figure 7-6 with corresponding reference wind speeds. Table 7-1 lists the acquired actual infiltration rate and the weather conditions, as well as the best-fit exponential functions and the coefficient of regression ( $R^2$ ). The  $R^2$  values were found to vary between 0.98 and 0.99. Therefore, the infiltration rate of the cube was about 10% of the total flow rate.

**Table 7-1 Infiltration test results using tracer gas decay technique**

SRI 6m Cube		25July01 [15:00~16:48]	26July01 [12:15~15:18]	26July01 [22:25~7:52]
Infiltration rate	(m <sup>3</sup> /s)	0.030	0.035	0.008
	(ACH)	0.49	0.58	0.13
Wind speed	Mean (m/s)	2.47	2.34	0.51
	Max (m/s)	4.63	5.06	2.44
Mean temperature difference	( $T_{in}-T_{out}$ ) (°C)	18.8	19.4	not measured
Decay curve constant		-0.000130	-0.000162	-0.000035
$R^2$ value		0.987	0.990	0.994



(a) Daytime test: CO concentration (ppm) and mean wind speed (m/s)



(b) Night-time test: CO concentration (ppm) and mean wind speed (m/s)

Figure 7-6 Infiltration test using tracer gas decay method

### 7.4.3 Building leakage/infiltration feature

Using the non-dimensional graph shown in Figure 7-7 [taken from Etheridge & Sandberg 1996, p165], and the  $a_T$  and  $b_T$  values evaluated from the leakage data in Figure 7-4, the total flow rate  $Q$  through adventitious openings of the cube can be estimated.

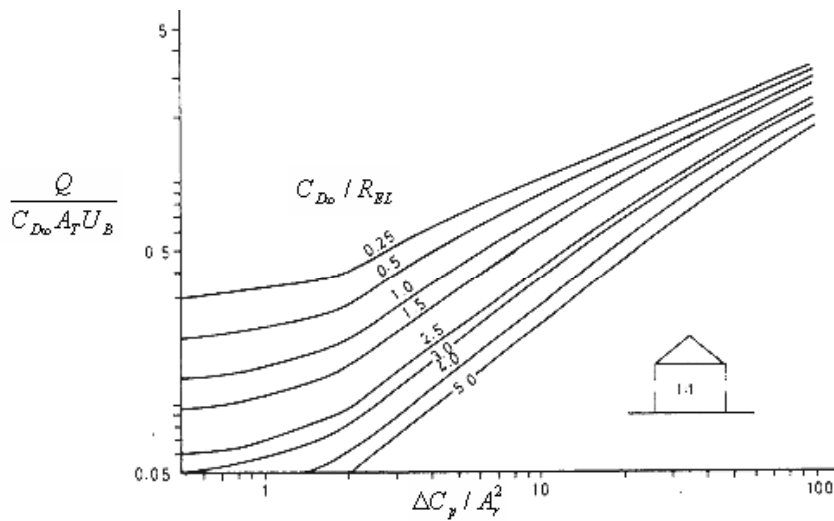


**Figure 7-7 Non-dimensional curves for determining ventilation of a building with openings on only two walls [Etheridge and Standberg, 1996]**

Assuming the nighttime test presented no thermal effect, the daytime data should be influenced by combined wind and buoyancy effects.

The relevant parameters can be calculated by the following equations:

$$C_{D\infty} A_T = \frac{1}{\sqrt{a_T}} \sqrt{\frac{\rho}{2}} \quad (7.2)$$

where

$A_T$  is the total area of adventitious openings

$C_{D\infty}$  is the discharge coefficient at high Reynolds number.

The equivalent wind speed  $U_b$  is defined by

$$U_b = \frac{1}{\sqrt{a_T}} \sqrt{\frac{(dT)gh}{T}} \quad (7.3)$$

The correlation of the discharge coefficient  $C_{D\infty}$  and the leakage Reynolds number of the building  $Re_L$  is expressed as

$$\frac{C_{D\infty}}{Re_L} = \frac{b_T}{\sqrt{a_T}} \frac{1}{U_b} \frac{1}{\sqrt{2\rho}} \quad (7.4)$$

For buoyancy effect alone

$$\frac{dC_p}{A_r^2} = 0 \quad (7.5)$$

For wind and buoyancy effects

$$\frac{dC_p}{A_r^2} = \frac{2(dp)}{(d\rho)gh} \quad (7.6)$$

where the Archimedes number is

$$Ar \equiv \sqrt{\frac{(d\rho)gh}{\rho U_{ref}^2}} = \frac{U_b}{U_{ref}} \quad (7.7)$$

Hence the calculated flow rate by combined wind and buoyancy effects was  $0.029 \text{ m}^3/\text{s}$ , which shows reasonable agreement with the measured values,  $0.030 \sim 0.035 \text{ m}^3/\text{s}$  listed in Table 7-1.

## **7.5 Ventilation flow rate measurements**

For these tests the openings of the cube were not sealed. In addition to the previous infiltration test equipment, two ultrasonic anemometers (10 samples per second (SPS)) and two static pressure probes with transducers were placed at the higher and lower openings separately.

### **7.5.1 Sampling system**

The detailed measuring instrument's layout and location at the centre of the opening are illustrated in Figure 7-8 from different viewpoints. Pressure tapping points are evenly distributed with 1m intervals along the central lines on the cube surface (Figure 7-9).

In Figure 7-10, the  $0^\circ$  indicates the direction of the wind blowing perpendicularly to the cube face through the lower level ventilation opening. The 10-minute mean wind speed and directions (Figure 7-11) were recorded by a 20.8 SPS ultrasonic anemometer on the reference mast.

Along with reference wind speed and direction recording, building surface pressure data captured by the tapping points were sampled at 20.8 SPS. Velocity measurements of the inflow/outflow through openings were recorded by the two 10 SPS ultrasonic anemometers simultaneously.



Lower opening located at 1m above ground



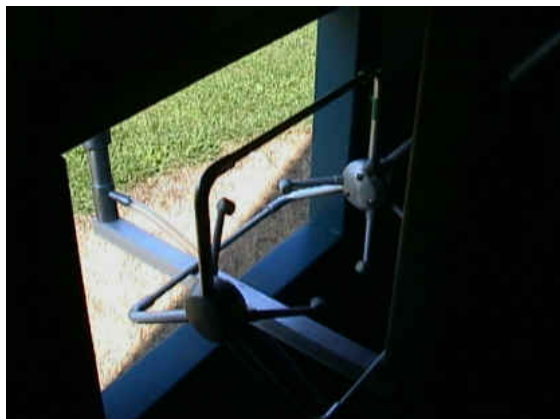
Higher opening located at 5m above ground



Ultrasonic anemometer & static pressure probe placed at lower opening (Outdoor close view)



Ultrasonic anemometer & static pressure probe placed at higher opening (Outdoor close view)



Outlook view from lower opening



Outlook view from higher opening

**Figure 7-8 Two ventilation openings on the opposite walls of the 6m cube**

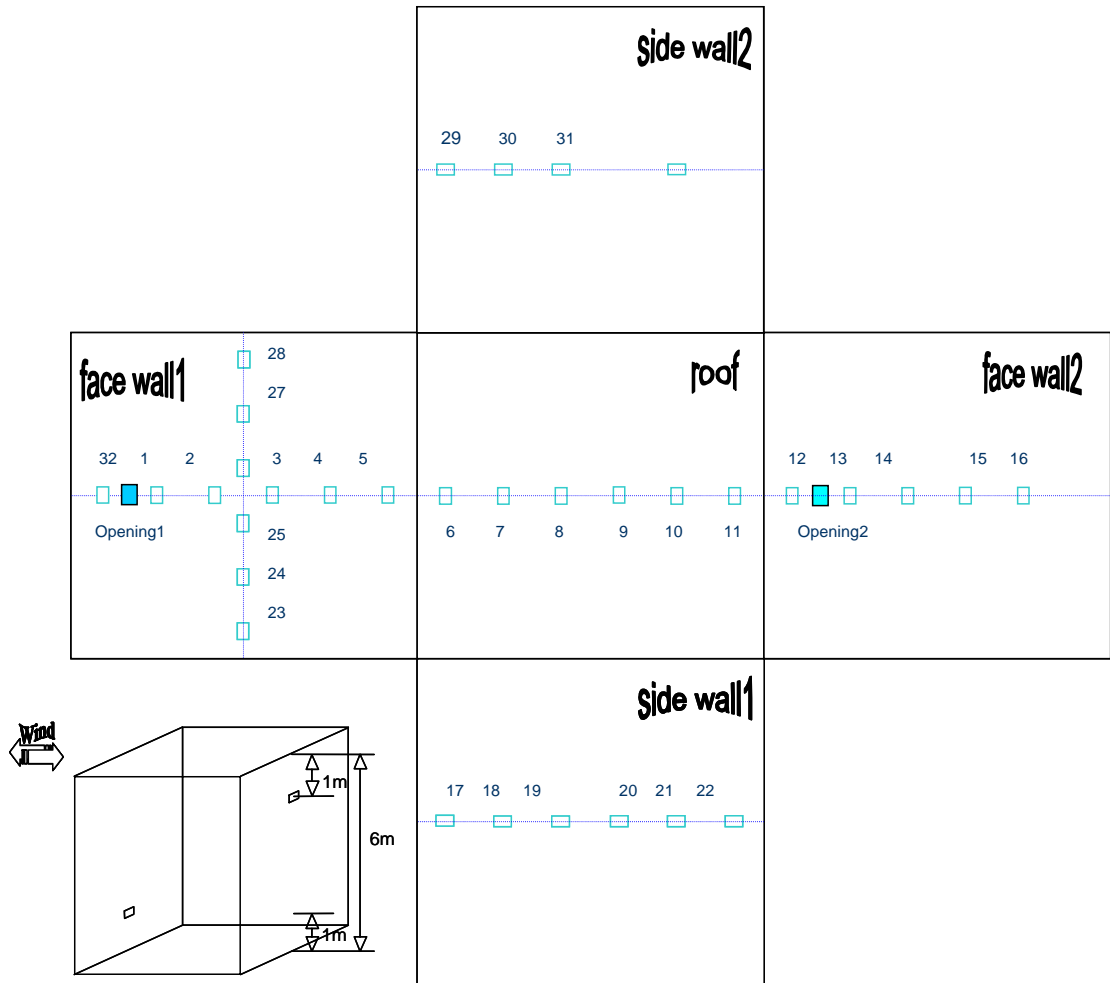


Figure 7-9 Pressure tapping points on the cube surface

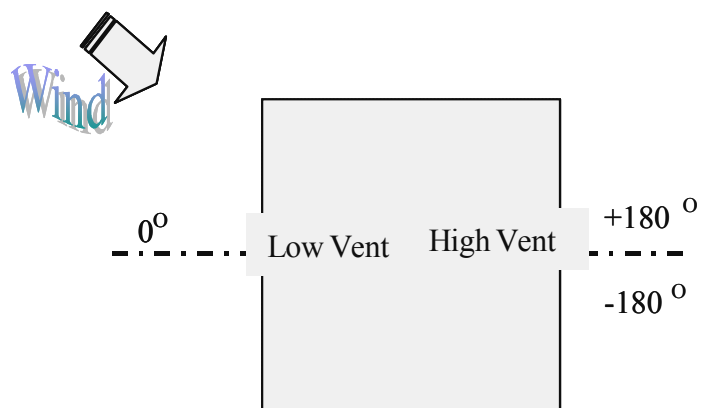
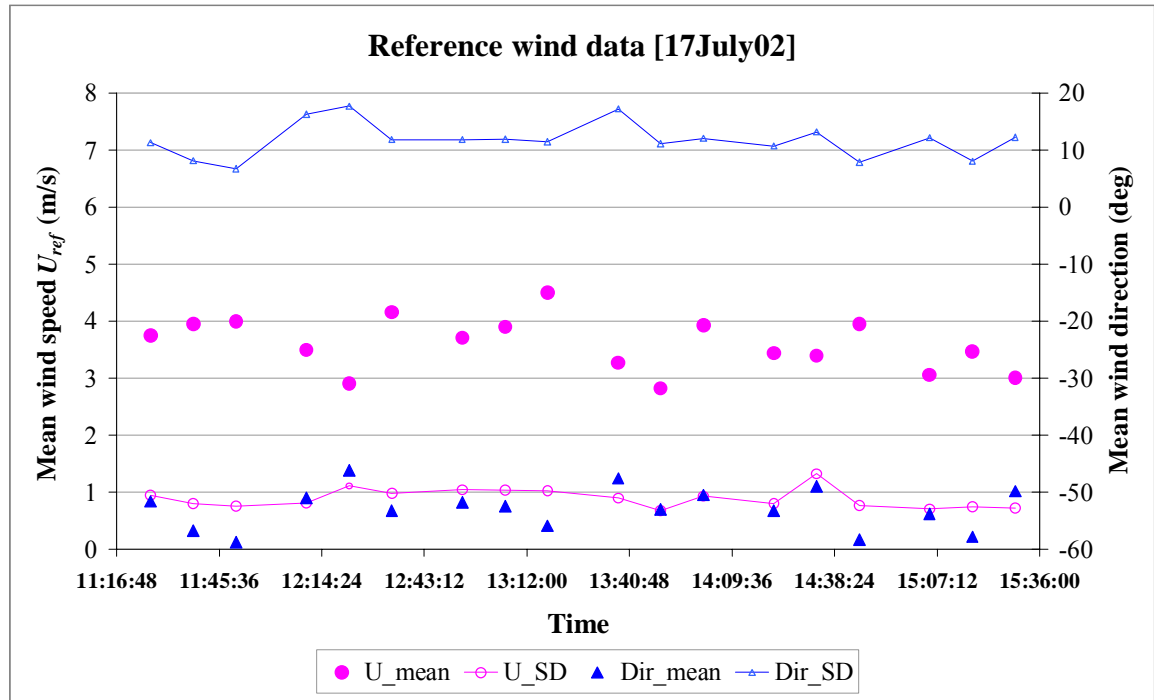


Figure 7-10 Wind incident angles (cube plan view)



**Figure 7-11 Reference weather data – 10-minute mean wind speed and direction**

The tracer gas injection point was placed near the floor level, mixing fan and the sampling point was set at the centre of the cube. In order to obtain uniform indoor concentration, five portable fans were placed evenly inside the cube at different heights.

The static pressure difference between the two openings was obtained by a manometer connected to individual static pressure probes at the lower and higher openings. Both static pressure probes were connected by piping with the same length of tubing and indoor layout, in order to minimise the signal response error.

A temperature and humidity probe recorded outdoor temperature near the lower opening. Three probes were placed inside the cube at the higher opening, mid-height and near ground level respectively. The temperature data in Figure 7-12 were recorded by a portable data logger (Squirrel 1000) at 1-minute intervals.

Tracer decay history, pressure difference between two openings and velocity components at the centre of each opening were collected by a data logger and recorded by a portable PC. The ADsonic data-logging program was used, which was a purpose written SRI software package for simultaneous combined data capture from anemometers and other equipment.

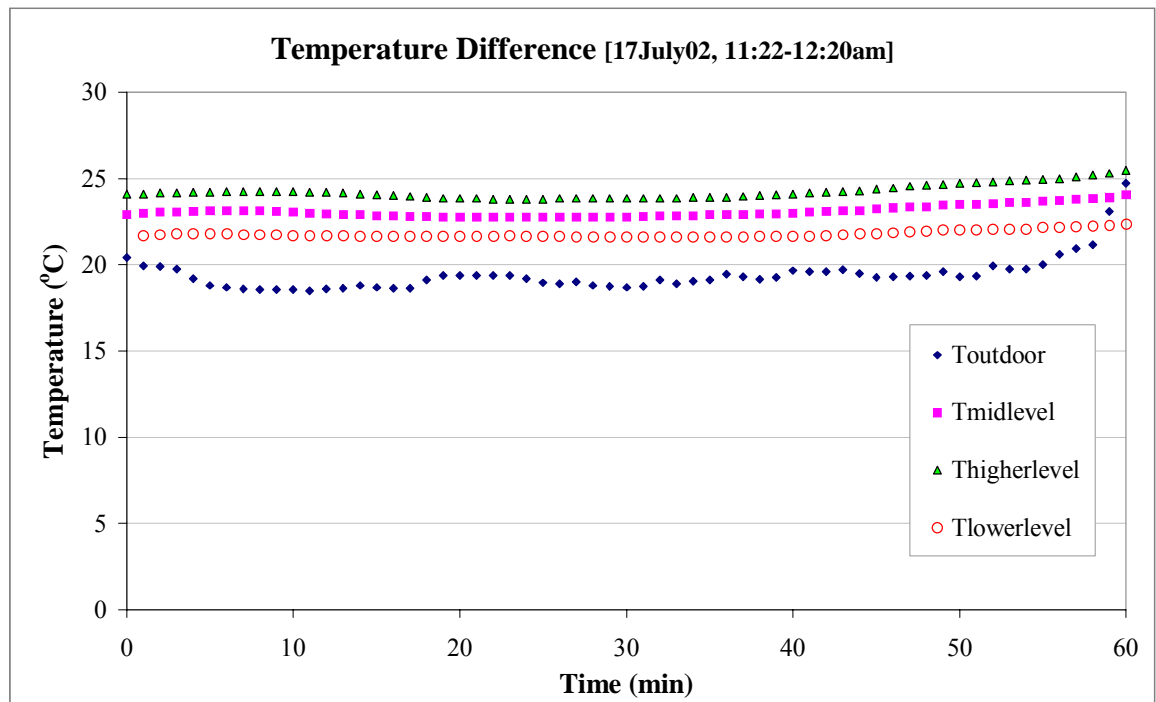


**Figure 7-12 Reference weather data - 1-minute mean outdoor & indoor temperatures**

### 7.5.2 Experimental methods

In order to assure the quality of the full-scale data, the ventilation rates through the cube were measured and calculated by the following four methods:

- (1) Method 1 - tracer gas decay measurement (COdecay);
- (2) Method 2 - mean static pressure and temperature difference measurement across the openings, which is referred as 'Point pressure difference method' (dP) and (dP+dT);

- (3) Method 3 - surface pressure difference measurement around the openings, named as ‘Surface pressure difference method’ ( $dP_{\text{taps}+dT}$ ); and
- (4) Method 4 – mean flow speed measurement at each opening (Sonic(in) and Sonic(out)).

### 7.5.2.1 Tracer gas decay method

As mentioned earlier in Section 3.6.2.1, the tracer gas (CO) concentration decay history was represented here by

$$C(t) = C(0)e^{-It} \quad (3.37, \text{p71})$$

where the slope of the natural logarithm of the concentration plot,  $I$ , indicates the ventilation flow rate in air change per hour (ACH), that is  $\frac{IV_{\text{cube}}}{3600}$  in  $\text{m}^3/\text{s}$ . A typical decay record is shown in Figure 7-13, at sampling rate 1 SPS.

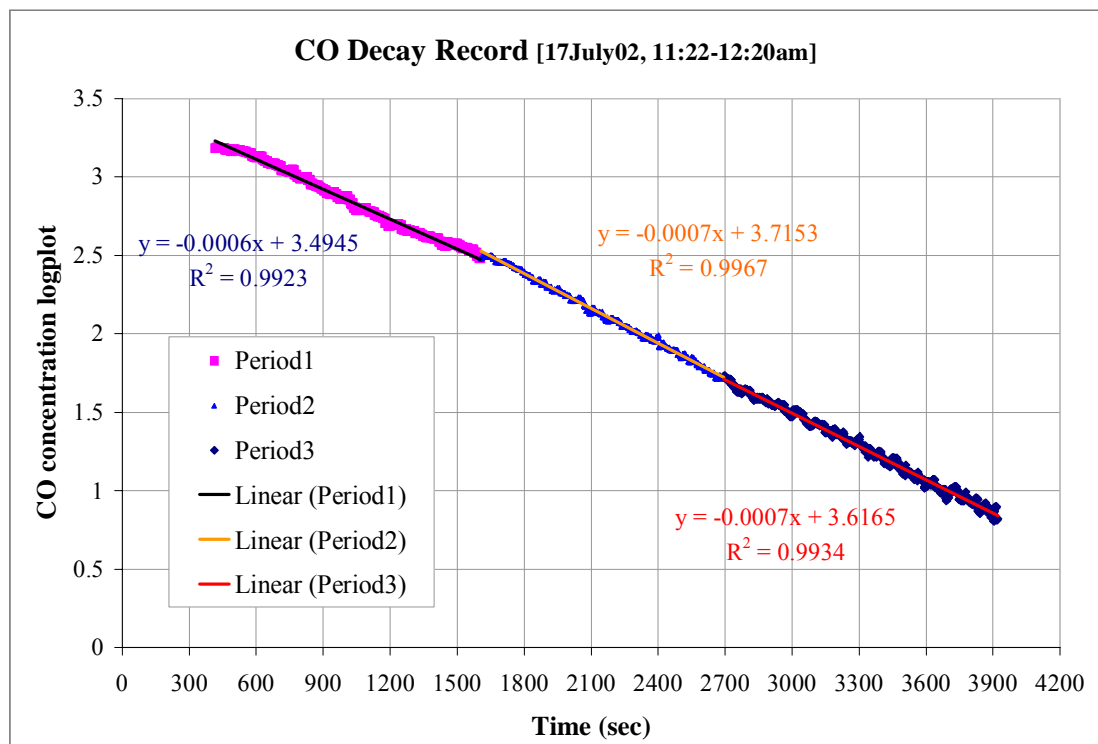


Figure 7-13 Tracer gas decay record (logarithm linear fitting-curve)

It is well known that the wind speed and direction can change frequently. There is a time lag between the moment the wind characteristics change and the resulting reaction in the concentration of the tracer gas. Baptista et al. [1999] analysed the data obtained in a greenhouse by the tracer gas decay method. They found that the most suitable correlation was 16 min. Chalabi and Fernandez [1992] also obtained a 13 ~ 18 min range in another similar greenhouse. In the present investigation, the time delay correlation was about 10 min (probably because of the smaller volume of the cube and the corresponding air change rate), which means the ventilation rate extracted from the linear regression analysis of the decay curve corresponds to the mean wind speed of the previous 10 min period record and that 10 mins is a suitable period for averaging.

### 7.5.2.2 Point pressure difference method

The pressure differences across the cube openings were recorded using a static pressure probe placed at the centre of each opening as shown in Figure 7-8.

Simultaneously the indoor & outdoor temperature differences were recorded by temperature probes located at the two opening levels.

The volume flow rate induced by combined wind and buoyancy effects was described in Section 3.5.2.1 and copied here (in temperature form)

$$Q = C_d A \sqrt{\left| \frac{dP}{\rho} + \frac{(dT)gh}{T_e} \right|} \quad \text{or} \quad Q = C_d A \sqrt{\left| \frac{dP}{\rho} - \frac{(dT)gh}{T_e} \right|} \quad (3.33, \text{p68})$$

The + or - sign indicates that the wind force complements or counteracts the buoyancy effect.

### 7.5.2.3 Surface pressure difference method

Two surface pressure taps were mounted 0.5m from the centre of each opening (Figure 7-9). The overall pressure difference was estimated by averaging the pressure difference from the two-pair tapping points. Eqn.3.33 was also employed to calculate the mean flow rates.

### 7.5.2.4 Mean flow speed method

The mean ventilation rate was estimated using the mean speed of the inflow or outflow through an opening multiplied by the opening area  $A$ .

## 7.5.3 Results and discussions

Full-scale measurements of mean ventilation rates were carried out under various natural conditions, i.e. summer, spring and winter seasons. Over 120 runs have been recorded and data were analysed and filed according to the above four methods.

Most data were taken on overcast days or at night with outdoor to indoor temperature differences up to 8°C, so the buoyancy effect was not significant during the experimental periods. Table 7-2 shows a typical summary datasheet for tests done on 13 Aug 02.

The measured ventilation flow rates were non-dimensionalised by the opening area  $A$  and mean reference wind speed  $U_{ref}$ , and are shown as a function of reference wind direction in Figures 7-14, 7-16 ~ 7-18. The outline of the Silsoe experiment site can be found in Appendix B Figure B-1.

Previous measurement of the adventitious leakage of the cube (Section 7.4.3) indicates that infiltration rates are probably of order 10% of the ventilation flow

Table 7-2 Ventilation flow rate data analysis

Date	Run No.	U <sub>ref_mean</sub> (m/s)	U <sub>ref_SD</sub> (m/s)	Dir <sub>mean</sub> (deg)	Dir <sub>SD</sub> deg	Q{COdecay}				Q{dP <sub>taps</sub> +dT}			Pressure taps			
						Curve const.	(m <sup>3</sup> /s)	(ACH)	Q/(AU <sub>ref</sub> )	dP <sub>taps</sub> (Pa)	(m <sup>3</sup> /s)	Q/(AU <sub>ref</sub> )	C <sub>p1_mean</sub>	C <sub>p1_SD</sub>	C <sub>p2_mean</sub>	C <sub>p2_SD</sub>
13/08/02	Run4-1	5.376	1.071	-21.648	14.895	-0.001278	0.2760	4.60	0.587	16.851	0.279	0.592	0.6	0.29	-0.305	0.14
13/08/02	Run4-2	6.025	1.359	-16.627	11.677	-0.001524	0.3292	5.49	0.624	20.178	0.305	0.578	0.58	0.27	-0.275	0.13
13/08/02	Run4-3	5.498	1.151	-12.931	12.211	-0.001468	0.3171	5.28	0.659	18.973	0.296	0.615	0.675	0.29	-0.295	0.13
13/08/02	Run5-1	6.173	1.424	-34.911	14.276	-0.001783	0.3852	6.42	0.713	20.361	0.307	0.568	0.46	0.28	-0.36	0.16
13/08/02	Run5-2	6.395	1.462	-21.642	12.086	-0.001594	0.3443	5.74	0.615	23.301	0.327	0.584	0.57	0.28	-0.305	0.16
13/08/02	Run5-3	5.980	1.398	-18.461	13.828	-0.001562	0.3374	5.62	0.645	20.674	0.308	0.589	0.59	0.31	-0.295	0.14
13/08/02	Run6-1	5.581	1.348	-28.187	14.654	-0.001268	0.2739	4.57	0.561	16.847	0.279	0.570	0.505	0.31	-0.32	0.14
13/08/02	Run6-2	5.689	1.157	-22.232	14.399	-0.001432	0.3093	5.16	0.621	17.827	0.287	0.577	0.555	0.25	-0.3	0.13
13/08/02	Run6-3	5.676	1.561	-21.362	14.243	-0.001301	0.2811	4.69	0.566	18.688	0.293	0.590	0.585	0.33	-0.285	0.18

Date	Run No.	U <sub>ref_mean</sub> (m/s)	U <sub>ref_SD</sub> (m/s)	Dir <sub>mean</sub> (deg)	Dir <sub>SD</sub> deg	Q{dP+dT}				Q{dP}			Sonic(in)		Sonic(out)	
						dT (K)	T <sub>out</sub> (K)	(m <sup>3</sup> /s)	Q/(AU <sub>ref</sub> )	dP (Pa)	(m <sup>3</sup> /s)	Q/(AU <sub>ref</sub> )	U <sub>in</sub> (m/s)	U <sub>in</sub> /U <sub>ref</sub>	U <sub>out</sub> (m/s)	U <sub>out</sub> /U <sub>ref</sub>
13/08/02	Run4-1	5.376	1.071	-21.648	14.895	1.78	299.36	0.252	0.536	13.735	0.249	0.530	3.404	0.633	1.550	0.288
13/08/02	Run4-2	6.025	1.359	-16.627	11.677	1.88	299.89	0.279	0.530	16.932	0.277	0.525	3.796	0.630	1.680	0.279
13/08/02	Run4-3	5.498	1.151	-12.931	12.211	2.04	299.38	0.269	0.560	15.695	0.267	0.554	3.722	0.677	1.612	0.293
13/08/02	Run5-1	6.173	1.424	-34.911	14.276	2.53	298.58	0.317	0.588	21.846	0.315	0.582	4.363	0.707	1.969	0.319
13/08/02	Run5-2	6.395	1.462	-21.642	12.086	1.80	299.35	0.278	0.497	16.823	0.276	0.493	3.900	0.610	1.770	0.277
13/08/02	Run5-3	5.980	1.398	-18.461	13.828	2.12	298.93	0.283	0.540	17.293	0.280	0.535	3.986	0.666	1.734	0.290
13/08/02	Run6-1	5.581	1.348	-28.187	14.654	1.78	299.11	0.255	0.522	14.044	0.252	0.516	3.341	0.599	1.623	0.291
13/08/02	Run6-2	5.689	1.157	-22.232	14.399	2.36	298.75	0.273	0.549	16.125	0.270	0.543	3.677	0.646	1.667	0.293
13/08/02	Run6-3	5.676	1.561	-21.362	14.243	1.90	298.94	0.250	0.503	13.504	0.247	0.498	3.351	0.590	1.534	0.270

through the two openings, which is small but not negligible. Hence the infiltration rate has been added to the ventilation flow rate obtained from Eqn.3.33.

In the next section the results within number of wind direction ranges are being considered to allow more general conclusions to be made.

### 7.5.3.1 Wind directions at 0°~30° cases

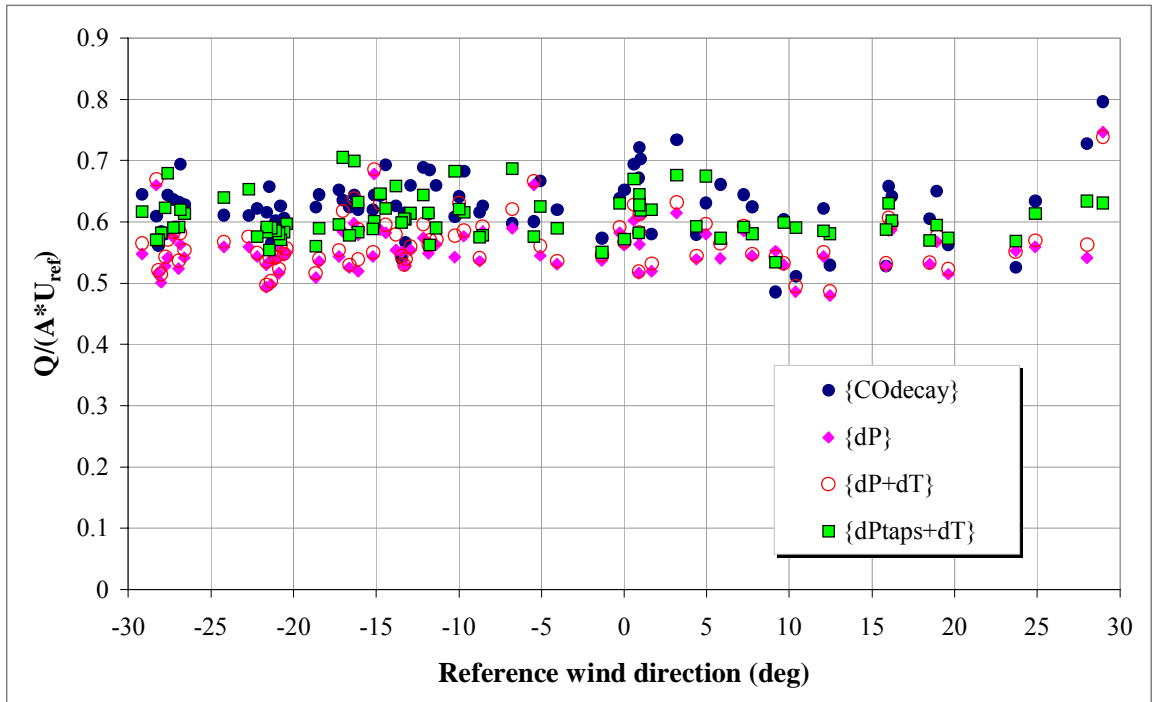
Table 7-3 summarises the measured cube ventilation rates for wind directions ranging from 0° to 30°, and their standard deviation (SD) values by the four methods stated in Section 7.5.2. Figure 7-14 shows the nondimensional ventilation rates for the 0°~30° cases, and indicates that there is no obvious trend with wind direction over this range.

The well-established tracer gas decay measurement (method 1 in Section 7.5.2.1) is regarded as the most accurate method and treated as the reference data for comparison. The overall non-dimensional ventilation rate measured by the CO decay method for these wind directions was  $0.63 \pm 0.05$ .

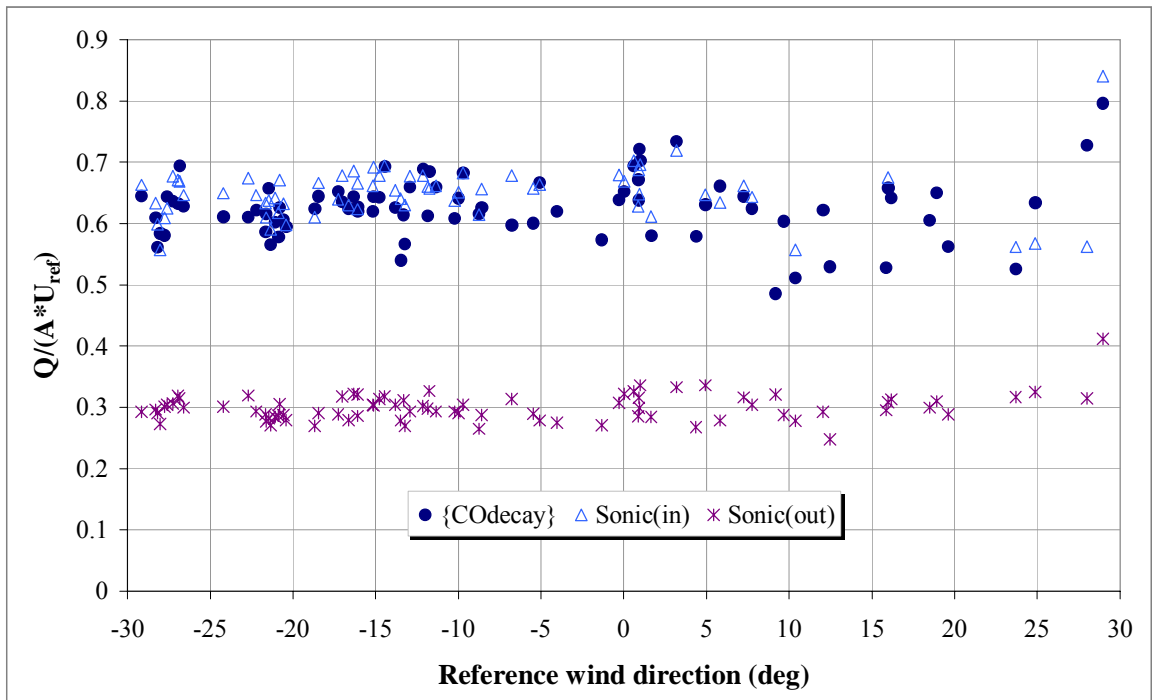
**Table 7-3 Nondimensional ventilation rates for 0°~30° cases**

82 Test cases 0°~30°		(Q/AU <sub>ref</sub> )			(Q-Q <sub>method1</sub> )/Q <sub>method1</sub> (%)		
		mean	SD	SD/mean(%)	mean	max.	min.
Method 1	{COdecay}	0.63	0.05	8.1	-	-	-
Method 2	{dP}	0.56	0.04	7.5	-11	14	-26
	{dP+dT}	0.57	0.04	7.8	-9	12	-23
Method 3	{dP <sub>taps</sub> +dT}	0.61	0.04	5.9	-3	16	-21
Method 4	Sonic(in)	0.65	0.04	6.6	4	19	-23
	Sonic(out)	0.30	0.02	7.4	-52	-34	-59

All the experiments were carried out while the thermal effect was not dominant, because the maximum indoor and outdoor temperature difference was 8°C, while the



(a) Measured ventilation rates by method 1 {COdecay}, method 2 {dP} & {dP+dT} and method 3 {dP<sub>taps</sub>+dT}



(b) Measured ventilation rates by method 1 {COdecay} & method 4 {Sonic(in) & Sonic(out)}

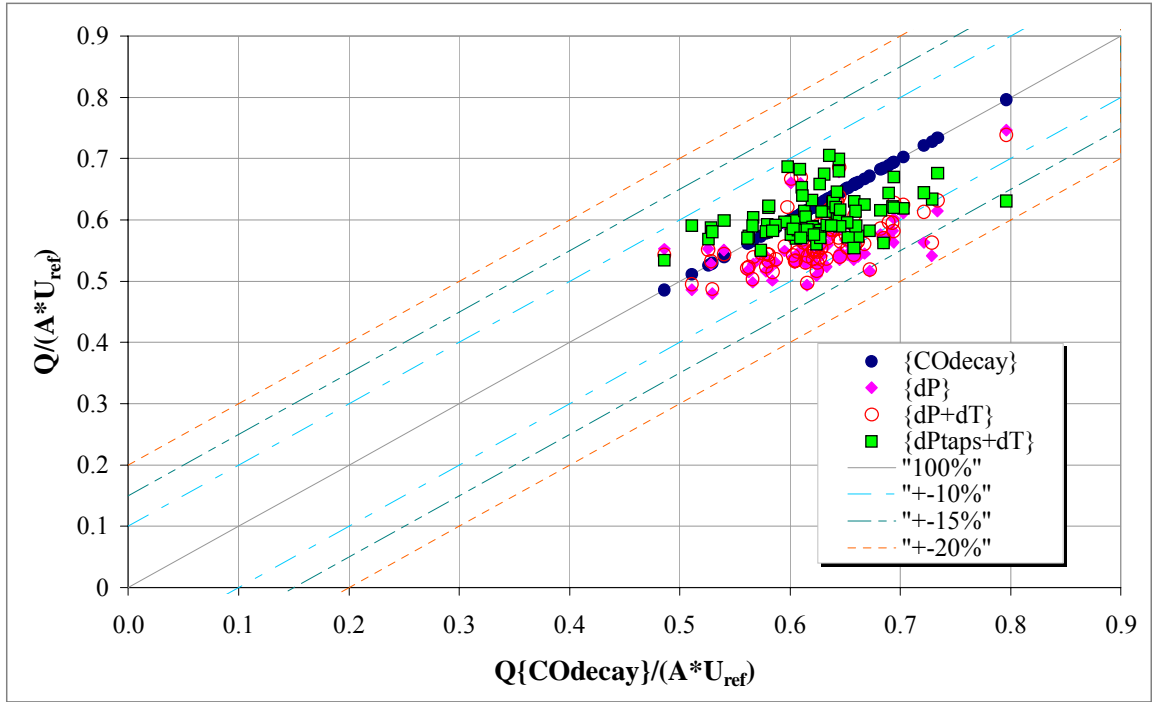
Figure 7-14 Nondimensional ventilation rates at wind directions 0°~30°

mean wind speed for the same run was 3.51 m/s. The simply steady state envelope model does not account for the local pressure fluctuation induced by turbulent wind, nor does it consider the pulsation of the flow in and out of the opening, or the depth of opening effect (Section 4.4). Therefore, to obtain a close agreement between theory and measurement, a higher discharge coefficient value  $C_d$ , 0.77 in Eqn.3.33 (see Section 7.5.2.2) is more appropriate than the theoretical value 0.6 for a sharp-edged circular orifice.

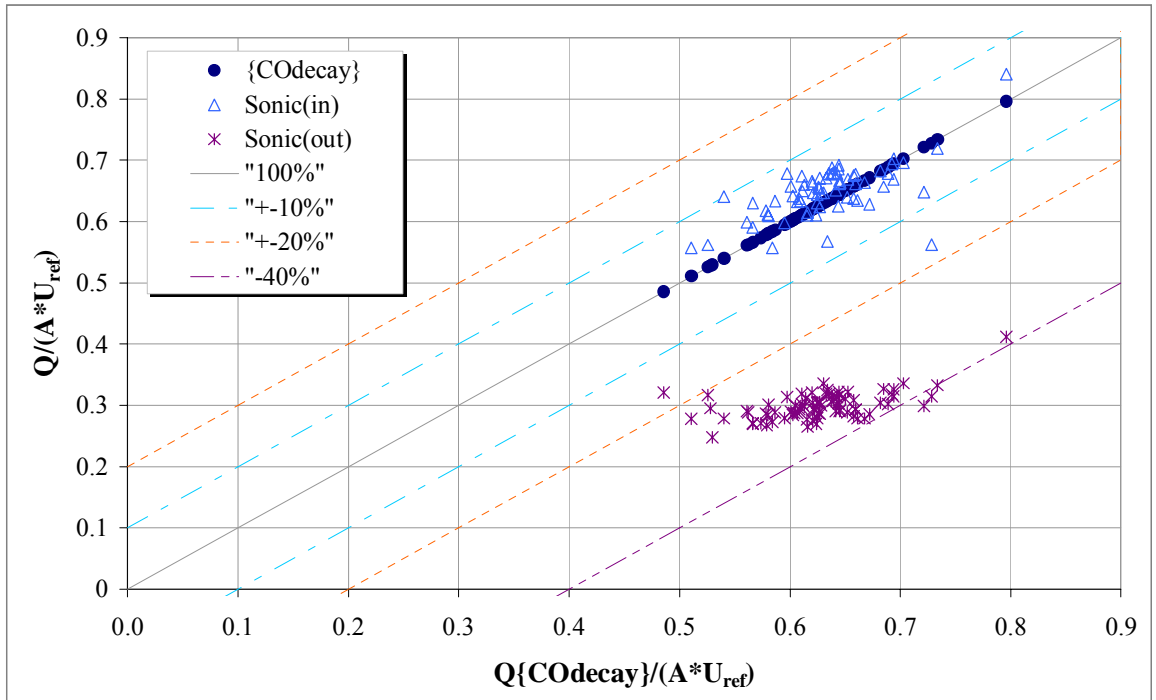
Similar results have been found in direct wind tunnel modelling tests for wind-alone cases [Carey and Etheridge 1999]. The unsteady nature of the velocity/pressure fields near the opening adds to the mean pressure difference driven ventilation and causes more discharge flow through openings hence the higher discharge coefficient.

Only considering the pressure difference caused by wind effects (method 2 in Section 6.5.2.2) results on average in 11% under-prediction of the total flow rates. Better estimations with both wind and thermal effects lead to values 2% closer to the effective ventilation rates measured by method 1. Therefore neglecting the  $dT$  element is not significant and we can compare with iso-thermal CFD simulations.

In method 3 (Section 7.5.2.3), the surface pressure recorded by tapping points, provides the estimation of averaged pressure drop across the cube. This estimation has a relatively lower level of error (3%) compared with the direct pressure measurement at the centre of the openings in method 2 (11%). Therefore method 3 gives even closer mean flow values of  $0.61 \pm 0.04$  comparing to method 1. The error band of method 3 ranged from -21% to 16%, which was also smaller than those predicted by the method 2, -26% to 14%.



(a) Method 2 {dP} & {dP+dT}, method 3 {dP<sub>taps</sub>+dT} comparing to method 1 {COdecay}



(b) Method 4 {Sonic(in) & Sonic(out)} comparing to method 1 {COdecay}

Figure 7-15 Relative error band of the measured ventilation rates at 0°~30°

Method 4 (in Section 7.5.2.4) measuring the flow speed at centre of the lower opening over-predicted the flow rate by 4% on average. Due to the turbulent external flow associated with horseshoe vortex upstream of the building's front face and the crossflow over the low level opening, the single centre-point record could under-predict the mean inflow rate by 23% or over-predict by up to 19% (see Table 7-3).

In contrast, the mean outflow speed captured at the high level opening under-predicted the outgoing flow rate by 52% on average. This is probably caused by the unsteadiness of velocity field in the wake of the building. The velocity fluctuation feature cannot be represented by the single point measurement at the centre of the higher opening.

Comparatively speaking, the ventilation flow rates in Figure 7-15(a) predicted by method 3 showed the closest agreement with method 1 mostly within 10%~15% error. Method 2 normally estimated lower mean flow rates than method 3, and it fitted within the error band range of 10%~20%.

Method 4 results (Figure 7-15(b)) mostly showed over-prediction by the inflow speed and under-prediction by the outflow speed measurements. The inconsistent correlation between the inlet and outlet opening made this method not very promising for the mean ventilation flow estimations.

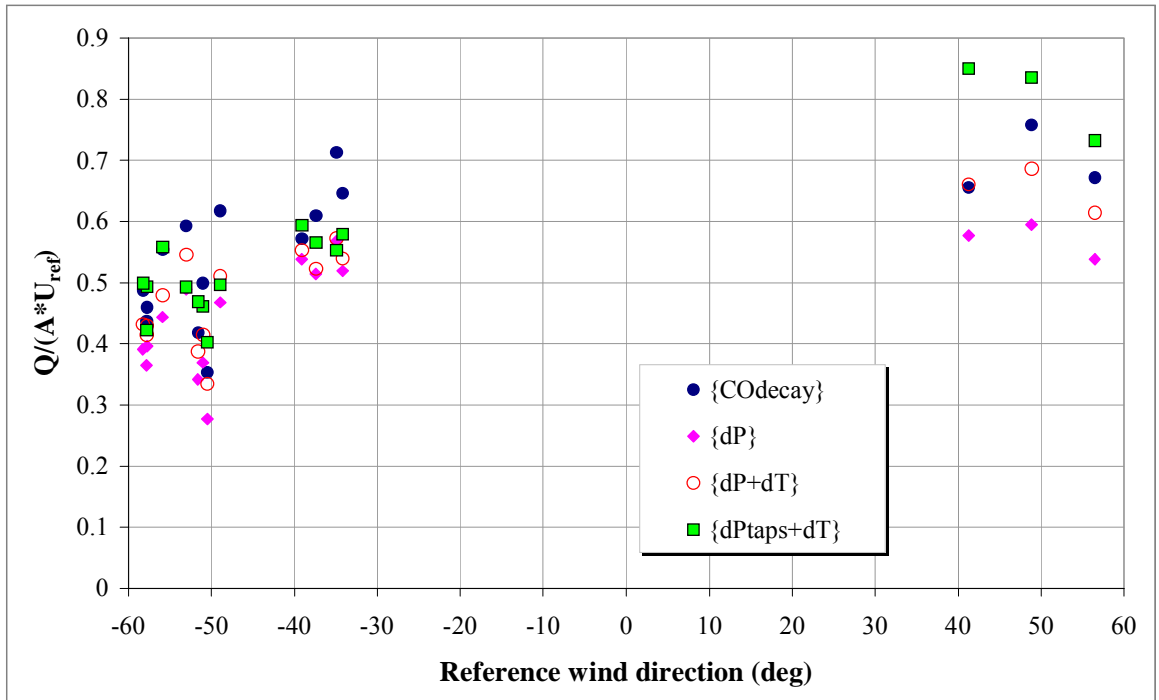
### 7.5.3.2 Wind directions at 34°~60° cases

There were 13 cases recorded between the wind directions of -34° ~ -60° and 3 cases between +40° ~ +60°. The maximum value of the difference between outdoor to indoor temperature was 7°C and the mean wind speed was 4.5 m/s. The accuracy of the four measurement methods is listed in Table 7-4. For the 13 cases the incoming wind travelled over building blocks some 200m distance from the test cube. For the other 3 cases, the cube was in the near wake region of the Silsoe structure building. Therefore, more variances were found in the mean flow rate data. Choosing the opening discharge coefficient as 0.75, the results of method 3 agreed well with the method 1.

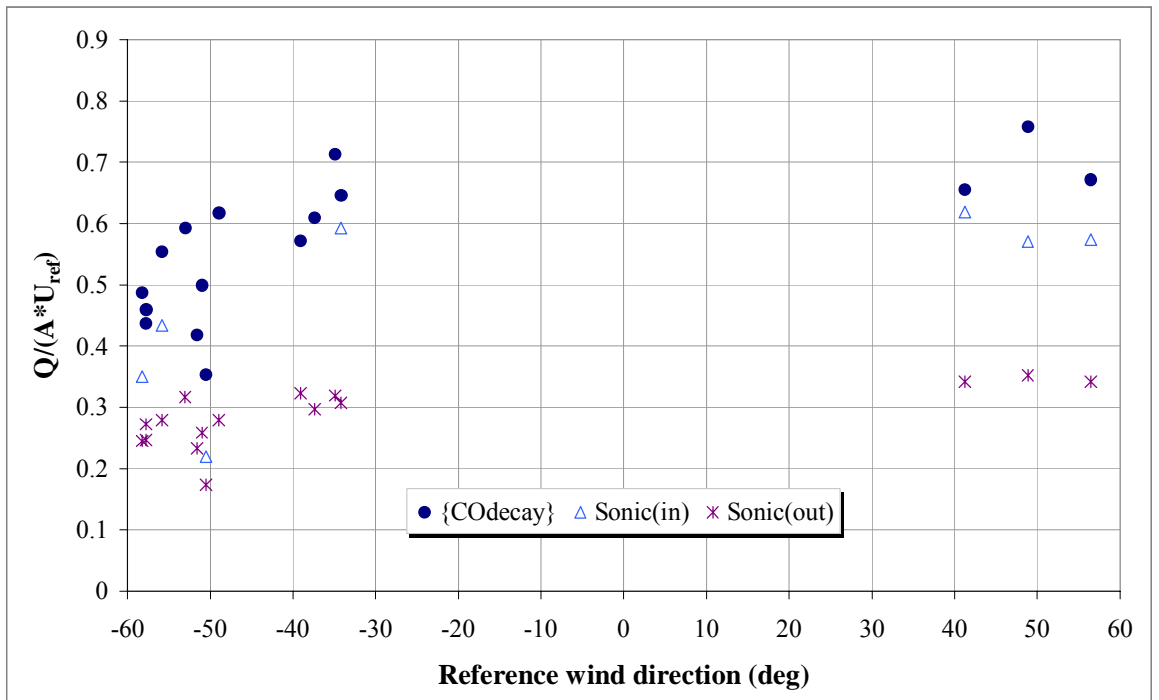
**Table 7-4 Nondimensional ventilation rates for 34°~60° cases**

16 Test cases 34°~60°		(Q/AU <sub>ref</sub> )			(Q-Q <sub>method1</sub> )/Q <sub>method1</sub> (%)		
		mean	SD	SD/mean(%)	mean	max.	min.
Method 1	{COdecay}	0.57	0.11	20.2	-	-	-
Method 2	{dP}	0.46	0.10	20.7	-18	-3	-32
	{dP+dT}	0.51	0.10	19.8	-10	-1	-22
Method 3	{dP <sub>taps</sub> +dT}	0.56	0.11	19.4	0	15	-25
Method 4	Sonic(in)	0.48	0.14	28.3	-15	10	-38
	Sonic(out)	0.29	0.05	16.7	-49	-41	-55

In Figure 7-16 the nondimensional ventilation rates are found to be scattered from 0.3 to 0.76. Especially around -50° cases method 2 recorded fewer changes than method 1. The mean speed at the high level opening indicated fewer fluctuations than the data obtained at the low level opening.



(a) Measured ventilation rates by method 1 {COdecay}, method 2 {dP} & {dP+dT} and method 3 {dP<sub>taps</sub>+dT}



(b) Measured ventilation rates by method 1 {COdecay} and method 4 {Sonic(in) & Sonic(out)}

Figure 7-16 Nondimensional ventilation rates at wind directions 34°~60°

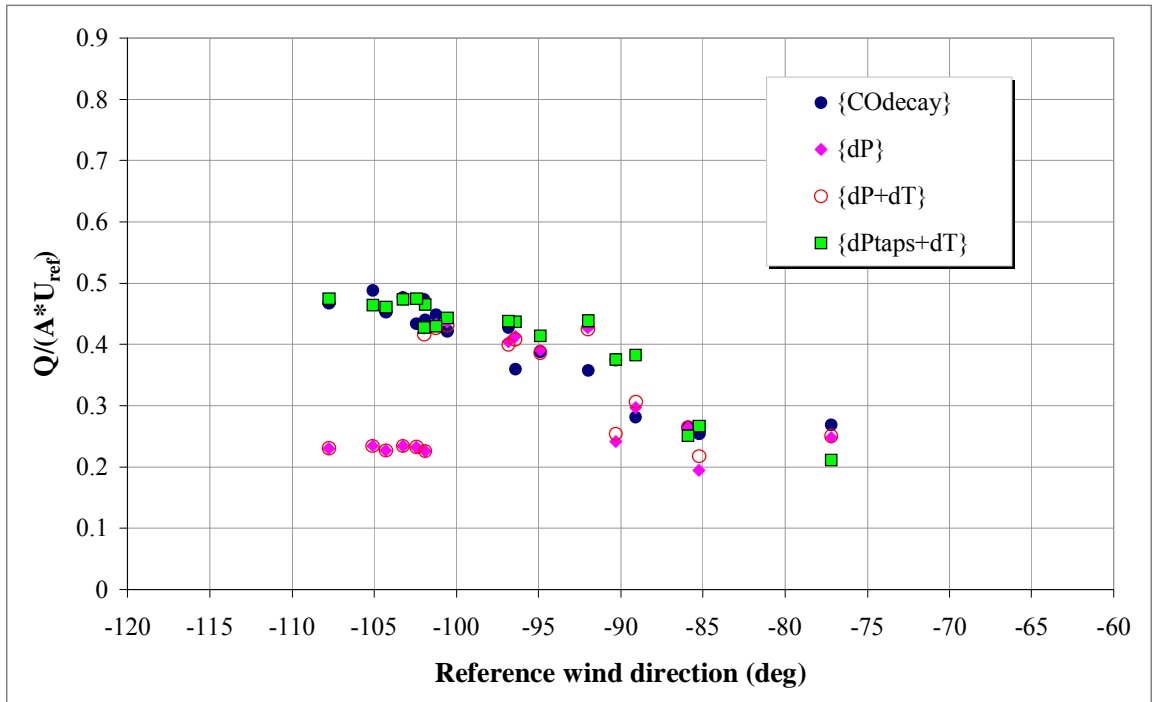
### 7.5.3.3 Wind directions at 75°~110° cases

The measurements of wind directions at 75° ~ 110° cases are summarised in Table 7-5. The maximum temperature difference of 5°C was found for the run while the mean wind speed was 4.4 m/s. With the choice of discharge coefficient as 0.6, the mean flow rate estimated by the method 3 showed close agreement (2% over-prediction) with method 1.

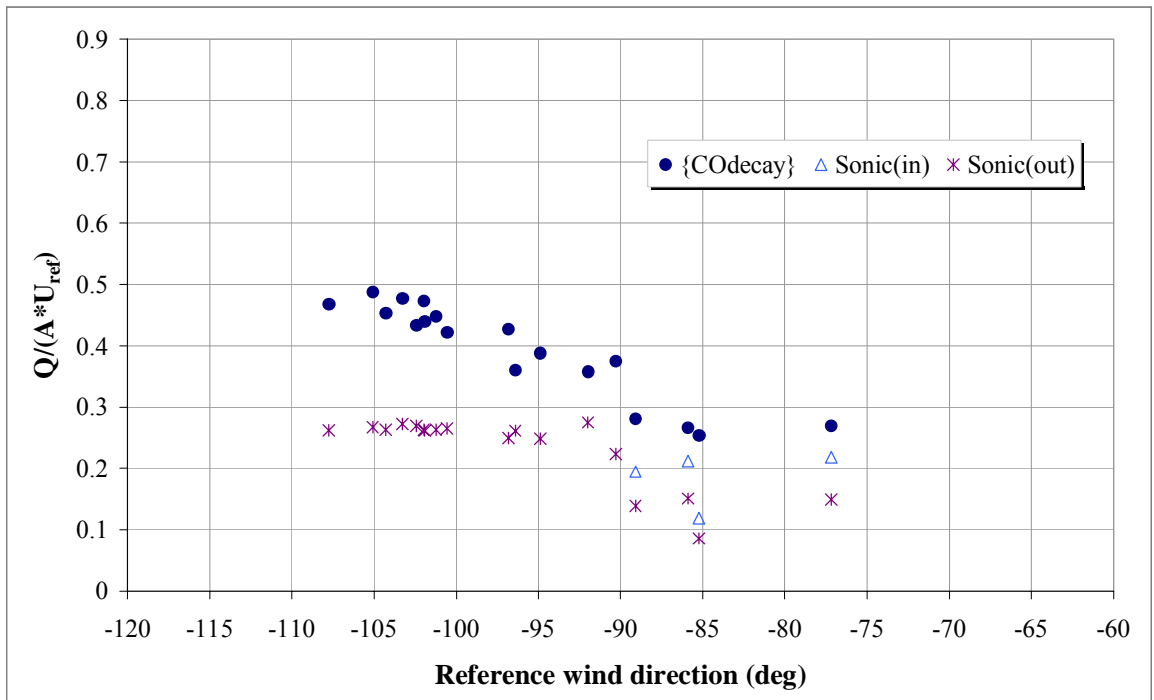
**Table 7-5 Nondimensional ventilation rates for 75°~110° cases**

19 Test cases 75°~110°		(Q/AU <sub>ref</sub> )			(Q-Q <sub>method1</sub> )/Q <sub>method1</sub> (%)		
		mean	SD	SD/mean(%)	mean	max.	min.
Method 1	{COdecay}	0.40	0.08	20.6	-	-	-
Method 2	{dP}	0.31	0.09	29.1	-22	19	-52
	{dP+dT}	0.31	0.09	27.7	-22	19	-52
Method 3	{dP <sub>taps</sub> +dT}	0.41	0.08	19.4	2	36	-22
Method 4	Sonic(in)	0.25	0.11	44.4	-38	-16	-53
	Sonic(out)	0.23	0.06	24.3	-42	-23	-66

It can be seen in Figure 7-17 that the total flow rate gradually increases as the wind direction changes from -85° to -105°. Again, the cube was located about 200m behind several blocks of buildings. Under this circumstance, all measurements recorded 19% to 44% fluctuating data. Method 2 showed large disagreement with method 1 & 3 between -95° to -110°. This is probably because both openings can be an inlet or outlet at different times, and the pulsating inflow and outflow cancel out the mean pressure drop across the openings.



(a) Measured ventilation rates by method 1 {COdecay}, method 2 {dP} & {dP+dT} and method 3 {dP<sub>taps</sub>+dT}



(b) Measured ventilation rates by method 1 {COdecay} and method 4 {Sonic(in) & Sonic(out)}

Figure 7-17 Nondimensional ventilation rates at wind directions 75°~110°

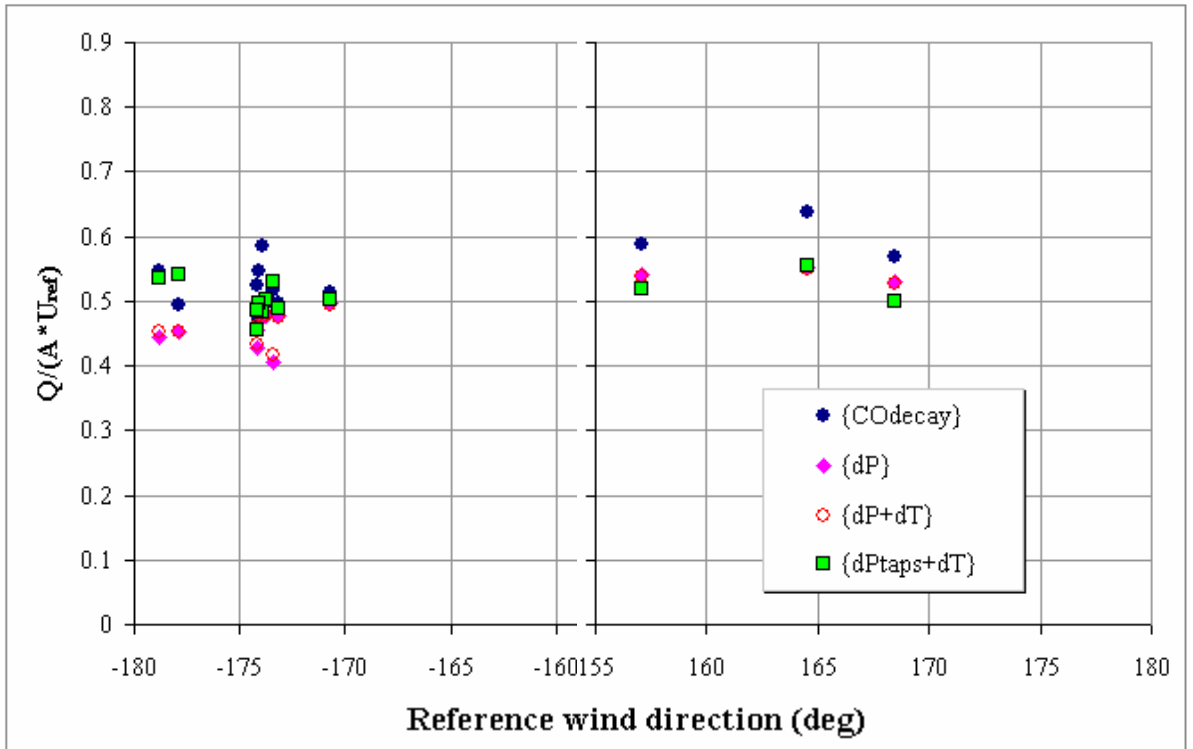
### 7.5.3.4 Wind directions at 155°~180° cases

When the wind blew into the cube through the high level opening, i.e. 155°~180° cases, the total ventilation rates were  $0.54 \pm 0.05$  which is generally lower than 0°~30° cases (in Table 7-3). With the opening discharge coefficient chosen as 0.6, the mean flow rate estimated by method 3 under-predicted by 6% of the total flow rate measured by method 1 (see Table 7-6).

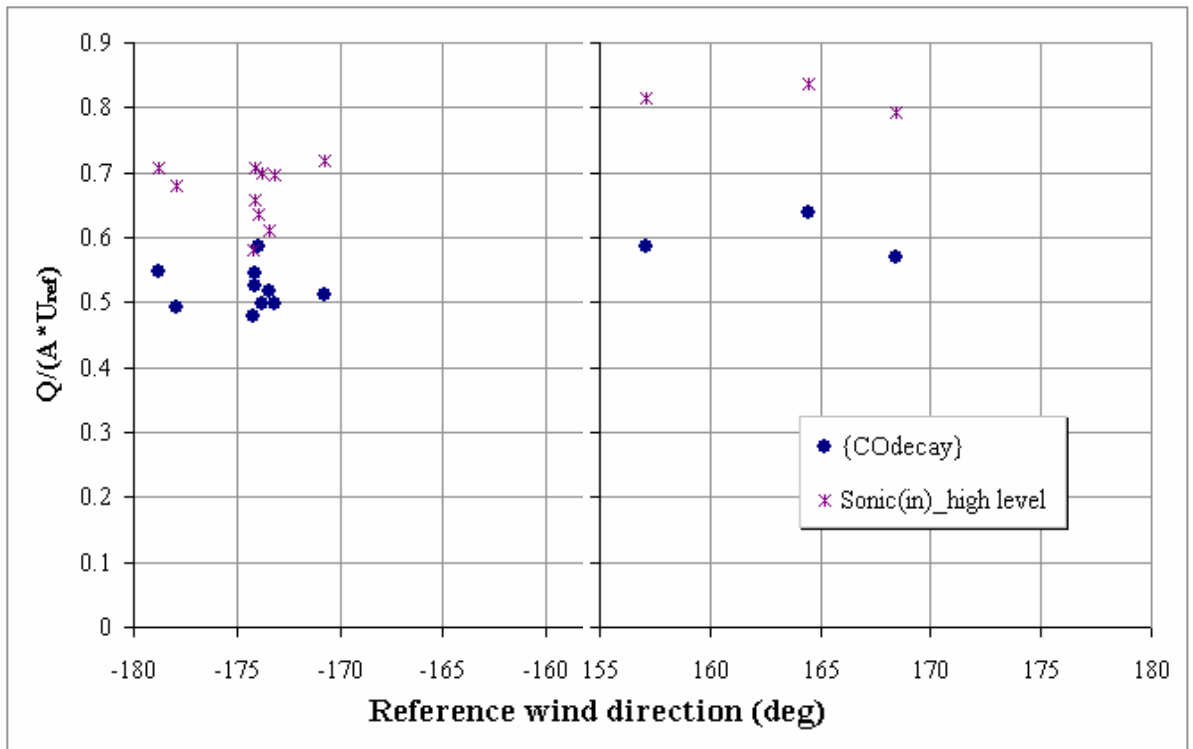
**Table 7-6 Nondimensional ventilation rates for 155°~180° cases**

13 Test cases 155°~180°		(Q/AU <sub>ref</sub> )			(Q-Q <sub>method1</sub> )/Q <sub>method1</sub> (%)		
		mean	SD	SD/mean(%)	mean	max.	min.
Method 1	{COdecay}	0.54	0.05	8.6	-	-	-
Method 2	{dP}	0.48	0.04	9.1	-11	-3	-22
	{dP+dT}	0.48	0.04	8.3	-11	-4	-19
Method 3	{dP <sub>taps</sub> +dT}	0.51	0.03	5.5	-6	10	-18
Method 4	Sonic(out)	-	-	-	-	-	-
	Sonic(in)_high level	0.70	0.08	10.7	31	41	9

Figure 7-18 shows that results by method 1, 2 & 3 agree well for the 155°~180° cases, which had a maximum 1°C indoor & outdoor temperature difference with the mean speed of 2.6 m/s. The inflow mean speed measurement at the high level opening by method 4 over-predicted the total flow rate by 31% on average. It should be noted that the upstream fetch in these cases was not as smooth as 0°~30° cases, as there were crop fields near the test cube. The rougher ground condition might cause a reduction in the wind speed. So to give better agreement with data by method 1 the opening discharge coefficient was selected as the theoretical value (0.6) not as high as 0.77 for the 0°~30° cases.



(a) Measured ventilation rates by method 1 {COdecay}, metho 2 {dP} & {dP+dT} and method 3 {dP<sub>taps</sub>+dT}



(b) Measured ventilation rates by method 1 {COdecay} and method 4 {Sonic(in) & Sonic(out)}

Figure 7-18 Nondimensional ventilation rates at wind directions 155°~180°

## 7.6 Summary of Field Study

The total or effective ventilation rate equals the mass of air entering or leaving the ventilated space and includes both mean and turbulent flows. The tracer gas decay method, called Method 1, provides the direct measurement of the total ventilation rate. Meanwhile, three other methods were also applied to obtain the mean ventilation rates:

Mean ventilation rates were calculated using the simple pseudo-steady envelope flow model in the design code [BSI 1991] with the measured data of

- (i) Method 2 - mean static pressure and temperature difference between openings,
- (ii) Method 3 - mean surface pressure difference around each opening,

Method 4 evaluates the mean ventilation rate by the mean flow speed measurement at the centre of each opening.

From Tables 7-3,4,5&6 (summarised in Appendix B, pB2) it can be seen that the variation of the tracer decay method was about 9% for wind directions perpendicular to the vent openings and within 30° range. It has been quoted by Standberg and Blomqvist [1985] that the accuracy of the tracer decay method should be about 10%~15% for building ventilation measurement. For wind directions around 45°±15° and 90°±20° in the present investigation, the upwind fetch conditions were not ideally uniform, and method 1 recorded the total flow rate through the cube with a 21% error band.

In the case of 0°~30° wind directions with the simple envelope model, the choice of discharge coefficient as 0.77 rather than the theoretical value of 0.6 in methods 2 & 3

would give good agreement to method 1. For the  $180^\circ$  wind direction, the relatively rougher upstream fetch causes the reduction of the wind speed, therefore the discharge coefficient value of 0.6 used in methods 2 & 3 gave better agreement with method 1. For the cases around  $45^\circ$ , the discharge coefficient as 0.75 was found to predict better results agreed to method 1. For the  $90^\circ$  cases, the discharge coefficient value of 0.6 was chosen to give an over-prediction of 2% by method 3 compared to method 1.

In all test periods, method 3 had similar or even lower variances than method 1, and up to 6% under-estimation and 2% over-estimation of the total flow rate for all wind directions.

Method 2 predicted that the mean ventilation rates were around 8% lower than the measurements made by method 1 for around normal wind directions. The results of  $45^\circ$  and  $90^\circ$  wind directions showed 16% and 29% discrepancy with method 1.

Due to the complicated flow profile through the openings, method 4 showed inconsistent results for the mean speeds at the centre of the openings. To obtain detailed velocity profiles, more probes should be placed within the opening. However, this may distort the real flow profile.

Comparatively speaking, method 3 would be the best choice amongst the methods for engineering design practice, because of its practical applicability with available design techniques, such as wind tunnel modelling and CFD simulations.

# **Chapter 8    Comparison of Results for CFD and Full-scale Tests**

## 8.1 Introduction

This chapter presents CFD predictions along with a selection of the experimental measurements (Chapter 7) for the Silsoe cube. Interest is focussed mainly upon the mean ventilation rates through the cube for wind directions of  $0^\circ$ ,  $10^\circ$ ,  $30^\circ$ ,  $90^\circ$  and  $180^\circ$ . It should be borne in mind that the measured indoor and outdoor temperature differences were well below  $8^\circ\text{C}$  in the full-scale tests, whilst the CFD simulations were performed under wind effect only. However, in previous chapter thermal effects were shown to be adding only 2% to the mean ventilation rates.

It has been shown in Chapter 7 that experimental method 1 of CO decay measurement recorded the nondimensional total ventilation rate as  $0.63\pm 0.05$  for  $0^\circ$  case. Meanwhile, experimental method 3 (Section 7.5.2.3) applying the simple pseudo-steady envelope flow model by taking surface pressure records at the tapping points near openings, estimated the nondimensional ventilation rate as  $0.61\pm 0.04$ . The error band of these two methods was 8% and 6% (see Table 7-3) respectively. The relative difference between these two methods was 3%, which possibly indicated the turbulence effect on the mean flow.

In Chapter 6, the CFD predictions (see Figure 6-9) of the surface pressure at the tapping points near openings on the coarse grid (Grid15) showed 3% (or 8%) difference at the lower (or higher) opening from the reference results on the fine grid (Grid40). Hence, the CFD solutions on the coarse grid fit in the potential range of error for the full-scale data. Therefore it is satisfactory to obtain the parametric CFD results using the standard  $k-\varepsilon$  model on the coarse grid (Grid15) converged to  $1\times 10^{-4}$  (RMS).

## 8.2 Measured Ventilation Rates and CFD Predictions

In total 47 CFD simulations were performed under various wind directions in line with the full-scale experimental data. These were divided into 5 groups and are listed in Table 8-1. The comparisons of the full-scale measured and CFD predicted ventilation rates are presented according to the wind direction range for  $0^{\circ}\sim 30^{\circ}$ ,  $90^{\circ}$  and  $180^{\circ}$  in the following sections.

**Table 8-1 Experimental values selected for CFD simulations**

Test	Wind direction				
	$0^{\circ}$	$10^{\circ}$	$30^{\circ}$	$90^{\circ}$	$180^{\circ}$
No. of cases	9	16	6	3	13
$U_{ref}$ (m/s)	3.51 ~ 5.12	2.97 ~ 5.61	2.70 ~ 5.58	3.81 ~ 4.55	2.64 ~ 4.51
dT ( $^{\circ}$ C)	0.8 ~ 5.6	-0.9 ~ 8.0	-1.0 ~ 4.6	0.4 ~ 2.3	-1.2 ~ 0.7

CFD simulations have only considered wind effects. Firstly, the mean pressure differences across the two openings were calculated from the points 0.5m apart from the centre of each opening. Secondly, the mean ventilation rates were obtained by method 3 (Section 7.5.2.3).

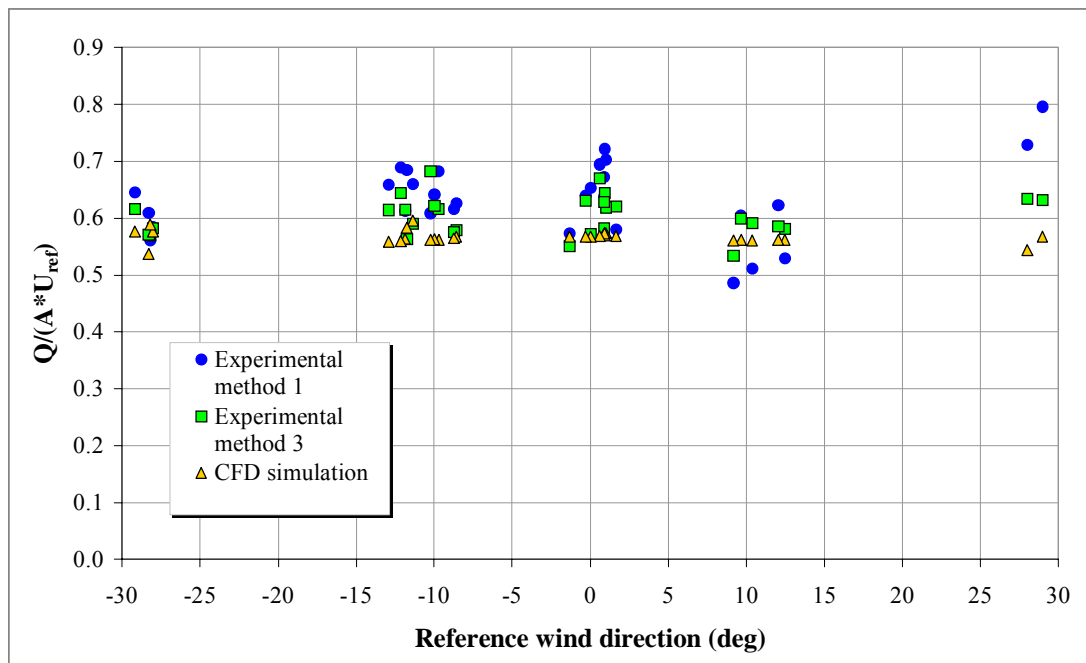
### 8.2.1 Wind directions between $0^{\circ}\sim 30^{\circ}$

Figure 8-1 shows the nondimensional ventilation rates for cases of  $0^{\circ}\sim 30^{\circ}$ . In general, the CFD simulations under-predict the effective ventilation rates and give rather constant mean values of 0.57, 0.566 and 0.565 for wind directions around  $0^{\circ}$ ,  $10^{\circ}$  and  $30^{\circ}$  respectively. The value of discharge coefficient was chosen as 0.77 for both experimental method 3 results and the CFD predictions of the mean ventilation rates for  $0^{\circ}\sim 30^{\circ}$  cases.

More scattered experimental data were found around  $+10^\circ$  and  $+30^\circ$  cases than  $-10^\circ$  and  $-30^\circ$  cases (Figure 8-1). From the test records around  $+10^\circ$  and  $+30^\circ$  on 11 Mar 02 and 11 July 02, it was found that the fluctuating wind pressures had significant effects on the mean flow rates. On these days, the ratio of the flow rate parameter

$$\frac{Q}{AU_{ref} \sqrt{dC_{p\_SD}}} \text{ against } \frac{dC_{p\_mean}}{dC_{p\_SD}}$$

unsteady wind effects on mean flow rates were noticeable [Etheridge 2002b].



**Figure 8-1 Measured and predicted nondimensional ventilation rates at  $0^\circ$ ~ $30^\circ$**

A closer inspection of the ventilation rates around  $0^\circ$  in Figure 8-2, shows that on average CFD gave predictions 12% lower than experimental method 1 (tracer decay method) and 7% lower than experimental method 3 (surface pressure difference method).

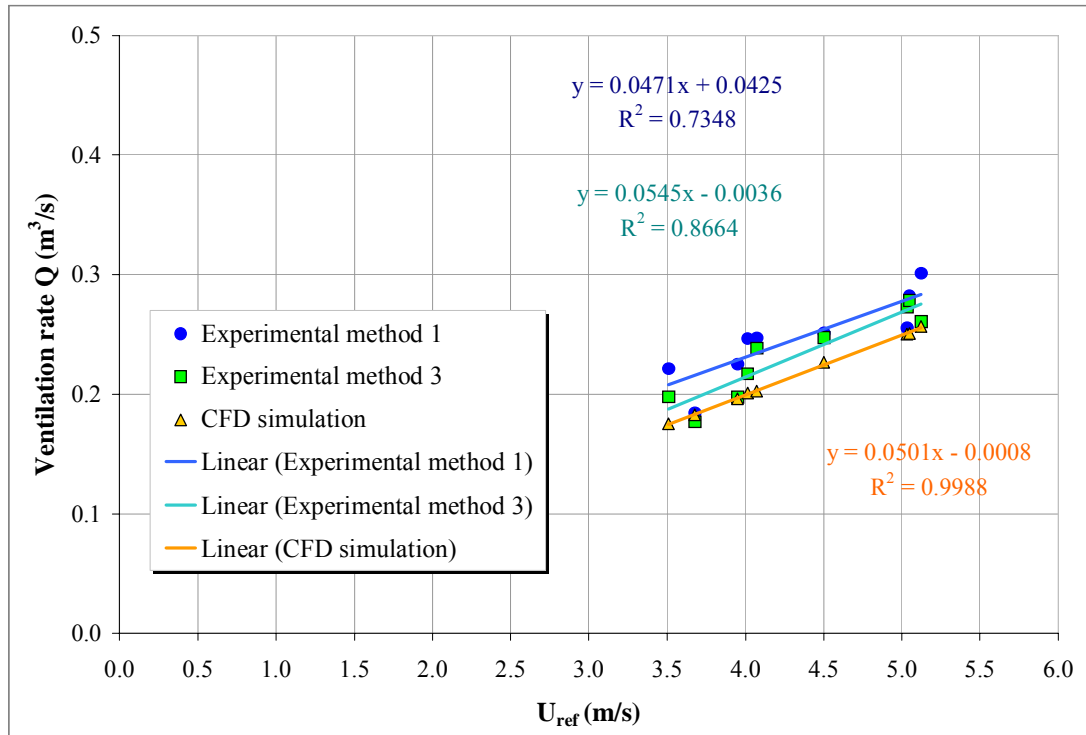


**Figure 8-2 Measured and predicted ventilation rates around  $0^\circ$**

Similar findings were also observed for the  $10^\circ$  and  $30^\circ$  cases in Figures 8-3 & 8-4. The CFD results were 8% (or 6%) lower than those obtained by experimental method 1 (or method 3) around  $10^\circ$  and mean CFD values were 11% (or 5%) lower than the field measurements around  $30^\circ$  by experimental method 1 (or method 3).

The best fitting trend lines for all data in Figures 8-2, 3 & 4 show that the ventilation rates increase with increasing wind speed as expected. A higher value of the coefficient of regression  $R^2$  can be found for the CFD results, which indicates that CFD predictions are less scattered than the experimental data. Therefore, it can be stated that fewer CFD modelling data is needed to extract the trend under specific weather conditions.

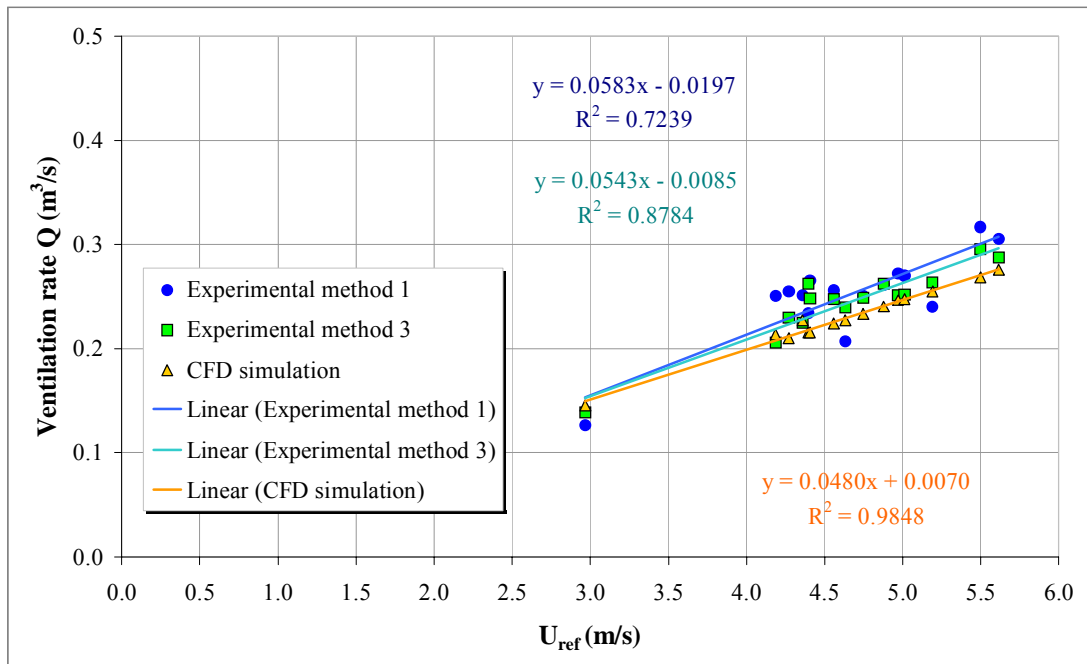


**Figure 8-3 Measured and predicted ventilation rates around 10°**

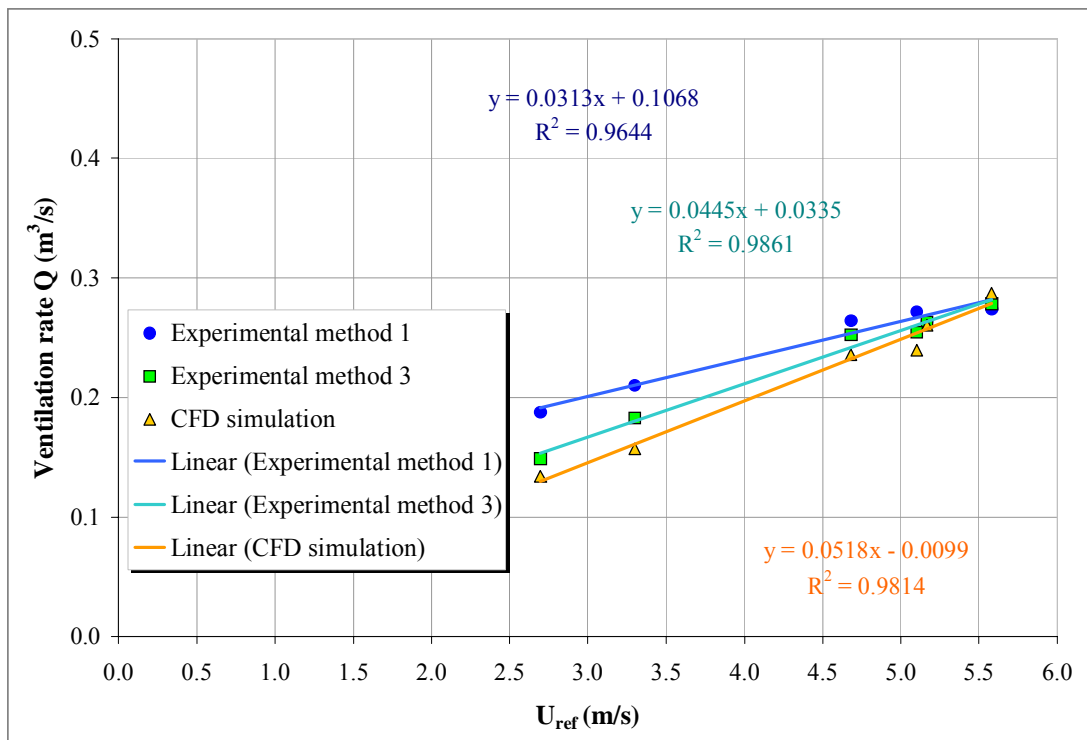


**Figure 8-4 Measured and predicted ventilation rates around 30°**

There appear to be some changes in trend with wind direction (Figures 8-2, 8-3 & 8-4) but it is not clear whether there are real effects or due to lack of data. In particular at a wind direction of  $30^\circ$ , there is less ventilation rate predicted by CFD than measurements when wind speed is less than 3.5 m/s. When wind approaches to the building at such an angle, the flow field around the building, especially at sidewalls and in the wake, has more complex features than the normal case. Apart from turbulence flow field around the openings, the overall complicated flow structure can not be fully described by the standard  $k-\varepsilon$  model.

### **8.2.2 Wind directions at $90^\circ$**

It is apparent in Figure 8-5 that CFD assessment of the mean ventilation rate at the wind direction about  $90^\circ$  shows about 71% under-prediction of the experimental measurements by both tracer decay and pressure difference methods. In this case, the actual surface pressure difference was mainly caused by turbulent fluctuations in the wind, which could not be picked up by the time-averaged, steady-state CFD simulations. Moreover, the standard  $k-\varepsilon$  model is not able to capture the dominant mechanisms around the cube side walls, e.g. the unsteady separation and reattachment of flow.

In terms of the measured surface pressures, the magnitude of the fluctuating component was very much higher than the magnitude of mean pressure.

Consequently, the accuracy of the pressure difference data was very much lower than the  $0^\circ$  wind direction cases. Therefore, RANS model is not able to simulate the flow field of  $90^\circ$  case correctly.

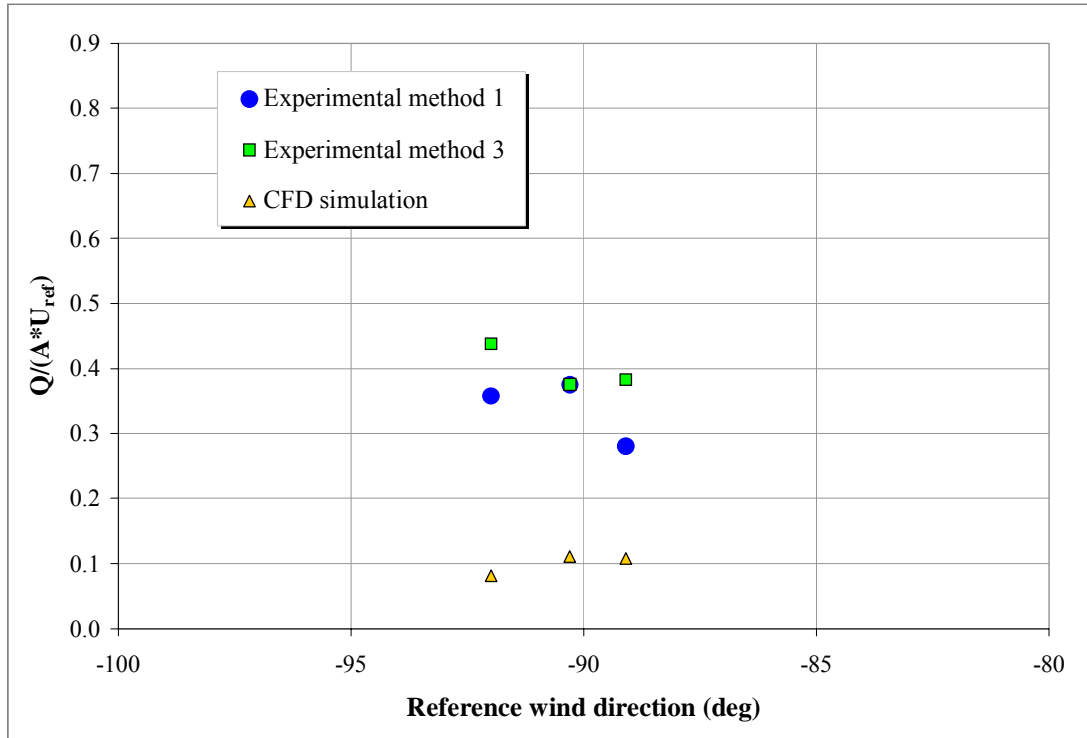


Figure 8-5 Measured and predicted nondimensional ventilation rates around 90°

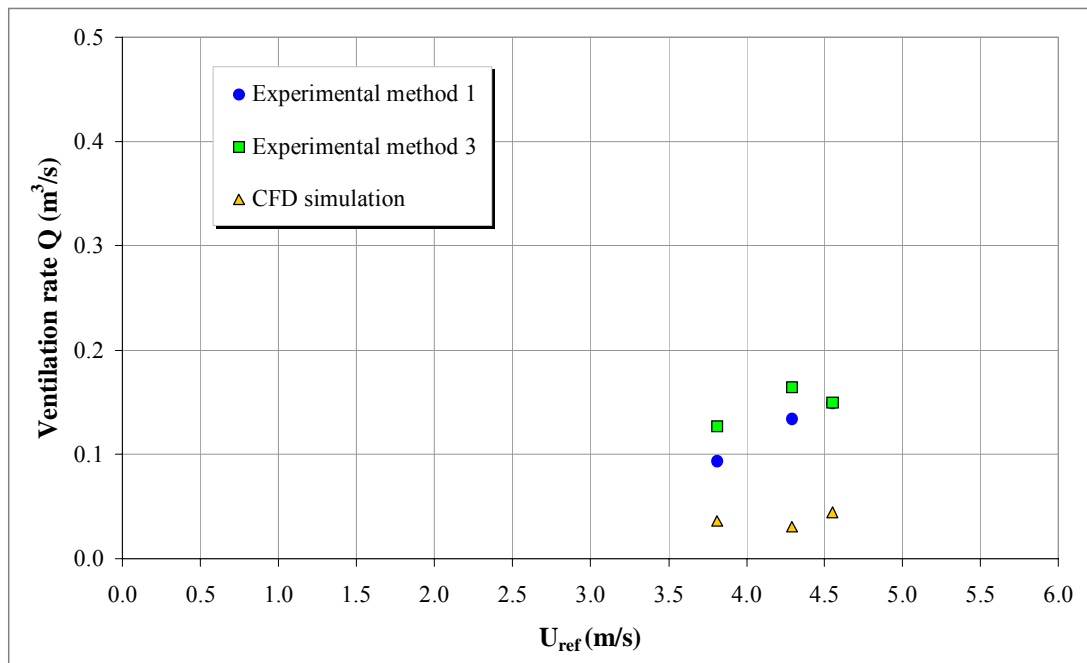


Figure 8-6 Measured and predicted ventilation rates around 90°

### 8.2.3 Wind directions at 180°

Figure 8-7 compares CFD simulation data with experimental measurements at 180° cases. The nondimensional ventilation rates from the CFD results had an almost constant value of 0.50. It should be noted that the experimental data were recorded at a wind direction with some buildings and growing crops on the upstream fetch. In these circumstances, the reference mast was located in the wake region of the cube.

The comparison in Figure 8-8 shows that the CFD results for mean ventilation rates agree well with the measurements, within 6.5% (or 1.4%) underprediction from the experimental method 1 (or the experimental method 3). The full-scale data were not scattered much although the upstream terrain was not uniform. It is more probable that the resulting surface pressure by the incoming flow around the high level opening had less turbulent effect than the inflow through the lower level opening.

For 180° cases the thermal effect suppressed wind effect rather than enhanced it, also the outgoing flow from the low level opening has to overcome the recirculation flow in the wake region. Therefore it is reasonable to choose a different value of discharge coefficient than for the 0° case and the choice of 0.6 agreed with the field data well.

### 8.3 Discussion

The wind induced mean ventilation rates predicted by CFD simulations compared well to the field measurements at wind directions of 0°, 10°, 30° and 180°. Without considering the minor temperature difference effect (maximum temperature difference 8°C) CFD results under-predicted the total effective flow rates through the building by up to 12%. Without taking account for opening geometry or cross flow effects, and applying the discharge coefficient as 0.77 (rather than the theoretical

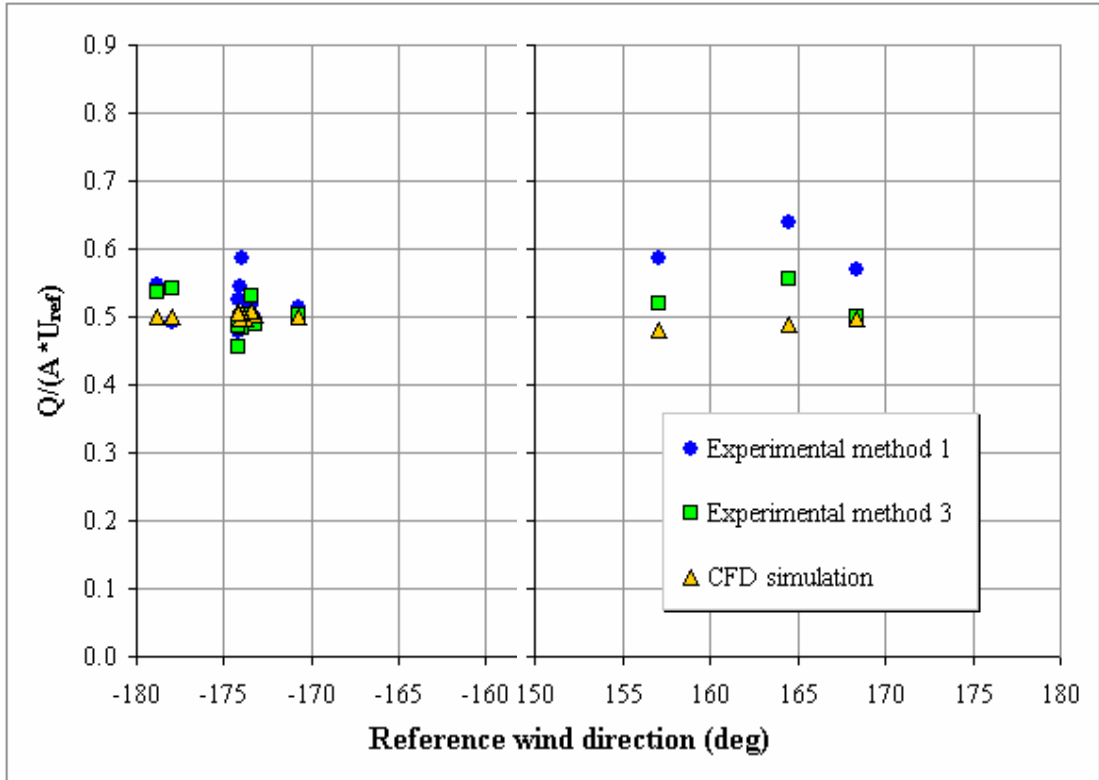


Figure 8-7 Measured and predicted nondimensional ventilation rates around  $180^\circ$

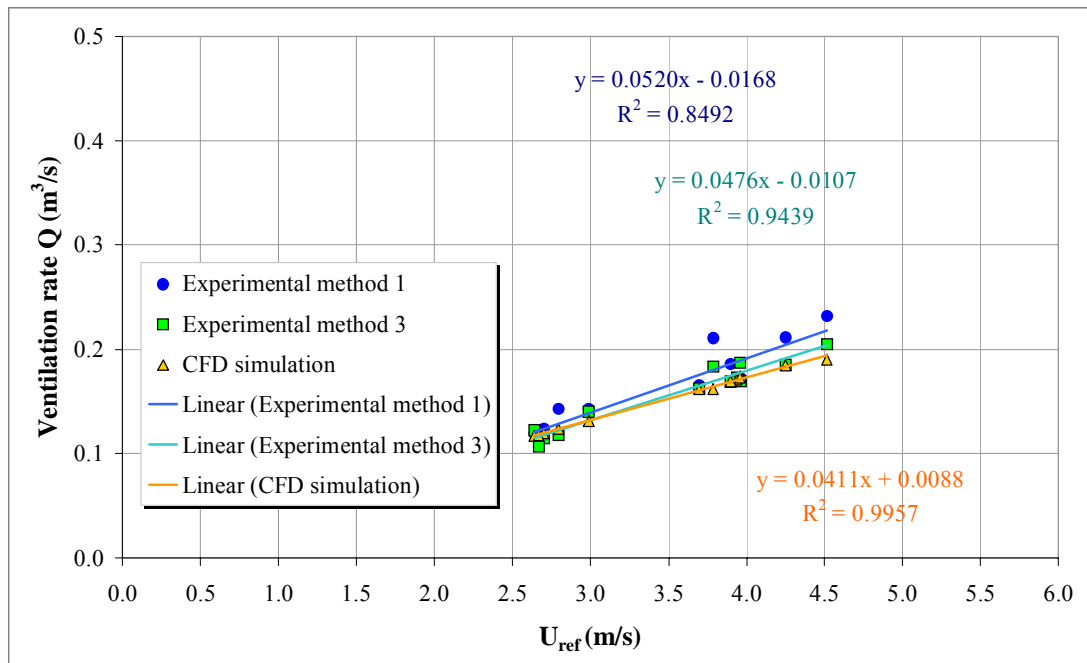


Figure 8-8 Measured and predicted ventilation rates around  $180^\circ$

value 0.6), CFD results underpredicted the total ventilation rates by 7% compared with the field measurements for  $0^{\circ}\sim 30^{\circ}$  cases.

For the  $180^{\circ}$  cases, CFD simulations with the discharge coefficient chosen as 0.6 a 8% (or 2%) underestimation of the measured total (or mean) ventilation rates.

In the  $90^{\circ}$  cases, CFD results accounted for less than 30% of actual ventilation rates.

When flow is parallel to the opening, the pulsation of the turbulent field around it and eddy penetration increases the flow through the opening. RANS model's averaging procedure cancels out the variation of pressure difference caused by turbulence. The application of time dependent CFD simulations with more sophisticated turbulence models, such as Large Eddy Simulation, would help to represent the turbulent flow field and therefore ventilation fluctuations with time.

For the wind direction of  $0^{\circ}$ , the mean component of ventilation flow was found to be significantly greater than the fluctuating component. Therefore, CFD predicted mean ventilation rates showed close agreement to the measured total ventilation rates. When the turbulent fluctuating component has a dominant role, for example when the wind direction is parallel to the openings, a RANS model would not give satisfactory predictions of the ventilation rates.

## **Chapter 9    Conclusions**

This investigation had been carried out to obtain a better understanding of natural ventilation in a 6m cubic building with two small openings, with particular focus on wind effect only and the combination of wind and thermal effects. Computational fluid dynamics (CFD) techniques, envelope flow theories and full-scale experimental studies have been utilised to predict and measure the natural ventilation flow rates in the building.

On a broader perspective, this thesis has provided a greater insight into the coupling of the external flow field and the internal flow of the cubic building. A contribution to the development of an analysis technique has been made and an addition has been made to the small database of information from full-scale testing. The results from this thesis can be used to calibrate similar results from wind tunnel and CFD models and, in conjunction with further work, recommendations for the future improvement of best practice guidelines for natural ventilation can be made.

### **9.1 Summary of Contributions**

The understanding of a naturally ventilated building is important for the successful development of design codes and simulation techniques, such as CFD modelling.

Using the reliable database of measurements collected from experiments at the Silsoe Research Institute, the results of this thesis make a novel contribution to the knowledge of natural ventilation in buildings by means of the following:

- 1) Full-scale testing of cross ventilation in a cubic building with two realistic small size ventilation openings, where four methods have been applied simultaneously for the prediction and measurement of ventilation rates under various weather conditions.
- 2) Feasibility studies of using a fully unstructured grid commercial CFD code

to model natural ventilation induced by wind force merely and the combination of wind and thermal forces in the cubic building.

- 3) Validated unstructured grid CFD predictions of the coupled external and internal flow field for fundamental cross ventilation through two openings at different vertical levels in line with full-scale measurements.

## 9.2 Main conclusions

The major conclusions drawn from this investigation are as follows:

1. Utilising CFD simulated external surface pressure difference close to ventilation openings in the simple envelope flow models stated in design code [BSI 1991], it is found that when wind directions are near normal to the ventilation openings, i.e.  $0^{\circ}$ ~ $30^{\circ}$ , the steady-state RANS model results proved reliable for predicting the total ventilation rate with an error band of  $\pm 12\%$ . When the fluctuating ventilation rate exceeds that due to the mean flow (at around  $90^{\circ}$ ) RANS models were incapable of predicting total ventilation rate. The turbulent kinetic energy ( $k$ ) simulated in RANS models is not taken into account in simple envelope model. Improved results for turbulence dominated flow ventilation prediction can be expected through the inclusion of the turbulence contribution in an envelope flow model or by applying more sophisticated turbulence models capable of resolving unsteady flow features.
2. CFD simulations give detailed information about basic features of indoor flow patterns, including distributions of temperature, air movement and local draught distribution, etc.. Therefore, CFD should be used as flow visualisation for guidance in placing probes in field or model measurements.

3. In a cubic building, two small size ventilation openings (with 0.24% as the ratio of opening area to wall area) located at different vertical level on opposite walls only affect the building surface pressure distribution locally. Therefore the external flow field simulation with a RANS turbulence model is adequate to obtain mean ventilation rates for wind directions ranging  $0^{\circ}\sim 30^{\circ}$ .

### 9.3 Other Conclusions

A number of points regarding the CFD simulations and full-scale studies have also been discovered as follows:

#### 9.3.1 CFD Simulations

This work has clearly demonstrated the good practice of CFD application in terms of computational domain size, grid independency, initial boundary condition settings, turbulence model selection and accuracy target.

1. It is noted that overall the effects of using different turbulence models, using a fully unstructured grid (i.e. CFX5) and other contributions (e.g. grid density) are not easy to distinguish. This can be outlined as the following:
2. The general flow features within the ventilated cube were well represented by both CFX5K-E and CFX5RNG models. The openings only affect the surface pressure distribution around them locally.
3. Applying the simple envelope flow model used in design code [BSI 1991]], the CFD predictions of wind induced ventilation with the standard  $k-\varepsilon$  model agreed well with experimental measurements of mean ventilation rates for wind direction were near normal to the vent openings.

4. The combined wind and convection force induced ventilation rates were studied in CFD with a heater placed at two different locations at medium wind speed (4m/s) for  $0^\circ$  wind direction. With the same amount of heat input, the central placed heater generated a higher ventilation rate than the side placed heater near the low opening, but resulted in lower indoor temperature than the latter case. For wind direction of  $0^\circ$ , better indoor air mixing can be achieved using the centre heater.
5. When the thermal effect is small (e.g. maximum temperature difference  $< 8^\circ\text{C}$ ), neglecting the  $dT$  element would not introduce significant errors and the full-scale test results can be compared with iso-thermal CFD simulations. The results showed under-prediction of the total effective flow rates through the building by up to 12%, which is acceptable in terms of the experimental studies.
6. Without the scattered data usually found in experiments, it can be stated that fewer CFD modelling data is needed to extract the trend under specific weather conditions. Therefore CFD simulation can play an important role for the parametric study of building ventilation in terms of cost efficient design.

### **9.3.2 Ventilation measurements in a full-scale cubic building**

1. Quantitative measurements have been achieved using four experimental methods simultaneously to evaluate the total effective ventilation rates through the test cube.
  - (a) Method 1 – tracer gas method.
  - (b) Method 2 – mean wind static pressure and temperature difference between internal and external
  - (c) Method 3 – mean surface pressure difference around each opening
  - (d) Method 4 – mean flow speed measurement at the centre of each opening.

2. For wind directions of  $0^\circ \sim 30^\circ$  and  $180^\circ$ , the discrepancy in total ventilation rate using method 1 was up to 9%. For wind directions around  $45^\circ$  and  $90^\circ$  method 1 recorded the total flow rates through the cube with a  $\pm 21\%$  error band.
3. In total data for 130 test cases data have been collected and analysed into four groups:  $0^\circ \sim 30^\circ$  (82 cases),  $34^\circ \sim 60^\circ$  (16 cases),  $75^\circ \sim 110^\circ$  (19 cases) and  $155^\circ \sim 180^\circ$  (13 cases). When applying method 2 and method 3, the selections of discharge coefficients for different wind directions were based on individual reasons in order to match the data by measured method 1. The discharge coefficient values used were 0.77 (for  $0^\circ \sim 30^\circ$  wind direction), 0.75 (for  $45^\circ$ ) and 0.6 (for  $90^\circ$  and  $180^\circ$ ) respectively. Further measurements by rotating the cube to face the ideal uniform country fetch are needed to clarify the effect of fetch or the wind turbulence on the selection of the discharge coefficient.
4. The single point speed measurement at the centre of the opening cannot represent the complex velocity profile at the opening. Therefore method 4 results showed the inconsistent values at the lower and the higher opening. Furthermore, compared to method 1 the values of method 4 had much higher percentage error in the mean than method 2 and 3.
5. Comparatively method 3 is the best choice amongst the methods for engineering design practice, because of its practicality with available design techniques, such as wind tunnel modelling and CFD simulations. For the time being due to computing costs and large computer power requirements, for fluctuating ventilation dominant cases, e.g.  $90^\circ$  case, method 1 can be used in wind tunnel to measure total ventilation rate directly, which can provide the most accurate data.

#### 9.4 Recommendations for Future Research

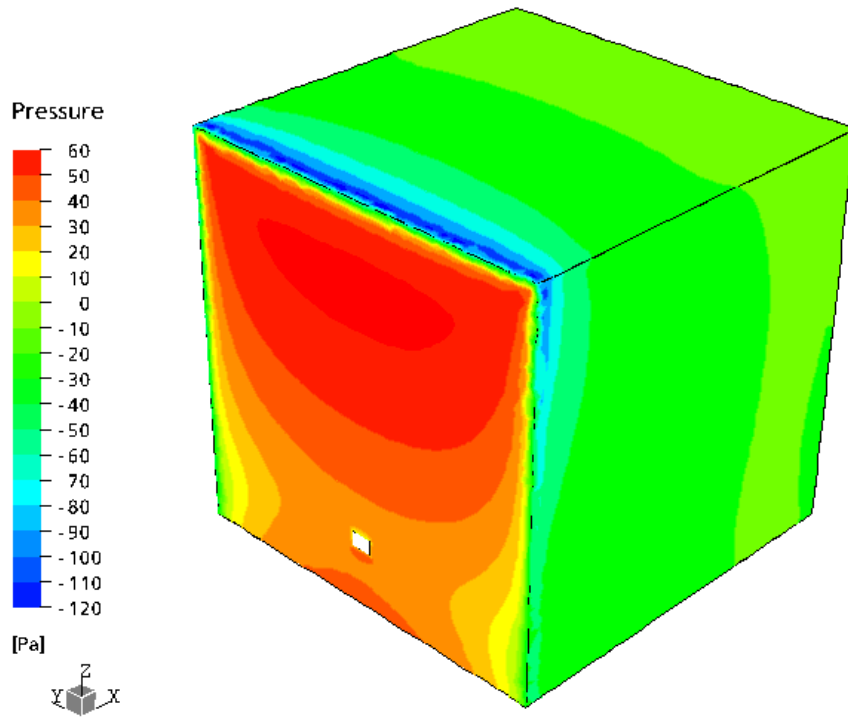
The findings and achievement of the current study have provided many opportunities for further work:

1. Continue the full-scale experimental measurements, especially for the wind direction of  $45^\circ$  and  $90^\circ$ . Collect more data for  $180^\circ$  to examine further the discharge coefficient difference from  $0^\circ$  wind direction found in this work.
2. Parallel wind tunnel experiments using the quarter scale cube model could be conducted in order to fill the gaps in full-scale data, and also investigate the difference for ventilation studies between wind tunnel tests and field tests, e.g. obvious Reynolds number effect [Hoxey et al. 2002].
3. Improved results for turbulence dominant flow prediction are expected by the following methods, which would need further investigation using the obtained field data for validation:
  - (a) including the turbulence contribution by using unsteady envelope flow models [Etheridge 2003], which is relatively simple with quick solutions but extensive knowledge of boundary conditions is needed; or
  - (b) applying more sophisticated turbulence models, e.g. LES, resolving flow development with time [Jiang and Chen 2002], which can predict a more realistic turbulence flow field, but demand considerable computational power and time; or
  - (c) incorporating the automatic facilities within CFD packages to obtain the quasi-steady approximation using  $80^\circ$ ,  $85^\circ$ ,  $95^\circ$  and  $100^\circ$  flow fields simulated by RANS models combined with a weighting factor to calculate the ventilation rate for  $90^\circ$  case could be tested [Richards 2004], which has been validated for wind engineering applications rather than ventilation studies.

4. Improve data output functions within CFX package – built-in internal boundary identifier and precise locator. Perform transient simulation and take account of changing flow direction to perform velocity integration over opening.
5. CFD software developments of parallel code running on a cluster of PCs to include more turbulence models, i.e. non-linear model [Wright and Easom 2003] and LES which are proved to be superior for wind engineering applications [Thomas and Williams 1999].
6. Automatic facilities within CFD package to speed up the parametric studies for optimum design.

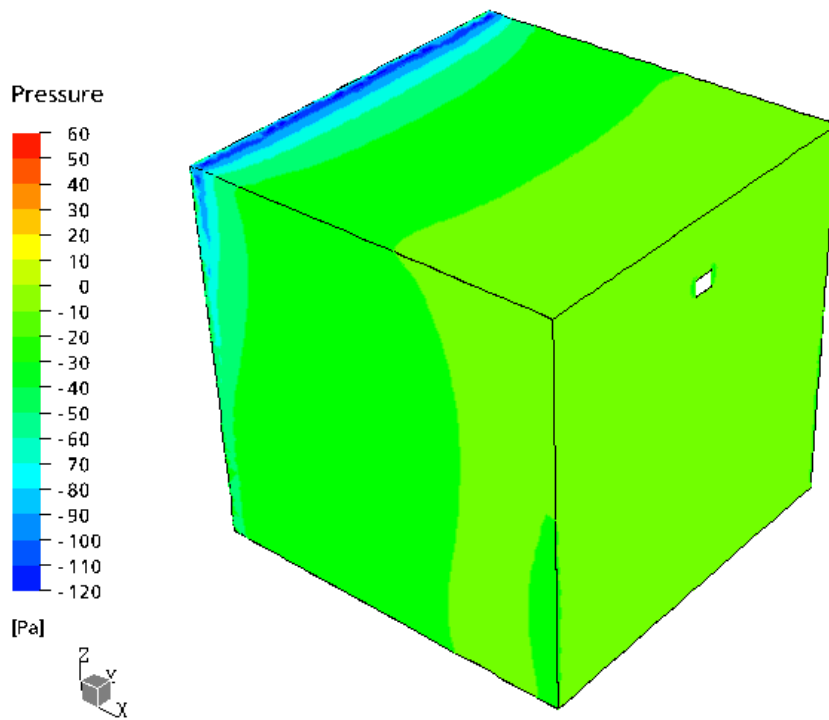
# Appendix A

	Page
Cube surface pressure distribution	A1 ~ A4
Indoor velocity vector plot	A5 ~ A8



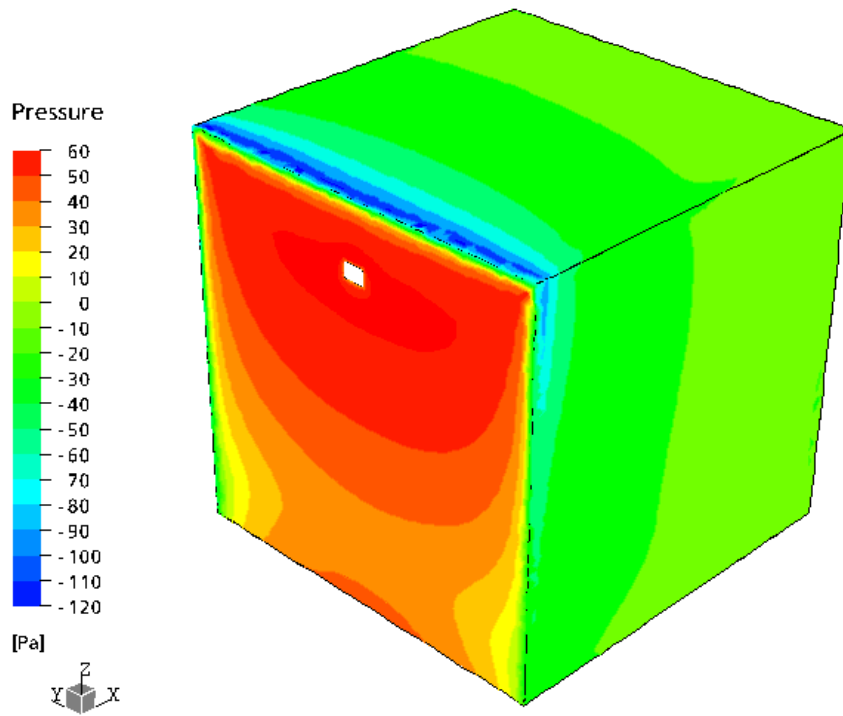
CFX

Figure A-1 Surface pressure distribution1 [0° case]



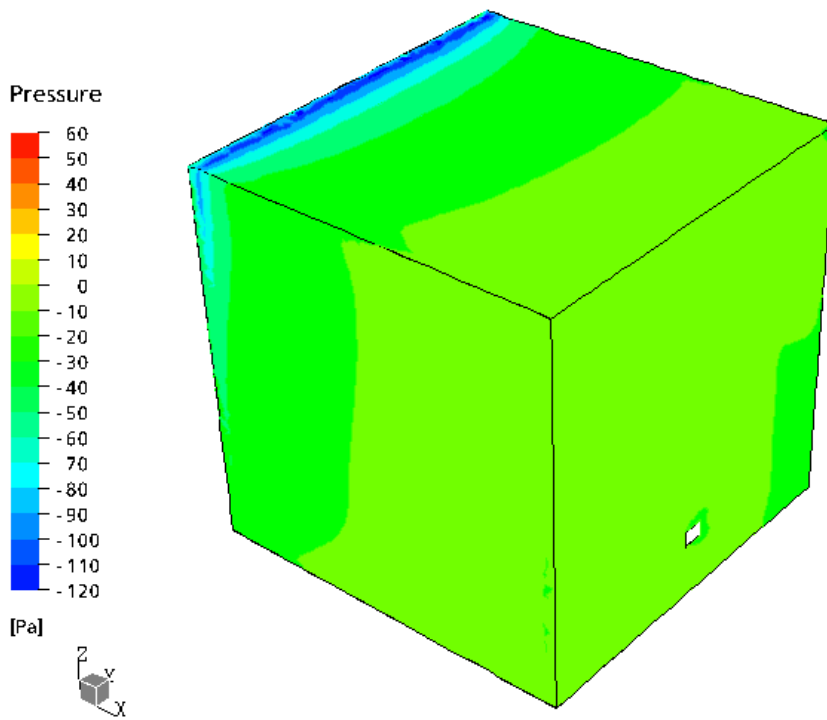
CFX

Figure A-2 Surface pressure distribution2 [0° case]



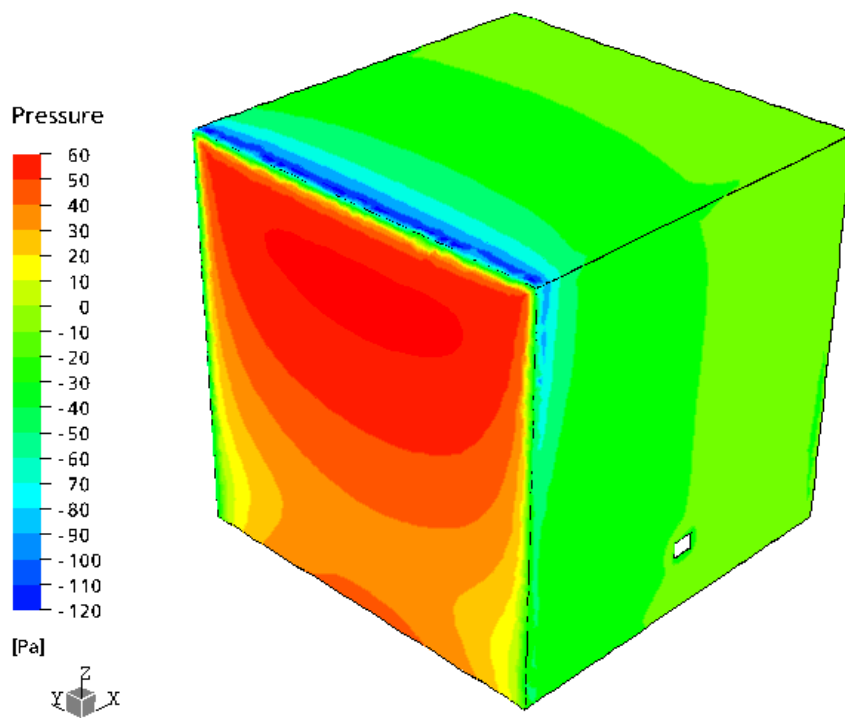
CFX

Figure A-3 Surface pressure distribution1 [180° case]



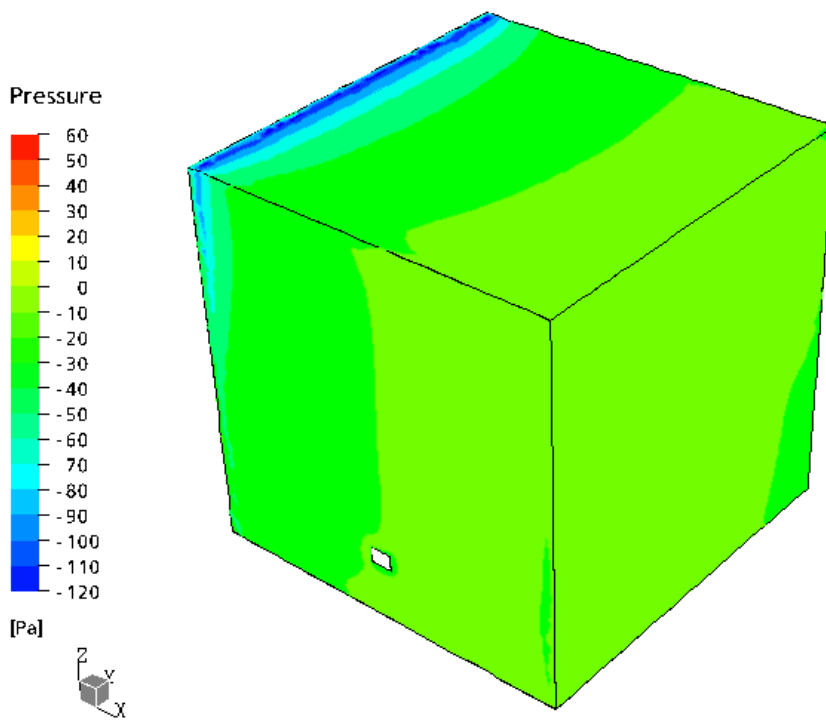
CFX

Figure A-4 Surface pressure distribution2 [180° case]



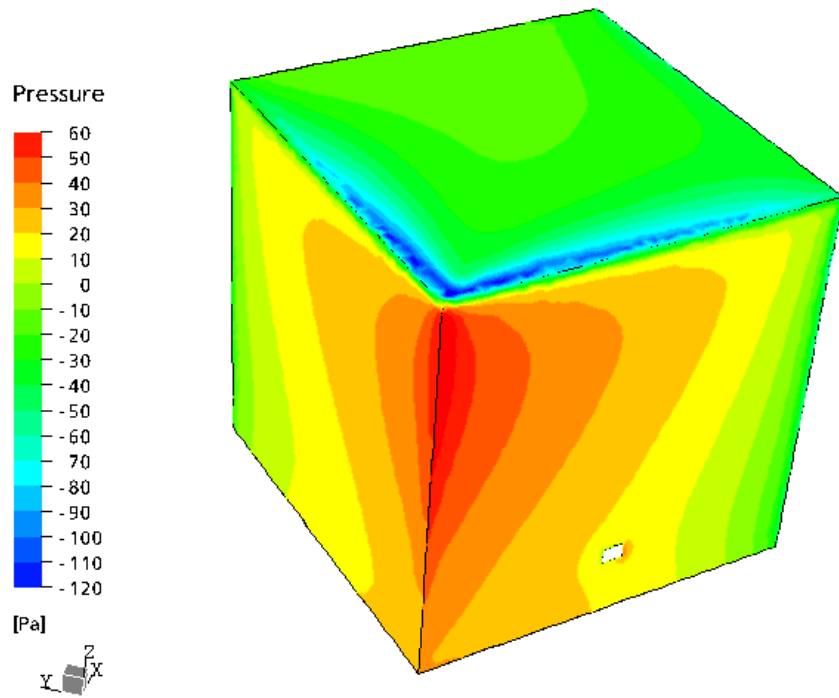
CFX

Figure A-5 Surface pressure distribution1 [90° case]



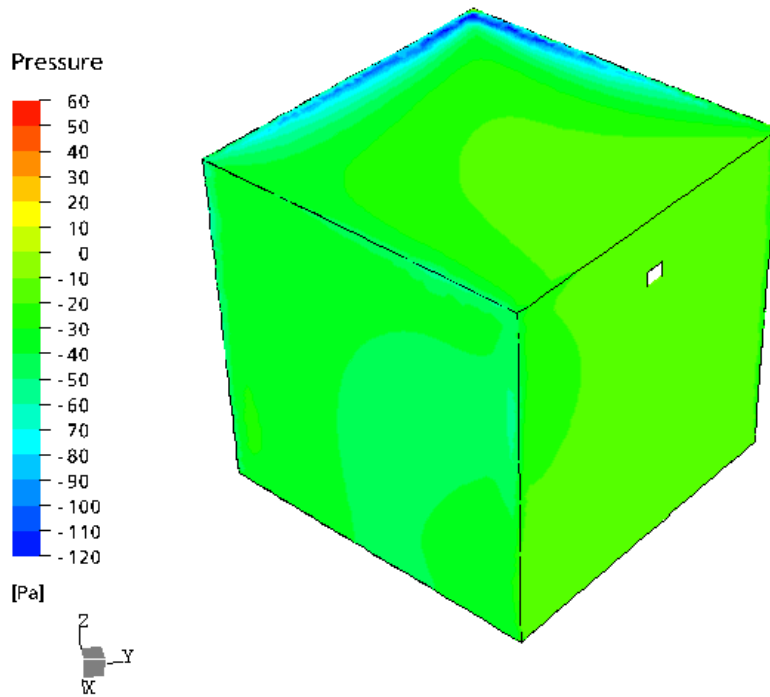
CFX

Figure A-6 Surface pressure distribution2 [90° case]



CFX

Figure A-7 Surface pressure distribution1 [45° case]



CFX

Figure A-8 Surface pressure distribution2 [45° case]

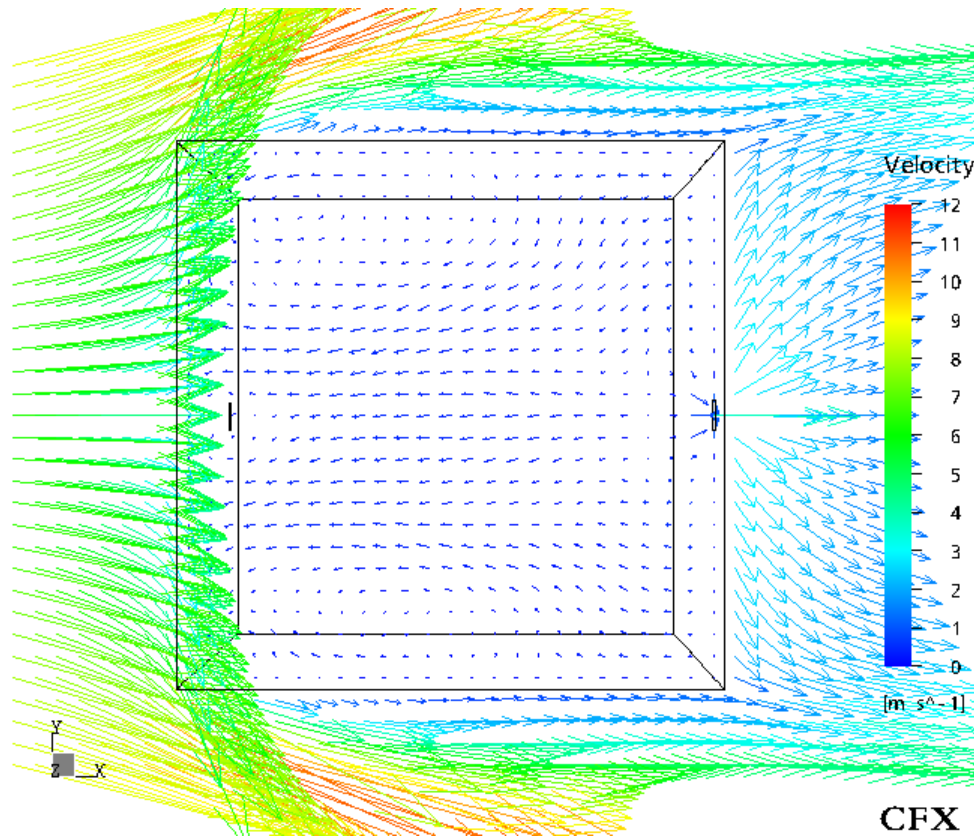


Figure A-9 Velocity vector plot plan view above the ground 5m [0° case]

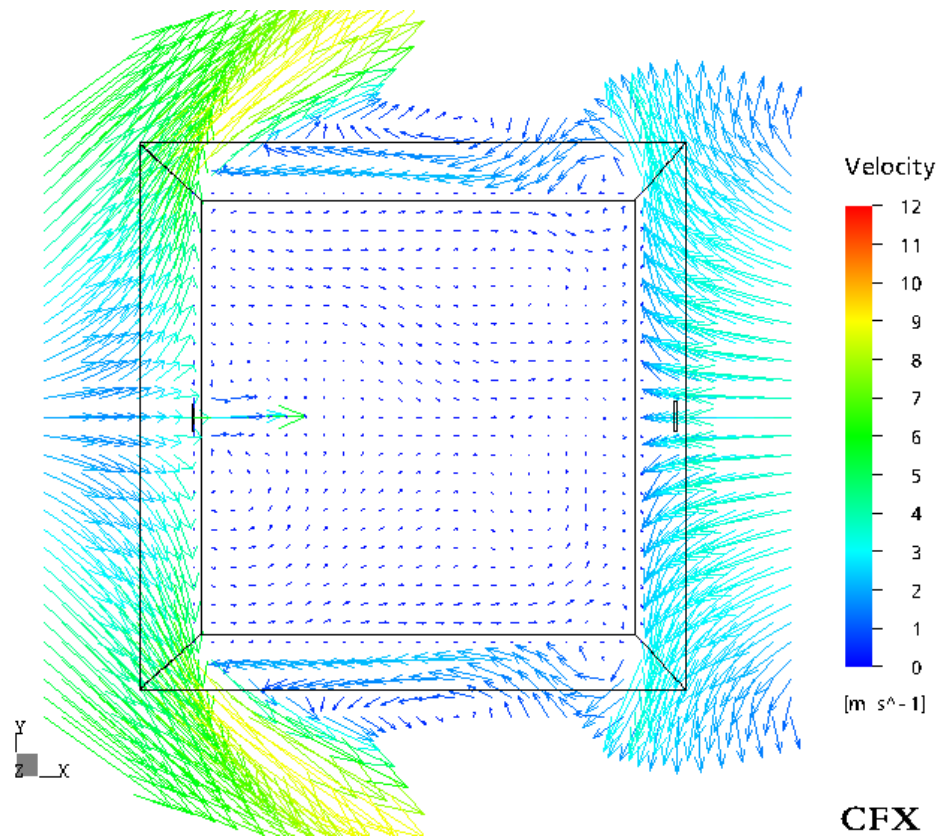


Figure A-10 Velocity vector plot plan view above the ground 1m [0° case]

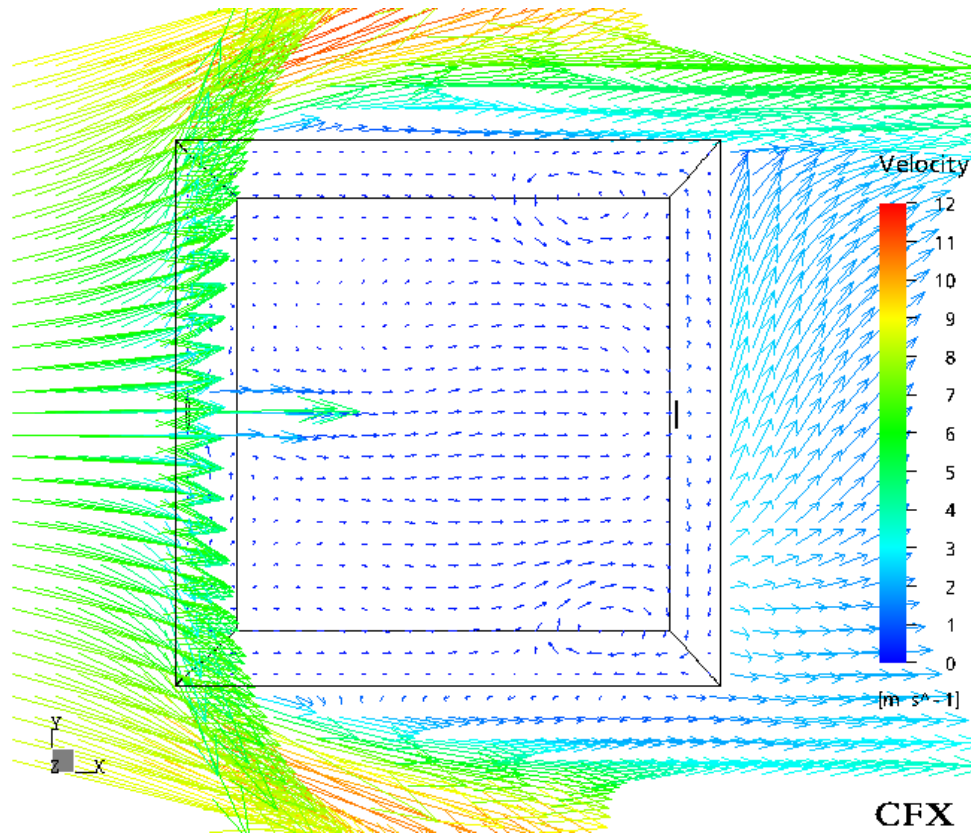


Figure A-11 Velocity vector plot plan view above the ground 5m [180° case]

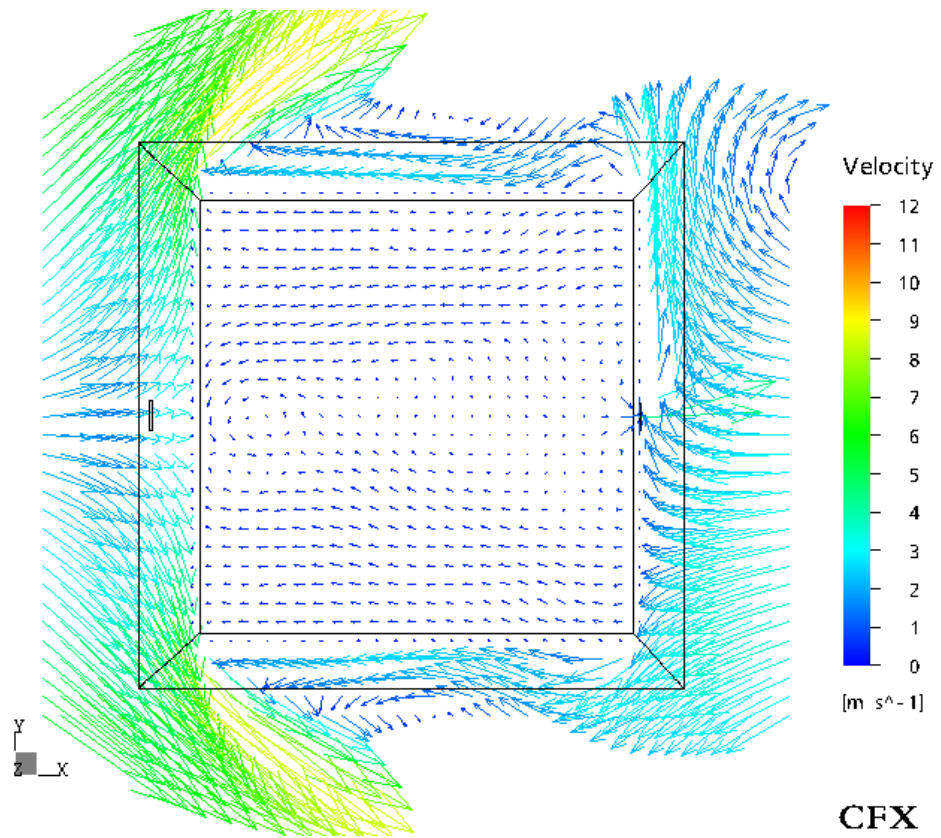


Figure A-12 Velocity vector plot plan view above the ground 1m [180° case]

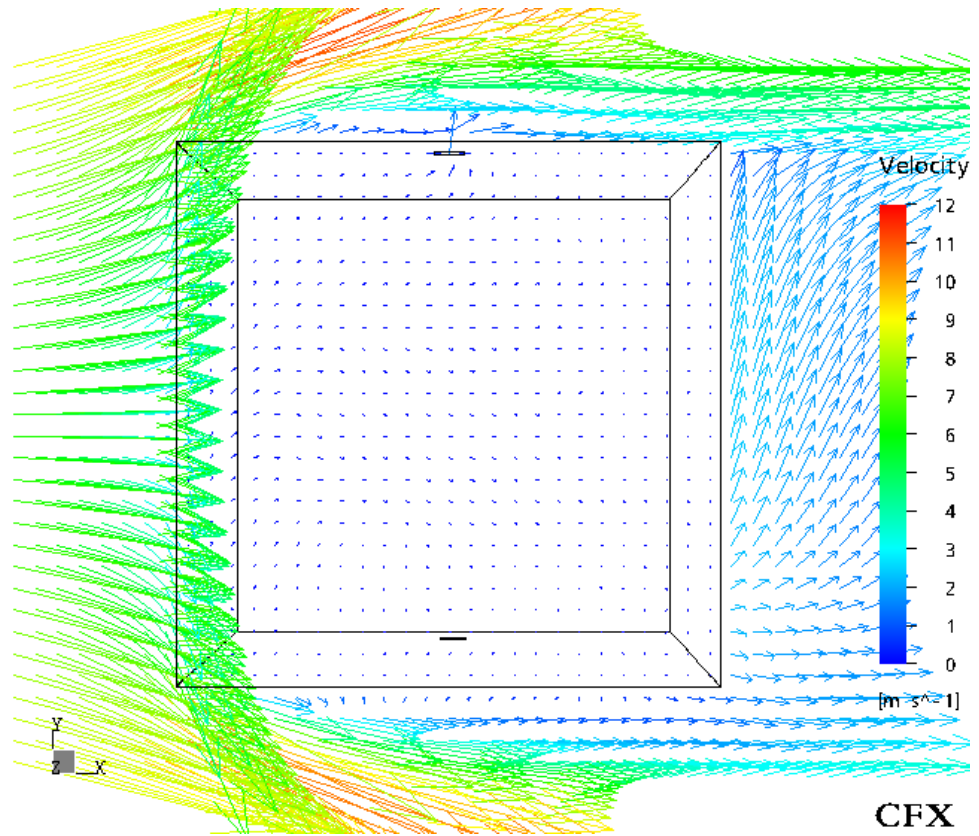


Figure A-13 Velocity vector plot plan view above the ground 5m [90° case]

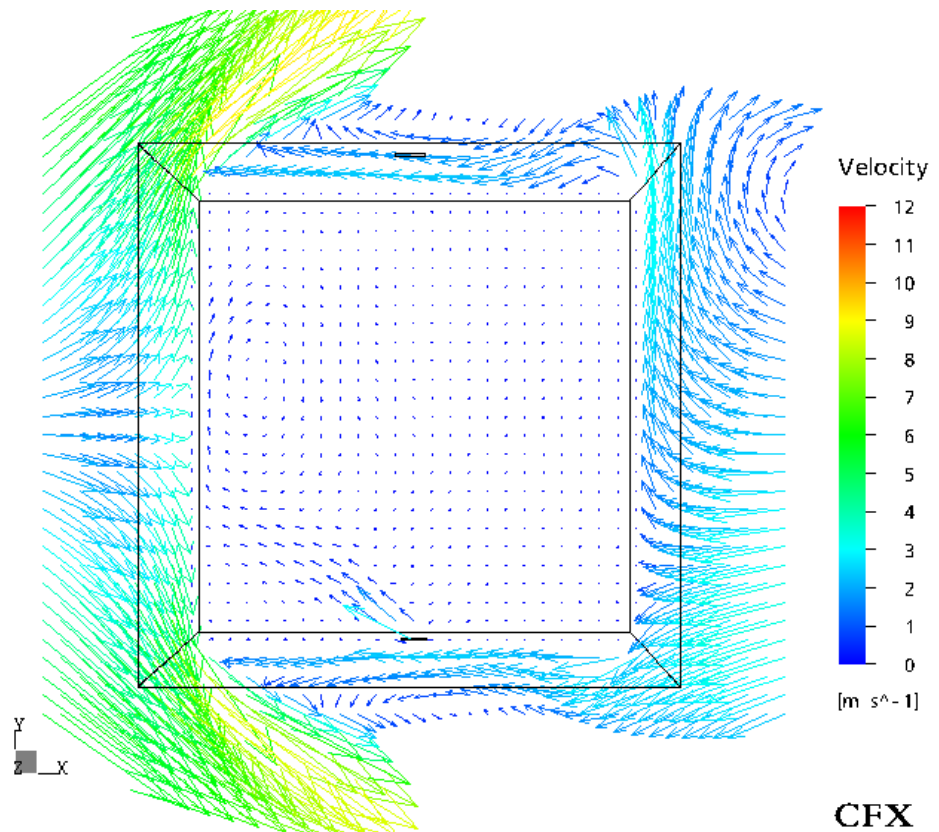


Figure A-14 Velocity vector plot plan view above the ground 1m [90° case]

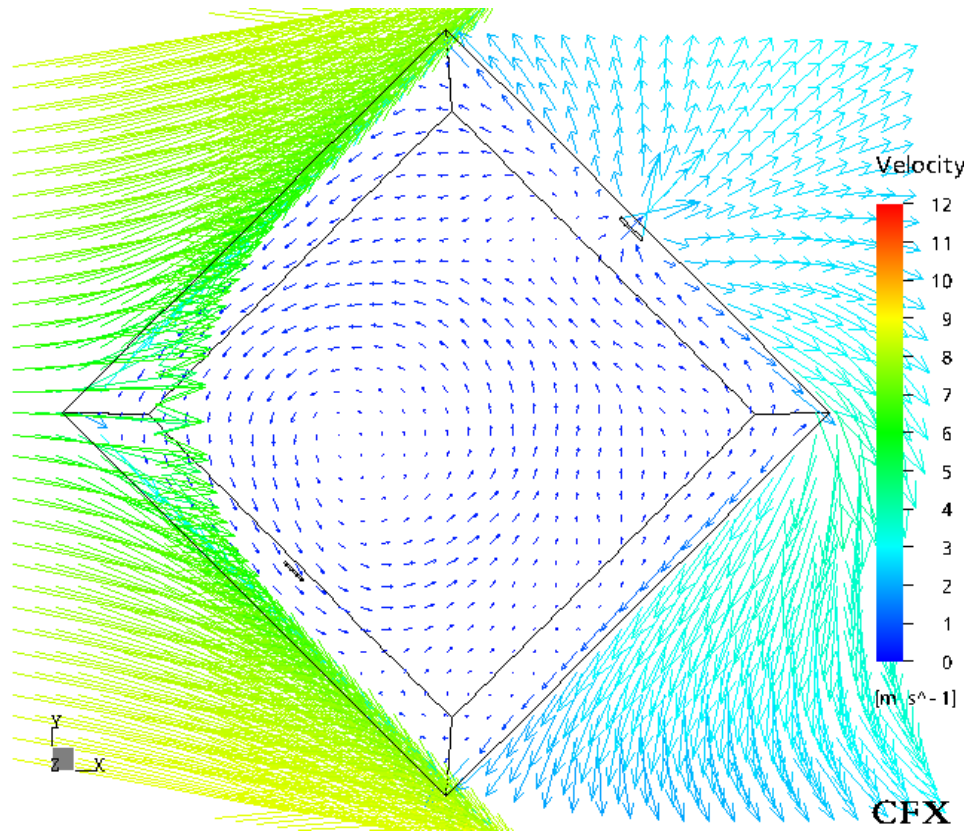


Figure A-15 Velocity vector plot plan view above the ground 5m [45° case]

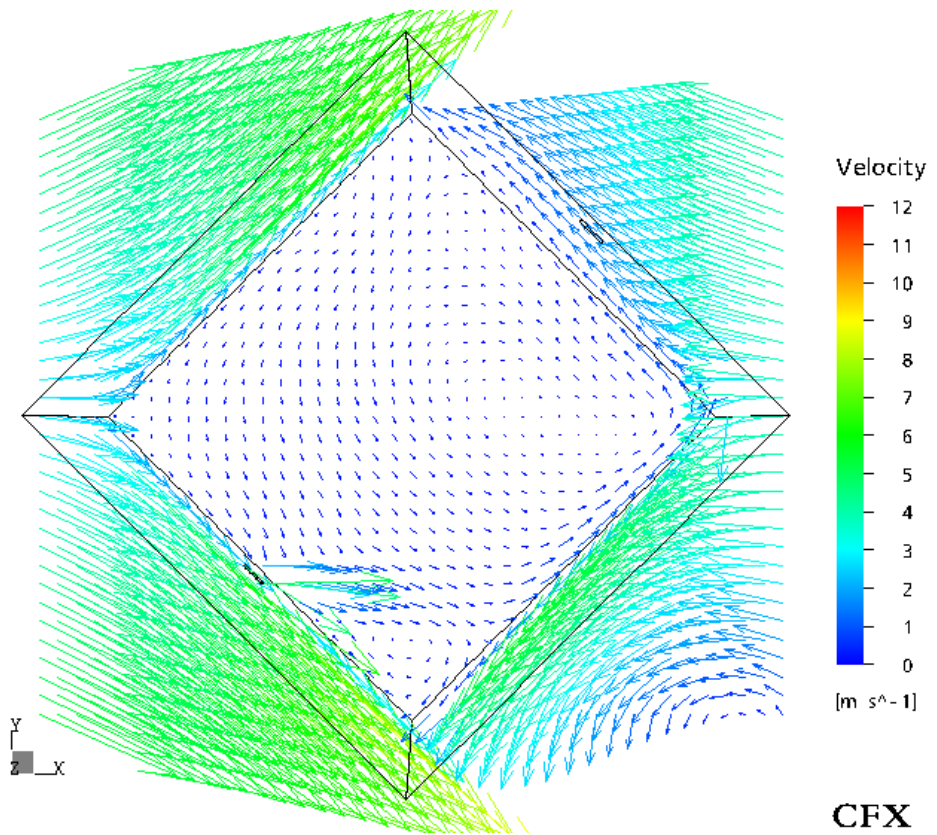


Figure A-16 Velocity vector plot plan view above the ground 1m [45° case]

# Appendix B

	Page
Site plan of the Silsoe 6m cube	B1
Summary of Tables 7-3, 4, 5 & 6	B2

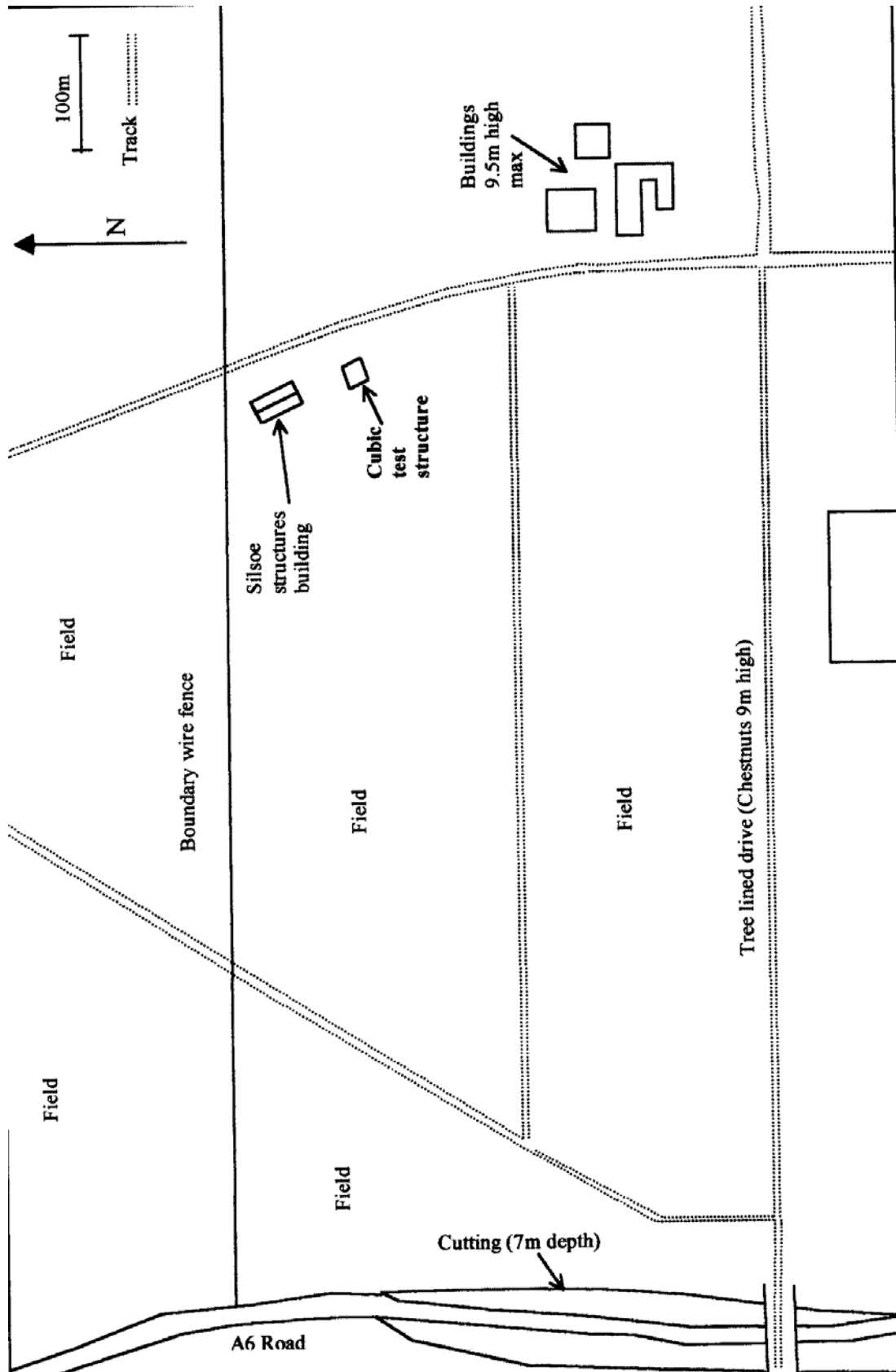


Figure B-1 Site plan of the Silsoe 6m cube

after Straw [2000]

## Summary of Tables 7-3, 4, 5 &amp; 6

82 Test cases 0°~30°		(Q/AU <sub>ref</sub> )			(Q-Q <sub>method1</sub> )/Q <sub>method1</sub> (%)		
		mean	SD	SD/mean(%)	mean	max.	min.
Method 1	{COdecay}	0.63	0.05	8.1	-	-	-
Method 2	{dP}	0.56	0.04	7.5	-11	14	-26
	{dP+dT}	0.57	0.04	7.8	-9	12	-23
Method 3	{dP <sub>taps</sub> +dT}	0.61	0.04	5.9	-3	16	-21
Method 4	Sonic(in)	0.65	0.04	6.6	4	19	-23
	Sonic(out)	0.30	0.02	7.4	-52	-34	-59

16 Test cases 34°~60°		(Q/AU <sub>ref</sub> )			(Q-Q <sub>method1</sub> )/Q <sub>method1</sub> (%)		
		mean	SD	SD/mean(%)	mean	max.	min.
Method 1	{COdecay}	0.57	0.11	20.2	-	-	-
Method 2	{dP}	0.46	0.10	20.7	-18	-3	-32
	{dP+dT}	0.51	0.10	19.8	-10	-1	-22
Method 3	{dP <sub>taps</sub> +dT}	0.56	0.11	19.4	0	15	-25
Method 4	Sonic(in)	0.48	0.14	28.3	-15	10	-38
	Sonic(out)	0.29	0.05	16.7	-49	-41	-55

19 Test cases 75°~110°		(Q/AU <sub>ref</sub> )			(Q-Q <sub>method1</sub> )/Q <sub>method1</sub> (%)		
		mean	SD	SD/mean(%)	mean	max.	min.
Method 1	{COdecay}	0.40	0.08	20.6	-	-	-
Method 2	{dP}	0.31	0.09	29.1	-22	19	-52
	{dP+dT}	0.31	0.10	30.5	-22	19	-52
Method 3	{dP <sub>taps</sub> +dT}	0.41	0.08	19.4	2	36	-22
Method 4	Sonic(in)	0.25	0.11	44.4	-38	-16	-53
	Sonic(out)	0.23	0.06	24.3	-42	-23	-66

13 Test cases 155°~180°		(Q/AU <sub>ref</sub> )			(Q-Q <sub>method1</sub> )/Q <sub>method1</sub> (%)		
		mean	SD	SD/mean(%)	mean	max.	min.
Method 1	{COdecay}	0.54	0.05	8.6	-	-	-
Method 2	{dP}	0.48	0.04	9.1	-11	-3	-22
	{dP+dT}	0.48	0.05	9.9	-11	-4	-19
Method 3	{dP <sub>taps</sub> +dT}	0.51	0.03	5.5	-6	10	-18
Method 4	Sonic(out)	-	-	-	-	-	-
	Sonic(in)_high level	0.70	0.08	10.7	31	41	9

## References

- AEATechnology (2001a). CFX5 User Manual, <http://www-waterloo.ansys.com/product/cfx-5/index.html>.
- AEATechnology (2001b). CFX Users Conference. Solihull, Birmingham.
- AIAA (1998). Guide for the Verification and Validation of Computational Fluid Dynamics Simulations (G-077-1998). American Institute of Aeronautics and Astronautics, <http://www.aiaa.org/store/storeproductdetail.cfm?ID=558>.
- Allard, F. (1998). Natural ventilation in buildings: a design handbook. London, James & James Ltd.
- Allard, F., V. B. Dorer, H. E. Feustel, E. R. Garcia, M. Grosso, M. K. Herrlin, M. Liu, H. C. Phaff, Y. Utsumi and H. Yoshino (1990). Fundamentals of the multizone air flow model - COMIS. International Energy Agency - Air Infiltration and Ventilation Centre, Technical Note AIVC 29, Coventry, UK.
- Awbi, H. B. (1991). Ventilation of Buildings. London, Spon Press.
- Aynsley, R. (1999). "Estimating summer wind driven natural ventilation potential for indoor thermal comfort." Journal of Wind Engineering and Industrial Aerodynamics **83**: 515-525.
- Baptista, F. J., B. J. Bailey, J. M. Randall and J. F. Meneses (1999). "Greenhouse ventilation rate: theory and measurement with tracer gas techniques." J. Agric. Eng. Res. **72**: 363-374.
- Blazek, J. (2001). Computational fluid dynamics: principles and applications. London, Elsevier.
- BRE (1994). Natural ventilation in non-domestic buildings, BRE Digest 399.
- BRE (1997). NATVENT- Overcoming technical barriers to low energy natural ventilation in office type buildings in moderate and cold climates, Building Research Establishment, <http://projects.bre.co.uk/natvent/index.html>.
- BRE (2003). Sustainability lessons from PFI and similar private initiatives and functionality in construction <http://projects.bre.co.uk/sustainabilitylessons>.
- BSI (1991). Code of practice for ventilation principles and designing for natural ventilation, British Standard BS5925.
- Carey, P. S. and D. W. Etheridge (1999). "Direct wind tunnel modelling of natural ventilation for design purposes." Building Serv. Eng. Res. Technol. **20**(3): 131-142.
- Chalabi, Z. S. and J. E. Fernandez (1992). "Greenhouse ventilation rate: theory and measurement with tracer gas techniques." Journal of Agriculture Engineering Research **51**: 139-151.
- Chen, Q. (1995). "Comparison of different k-e models for indoor air flow computations." Numerical Heat Transfer, Part B - Fundamentals **28**(3): 353-369.
- Chen, Q. (2004). "Using computational tools to factor wind into architectural environment design." Energy and Buildings(in press).
- Chen, Q. and W. Xu (1998). "A zero-equation turbulence model for indoor airflow simulation." Energy and Buildings **28**: 137-144.
- Chen, Z. D., Y. Li and J. Mahoney (2001). "Experimental modelling of buoyancy-driven flows in buildings using a fine-bubble technique." Building and Environment **36**(4): 447-455.
- Cheng, Y., F. S. Lien, E. Yee and R. Sinclair (2003). "A comparison of large eddy simulations with a standard k-e Reynolds-averaged Navier-Stokes model for the prediction of a fully developed turbulent flow over a matrix of cubes." Journal of Wind Engineering and Industrial Aerodynamics **91**: 1301-1328.

- Cheong, K. W. (2001). "Airflow measurement for balancing of air distribution system -- tracer-gas technique as an alternative?" Building and Environment **36**: 955-964.
- Chiu, Y. H. and D. W. Etheridge (2004). "Experimental technique to determine unsteady flow in natural ventilation stacks at model scale." Journal of Wind Engineering and Industrial Aerodynamics **92**: 291-313.
- CIBSEAM10 (1997). Natural ventilation in non-domestic buildings, Chartered Institute of Building Services Engineers, Applications manual.
- CIBSEBriefing6 (2003). Energy performance of buildings. London, The Chartered Institution of Building Services Engineering.
- CIBSEBriefing8 (2003). Reducing emissions through energy efficiency - key issues to address in designing and operating buildings. London, The Chartered Institution of Building Services Engineering.
- Cook, M. J., Y. Ji and G. R. Hunt (2003). "CFD modelling of natural ventilaiton: combined wind and buoyancy forces." International Journal of Ventilation **1**(3): 169-179.
- Cook, N. J. (1985). The designer's guide to wind loading of building structures - Part 1: Background, damage survey, wind data and structural classification. London, Butterworths.
- Cook, N. J. (1985). The designer's guide to wind loading of building structures-Part 1: Background, damage survey, wind data and structural classification. London, Butterworths.
- Craft, T. J., B. E. Launder and K. Suga (1996). "Development and application of a cubic eddy-viscosity model of turbulence." International Journal of Heat and Fluid **17**: 108-115.
- Dascalaki, E., M. Santamouris, M. Bruant, C. A. Balaras, A. Bossaer and D. Ducarme (1999). "Modeling large openings with COMIS." Energy and Buildings **30**: 105-115.
- DTIEnergyWhitePaper (2003). Our energy future - creating a low carbon economy. London, Department of Trade and Industry [www.dti.gov.uk/energy/whitepaper/index.shtml](http://www.dti.gov.uk/energy/whitepaper/index.shtml).
- Easom, G. (2000). Improved turbulence models for computational fluid dynamics. School of Civil Engineering. Nottingham, University of Nottingham, UK <http://www.nottingham.ac.uk/~evzngw/download.htm>.
- EC2000InformationDossier2 (2000). Natural ventilation and cooling strategies in new office designs. European Commission Thermie Project to reduce energy and improve comfort and environment, W/E Consultants & University of Athens.
- ERCOFTAC (2000). European Research Community On Flow, Turbulence And Combustion "Best Practice Guidelines for Industrial Computational Fluid Dynamics" <http://imhefwww.epfl.ch/lmf/ERCOFTAC/SIGs/BPG.html>.
- Etheridge, D. W. (1998). "A note on flow equations for ventilation modelling." Building and Environment **33**(5): 325-327.
- Etheridge, D. W. (2000a). "Unsteady flow effects due to fluctuating wind pressures in natural ventilation design--mean flow rates." Building and Environment **35**(2): 111-133.
- Etheridge, D. W. (2000b). "Unsteady flow effects due to fluctuating wind pressures in natural ventilation design--instantaneous flow rates." Building and Environment **35**(4): 321-337.

- Etheridge, D. W. (2002a). "Nondimensional methods for natural ventilation design." Building and Environment **37**: 1057-1072.
- Etheridge, D. W. (2002b). Theoretical and physical modelling of unsteady wind effects on time-averaged natural ventilation. 5th UK Conference on Wind Engineering (WES2002), Nottingham.
- Etheridge, D. W. (2003). "Natural ventilation through large openings - measurements at model scale and envelope flow theory." International Journal of Ventilation **2**(4): 325-342.
- Etheridge, D. W. and M. Standberg (1996). Building ventilation: theory & measurement. Chichester, John Wiley & Sons.
- FLUENT (1992). FLUENT version 4.22 users' manual. <http://www.fluent.com/software/fluent/index.htm>.
- Gan, G. (1999). Lecture Notes - Building Ventilation. MSc in Renewable Energy and Architecture Course. University of Nottingham.
- Gaskell, P. H. and A. K. C. Lau (1988). "Curvature Compensated Convective Transport: Smart, A new boundedness transport algorithm." International Journal for Numerical Methods in Fluids **8**: 617-714.
- GillInstrumentsLtd (2000). Ultrasonic research anemometer manual, <http://www.gill.co.uk/products/anemometer/anemometer.htm>.
- Green, N. E. (1999). Investigations into the impacts of traffic pollution on building ventilation. School of the Built Environment. Nottingham, University of Nottingham, UK.
- Heiselberg, P. (1998). "HybVent - Hybrid ventilation in new and retrofitted office building." Air Infiltration Review **19**(2).
- Heiselberg, P. (1999). "The hybrid ventilation process - theoretical and experimental work." Air Infiltration Review **21**(1).
- Holmes, M. J. and G. M. J. Davies (2003). "Data exchange for thermal modelling and ventilation simulation." International Journal of Ventilation **2**(1): 55-63.
- Hoxey, R. P., P. J. Richards and J. L. Short (2002). "A 6m cube in an atmospheric boundary layer flow Part I. Full-scale and wind-tunnel results." Wind and Structures **5**(2-4): 177-192.
- Hunt, G. R. and P. F. Linden (1999). "The fluid mechanics of natural ventilation - displacement ventilation by buoyancy-driven flows assisted by wind." Building and Environment **34**(6): 707-720.
- Jiang, Y., D. Alexander, H. Jenkins, R. Arthur and Q. Chen (2003). "Natural ventilation in buildings: measurement in a wind tunnel and numerical simulation with large-eddy simulation." Journal of Wind Engineering and Industrial Aerodynamics **91**(3): 331-353.
- Jiang, Y., D. Alexander, H. Jenkins, R. Arthur and Q. Chen (2003a). "Natural ventilation in buildings: measurement in a wind tunnel and numerical simulation with large-eddy simulation." Journal of Wind Engineering and Industrial Aerodynamics **91**(3): 331-353.
- Jiang, Y., C. Allocca and Q. Chen (2003b). "Validation of CFD simulations for natural ventilation." International Journal of Ventilation **2**(4): 359-369.
- Jiang, Y. and Q. Chen (2002). "Effect of fluctuating wind direction on cross natural ventilation in buildings from large eddy simulation." Building and Environment **37**: 379-386.
- Jozwiak, R., J. Kacprzyk and J. A. Zuranski (1995). "Wind tunnel investigations of interference effects on pressure distribution on a building." Journal of Wind Engineering and Industrial Aerodynamics **57**(2-3): 159-166.

- Kaimal, J. C. and J. J. Finnigan (1994). Atmospheric boundary layer flows: their structure and measurement. New York, Oxford University Press.
- Kendrick, J. F. (1993). An overview of combined modeling of heat transport and air movement, AIVC Technical Note 40, Air Infiltration and Ventilation Centre, Coventry, UK, [www.aivc.org/Publications/Technical\\_reports/TN40.htm](http://www.aivc.org/Publications/Technical_reports/TN40.htm).
- Knapp, G., N. G. Wright and J. Owen (2003). Comparison of full-scale and CFD results for the Silsoe 6m cube. 11th International Conference on Wind Engineering (ICWE2003), Lubbock, Texas, USA, Texas Tech University.
- Kolokotroni, M. and A. Aronis (1999). "Cooling-energy reduction in air-conditioned offices by using night ventilation." Applied Energy **63**: 241-253.
- Kukadia, V., M. Kolokotroni, E. Perera, P. Ajiboye, M. Hesketh and P. Willan (1998). Barriers to natural ventilation design of office buildings, National Report: Great Britain. NatVent Publications, BRE, <http://projects.bre.co.uk/natvent/reports/barrier/ukbar.pdf>.
- Launder, B. E., G. J. Reece and W. Rodi (1975). "Progress in the development of Reynolds stress turbulence closure." J. Fluid Mech. **68**: 537-566.
- Launder, B. E. and D. B. Spalding (1974). "The numerical computation of turbulent flows." Computer Methods in Applied Mechanics and Engineering **3**: 269-289.
- Leonard, B. P. (1979). "A stable and accurate convective modeling procedure based on Quadratic Upstream Interpolation." Comput. Methods Appl. Mech. Eng. **19**: 59-98.
- Li, Y. and A. Delsante (2001). "Natural ventilation induced by combined wind and thermal forces." Building and Environment **36**(1): 59-71.
- Li, Y., A. Delsante, J. G. Symons and L. Chen (1998). Comparison of zonal and CFD modelling of natural ventilation in a thermally stratified building. 6th International Conference on Air Distribution in Rooms - Roomvent 98, Stockholm, Sweden.
- Liddament, M. W. (1991). A review of building air flow simulation, AIVC Technical Note 33, Air Infiltration and Ventilation Centre, Coventry, UK, [www.aivc.org/Publications/Technical\\_reports/TN33.htm](http://www.aivc.org/Publications/Technical_reports/TN33.htm).
- Liddament, M. W. (1996). A guide to energy efficient ventilation. Air Infiltration and Ventilation Centre, Coventry, UK.
- Liddament, M. W. and M. Orme (1998). "Energy and ventilation." Applied Thermal Engineering **18**: 1101-1109.
- Linden, P. F., G. F. Lane-Serff and D. A. Smeed (1990). "Emptying filling boxes: the fluid mechanics of natural ventilation." Journal of Fluid Mechanics **212**: 300-335.
- Lomax, H. and T. H. Pulliam (2001). Fundamentals of computational fluid dynamics. New York, Springer.
- Lumley, J. L. (1978). "Computational modeling of turbulent flows." Adv. Appl. Mech. **18**: 123-176.
- Luu, A. (2003). STAR-CD performance, CD Adapco Group, Paris Office <http://www.cd-adapco.com/>.
- Marmont, T. (2003). Renewable energy in the new millennium - economic, environmental and social aspects, Ellis memorial lecture, Midland branch of the Institute of Energy, Beacon Energy. Botanical garden, Birmingham, 8 May 2003.
- Menter, F. R. (1994). "Two equation eddy-viscosity turbulence models for engineering applications." AIAA J. **32**: 1598-1605.

- Meroney, R. N., B. M. Leidl, S. Rafailidis and M. Schatzmann (1999). "Wind-tunnel and numerical modeling of flow and dispersion about several building shapes." Journal of Wind Engineering and Industrial Aerodynamics **81**: 333-345.
- Mochida, M., Y. Tominaga, S. Murakami, R. Yoshie, T. Ishihara and R. Ooka (2002). "Comparison of various k-e models and DSM applied to flow around a high-rise building." Wind and Structures **5**(2-4): 227-244.
- Morvan, H. (2002). CFD Training Course. CFX Support, School of Civil Engineering, University of Nottingham, Nottingham.
- Murakami, S. (1997). "Current status and future trends in computational wind engineering." Journal of Wind Engineering and Industrial Aerodynamics **67-68**: 3-34.
- Murakami, S., A. Mochida, Y. Hayashi and S. Sakamoto (1992). "Numerical study on velocity-pressure field and wind forces for bluff bodies by k-e, ASM and LES." Journal of Wind Engineering and Industrial Aerodynamics **41-44**: 2841-2852.
- Niachou, A., M. Santamouris and M. Kolokotroni (2000). Proposals for a legislative framework, Solar ventilation for urban buildings (SOL-VENT), Group of Building Environmental Studies, National and Kapodistrian University of Athens, Greece, Brunel University, Uxbridge Middlesex.
- Nishizawa, S., T. Sawachi, K. Narita, H. Seto and Y. Ishikawa (2003). "A wind tunnel full-scale building model comparison between experimental and CFD results based on the standard k-e turbulence representation." International Journal of Ventilation **2**(4): 419-429.
- Orme, M. (1999). Applicable models for air infiltration and ventilation calculations, AIVC Technical Note 51, Air Infiltration and Ventilation Centre, Coventry, UK, [www.aivc.org/Publications/Technical\\_reports/TN51.htm](http://www.aivc.org/Publications/Technical_reports/TN51.htm).
- Paassen, A. H. C. v., S. H. Liem and B. P. Groninger (1998). Control of night cooling with natural ventilation - sensitivity analysis of control strategies and vent openings. 19th Annual AIVC Conference, Oslo, Norway.
- Patel, V. C., W. Rodi and G. Scheuerer (1985). "Turbulence models for near-wall and low Reynolds number flows: A review." AIAA J. **23**(9): 1308-1319.
- Prevezer, T. and J. Holding (2002). "Bluff body asymmetric flow phenomenon - real effect or solver artefact?" Wind and Structures **5**(2-4): 359-368.
- Prianto, E. and P. Depecker (2002). "Characteristic of airflow as the effect of balcony, opening design and internal division on indoor velocity: A case study of traditional dwelling in urban living quarter in tropical humid region." Energy and Buildings **34**(4): 401-409.
- Raw, M. (1996). Robustness of coupled algebraic multigrid for the Navier-Stokes equations. 34th Aerospace and sciences meeting & exhibit, Reno.
- Richards, P. J. (2004). Quasi-steady theory developed with experimental verification. Silsoe Research Institute Seminar, Bedford, UK, 23 Jan 2004.
- Richards, P. J. and R. P. Hoxey (1993). "Appropriate boundary conditions for computational wind engineering models using the k-epsilon turbulence model." Journal of Wind Engineering and Industrial Aerodynamics **46&47**: 145-153.
- Richards, P. J. and R. P. Hoxey (2002). "Unsteady flow on the sides of a 6m cube." Journal of Wind Engineering and Industrial Aerodynamics **90**: 1855-1866.

- Richards, P. J., A. D. Quinn and S. Parker (2002). "A 6m cube in an atmospheric boundary layer flow Part 2. Computational solutions." Wind and Structures **5**(2-4): 177-192.
- Roache, P. J. (1998). Verification and validation in computational science and engineering. Albuquerque, New Mexico, Hermosa.
- Sharma, R. N. and P. J. Richards (1999). "The influence of Reynolds stresses on roof pressure fluctuations." Journal of Wind Engineering and Industrial Aerodynamics **83**: 147-157.
- Shea, A. and A. Robertson (2004). Discharge coefficients vary with depth of opening. Silsoe Research Institute Seminar, Bedford, UK, 23 Jan 2004.
- Sinai, Y. (2004). Fire and Fire modelling. CFD@Nottingham lecture, University of Nottingham, Nottingham, UK, 15 May 2004.
- Speziale, C. G. (1987). "On non-linear k-l and k-e models of turbulence." J. Fluid Mech. **178**: 459-475.
- Speziale, C. G., S. Sarkar and T. B. Gatski (1991). "Modelling the pressure-strain correlation of turbulence: an invariant dynamical systems approach." J. Fluid Mech. **277**: 245-272.
- Standberg, M. and C. Blomqvist (1985). "A quantitative estimate of the accuracy of tracer gas methods for the determination of the ventilation flow rate in buildings." Building and Environment **20**(3): 139-150.
- Stangroom, P. and N. G. Wright (2003). CFD modelling of the Askervein Hill. 11th International Conference on Wind Engineering (ICWE2003), Lubbock, Texas, USA, Texas Tech University.
- Stathopoulos, T. (2002). "The numerical wind tunnel for industrial aerodynamics: Real or virtual in the new millennium?" Wind and Structures **5**(2-4): 193-208.
- Straw, M. P. (2000). Computation and measurement of wind induced ventilation, PhD thesis. School of Civil Engineering. Nottingham, University of Nottingham, UK <http://www.nottingham.ac.uk/~evzngw/download.htm>.
- Thomas, T. G. and J. J. R. Williams (1999). "Simulation of skewed turbulent flow past a surface mounted cube." Journal of Wind Engineering and Industrial Aerodynamics **81**: 347-360.
- Tsuchiya, M., S. Murakami, A. Mochida, K. Kondo and Y. Ishida (1997). "Development of new k-e model for flow and pressure fields around bluff body." Journal of Wind Engineering and Industrial Aerodynamics **67 & 68**: 168-182.
- Turner, J. S. (1973). Buoyancy effects in fluids. London, Cambridge University Press.
- Versteeg, H. K. and W. Malalasekera (1995). Introduction to computational fluid dynamics: the finite volume method. Harlow, Longman Scientific & Technical.
- White, B. R. (2001). Physical modeling of atmospheric flow and environmental applications, Department of Mechanical and Aeronautical Engineering, University of California, Davis, USA: <http://mae.ucdavis.edu/~wind/publications/modeling.html>.
- Wilcox, D. C. (1993). Turbulence modelling for CFD. California, DCW Industries, Inc.
- Wilson, A. G. (1961). CBD-23. Air Leakage in Buildings, Institute for Research in Construction (IRC), Canadian building digest, <http://irc.nrc-cnrc.gc.ca/cbd/cbd023e.html>.

- Wright, N. G. (2000). Computational Fluid Dynamics. Graduate School Training Course, University of Nottingham, Nottingham.
- Wright, N. G. (2002). Supervision meetings. School of Civil Engineering, University of Nottingham, Nottingham.
- Wright, N. G. and G. J. Easom (1999). "Comparison of several computational turbulence models with full-scale measurements of flow around a building." Wind and Structures **2**(4): 305-323.
- Wright, N. G. and G. J. Easom (2003). "Non-linear k-e Model results for flow over a building at full-scale." Applied Mathematical Modelling **27**: 1013-1033.
- Wright, N. G., G. J. Easom and R. J. Hoxey (2001). "Development and Validation of a Non-linear k-e Model for Flow over a Full-scale Building." Wind and Structures **4**(3): 177-196.
- Yakhot, V., S. A. Orsag, S. Thamgam, T. B. Gatski and C. G. Speziale (1992). "Development of turbulence models for shear flows by a double expansion technique." Physics of Fluids, Part A - Fluid Dynamics **4**(7): 1510-1520.
- Zhai, Z. and Q. Chen (2003). "Solution characters of iterative coupling between energy simulation and CFD programs." Energy and Buildings **35**(5): 493-505.
- Zhai, Z. and Q. Chen (2004). "Numerical determination and treatment of convective heat transfer coefficient in the coupled building energy and CFD simulation." Building and Environment(in press).